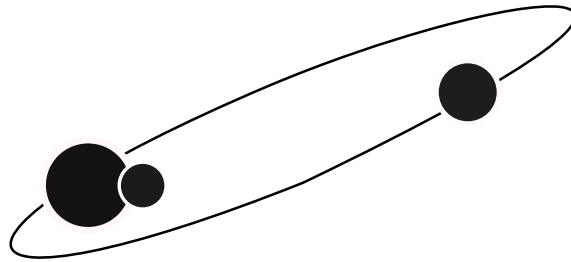


Comprehensive study of low-mass Compact Hierarchical Triples using Eclipsing Binaries



Ayush Moharana

under the supervision of
Dr. hab. K.G. Hełminiak

A thesis submitted in fulfilment of the requirements
for the degree of Doctor of Philosophy



Nicolaus Copernicus Astronomical Center
of the Polish Academy of Science

To Mama and Baba ...

Declaration

I hereby declare that, except where acknowledged appropriately either below or in the text, this thesis is my original work undertaken at the Nicolaus Copernicus Astronomical Center, of the Polish Academy of Sciences, between December 2019 and May 2024.

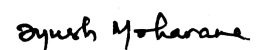
This thesis has been submitted as a 'Thesis by Compilation' in accordance with the 'Procedure and rules for the award of the degree of doctor' of the NCAC PAS. Two of the three main chapters are therefore a completely self-contained articles that have been published in a peer-reviewed journal, and one of them has been submitted.

Chapter 2 contains the paper "[Solaris photometric survey: Search for circumbinary companions using eclipse timing variations MNRAS, 2024, 527, 53](#)". I am the leading author of the paper and I contributed 60% to the paper including creation of the *Solaris* inventory, the photometric pipeline, light curve analysis, search for periodicity, modelling of eclipse timing variations and drafting the manuscript.

Chapter 4 contains the paper "[Detached eclipsing binaries in compact hierarchical triples: triple-lined systems BD+442258 and KIC 06525196](#)", *MNRAS*, 2023, 521, 2, 1908. I am the leading author of this paper and contributed to 70% of the work in the paper. I contributed to the light curve modelling, spectral disentangling, spectral analysis, numerical integrations of the orbital evolution, and constraining the spot evolution in the system. The contribution also includes drafting the paper and creating the plots in it.

Chapter 5 contains the paper "Spectroscopy of Eclipsing Compact Hierarchical Triples" which is submitted to *Astronomy and Astrophysics*. I am the leading author of this paper and contribute to 70% of the work. I contributed to light curve modelling, spectral disentangling, spectral analysis, numerical integration of the orbit, isochrone fitting of two systems, and the statistical study in the paper, along with the drafting of the manuscript.

The remainder of this thesis was drafted solely by the candidate conditioned to the changes suggested by the supervisor Dr. hab. K.G. Hełminiak.



Ayush Moharana

Supplementary Research

In addition to the work presented in this thesis, the candidate has contributed to several other research projects during the PhD program. A complete list of peer-reviewed journal articles authored or co-authored by the candidate during the 4.5 years are listed here in reverse chronological order:

“Discovery of a hot post-AGB star in Galactic globular cluster E3 ”

Kumar, R. ; Moharana, Ayush ; Piridi, S. ; Pradhan, A. C. ; Hełminiak, K. G. ; Ikonnikova, N. ; Dodin, A. ; Szczerba, R. ; Giersz, M. ; Ojha, D. K. ; Samal, M. R., *A&A Letters*, 2024, Volume 685, L6, p.1-11

“Solaris photometric survey: Search for circumbinary companions using eclipse timing variations ”

Moharana, Ayush; Hełminiak, K. G.; Marcadon, F. ; Pawar, T.; Pawar, G.; Garczyński, P. ; Perla, J. ; Kozłowski, S. K. ; Sybilski, P. ; Ratajczak, M. ; & Konacki, M., *MNRAS*, 2024, Volume 527, Issue 1, pp.53-65

“Detached eclipsing binaries in compact hierarchical triples: triple-lined systems BD+442258 and KIC 06525196 ”

Moharana, Ayush; Hełminiak, K. G.; Marcadon, F. ; Pawar, T. ; Konacki, M. ; Ukita, N. ; Kambe, E. ; & Maehara, H. , *MNRAS*, 2023, Volume 521, Issue 2, pp.1908-1923

“Comprehensive spectroscopic and photometric study of pulsating eclipsing binary star AI Hya ”

Kahraman Alıçavuş, F.; Pawar, T.; Hełminiak, K. G. ; Handler, G. ; Moharana, Ayush ; Alıçavuş, F.; De Cat, P.; Leone, F.; Catanzaro, G.; Giarrusso, M. ; Ukita, N. ; & Kambe, E., *MNRAS*, 2023, Volume 520, Issue 2, pp.1601-1612

“The Cluster Ages Experiment (CASE) - IX. Analysis of four detached eclipsing binaries in the globular cluster NGC 3201 ”

Rozyczka, M. ; Thompson, I. B. ; Dotter, A. ; Mazur, B. ; Narloch, W. ; Pych, W. ; Hełminiak, K. G. ; Moharana, Ayush; Beletsky, Y. ; Burley, G. S. ; Marshall, J. L. ; Morrell, N. ; Osip, D. ; Shtetman, S. A. ; Bernstein, R. ; Pilecki, B. ; Zgirski, B. , *MNRAS*, 2022, Volume 517, Issue 2, pp.2485-2501

“Orbital and physical parameters of eclipsing binaries from the ASAS catalogue - XII. A sample of systems with K2 photometry ”

Hełminiak, K. G. ; Moharana, Ayush ; Pawar, T. ; Ukita, N. ; Sybilski, P. ; Espinoza, N. ; Kambe, E. ; Ratajczak, M. ; Jordán, A. ; Maehara, H. ; Brahm, R. ; Kozłowski, S. K. ; Konacki, M. , *MNRAS*, 2021, Volume 508, Issue 4, pp.5687-5708

“Ultraviolet Imaging Telescope (UVIT) observation of the Galactic globular cluster NGC 7492 ”

Kumar, Ranjan ; Pradhan, Ananta C. ; Mohapatra, Abhisek ; Moharana, Ayush ; Ojha, Devendra K. ; Parthasarathy, M. ; Murthy, Jayant , MNRAS, 2021, Volume 502, Issue 1, pp.313-327

“Consequences of parameterization choice on eclipsing binary light curve solutions ”

Korth, J. ; Moharana, Ayush ; Pešta, M. ; Czavalinga, D. R. ; Conroy, K. E. , Contributions of the Astronomical Observatory Skalnaté Pleso, Volume 51, No. 1, p. 58-67

Acknowledgements

" In this terrifying world,
all we have are the connections we make."
–Raphael Bob-Waksberg, Creator, Bojack Horseman

This thesis was drafted within a few months. But the foundations for it were set up over a longer period. To sustain it this long was not a solo effort.

I am greatly indebted to my supervisor Dr. Krzysztof Hełminiak. His support from day one has been unwavering. A major portion of my work and this thesis stands on the scientific and moral support he offered. I am thankful for his patience when I randomly bombarded his office with weird ideas and silly questions. Even outside the office, he helped me manoeuvre through documents, contracts and life in general. I still remember thanking him for helping me move and he replied, "It's okay, we just help each other". For this I am grateful.

I want to thank Dr. Tomek Kamiński for being my first friend both in the office and in Toruń. Starting from the first day Tomek has been an amazing support and also been the person who gives you necessary reality checks. I am also thankful for his patience when I randomly bombarded his office with weird ideas and silly questions. I am grateful for all those lunch discussions about science, academia, science fiction and his favourite, CrossFit.

I acknowledge the support from Prof. Maciej Konacki whose generous support helped me through my PhD, publications and job interviews. I am also thankful to Frédéric Marcadon, who has been ready to help me out with light curves and manuscripts from Torun, Paris, and Villanova.

I acknowledge the help and support that I got from Dr. Radek Smolec during my doctoral studies. I am also thankful to people behind the scenes, Jurek, Kasia, Dominika, Angelika, and Natasha. Doing science was a lot easier because of you.

I am eternally grateful to people who have driven my curiosity for science. I would like to thank my professors from NIT Rourkela Dr. A.C. Pradhan, and Dr. J.P. Kar who helped me develop a knack for research. I am also grateful to Dr. Debbijoy Bhattacharya at MCNS Manipal, whose influence was pivotal in my decision to pursue research. I thank Swayamtrupta Panda, who has always inspired me to aim for the stars. Finally, I thank Ranjan Kumar for showing me the importance of small details in research.

I appreciate the support I got from Rajeev Singh Rathour. Going together through Arxiv,

codes and gossip at 4 AM, Rajeev always encouraged me to never settle for less. I thank Abinash for his support and help with things that I could never do on my own.

My colleagues at work, Tilak, Ganesh, Tom and Zain have been a blessing both at work and outside of work. Fussing about codes, lectures, and paperwork bonded us more than all the life-changing events that we all went through during the weekends. I am thankful for them heading out for pool or a drink, whenever I needed to clear my mind. For this, and every other thing that I am not able to recall right now, I am grateful.

I would like to thank my colleagues and friends who made my visits to Warsaw memorable: Suhani, Ishika, Ruchi, Chandra, and Ankan.

Back in India, I am lucky to have a big support system in Animesh, Subendra, Anshuman, Saswat, Ardhendu, Satyajit, Adithyan, NC, Pratap, Gagan, Amrit, Sai and Siddhanta. I also acknowledge the support my fellow physicists gave me during my Masters: Aditya, Swaroop, Hardik, Prathemesh, Disha and Baishali.

I was grateful to have people in Piwnice who made doing Astronomy in Torun, fun: Nicolas, Helena, Matteo, Marius, Eleonora, Quentin, Antoine, and Ngan. I acknowledge my mates at the Sunday football who helped we replenish myself to go back to my work stronger. To Anuradha, Dhraști, and Thiliban, the people who never made me feel homesick. To Seiji, Jola, Sylwia, Sagnik, Kamil, Steffi, Gula, and Radik, thank you for all the good memories in Toruń.

To Simran and Asia, you made Toruń feel like my second home. Thank you, for your patience when I rambled about my work. All the things you did, made my life outside of work peaceful.

I am blessed to have a supporting family. I am also grateful for all the wishes conferred by my late grandmother. May her soul rest in peace.

Last but not least, I am indebted to my parents. They made me what I am today.

Abstract

The multiplicity of stars is a well-established phenomenon. But still, the theory of formation, evolution, and stability of multiple-star systems is a field that has a lot of unanswered questions. One of the least studied aspects in one of the simplest multiplicities is the evolution of hierarchical triple systems. Triple systems have been used as an explanation for the formation of close binaries, blue stragglers, planetary nebulae, and also the merger of several black holes. But most of these systems have long outer periods and their dynamic effects can have timescales of years and decades. Therefore studying them in detail can be a time-consuming process.

Meanwhile, there is a subset of these triples called the Compact Hierarchical Triple (CHT), which offers more potential for observational astrophysics. These are triple systems with an outer orbit period of fewer than 1000 days. CHT were once considered to be rare but with new observations from photometric space missions, we are discovering more of these systems. CHTs lay in the domain where we can see most, if not all, of the different dynamical interactions that occur in a triple star system. The dynamic processes in CHTs can be observed in time scales less than a human lifetime. Since most of the triples known previously have wide orbits, these systems are one of the remaining candidates to explore the full scale of triple systems. Therefore CHTs can act as probes to multiple-star formation, dynamics and evolution. The orbital separations of these systems are similar to planetary systems. Understanding CHTs can thus act as a stepping stone for understanding planetary formation and evolution. Till now, the number of CHT candidates is less than 700. Only 43 have been completely characterised. Therefore, we need to (i) detect more CHTs to improve the sample, and (ii) characterise the stellar, orbital and atmospheric parameters to understand the configurations of these systems.

Detached Eclipsing Binaries (DEB) are known as the source of the most accurate stellar parameters. We can reach accuracy up to less than 1% with high-quality observations. Such accurate stellar parameters are difficult to obtain with other methods. If a CHT has a DEB as their inner binary, we have an added advantage of obtaining very accurate stellar parameters of not only the binary but of the tertiary as well. In this thesis, we detect and also obtain an accurate picture of the orbits, geometry, metallicity, age, and evolutionary status of a sample of CHTs.

We search for CHT with the method of eclipse timing variations (ETV) using observations from the *Solaris* photometric survey. A radial velocity search, using doubled-lined and triple-lined DEB, is carried out using high-resolution spectroscopy. We supplement the spectroscopy with high-precision *TESS* photometry for our sample of CHT. Using complex contemporary techniques in modern astronomy, we obtain stellar, orbital, and atmospheric parameters of all three stars in a CHT. Light curve modelling, radial velocity modelling, spectral disentangling, and spectral analysis are all carried out to get a set

of independent and consistent set of parameters. Using these parameters we probe the evolution, dynamics and distribution of the parameters, with a goal of constraining the formation theories of these rare systems.

In this thesis, we report the detection of nine low-mass CHTs. 6 CHTs are analysed in detail to give the first detailed spectroscopic analyses of these CHTs. In our detailed analyses, we find the ages of the CHTs as well as the evolutionary states of all stars in the system. There exist around 43 CHTs in the literature with the same detail in analyses as our work provides. We add our systems to this sample to visualise distributions of different parameters and study their implication on the current CHT formation and evolution theories. Apart from contributing to studies of CHTs, we add 6 DEBs to the collection of accurate parameters of eclipsing binaries. While this is a small addition to a small sample, the work sets the foundation for future studies of CHTs and multiples using upcoming high-resolution spectrographs and precision space telescopes.

Streszczenie

Wielokrotność gwiazd jest zjawiskiem dobrze znanym. Jednak teoria powstawania, ewolucji i stabilności dynamicznej układów wielokrotnych gwiazd to dziedziny, w których wciąż pozostaje wiele pytań bez odpowiedzi. Jednym z najsłabiej zbadanych aspektów, w jednej z najprostszych konfiguracji, jest ewolucja hierarchicznych układów potrójnych. Układy potrójne wykorzystano jako wyjaśnienie powstawania ciasnych układów podwójnych, niebieskich maruderów, mgławic planetarnych, a także łączenia się kilku czarnych dziur. Jednak większość tych systemów ma długie okresy orbity zewnętrznej, a ich oddziaływania dynamiczne mierzy się w skali czasowej wielu lat i dziesięcioleci. Dlatego szczegółowe ich studiowanie może być procesem bardzo czasochłonnym.

Tymczasem istnieje podzbiór tych układów potrójnych, zwany *Compact Hierarchical Triples* (CHT), który oferuje większy potencjał z punktu widzenia astrofizyki obserwacyjnej. Są to układy potrójne z okresem orbity zewnętrznej krótszym niż ~ 1000 dni. Kiedyś uważano, że CHT są nieliczne, ale dzięki nowym obserwacjom z fotometrycznych misji kosmicznych odkrywamy więcej takich układów. W przypadku CHT możemy obserwować większość, jeśli nie wszystkie, różnych dynamicznych interakcji zachodzących w układzie trzech gwiazd. Procesy dynamiczne w CHT można obserwować w skalach czasowych dużo krótszych niż czas życia człowieka. Ponieważ większość znanych wcześniej trójek ma szerokie orbity, układy CHT są jednymi z brakujących składników do badania układów potrójnych w pełnej skali. Dlatego też CHT mogą działać jako narzędzia do badania powstawania, dynamiki i ewolucji gwiazd wielokrotnych. Odległości między składnikami tych układów są podobne do rozmiarów orbit układów planetarnych. Dlatego zrozumienie CHT może również przyczynić się do zrozumienia powstawania i ewolucji planet. Do chwili obecnej liczba kandydatów na CHT wynosi niecałe 700. Dokładniej przestudiowano jedynie 43. Należy zatem (i) odkryć więcej CHT, aby zwiększyć ich próbkę, oraz (ii) scharakteryzować parametry gwiazdowe, orbitalne i atmosferyczne, aby zrozumieć właściwości tych układów.

Rozdzielone układy podwójne zaćmieniowe (*detached eclipsing binaries*; DEB) są znane jako źródło najdokładniejszych parametrów gwiazdowych. Dzięki wysokiej jakości obserwacjom możemy osiągnąć dokładność lepszą niż 1%. Tak dokładne parametry gwiazdowe są trudne do uzyskania innymi metodami. Jeśli CHT ma DEB-a jako swój wewnętrzny układ podwójny, mamy dodatkową zaletę w postaci otrzymania bardzo dokładnych parametrów gwiazdowych nie tylko układu podwójnego, ale także trzeciej gwiazdy. W tej pracy wykrywamy, a także uzyskujemy dokładny obraz orbit, geometrii, metaliczności, wieku czy statusu ewolucyjnego dla próbki układów CHT.

CHT poszukujemy m.in. metodą chronometrażu zaćmień (*eclipse timing variations*; ETV), wykorzystując obserwacje z projektu fotometrycznego *Solaris*. Wykorzystujemy także spektroskopię wysokiej rozdzielczości potrójnych układów zaćmieniowych dwu- i trójliniow-

ych, szukając zmian w prędkościach radialnych. Dane dla naszej próbki CHT uzupełniamy o bardzo precyzyjną fotometrię z satelity *TESS*. Stosując złożone, współczesne techniki współczesnej astronomii, uzyskujemy parametry gwiazdowe, orbitalne i atmosferyczne wszystkich trzech gwiazd w układzie. Modelowanie krzywej blasku, modelowanie prędkości radialnych, rozplątywanie widm i analiza widmowa są przeprowadzane w celu uzyskania zestawu niezależnych i spójnych parametrów. Korzystając z tych parametrów, badamy ewolucję, dynamikę i rozkład parametrów w celu lepszego zrozumienia procesu powstawania tych rzadkich układów.

W tej pracy opisujemy wykrycie dziewięciu CHT o małej masie. Cztery z tych dziewięciu, oraz dwa wcześniej zidentyfikowane CHT, są szczegółowo badane w celu uzyskania pierwszych analiz spektroskopowych tych układów. W naszych szczegółowych analizach wyznaczamy wiek CHT, a także fazy ewolucyjne wszystkich gwiazd w układzie. W literaturze istnieje około 43 CHT zbadanych w sposób podobny do tego, jaki opisuje niniejsza praca. Dodajemy nasze systemy do tej próbki, aby zobrazować rozkłady różnych parametrów i badać ich wpływ na obecne teorie powstawania i ewolucji CHT. Oprócz wkładu w badania CHT, dodajemy 6 układów do zbioru układów zaćmieniowych z bardzo dokładnie wyznaczonymi parametrami. Chociaż jest to niewielki dodatek do małej próbki, praca ta stanowi podstawę dla przyszłych badań CHT i wielokrotności gwiazdowej, z wykorzystaniem nowych spektrografów wysokiej rozdzielczości i precyzyjnych teleskopów kosmicznych.

Contents

Declaration	i
Supplementary Research	ii
Acknowledgements	v
Abstract	vii
Streszczenie	ix
List of Figures	xiii
List of Tables	xvii
1 Twinkle, twinkle multiple stars: Stellar multiplicity at a glance	1
1.1 History of stellar multiplicity	1
1.2 Multiple stars in large surveys	2
1.3 Multiple stars in the era of space-telescopes	3
1.3.1 Eclipsing binaries	4
1.3.1.1 Detached Eclipsing Binaries	5
1.3.2 Renaissance of the triples	5
1.4 Compact hierarchical triples	8
1.4.1 CHT formation scenarios	9
1.4.2 CHT evolution scenarios	12
2 Three in one: Search for Compact Hierarchical Triples	17
2.1 Broadening Functions	18
2.2 Radial Velocities	19
2.3 Eclipse timing variations	20
2.3.1 The Solaris Photometric Survey	22
3 Everything in the Arsenal: Extraction of absolute parameters	37
3.1 Stellar and orbital parameters	37

3.1.1	Light curve modelling	37
3.1.2	Radial velocity modelling	41
3.1.3	Numerical integration of dynamics	42
3.2	Atmospheric parameters	44
3.2.1	Spectral disentangling	44
3.2.1.1	Fourier-space disentangling	44
3.2.1.2	Velocity-space disentangling	45
3.2.1.3	Bias progression and cleaning trends	45
3.2.2	Spectral analysis	46
4	Written in the stars: Parameters to evolution and dynamics	49
4.1	Detached eclipsing binaries in compact hierarchical triples	50
5	Three in a crowd: Distributions of CHT parameters	67
5.1	Orbital elements from CHT searches	67
5.2	Spectroscopy of Eclipsing Compact Hierarchical Triples	69
6	Conclusions	91
6.1	Detection of CHTs	91
6.2	Extraction of absolute parameters	92
6.3	Formation and evolution of CHTs	93
6.4	Future scope	95
	Appendix A Line lists for spectral fitting	97
	Appendix B Mass distributions from surveys	101
	List of acronyms	101
	Bibliography	106

List of Figures

1.1	Bias-corrected multiplicity fraction (left; thick), triple/high-order fraction (left; thin), and companion frequency (right) of BDs and MS stars. All three quantities increase monotonically with primary mass. The indicated spectral types at the top roughly correspond to the mean primary masses of field dwarfs. Figure credits: Offner et al. (2023).	3
1.2	Morphologies of stars in EBs and their resultant light curves. Figure credits: Kang (2010).	5
1.3	Spread of parameters obtained by LC modelling with different methodology (different markers) for the same observation of AI Phe. Figure credits: Maxted et al. (2020).	6
1.4	Different ETV (O-C signals) for different hierarchical triple systems. Figure credits: Borkovits et al. (2016).	7
1.5	Various light curve morphologies of triply eclipsing systems. The red lines show the model obtained by LIGHTCURVEFACTORY. Figure credits: Rappaport et al. (2023).	7
1.6	Different light curve morphologies of EDV systems as observed by <i>Kepler</i> . Figure credits: Borkovits (2022).	8
1.7	Different orbital configurations of the first 6 E3CHTs in Figure 1.5. Figure credits: Rappaport et al. (2023).	9
1.8	The left and right panels show the binary formation channels, disk instability and core fragmentation respectively. The end products of both the stars undergo migration to come to smaller scales that we observe. Figure credits: Tokovinin (2021).	10

1.9 (Left) Distribution of mass and period of known BD companions compiled by Ma & Ge (2014). The curves at the bottom denote different RV precision. The box shows the approximate location of the BD desert. (Right) Period histogram of BD companions around solar-type stars. Figure credits: Ma & Ge (2014). 12

1.10 3D geometry of a triple star system, with the primary (m_1) as the origin. m_1, m_2 denote the masses of the two inner binary while m_3 denotes the tertiary mass. M_{12} represents $m_1 + m_2$. w, w' represent the true longitudes of the secondary and tertiary respectively, measured from the intersection of the orbits. u, u' represents the same with respect to the sky plane. i, i' denote the inclinations with the sky plane and i_m denotes the mutual inclination of the inner and outer orbits. ρ denotes Jacobian position vectors. The various symbols are described in detail in Borkovits et al. (2003). 13

1.11 Different evolutionary products possible from triple systems. a) is a hierarchical triple for reference, M_1 is the primary and most massive star in the inner binary, M_2 is the secondary and least massive star in the inner binary, M_3 is the outer tertiary. The semi-major axis of the inner binary is a_1 and the outer tertiary is a_2 . b) shows the colours used to represent different evolutionary stages. c) are various orbital configurations. The formation channels leading to triple, binary and single-star products are shown. Figure credits: Preece et al. (2022). 16

2.1 (Left) A comparison of CCF and BF for the same observed spectrum and template. (Right) BF shapes for different physical processes and configurations of a stellar system. 19

2.2 Inner binary period (P_1) vs tertiary period (P_2) of CRÉME CHT discoveries. The square (in pink) represents initially published CHT while triangles (in blue) show the CHTs discovered during this work. The grey points denote CHTs discovered in the literature. The empty space on the bottom right is the instability space of triples (see Equation 1.1). 20

2.3 Time scales of different ETV signatures. (Top left) A LTTE fit to O-C (τ in secs). (Top right) A combined LTTE and dynamical fit to the same set of observations. Adopted from Marcadon et al. (2020). (Bottom left) A zoomed-in view of the ETV signals comprising of LTTE and dynamical variations. (Bottom right) A zoomed-out view of the same target shows long-term apse-node perturbations on top of the LTTE and the dynamical effects. Adopted from Borkovits et al. (2022). 21

3.1	A simple, geometric model of an eclipse of two uniform disks. The important times for LC modelling are also marked. From: Michael Richmond (http://spiff.rit.edu/classes/phys370/lectures/eclipse_1/eclipse_1.html)	38
3.2	Geometry of a binary system in the Roche model. Figure credits: Prša (2018)	39
3.3	Different Roche potentials for different binary morphologies. The blue and green lines show the potential for detached systems, black for semi-detached and pink and red represent contact systems. Figure credits: Prša (2018).	40
3.4	Translating RV from a 3D geometry. (Left) Top-down view of a 2-body orbit (a planet and a star here) with relevant parameters labelled. The orbit of interest, and the one which is translated, is in blue and in the same plane as the paper. (Right) The RV translation of the motion of the star. Figure credits: Fulton et al. (2018).	41
3.5	(Left) Examples of bias progression in disentangled spectra. (Right) A method to model the bias signals and remove it to get clean spectra. Figure credits: Hensberge et al. (2008).	46
5.1	Distributions of outer orbital eccentricities. (Left) Differential probability distribution of the outer orbit eccentricities for GAIA hierarchical triple star candidates. Different colours represent different types of Gaia NSS orbital solutions. The magenta line shows the analytical function described in Czavalinga et al. (2023). (Right) Cumulative eccentricity distributions. Green – OGLE; blue – <i>Kepler</i> ; red – GAIA; purple – $dN/de = \text{constant}$; black – a so-called thermal distribution with $dN/de \propto e$. Figures from Czavalinga et al. (2023).	68
5.2	Approximate tertiary to binary mass ratio, $M'_3/(M'_1 + M'_2)$, from different CHT searches. GAIA- green, <i>Kepler</i> - red, and OGLE - blue. The two prominent peaks are approximately around 0.4 and 0.9.	68

List of Tables

3.1	Table of the planned properties to be studied and the methods to obtain them.	48
A.1	LL1: Line list for metallicity and abundance estimation.	98
A.2	LL2: Line list for parameters estimation.	99

CHAPTER 1

Twinkle, twinkle multiple stars: Stellar multiplicity at a glance

तारा, तारे , ताराः ।

"Tara, Tare, Tarah."

"Star, two stars, more than two stars."

– Sanskrit word-forms¹ for stars

Stars have been one of the oldest natural objects that have fascinated humans. Advancing through all those centuries of fascination and its use for navigation, time-keeping, and simply understanding our purpose, an important revelation was when we realised that the Sun itself is a star like the many in our night sky. This created a simple idea that probably still exists among a lot of non-astronomers: The other stars out there are just distant Suns, floating in isolation from other stars. But this idea was long debunked when astronomers discovered that stars can exist in pairs.

1.1. History of stellar multiplicity

During the initial phases of modern astronomy, binary stars (or double stars, as they were called) were the ones which seemed close by when seen by the naked eye. Some of the first documented mentions of gravitationally bound binary stars include Mizar and Acrux. Back around 800 AD, *Arundhati* (Alcor) and *Vashista* (Mizar) were mentioned as

¹Sanskrit has dual form of words, along with singular and plural forms

"couple" stars in the old Indian scripture, *Bhagawata Purana* and are still symbolic in rituals of Indian weddings. In recent recorded history, Mizar was (reportedly) observed to be a double by Giovanni Battista Riccioli in 1650 (and probably earlier by Benedetto Castelli and Galileo). Surprisingly, upon further investigation (as in the case of this thesis), the components were found to be multiple stars themselves.

The first systematic study of binary stars was done by William Herschel in the 1700s when he found pairs of stars in his 'Catalogue of One Thousand New Nebulae and Clusters of Stars' (Herschel 1786). It was Herschel himself who coined the term "binary star". The initial binaries discovered were all visual binaries. Castor, with an orbital period of 342 yr (modern estimates suggest 420 yr) was the first binary star characterised by its orbital motion (Herschel 1803). Algol was classified as a binary by John Goodricke in 1783, to explain the observed eclipses in the photometric light curve. Algol was also classified as a spectroscopic binary, when Vogel (1890) discovered the components moving differently, before and after an eclipse. After binary stars became a norm, more observations revealed that multiplicity is not a rare phenomenon. Surprisingly, after more spectroscopic follow-up (as in the case of this thesis), Algol was found to be a triple star (Meltzer 1957).

Subsequently, the idea of hierarchical multiple systems was built on the observations that the system exists in hierarchies, where each hierarchy acts as a binary system.

1.2. Multiple stars in large surveys

Multiplicity studies have come a long way. Starting from identifying single systems, and crude descriptions of small samples, we have moved to detailed studies of multiplicity statistics and its dependency on mass, metallicity and its environment. In the 70s, Batten (1973) and Abt & Levy (1976) showed that obtaining orbital parameters and mass distributions from observation can help us understand the formation and evolution physics of multiple systems. While in the 80s, Fekel (1981) published the first list of triple stars.

In the 90s, a revolutionary improvement in multiplicity studies came with the advent of cross-correlation spectroscopy (Duquennoy et al. 1991). Working on the foundations of the technique, Duquennoy & Mayor (1991) were able to provide a sample with 4206 radial velocity (RV) measurements for 181 multiple systems in the solar neighbourhood. Using the distribution or eccentricities of orbits, mass ratio and multiplicity fraction, they were able to observe signatures of tidal circularisation and the absence of brown dwarf desert (though wrongly). Raghavan et al. (2010) revised the results of Duquennoy & Mayor (1991) using better observing methods and a larger sample and presented the largest sample (454 systems) of multiple solar-type stars.

A more extended work by Moe & Di Stefano (2017) reveals that multiplicity is essentially a

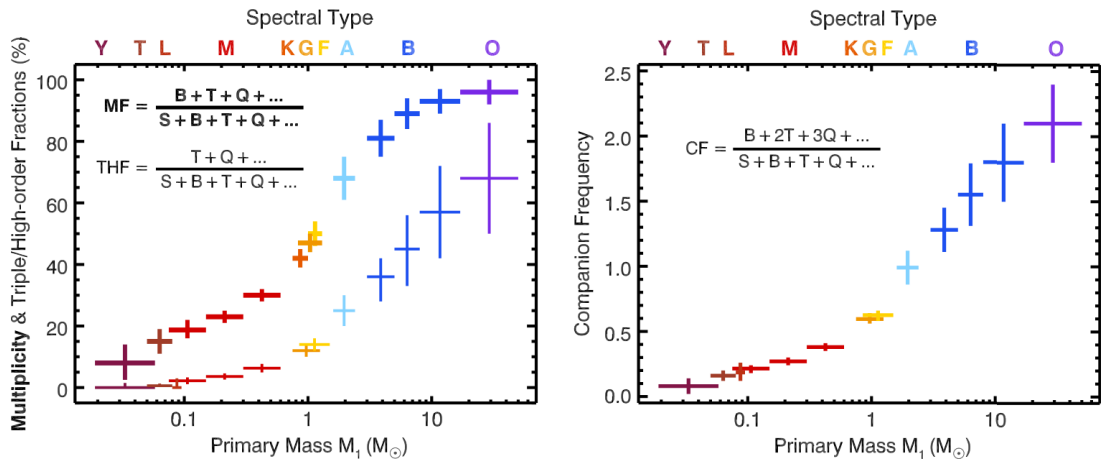


Figure 1.1 Bias-corrected multiplicity fraction (left; thick), triple/high-order fraction (left; thin), and companion frequency (right) of BDs and MS stars. All three quantities increase monotonically with primary mass. The indicated spectral types at the top roughly correspond to the mean primary masses of field dwarfs. Figure credits: [Offner et al. \(2023\)](#).

function of the spectral type (and therefore mass). A compilation of different multiplicity ([Offner et al. 2023](#)) studies till the current date is shown in [Figure 1.1](#) which summarises the distribution of multiplicity for different masses.

Spectroscopic surveys of the millennium like the Radial Velocity Experiment (RAVE; [Steinmetz et al. 2006](#)), Apache Point Observatory Galactic Evolution Experiment (APO-GEE; [Majewski et al. 2017](#)), and Galactic Archaeology with HERMES (GALAH; [De Silva et al. 2015](#)) now provide us with temperatures, and metallicity along with the orbital properties of thousands of stars.

Important additions to this arsenal of telescopes are the ground-based photometric surveys. The Optical Gravitational Lensing Experiment (OGLE; [Udalski et al. 1992](#)) and the All Sky Automated Survey (ASAS; [Pojmanski 1997](#)) led to the discovery of a large number of eclipsing binaries and more multiples using time-series photometry of eclipsing binaries ([Hełminiak et al. 2015](#)) and other variable stars ([Singh Rathour et al. 2024](#)).

To keep track of the surmounting numbers of new multiple systems and their parameters, the Multi Star Catalogue² (MSC; [Tokovinin 1997](#)) was created. This is a catalogue of hierarchical multiple stellar systems with three or more components. After the last update ([Tokovinin 2018](#)), the catalogue consists of about 2000 systems with 3-7 components each.

1.3. Multiple stars in the era of space-telescopes

The improvements in the multiplicity surveys by [Raghavan et al. \(2010\)](#) were facilitated by the Hipparcos Space Astrometry Mission ([Perryman et al. 1997](#)). What followed after this

²<http://www.ctio.noirlab.edu/~atokovin/stars/>

brought in a golden era for studying multiple stars. With the discovery of exoplanets, space-based photometric missions started becoming important. But while the major goal of these missions was the detection of exoplanets, they revitalised the field of stellar astrophysics and multiplicity studies. Convection, Rotation et Transits planétaires (CoRoT; [Baglin et al. 2006](#)) was the first of the photometric space fleet to demonstrate the fascinating stellar science that one can do from precise, time-series photometric missions. Following the success of CoRoT, *Kepler* ([Borucki et al. 2010](#)) was launched. What followed *Kepler* (and subsequently K2; [Howell et al. 2014](#)) was a revolution in the understanding of asteroseismology ([Gilliland et al. 2010](#); [Huber et al. 2013](#)), stellar rotation ([Reinhold et al. 2013](#); [McQuillan et al. 2014](#)), stellar structure ([Mosser et al. 2012](#); [Cantiello et al. 2014](#)), stellar activity ([Balaji et al. 2015a](#)), limb-darkening ([Claret & Bloemen 2011](#)), eclipsing binaries ([Prša et al. 2011](#)), and multiplicity ([Ciardi et al. 2015](#); [Borkovits et al. 2016](#)). The momentum of these discoveries has now been transferred to the Transiting Exoplanet Survey Satellite (*TESS*; [Ricker et al. 2015](#)) and is being planned to be extended to the PLAnetary Transits and Oscillations of stars (PLATO; [Rauer et al. 2014](#)) mission which is scheduled to be in orbit by 2026. Compounding on this, *Gaia* ([Gaia Collaboration et al. 2016](#)) also has been brilliant in finding multiples ([El-Badry et al. 2021](#); [Czavalinga et al. 2023](#)).

Simultaneously, we had an exponential improvement in the precision of RV instruments and this has brought us to the era of Extreme Precision RV (EPRV; [Fischer et al. 2016](#)). It is now possible to completely characterise millions of stars and multi-star systems.

1.3.1. Eclipsing binaries

Stars in an eclipsing binary (EB) provide the best scope for complete stellar characterisation. EBs are binary stars whose orbital plane is aligned to our line of sight. This causes periodic changes in the brightness of the unresolved star system. Measuring the shape of such an eclipse gives us the measurement of the masses and radii of the two stars. [Stebbins \(1911\)](#) attained the first direct measurement of the masses and radii of stars in an EB, β Aur. The values found for its masses and radii back then agree reasonably well with modern values ([Southworth et al. 2007](#)). Such precision and accuracy make EBs a swiss-knife of stellar astrophysics.

Precise parameters obtained from EBs have been used to calibrate theoretical stellar models ([Stassun et al. 2009](#); [Li et al. 2018](#)), calibrate convective core overshooting ([Claret & Torres 2016](#)), constraining structure of stars ([Debusscher et al. 2013](#); [Tkachenko et al. 2014](#); [Handler et al. 2020](#)), estimate distances to nearby galaxies ([Pietrzyński et al. 2013](#)), and also study multiplicity of stars.

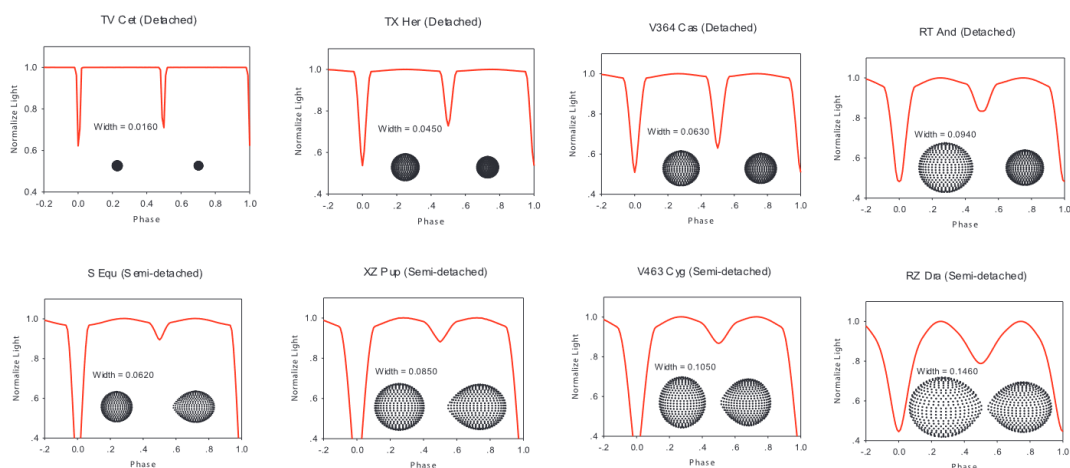


Figure 1.2 Morphologies of stars in EBs and their resultant light curves. Figure credits: [Kang \(2010\)](#).

1.3.1.1. Detached Eclipsing Binaries

The basic morphological classification ([Prša 2018](#)) of EBs defines it into three classes: (i) Contact; (ii) Semi-detached ([Figure 1.2](#); bottom row); and (iii) Detached ([Figure 1.2](#); top row). In the context of this thesis, we will focus on the Detached EB (DEB) case. DEBs do not interact with each other (only gravitationally). This makes them evolve as single stars and therefore are simple systems to measure stellar parameters. In fact, DEBs are known as the source of the most precise stellar parameters (*e.g.*, mass, radius, etc.). A precision of less than 1% can be attained by coupling high-precision photometry ([Torres et al. 2010](#)) and high-resolution spectroscopy ([Hełminiak et al. 2017b](#)). The accuracy is robust and independent of different models and methods, even varying slightly due to different numerical implementations ([Maxted et al. 2020](#); [Korth et al. 2021](#)). This can be seen in the small spread in [Figure 1.3](#) where each point depicts independent measurements of parameters of a famous, well-studied AI Phe, a DEB. Using radial velocities (RVs) simultaneously with light curves (LCs) further improves the accuracy.

The unparalleled precision of the obtained stellar and orbital parameters has been exploited to precisely estimate the local value of Hubble constant ([Riess et al. 2016](#)), calibrate the tip of the Red Giant Branch (TRGB) method ([Freedman et al. 2020](#)), constrain rotational mixing in massive stars ([de Mink et al. 2009](#)), along with testing stellar evolution models ([Pols et al. 1997](#)).

1.3.2. Renaissance of the triples

While [Chambliss \(1992\)](#) was the first to use EB to study multiples, now it is one of the first approaches in any photometric survey to look for multiple companions, especially with *Kepler* and *TESS*. The last two decades have seen an increasing rise in the study of triple systems. One of the reasons for this is the increased use of EBs and DEBs as a tool to look

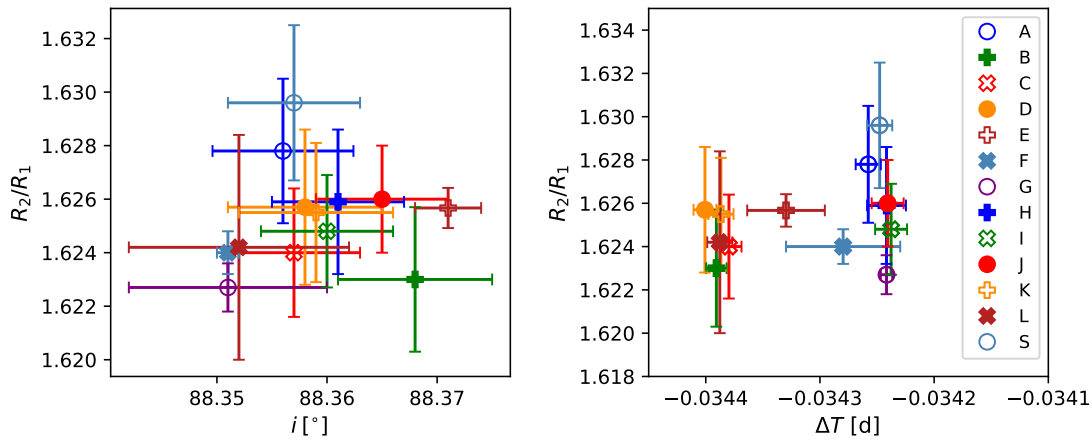


Figure 1.3 Spread of parameters obtained by LC modelling with different methodology (different markers) for the same observation of AI Phe. Figure credits: [Maxted et al. \(2020\)](#).

for circumbinary companions. One of the most common techniques for this is Eclipse Timing (ET). ET is the measurement of time of minima in an eclipse over each cycle or binary period. While these times for an isolated binary will be periodic, the times will vary for an EB with a companion. This phenomenon is due to the light-travel time effect (LTTE; [Chandler 1888](#)) which causes the ET variations (ETV). These variations can be visualised in observed-calculated (O-C) diagrams, which can show periodic variations due to a tertiary ([Figure 1.4](#)). *Kepler*, with its precise photometry and comparatively better cadence (time between each observation), turned out to be a game changer in this case. Building upon the work of [Gies et al. \(2012\)](#), [Rappaport et al. \(2013\)](#) and especially [Conroy et al. \(2014\)](#), [Borkovits et al. \(2016\)](#) used 5 years of *Kepler* observation to create the first extensive catalogue of *Kepler* triples. The catalogue listed orbital period and tertiary mass estimates of 222 triple candidates. Using the same methodology, [Hajdu et al. \(2019, 2022\)](#) used ETV from OGLE EBs to find around a thousand hierarchical triples. Recently, [Mitnyan et al. \(2024\)](#) found 125 new hierarchical triples in the Continuous Viewing Zone (CVZ) of *TESS*. *Gaia* DR3 has also contributed to the discovery of triples ([Czavalinga et al. 2023](#)). These discoveries revealed several peculiar morphologies of triple-star LCs. Long-term observations using *Kepler* and *TESS* revealed eclipses of the third body along with the EB eclipses in the system ([Borkovits et al. 2013](#); [Mitnyan et al. 2020](#); [Rappaport et al. 2022, 2023](#)). These systems also encouraged the development of complex dynamical modelling codes (LIGHTCURVEFACTORY; [Borkovits et al. 2013](#)) to model these eclipses ([Figure 1.5](#)). These long-term LCs also reignited interest in EB systems which showed variation in eclipse depth. Eclipse depth variation (EDV) systems show changes in eclipse depth due to their changing inclination ([Figure 1.6](#)). This is usually due to the dynamical effects of having a close tertiary. These systems have been found in both *Kepler* ([Borkovits et al. 2022](#)) and in *TESS* ([Borkovits et al. 2020](#)).

Now, we have interferometric studies finding triple stars in formation ([Czekala et al.](#)

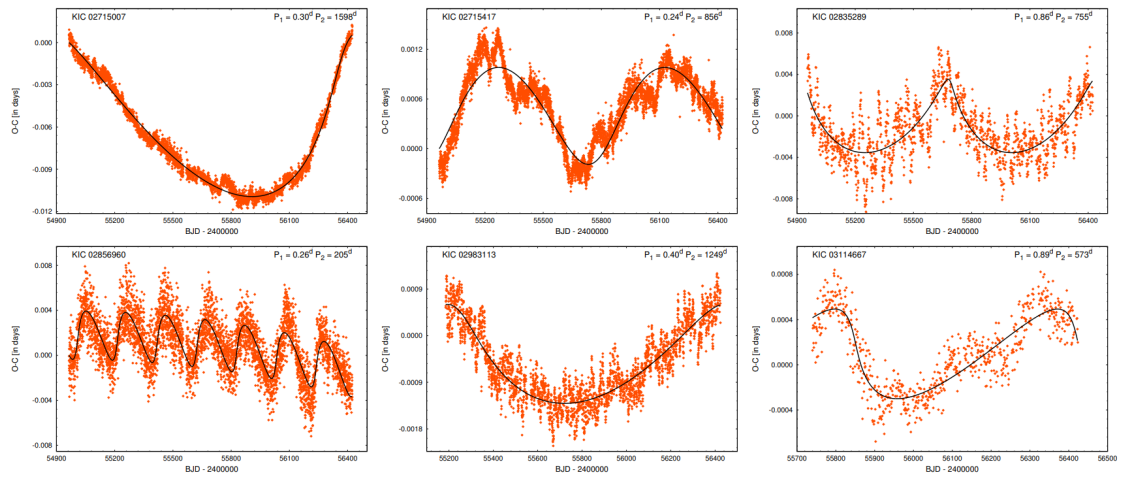


Figure 1.4 Different ETV (O-C signals) for different hierarchical triple systems. Figure credits: [Borkovits et al. \(2016\)](#).

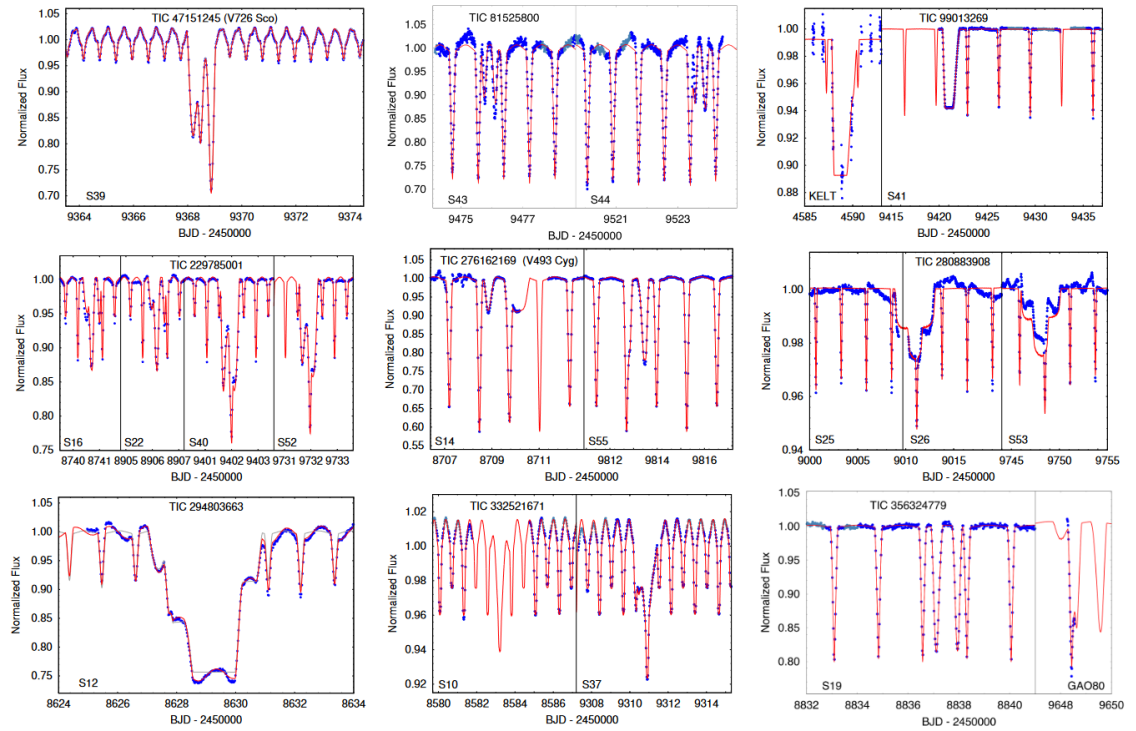


Figure 1.5 Various light curve morphologies of triply eclipsing systems. The red lines show the model obtained by LIGHTCURVEFACTORY. Figure credits: [Rappaport et al. \(2023\)](#).

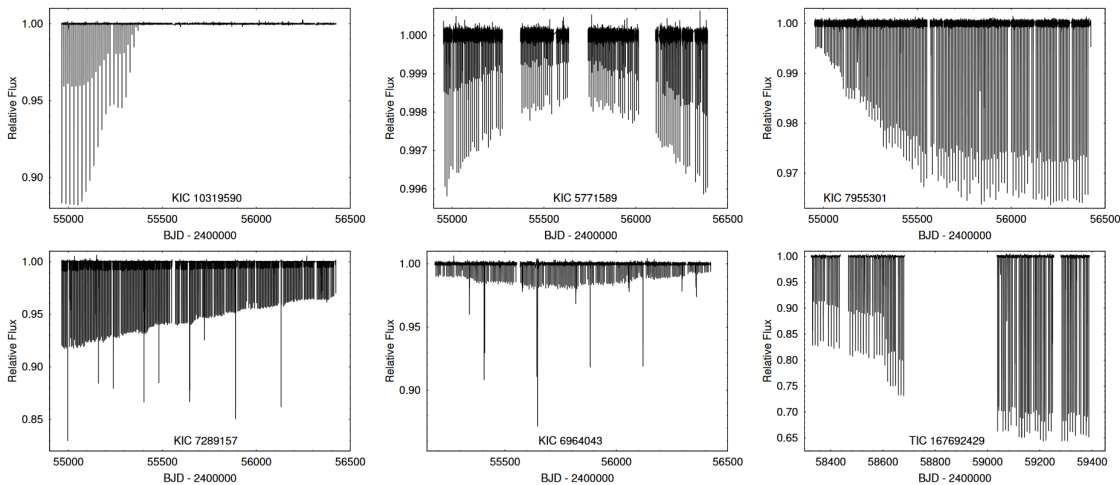


Figure 1.6 Different light curve morphologies of EDV systems as observed by *Kepler*. Figure credits: [Borkovits \(2022\)](#).

2017), population synthesis codes exploring the distribution of triples ([Toonen et al. 2020](#); [Hamers et al. 2021](#)) and stellar evolution codes are constraining the evolution of triples ([Toonen et al. 2017](#)). The foundations have been laid for new explorations in the science of hierarchical triple stars.

1.4. Compact hierarchical triples

A subset of hierarchical triples has been getting more attention recently. Compact Hierarchical Triples³ (CHTs) are systems where the tertiary star orbits the inner binary on an orbit of period less than ~ 1000 days ([Tokovinin 2021](#); [Borkovits 2022](#)). The scale of compactness can be seen in the orbits of these systems ([Figure 1.7](#)).

While the period limit is not a strict one, there have been suggestions that the formation scenario of most systems in this range differs from normal triples ([Tokovinin 2021](#)). Further, these systems show third-body perturbations of order higher than in a wide triple. This can also materialise in tight triples, where the outer orbit period (P_{out}) to the inner orbit period (P_{in}) ratio is less than 50. But not all tight triples need to be CHTs, *e.g.*, the tightest known triple star is LHS 1070 ([Xia et al. 2019](#)) with P_{out} of 99 years and P_{in} of 18.2 years, close to the stability of triples defined by [Mardling & Aarseth \(2001\)](#). The observational advantage of observing higher-order dynamics (and their subsequent effect on stellar evolution) in a CHT is that the dynamical signatures can be observed and contained in timescales of few years (say 1 PhD thesis). Short-term perturbations in hierarchical systems are driven by the same physical quantities that drive the long-term evolution ([Naoz et al. 2013](#)). Therefore, constraining the perturbations in a CHT allows us to calculate the parameters of stellar and dynamical evolution with high accuracy. If we have an eclipsing CHT (ECHT), we can obtain most of the parameters with high precision

³Also called "tight triples" in some literature. Tight triples are now defined as a different class of systems.

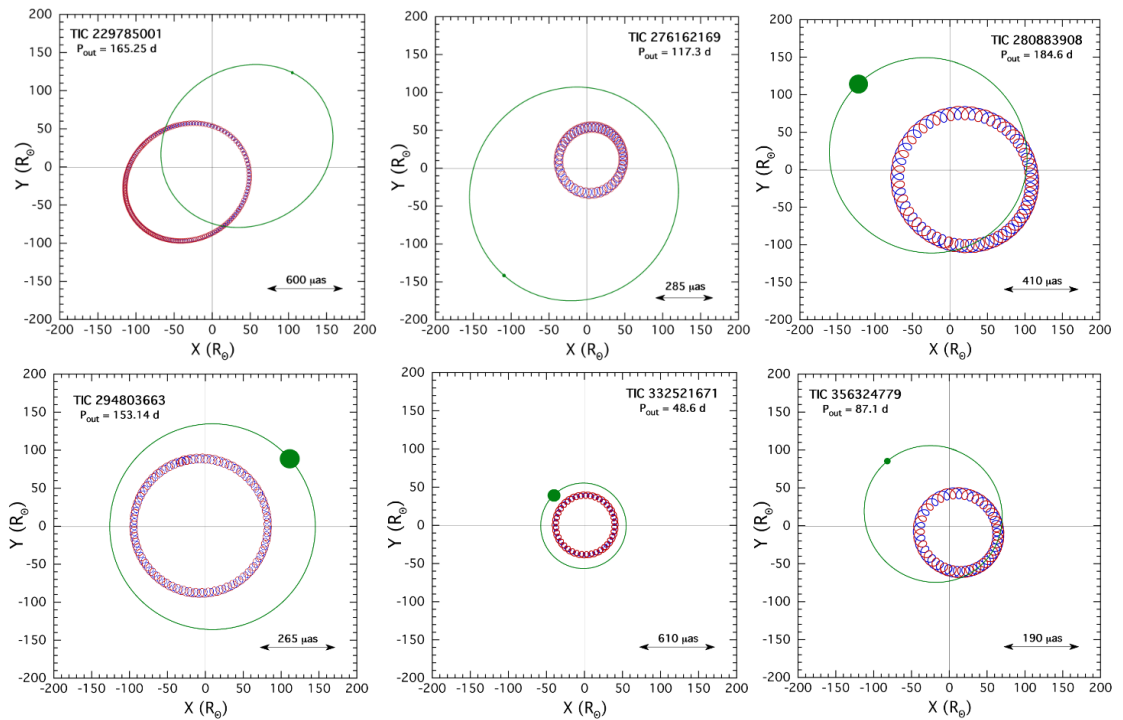


Figure 1.7 Different orbital configurations of the first 6 E3CHTs in [Figure 1.5](#). Figure credits: [Rappaport et al. \(2023\)](#).

too. Most of the ECHTs discovered manifest as a doubly eclipsing CHT (E2CHT) or as triply eclipsing CHT (E3CHT). This makes them good tools to study hierarchical triple systems.

CHTs were considered rare before the *Kepler* and *TESS* era ([Tokovinin 2004](#)). The recent surge in detections of triple stars also detected hundreds of CHTs. In the last decade, CHTs have gained importance in the context of star formation and stellar evolution, along with their interesting dynamics. The following sections discuss these themes.

1.4.1. CHT formation scenarios

A general idea about the process of star formation is that they form from the hierarchical collapse of molecular clouds. A detailed look into it reveals more complex processes that bring together cold molecular gas to form 1D filaments or 2D sheets. The fragmentation of the larger entities begins at the onset of the Jeans mass limit due to increasing density. Further fragmentation stops at the opacity limit. This limit decides the mass distribution of a star-forming cloud. For a comprehensive discussion of the hierarchical collapse process, refer [Vázquez-Semadeni et al. \(2019\)](#).

The formation of a low-mass binary star proceeds by two major channels ([Figure 1.8](#)): i) Disk instability (DI), and ii) Core fragmentation (CF). The hierarchical collapse of a cloud requires losing angular momentum. An accretion disk is usually formed when the angular momentum redistribution is slowed than its influx. DI happens when a

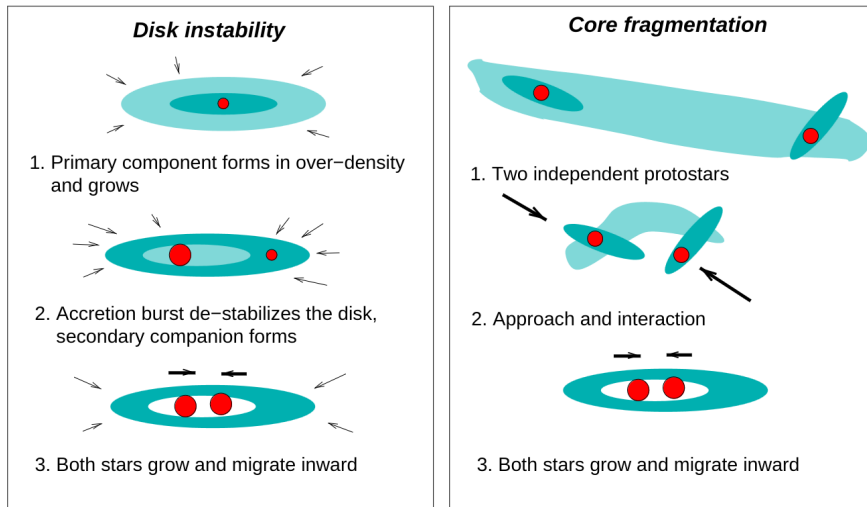


Figure 1.8 The left and right panels show the binary formation channels, disk instability and core fragmentation respectively. The end products of both the stars undergo migration to come to smaller scales that we observe. Figure credits: Tokovinin (2021).

massive disk, around a nascent protostar, becomes unstable and fragments to form one or more companions (Kratte et al. 2010). The opacity in the disk fragmentation limits the initial separation between the components to be larger than 10 AU. The secondary component usually migrates, across the disk, to smaller separations. This is one of the reasons why the final mass of the companion increases compared to the fragmented mass (Heath & Nixon 2020). The complex physics during migration also decides if the companion stabilises or merges to form more massive stars. CF is the dominant binary formation channel for low-mass binaries (Offner et al. 2010). The hierarchical collapse in this case (and the opacity limit) sets the minimum separation between components to be ~ 10 AU. Two neighbouring protostars may end up bound if their relative velocity is less than the escape velocity (Tokovinin 2017a). In a dense cluster, a third route, namely N-body dynamics, can bring together different protostars (or stars) to form a bound binary system.

In a triple system (or a hierarchical multiple), the complexity of the formation mechanism increases. The different formation scenarios usually involve both DI and CF, simultaneously or in a sequence. When a DI component migrates inward, another companion can be formed by DI on the periphery of the system (Tokovinin & Moe 2020). This is called sequential disk instability (DI+DI). DI+DI scenario is an inside-out assembly, where the inner system is formed first. The physics of migration and formation of the final component puts a strict limit on the tertiary mass ratio *i.e.*, $q \simeq 1$. Observational signatures of such a process in action have been found in Tobin et al. (2016). Similarly, sequential CF (CF+CF) is another scenario predicted by simulations (Kuffmeier et al. 2019). While a CF+DI scenario is unlikely, simulations show the feasibility of the DI+CF scenario (Rohde et al. 2021). Other possible scenarios include the collision of nascent protostars and/or

dynamical interactions which are usually followed by ejection or capture of additional components. A complete discussion of these scenarios and their expected products can be found in [Tokovinin \(2021\)](#).

While recent developments in interferometry have given us the power to observe binary and triple star formation ([Looney et al. 2000](#); [Czekala et al. 2017](#); [Lee et al. 2023](#)), historically it has been large-scale binary statistics that have helped us constrain the star-formation theories ([Abt & Levy 1976](#); [Fekel 1981](#)). While binary statistics are well established (see [Sana et al. 2012](#); [Moe & Di Stefano 2017](#); [Tokovinin 2021](#) for details), a general idea about triples is still under construction. Most of the triples have been found in hierarchies. A simplistic approach to understanding triple statistics can be made by translating binary statistics to the wide tertiary hierarchy. Such an approach would imply that pairs in a hierarchy could be formed independently of each other and such a model is called the Independent Multiplicity Model (IMM; [Tokovinin \(2021\)](#)). IMM roughly matches the statistics of solar-type binaries when translated from solar-type single stars ([Duchêne & Kraus 2013](#)). For example, the frequency of a wide visual companion to a spectroscopic binary is comparable to the companion frequency for a single star. But IMM does not hold in its full entirety when translated to triples. For example, IMM suggests that there should be an equal number of co-rotating and counter-rotating triples but current statistics of wide triples suggest an excess of co-rotating triples ([Worley 1967](#); [Sterzik & Tokovinin 2002](#); [Tokovinin 2017b](#)). Therefore, statistics of orbital elements are still an important tool for understanding the formation scenarios. A review of current knowledge of observations and their translation to the theory of the formation of multiple star systems can be found in [Offner et al. \(2023\)](#).

The recent discoveries of CHTs have provided us with sufficient systems to extract meaningful statistics. Looking at the periods and the orbital sizes of CHT one would imply that a CF+CF will be dominant at these scales. But most of the CHT are co-planar or near co-planar (average mutual inclination is $\sim 20^\circ$). The planar orbits, along with moderate eccentricities suggest a DI+DI formation scenario where the tertiary forms later and adds mass by accretion ([Tokovinin 2017b](#)). This suggests that both the binary mass ratio (q_B) and the triple mass ratio (q_T) should be close to 1. However, the current statistics are incomplete and are influenced by observational biases. While there are limits to masses that can be estimated by ETV, E3CHT detections are biased towards planarity. Further, any dependency on metallicity and environment has not been explored in detail as it has been in binary stars ([Moe et al. 2019](#); [Mazzola et al. 2020](#)).

In contrast, such studies have been abundant in the substellar regimes. [Ma & Ge \(2014\)](#) showed that the metallicity distribution of binary brown dwarfs (BDs) supports DI mechanism. For giant planets, a different process has been favoured, *i.e.*, core accretion (from disks around protostars), based on the metallicity and giant planet occurrence rates ([Santos et al. 2001](#); [Fischer & Valenti 2005](#); [Alibert et al. 2005](#)). Another result of the improved

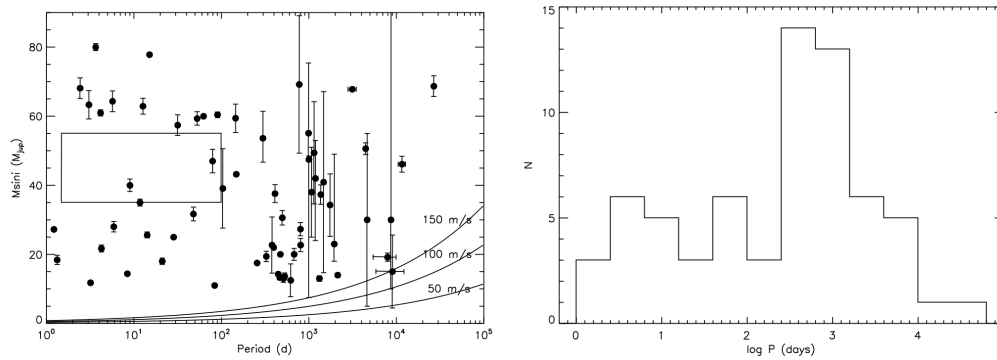


Figure 1.9 (Left) Distribution of mass and period of known BD companions compiled by [Ma & Ge \(2014\)](#). The curves at the bottom denote different RV precision. The box shows the approximate location of the BD desert. (Right) Period histogram of BD companions around solar-type stars. Figure credits: [Ma & Ge \(2014\)](#).

statistics in this regime has been the identification of the BD desert ([Marcy & Butler 2000](#); [Grether & Lineweaver 2006](#)). BD desert is a space around the central star where the probability of finding a BD companion is low. A look into the period distribution of BD companions shows a peak around 1000 days ([Figure 1.9](#)) which interestingly coincides with the observers' limit for CHT.

Therefore, further exploration and observations are needed to understand if low-mass CHT are the upper limit to planet formation or the lower limit to star formation.

1.4.2. CHT evolution scenarios

The interest in binaries increased through the decades mostly because they can be used to explain a lot of evolutionary phenomena which could not be explained by single stars ([Paczynski 1971](#)). With their complex geometry ([Figure 1.10](#)), we can extend this reasoning to triple stars.

The interest in triples started with certain observational evidence in binaries, which pointed to a different evolutionary scenario in a triple system. While looking at the period distribution of close binary stars, a pile-up of systems was observed near the 3-day period. This was explained by the von Zeipel-Lodov-Kozai (see discussion below) effect from a tertiary body, along with tidal friction ([Eggleton & Kiseleva-Eggleton 2001](#); [Fabrycky & Tremaine 2007](#); [Naoz & Fabrycky 2014](#)). This paved the way to a detailed understanding of different processes that affect triple star evolution:

- **Stability:** The stability of triple systems is a well-known physical problem which even compelled Isaac Newton to study the Earth-Moon-Sun system. The three-body problem is tricky to solve as it does not have a closed-form like a two-body problem. Unstable systems tend to break down to lower order. Therefore, its stability criteria are varied. The commonly used stability criteria is that of [Mardling & Aarseth](#)

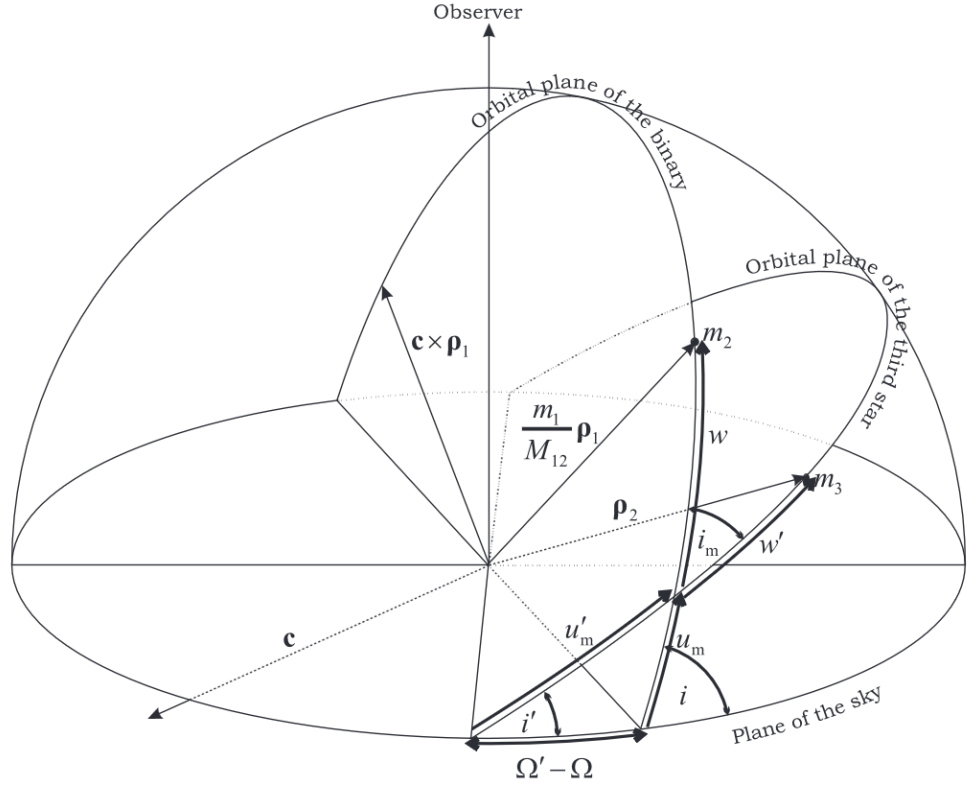


Figure 1.10 3D geometry of a triple star system, with the primary (m_1) as the origin. m_1, m_2 denote the masses of the two inner binary while m_3 denotes the tertiary mass. M_{12} represents $m_1 + m_2$. w, w' represent the true longitudes of the secondary and tertiary respectively, measured from the intersection of the orbits. u, u' represents the same with respect to the sky plane. i, i' denote the inclinations with the sky plane and i_m denotes the mutual inclination of the inner and outer orbits. ρ denotes Jacobian position vectors. The various symbols are described in detail in [Borkovits et al. \(2003\)](#).

(2001) which is defined in a complex form as :

$$\frac{a_2}{a_1} \Big|_{\text{crit}} = \frac{2.8}{1 - e_2} \left(1 - \frac{0.3i}{\pi}\right) \left(\frac{(1 + q_2)(1 + e_2)}{\sqrt{1 - e_2}}\right)^{2/5} \quad (1.1)$$

where a_1 is the semi-major axis of the inner binary orbit, a_2 is that of the tertiary orbit, e_2 is the eccentricity of the tertiary orbit, and q_2 is the tertiary to inner binary mass ratio. The triple can become unstable (either during formation or evolution) if the real part satisfies $\frac{a_2}{a_1} < \frac{a_2}{a_1} \Big|_{\text{crit}}$.

- **von Zeipel-Lidov-Kozai effect:** There is a mutual torque between the inner and outer orbits, and angular momentum may be exchanged between the orbits. This can cause periodic variations in e_1 and the mutual inclination (i_m). This phenomenon is called the von Zeipel-Lidov-Kozai (ZLK) effect ([von Zeipel 1910](#); [Lidov 1962](#); [Kozai 1962](#)). The timescale of the ZLK cycles/oscillations (t_{ZLK}), from the three-body Hamiltonian expansion in the quadruple order of a_1/a_2 , is given by

(Kinoshita & Nakai 1999),

$$t_{\text{ZLK}} = \alpha \frac{P_2^2}{P_1} \frac{m_B + m_T}{m_T} (1 - e_2^2)^{3/2} \quad (1.2)$$

where P_1 and P_2 are the periods of inner and outer orbits respectively, α depends on i_m and e_1 (Antognini 2015), m_B is the binary mass and m_T is the mass of the tertiary. In the quadruple approximation, the maximum eccentricity (e_{max}) of the inner binary is given by (Innanen et al. 1997),

$$e_{\text{max}} = \sqrt{1 - \frac{5}{3} \cos^2 i_m} \quad (1.3)$$

In the test particle approximation, it would be possible to have the ZLK cycles when the i_m is between 39.2 - 140.8° (Naoz et al. 2013). For higher-order approximations, *i.e.*, octupole approximation, the dynamics becomes complicated. It is then possible that the i_1 can flip from prograde to retrograde and vice versa. This is called the eccentric ZLK (EZLK) effect (Naoz 2016). If any star in the triple system undergoes mass transfer, the system can move in and out of the EZLK regimes. This process is called as mass-loss induced ZLK (MIEK; Michaely & Perets 2014; Shappee & Thompson 2013). Tidal effects along with ZLK (or EZLK) effects play a major role in the migration of hot Jupiters in a binary system (Wu & Murray 2003; Naoz et al. 2012).

- **Precession:** While ZLK can cause precession of orbits in certain configurations, triple systems encounter precession due to general relativistic effects (Blaes et al. 2002), tidal distortions by stars (Smeyers & Willems 2001), and intrinsic stellar rotation (Fabrycky & Tremaine 2007). If the precession timescales of these processes are comparable (or smaller) with that of ZLK, the ZLK cycles get repressed. This further restricts the range of i_m stated above.
- **Tides and gravitational waves:** In certain configurations (eccentric CHT or specific phase of ZLK cycle), the separations between the stars in a triple system are reduced. During these close passages, gravitational wave (GW) emission and tidal effects can alter the orbit. When combined with ZLK effects, these effects can circularise the inner binary and shorten the P_1 . While there are a lot of studies of this process in binaries (Eggleton & Kiseleva-Eggleton 2001; Fabrycky & Tremaine 2007), we lack a study of the effectiveness of the process in triples as a whole.
- **Mass transfers:** Roche lobe in an eccentric binary is significantly smaller than that in a circular binary. In a triple system where e_1 can vary a lot, Roche Lobe Overflow (RLOF) can be episodic (Church et al. 2009; Davis et al. 2013). RLOF for a large enough tertiary can also transfer mass to the inner binary system. Mass transfer/losses via Common Envelope Evolution (CEE) are also a viable process both in the inner binary and the whole system itself. Mass transfers in massive

triples can occur via stellar winds. Supernova explosions and planetary nebulae can also create channels of mass transfer along with orbital changes.

Toonen et al. (2020) included all the above processes in their triple evolution code `TRES` to explore the long-term evolution of triple stars. They found that $\sim 70\%$ of all triples undergo mass transfer at some point in their lifetime. They also found that most of the evolved donors exist in circular systems while in the cases where the donor was a main sequence (MS), the system was eccentric. Compared to isolated binaries, they found that mass transfers in the inner binary of a triple were initiated faster. A small fraction of all triples ended due to dynamical instability ($\sim 3\%$), and the rest of the models in their modelling did not have any interaction between the stars. Observations confirmed such a possibility when a triple white dwarf was discovered recently (Perpinyà-Vallès et al. 2019).

While only 3% (4% for low-mass systems) of triples underwent dynamical instability, they form a variety of products. Toonen et al. (2022) predict that 10^{-3} MS-MS collisions happen per year due to triple interactions. Such a collision can explain the great eruption of Eta Carina which occurred in the nineteenth century (Portegies Zwart & van den Heuvel 2016; Smith et al. 2018). Triples can also explain the formation of blue stragglers stars (Perets & Fabrycky 2009), red novae (Kamiński et al. 2021), SNe-I (Maoz et al. 2014), asymmetry of planetary nebulae (Jones et al. 2019), compact binaries and runaway stars (Toonen et al. 2022). Various different interactions between stars in triple systems can create a zoo of products (Figure 1.11) hosting sub-dwarf O-type stars (Preece et al. 2022).

The short distance and time scales of CHTs make them more potent to undergo such evolutionary changes. There is an increased probability of easily having stars evolve and exceed the Roche lobe and even the size of the orbits. OW Gem seems to be such a case where the inner binary in a CHT merged to produce a yellow giant binary of a 1240-day period (Eggleton 2002). While present CHTs like TIC 470710327 can undergo interactions to form exotic (and currently only in theory) products like the Thorne-Żytkow objects (Eisner et al. 2022).

Surprisingly, most of the CHTs with detailed estimates of masses and radii, do not show any sign of peculiar evolution. Most of the CHTs follow co-evolution, where all three stars evolve independently as single stars and therefore can be explained by one single stellar isochrone. While there are examples of non-coeval systems *e.g.*, V1200 Cen (Marcadon et al. 2020) and HD 144548 (David et al. 2019), the specific reason behind it has not been explored. The current literature of detailed measurements (masses, radii and temperatures) of CHT, which is limited (~ 50), is biased towards planar systems even when population synthesis predicts no such excess (Bataille et al. 2018). Therefore, more detailed and independent measurements of CHTs are needed to explore both the formation and evolution of CHTs.

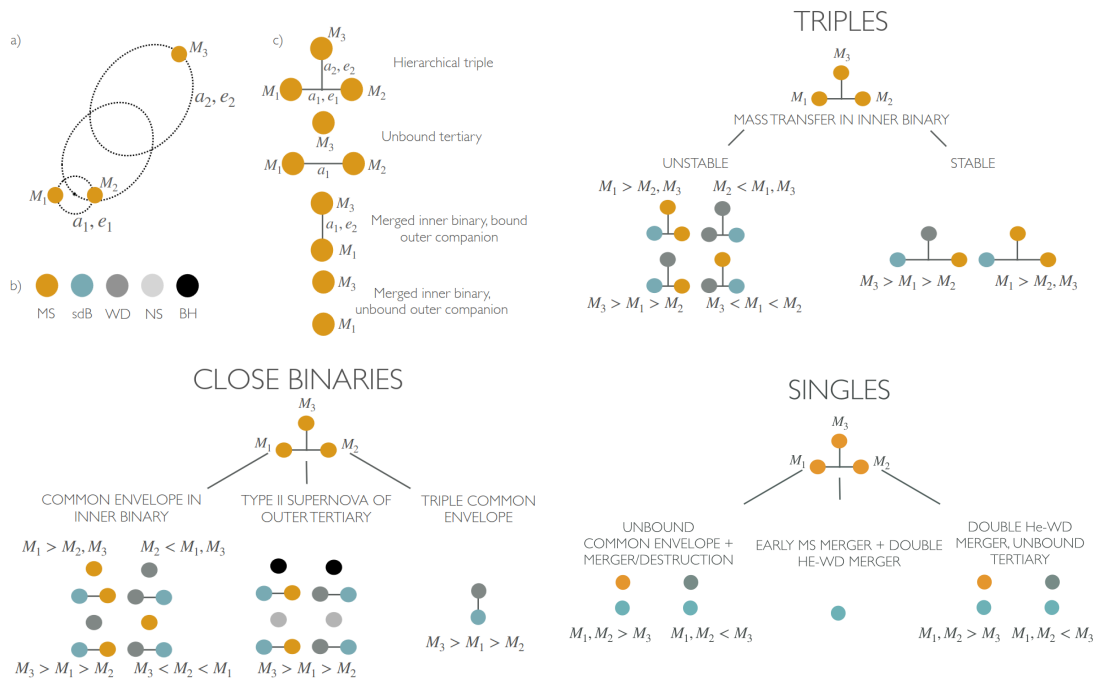


Figure 1.11 Different evolutionary products possible from triple systems. a) is a hierarchical triple for reference, M_1 is the primary and most massive star in the inner binary, M_2 is the secondary and least massive star in the inner binary, M_3 is the outer tertiary. The semi-major axis of the inner binary is a_1 and the outer tertiary is a_2 . b) shows the colours used to represent different evolutionary stages. c) are various orbital configurations. The formation channels leading to triple, binary and single-star products are shown. Figure credits: [Preece et al. \(2022\)](#).

In this thesis, we try to address two challenges in the domain of observational study of CHTs. The first one is detection of new CHTs and make the sample of CHTs less unbiased. The work on this problem is described in [chapter 2](#). The second challenge is to characterise the stars in the system to get precise stellar, orbital, and atmospheric parameters. The methods to tackle this problem is described in [chapter 3](#). This is then used to study the dynamics and evolution of two systems and the findings are discussed in [chapter 4](#). Solving four more CHT in this way, we present the current distribution of CHT systems with detailed solutions in [chapter 5](#). The main findings of all these chapters are summarised in [chapter 6](#), where we also discuss the implications of this work and give some directions for future research.

CHAPTER 2

Three in one: Search for Compact Hierarchical Triples

"Someone else always has to carry on the story."

– J.R.R. Tolkien, Author, The Lord of the Rings

A part of this chapter has been published in Monthly Notices of Royal Astronomical Society as 'Solaris photometric survey: Search for circumbinary companions using eclipse timing variations', Moharana, Ayush ; Hełminiak, K. G. ; Marcadon, F. ; Pawar, T. ; Pawar, G. ; Garczyński, P. ; Perła, J. ; Kozłowski, S. K. ; Sybilski, P. ; Ratajczak, M. ; Konacki, M. , MNRAS, Volume 527, Issue 1, January 2024, Pages 53–65.

The current state and precision of observational instruments have immensely helped the detection of multiple star systems. The added precision of finding a companion through parameter variation of an EB has also helped us improve the detection rate of multiples in general. To detect triple-star systems using an EB, there are at least 6 generic methods:

- Visually resolving with adaptive optics and optical/IR interferometry ([Raghavan et al. 2010](#))
- Observing the presence of three different stellar lines in a spectrum ([Lu et al. 2001](#))
- Doppler spectroscopy (i.e., measurements of radial velocity; [Hełminiak et al. 2017b](#))
- Direct observations of eclipses by all three bodies ([Alonso et al. 2015](#); [Rappaport et al. 2022](#))

- Long-term timing of binary eclipses to look for periodic perturbations to the otherwise fixed time intervals (Borkovits et al. 2016; Hajdu et al. 2019)
- Presence of additional light, called the “third light” parameter in the light curve solution

This thesis uses three of the above techniques, keeping in mind the availability and ease of access to observations, the reliability of tertiary signals, and the aim to reduce observation bias in the parameter space. The latter is the reason to use EB for our work, avoiding triply eclipsing systems as they are all co-planar. In this section, we discuss the use of the methods of broadening functions, radial velocities, and eclipse timing variations to search for CHTs.

2.1. Broadening Functions

To detect a CHT with spectroscopy, just one spectrum would suffice. This is because the velocity of the stars in such a compact orbit is of the same order. But this is subject to the conditions that (i) the stars do not have the same velocity at that instance, (ii) the three stars have comparative flux contribution, and (iii) do not rotate fast, so that their spectral lines merge with the lines of the other stars. While it is possible to spot multiple components in the spectrum in the wavelength domain, the convolution of the spectrum and changing it to the velocity domain gives us a more powerful diagnostic. While cross-correlation functions (CCF) have been quite popular in doing this, they have their demerits. Consider a sharp stellar line ($S(\lambda)$) which is broadened intrinsically (thermal, micro-turbulence effects etc.) by $T(\lambda)$ (Rucinski 1999),

$$S(\lambda) = \left(\sum_i a_i \delta(\lambda_i) \right) * T(\lambda) \quad (2.1)$$

where $\sum_i a_i \delta(\lambda_i)$ denotes the ideal elemental line. An additional extrinsic broadening ($B(\lambda)$) creates the observed spectral line ($O(\lambda)$) that can be represented as,

$$O(\lambda) = S(\lambda) * B(\lambda) = \left(\sum_i a_i \delta(\lambda_i) \right) * T(\lambda) * B(\lambda) \quad (2.2)$$

Recovering $B(\lambda)$ can help us identify the true contribution from the stellar component. In a CCF we do a cross-correlation (represented by \otimes) to estimate $B(\lambda)$,

$$\hat{B}(\lambda) = S(\lambda) \otimes O(\lambda) \quad (2.3)$$

$$= T(\lambda) * T(\lambda) * B(\lambda) \quad (2.4)$$

This gives us repeated convolutions of the intrinsic broadening. Meanwhile, there exists another method to extract the true $B(\lambda)$, called the broadening function (BF) method.

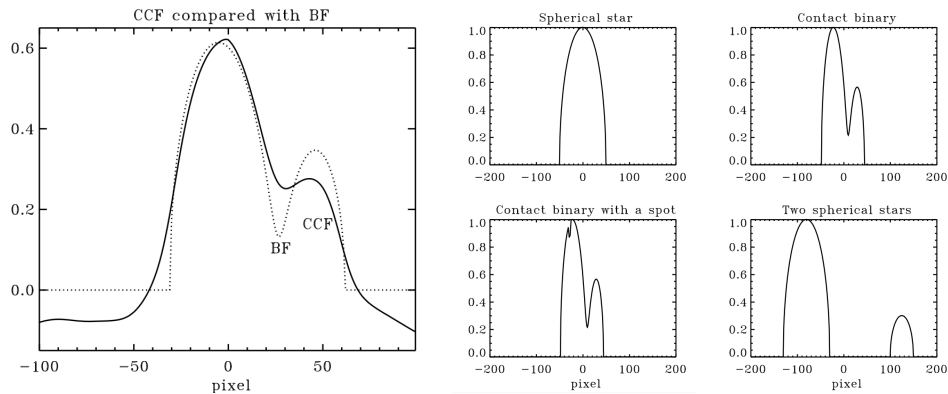


Figure 2.1 (Left) A comparison of CCF and BF for the same observed spectrum and template. (Right) BF shapes for different physical processes and configurations of a stellar system.

This uses the property that Fourier transform can convert convolutions to a product in the respective domain. And therefore a BF is calculated as,

$$B(\lambda) \simeq \mathcal{F}^{-1}\{\mathcal{F}\{O(\lambda)\}/\mathcal{F}\{S(\lambda)\}\} \quad (2.5)$$

This gives us a better estimate of the stellar profiles than the CCF (Figure 2.1; left) and can be used to identify additional companions and also other physical effects on the components (Figure 2.1; right).

In our work, we use the code `BF-RVLOTTER`¹ which is based on the algorithm described in Rucinski (1999). We use BF to detect CHT candidates from previously identified EB spectra (see next section) along with validation of CCF estimation of radial velocities. We also use BF to calculate light fractions of each component and also an estimate of their rotational velocity.

2.2. Radial Velocities

The BFs can help us detect CHTs but for confirmation of the orbital period of the tertiary, we need to use time-series radial velocity (RV) measurements. Most of our RV measurements are obtained via the CRÉME project (Hełminiak et al. 2022). *Comprehensive Research with Échelles on the Most interesting Eclipsing binaries* or CRÉME is a high-resolution spectroscopic survey of double-lined (SB2) EBs. CRÉME contains around 7000 spectra of over 300 low-mass (primary star mass of 0.3-7 M_{\odot}) from nearly twenty high-resolution spectrographs. An extensive RV modelling of the observations showed a number of systems where we observed the variation of the centre of mass (COM) velocity of the EB. We classified such systems as candidate spectroscopic triple-lined triple (ST3) or double-lined triple (ST2). This prompted further monitoring and finally the detection of new CHT targets ($P_{\text{out}} < 1000$ d). Further, to supplement the CRÉME observations, we had two successful observing programmes focused on time-series spectroscopy of CHTs:

¹<https://github.com/mrawls/BF-rvplotter>

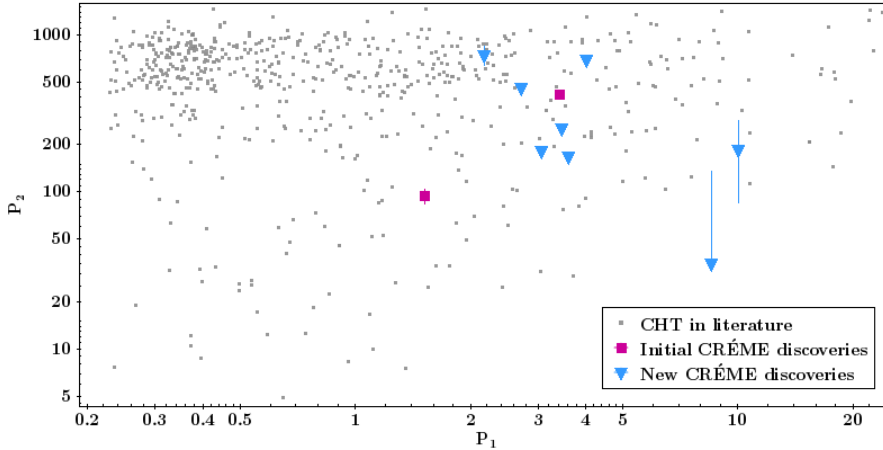


Figure 2.2 Inner binary period (P_1) vs tertiary period (P_2) of CRÉME CHT discoveries. The square (in pink) represents initially published CHT while triangles (in blue) show the CHTs discovered during this work. The grey points denote CHTs discovered in the literature. The empty space on the bottom right is the instability space of triples (see Equation 1.1).

- Long-term Science Programme (2021-2-MLT-006; P.I. A. Moharana) on the South African Large Telescope (SALT) using the High-Resolution Spectrograph (HRS). The program observed 11 systems for a period of 4 observing semesters.
- 60hrs (funded with the NCN grant PRELUDIUM-2021/41/N/ST9/02746) on the Cerro Tololo Inter-American Observatory (CTIO) using the CHIRON instrument. Within this program, 5 systems were observed for over 1 year.

CRÉME’s RV follow-up detected 10 candidate CHT out of which 2 have been published (and identified as triples) prior to the start of my PhD (Helminiak et al. 2017a,b). The period estimates of the rest of the CHT candidates from CRÉME are shown in Figure 2.2. Further, this thesis presents 4 discoveries and two previously discovered systems, with detailed spectroscopic analysis. They are discussed in chapter 4 and chapter 5.

2.3. Eclipse timing variations

Eclipse timing variations or ETVs are the most popular method of CHT detection in the *Kepler* and *TESS* era. If an EB is isolated, we would expect the primary (or secondary) minima to repeat at a certain period. But this is sometimes not the case when different physical processes change the eclipse timing, causing ETV (Applegate 1992; Bradstreet & Guinan 1994; Kalimeris et al. 2002; Balaji et al. 2015b). One cause of ETV is the presence of a third body around the EB. The identification of a third body can be done by modelling the light travel time effect (LTTE) which causes sinusoidal-like variation in the O-C (observed-calculated) variation over time. The O-C for an EB is calculated by,

$$\Delta_{obs} = T(E) - T_0 - P_B E \quad (2.6)$$

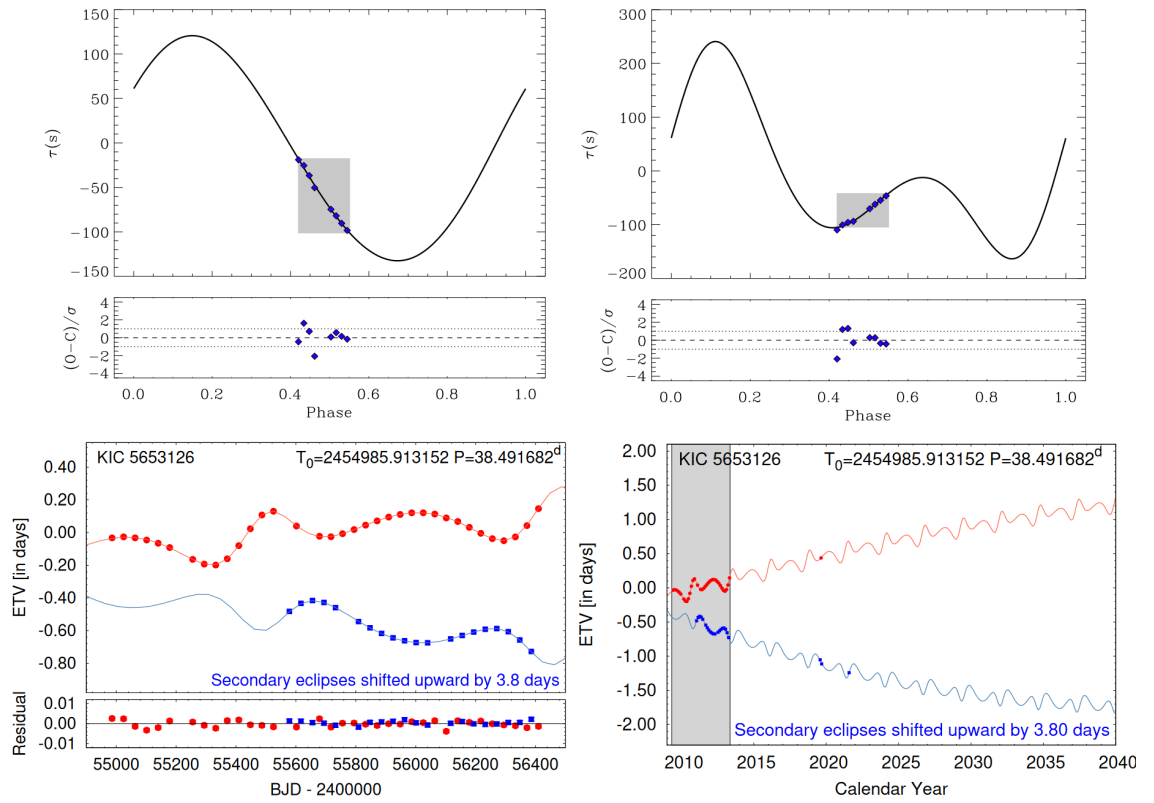


Figure 2.3 Time scales of different ETV signatures. (Top left) A LTTE fit to O-C (τ in secs). (Top right) A combined LTTE and dynamical fit to the same set of observations. Adopted from [Marcadon et al. \(2020\)](#). (Bottom left) A zoomed-in view of the ETV signals comprising of LTTE and dynamical variations. (Bottom right) A zoomed-out view of the same target shows long-term apse-node perturbations on top of the LTTE and the dynamical effects. Adopted from [Borkovits et al. \(2022\)](#).

where $T(E)$ denotes the observed time of E -th eclipse and T_0 is the reference epoch and P_B is the period between two eclipses. The LTTE O-C signal can be represented as ([Borkovits et al. 2016](#)),

$$\Delta_{\text{LTTE}} = -\frac{a_{\text{AB}} \sin i_2}{c^2} \frac{(1 - e^2) \sin(\nu_2 + \omega_2)}{1 + e_2 \cos \nu_2} \quad (2.7)$$

where a_{AB} is the absolute semi-major axis of the EB, i_2 is the inclination or the tertiary orbit to the plane of the sky, e_2 is the eccentricity, ν_2 is the true anomaly, and ω_2 is the argument of periastron of the tertiary orbit. c denotes the speed of light. In a CHT, there can be higher-order ETVs which are due to individual dynamical interactions between the three components. These ETVs can be mathematically represented as,

$$\Delta_{\text{dyn}} = \frac{2}{4\pi} \frac{m_C}{m_{\text{ABC}}} \frac{P_1^2}{P_2} (1 - e_2^2)^{-3/2} \times \left[\left(\frac{2}{3} - \sin^2 i_m \right) \mathcal{M} + \frac{1}{2} \sin^i m \mathcal{S} \right] \quad (2.8)$$

where \mathcal{M} and \mathcal{S} are functions of mean anomalies, true anomalies and geometrical argument of periastrons ([Borkovits et al. 2016](#)). m_C and m_{ABC} represent the tertiary mass and the total mass of the triple respectively. i_m is the mutual inclination, the

angle between the angular momentum vectors of the inner and outer orbits. With the precision of space telescopes and EBs, CHTs give us an alternative method to calculate the i_m , which was traditionally calculated using astrometry. Dynamical perturbations of a longer timescale (e.g. the apse-node perturbation Δ_{apse} ; [Borkovits 2022](#)) can also materialise in the ETVs but are visible in observations of a long time base. To summarise, the ETV variations due to a tertiary can be represented as ([Borkovits et al. 2016](#)),

$$\Delta = \sum_{i=0}^3 c_i E^i + [\Delta_{\text{LTTE}} + \Delta_{\text{dyn}} + \Delta_{\text{apse}}]_0^E \quad (2.9)$$

The visual representation of the different time scales are shown in [Figure 2.3](#).

2.3.1. The Solaris Photometric Survey

We looked for CHTs using our own ETV survey called the *Solaris* survey. *Solaris* (P.I. M. Konacki) is a network of four 0.5m robotic telescopes in the southern hemisphere at the same latitude. This allows for complete coverage of an EB eclipse with a cadence comparable to that of space telescopes. Starting in 2010, the *Solaris* survey targeted DEBs which showed signs of harbouring a tertiary. Observing around 150 systems over a period of 8 years, the *Solaris* survey was a good starting point to look for more CHTs. While in principle it is possible to measure both Δ_{LTTE} and Δ_{dyn} , due to certain observational constraints, we focus on finding LTTE signatures. The details of our first results from this search are detailed in the following publication. It also describes the photometric pipeline that has been developed, dedicated to *Solaris* data reduction and analysis.

Solaris photometric survey: Search for circumbinary companions using eclipse timing variations

A. Moharana¹,^{1*} K. G. Hełminiak¹,¹ F. Marcadon,² T. Pawar,¹ G. Pawar¹,¹ P. Garczyński,³ J. Perła,⁴ S. K. Kozłowski,⁵ P. Sybilski,⁶ M. Ratajczak⁷ and M. Konacki⁸

¹Nicolaus Copernicus Astronomical Center, Polish Academy of Sciences, ul. Rabiańska 8, 87-100 Toruń, Poland

²Villanova University, Department of Astrophysics and Planetary Sciences, 800 East Lancaster Avenue, Villanova, PA 19085, USA

³Faculty of Physics, University of Warsaw, Pasteura 5, 02-093 Warszawa, Poland

⁴Astronomical Observatory Institute, Faculty of Physics, Adam Mickiewicz University, Stoleczna 36, 60-286 Poznań, Poland

⁵Cilium Engineering Sp. z o.o., ul. Łokietka 5, 87-100 Toruń, Poland

⁶Sybilla Technologies Sp. z o.o., ul. Toruńska 59, 85-023 Bydgoszcz, Poland

⁷Astronomical Observatory, University of Warsaw, Al. Ujazdowskie 4, 00-478 Warszawa, Poland

⁸Nicolaus Copernicus Astronomical Center, Polish Academy of Sciences, ul. Bartycka 18, 00-716 Warszawa, Poland

Accepted 2023 October 9. Received 2023 October 9; in original form 2023 June 29

ABSTRACT

Eclipse timing variations (ETVs) have been a successful tool for detecting circumbinary companions to eclipsing binaries (EBs). While *TESS* and *Kepler* have been prolific for ETV searches, they sometimes can be limited by time and sky coverage, a limitation that can be addressed by specialized ground-based ETV surveys. We present the initial results from the Solaris photometric survey, which uses four 0.5-m robotic telescopes in the Southern hemisphere to look for circumbinary companions. We present the method of light-curve extraction, detrending, and EB modelling using observations from the Solaris network. Using these light curves, we extract precise eclipse timings for seven EBs and look for companions using a Lomb–Scargle periodogram search. We find two possible periodic signals for the target GSC 08814–01026. With the system having strong activity, we check for the feasibility of orbital solutions at these two periods. We find that the 245 ± 1 d period is due to an M dwarf-mass companion. This makes GSC 08814–01026 a candidate compact hierarchical triple system. The other periodic signal at 146 ± 1 d is an artefact of stellar activity.

Key words: techniques: photometric – binaries: eclipsing – stars: individual: GSC 08814-01026 – SU Ind – BK Ind – HD 60637 – TYC 8504-1018-1 – V889 Ara – CPD-52 10541.

1 INTRODUCTION

The detection of companions to stars has been crucial for understanding the formation, evolution, and dynamics of stars. It paved the way for the study of stellar multiplicity. The theory of the formation of low-mass objects such as brown dwarfs and planets has also been heavily influenced by observations of stellar multiplicity.

Most of the early surveys of multiplicity began with astrometric, radial velocity, and visual detections of companions (Finsen & Worley 1970; Batten 1973; Abt & Levy 1976). Fekel (1981) examined one such survey and identified an eclipsing binary (EB) in one of the stars in a resolved binary. This led to the detection of one of the first tertiaries around an EB. Since then, EBs have been used extensively for multiplicity studies using photometry, in addition to other avenues of detection. Photometry itself can be used in three distinct ways to detect a companion to an EB: (i) a third light in light-curve solutions, (ii) eclipse depth variations (EDVs), and (iii) eclipse timing variations (ETVs). While the first method is a

qualitative approach, EDV is prominent in highly dynamic systems. Furthermore, ETV has proved to be quite reliable in observing the light travel-time effect (LTTE) since the work of Chandler (1888), who was the first to give a possible reason for period changes in Algol.

The LTTE is observed owing to the movement of the EB with respect to the barycentre of the multiple system. It causes eclipses to occur earlier or later than the time expected for an isolated EB. However, variations in the eclipse timings can also be triggered by various other physical processes, such as the transfer of magnetic and orbital momentum (Applegate 1992), the loss of angular momentum (Bradstreet & Guinan 1994), and starspots (Kalimeris, Rovithis-Livaniou & Rovithis 2002; Balaji et al. 2015). However, these effects have different time-scales and can be distinguished from the long-term monitoring of the eclipse timings (ETs). This is where large-scale photometric surveys have been helpful for companion detection.

Photometric surveys such as the Optical Gravitational Lensing Experiment (OGLE; Udalski et al. 1992), All-Sky Automated Survey (ASAS; Pojmanski 1997), Super Wide Angle Search for Planets (SWASP; Street et al. 2003), Hungarian Automated Telescope (HAT;

* E-mail: ayushm@ncac.torun.pl

© The Author(s) 2023.

Published by Oxford University Press on behalf of Royal Astronomical Society. This is an Open Access article distributed under the terms of the Creative Commons Attribution License (<https://creativecommons.org/licenses/by/4.0/>), which permits unrestricted reuse, distribution, and reproduction in any medium, provided the original work is properly cited.

54 *A. Moharana et al.*

Bakos et al. 2004), and North Sky Variability Survey (NSVS; Woźniak et al. 2004) have generated a large number of observations for companion detection through ETVs (Kozłowski, Konacki & Sybilski 2011; Hajdu et al. 2019). Furthermore, space-based photometric missions such as Convection, Rotation and planetary Transits (CoRoT; Baglin et al. 2006), *Kepler* (Borucki et al. 2010) and the *Transiting Exoplanet Survey Satellite* (*TESS*; Ricker et al. 2015) have been prolific in providing precise ETs and circumbinary companions (Borkovits et al. 2016; Hajdu et al. 2017, 2022).

Meanwhile, in 2010, the Solaris project, a specialized ground-based photometric survey, started to target short-period EBs for ETs. In this paper, we present the first results from the ETV search using this telescope network. We discuss the setup of the telescopes and the photometric pipeline in Sections 2 and 3, respectively. In Sections 4 and 5 we describe how we use the light curves for EB modelling and ET extraction. Finally, in Section 6 we present our results and a positive detection.

2 SOLARIS NETWORK OF TELESCOPES

Numerical simulations have shown that in order to detect circumbinary companions, multiple 0.5-m telescopes are required to continuously monitor short-period binaries (binary period < 3 d) at high cadence (Sybilski, Konacki & Kozłowski 2010). This was the idea behind the establishment of the Solaris network.

The Solaris network is a global network of telescopes consisting of four fully autonomous observatories located in the Republic of South Africa (Solaris-1 and -2), Australia (Solaris-3), and Argentina (Solaris-4). The headquarters and main database are located in Poland. Each observatory consists of a telescope with a 0.5-m-diameter primary mirror, installed on a modified German equatorial mount from Astrosysteme Austria and equipped with fast and precise direct drives and high-resolution rotary-pulsing encoders. The Solaris-3 telescope is a Schmidt–Cassegrain $f/9$ optical system with a corrector, while the other telescopes are Ritchey–Cretien $f/15$ optical systems. For imaging, we use professional grade Andor Icon-L CCD cameras with a resolution of 2048×2048 pixels, thermoelectrically cooled to -70°C . The filter wheels allow multi-colour photometry in 10 bands: U, B, V, R, I (Johnson), and u', g', r', i', z' (Sloan). The commissioning of the network and its hardware, software, and processing capabilities are described in Kozłowski et al. (2017).

3 THE PHOTOMETRIC PIPELINE

The Solaris observations are stored in databases in Toruń, Poland. The Solaris pipeline processes these observations and produces multiband light curves (LCs) for each target. The steps and processes that the pipeline executes are described in the subsections below.

3.1 Inventory

The Solaris survey observed about 200 different eclipsing binaries over 5 years. The initial target sample was filtered from the ASAS Catalogue based on the maximum timing precision obtainable and other filters such as duration, depth of the eclipses, and brightness of the targets (Sybilski, Konacki & Kozłowski 2010). To systematically look for targets with sufficient observations, we created an inventory of the observations.

The inventory consisted of observations performed with Solaris from 2015 June to 2022 September. The targets were identified by the right ascension and declination in their image file headers and were

sorted according to the number of frames in all filters and then the number of nights of observations. The inventory also contains frame lists for every target observed. These frame lists contain the full path to the observations, which makes it easier for the photometric routine to search for the image files.

For this paper, we filtered targets with at least 16 000 frames of observations, spread across a minimum of 30 nights. We further narrowed down this sample to seven targets based on the quantity and quality of the eclipses in the final LC. The periods of these targets range from 0.7 to 2 d with a bias towards a 1-d period, which may be due to eclipse visibility in the basic telescope scheduling, but because these targets make up a small sample, it is difficult to draw any conclusions.

3.2 Calibration, reduction, and astrometry

We processed two types of calibration frames: (i) bias and (ii) flats. It is possible to acquire dark frames with the Solaris telescopes, but because the CCDs are cooled while taking images, the calibration is unaffected by the lack of dark frames. The inventory eases the process of collecting calibration frames specific to a star. We used CCDPROC¹ to median-combine and create the master-bias frames.

The flats are sky-flats and are of two distinct configurations depending on the orientation of the CCD. To create a master-flat, we first selected the frames with mean-counts of more than 15 000. The flats were also median-combined using CCDPROC, after being bias-corrected with the master-bias for the respective night. Although *Solaris* takes calibration frames for every night of observation, there are a few nights when it fails to do so. We added a calibration-frame matching module to improve the yield of image frames. For every science frame, we calculated the nearest possible night (past and future) from the available calibration frames. We rejected the nights that did not have the best match within a 50-d time difference. For the sake of consistency, we rotated the frames to a single orientation using the rotation module available in NUMPY.² After this, we used the CCDPROC module `gain.correct`, before proceeding to the standard calibration process. This gave us the final science image. Before proceeding to the photometry of the science frames, we applied astrometric corrections. This is to facilitate the selection of the correct target and reference star in all the photometric frames. We implemented the blind astrometry algorithm (Lang et al. 2010) from Astrometry.net. The frames for which the algorithm failed to identify the stars were rejected in further steps.

3.3 Photometry

Because the observations are spread over a long period, some of the observations are affected by seeing. Having a single aperture for different nights does not work in this case, and neither does creating a single point spread function (PSF). This is due to the lack of stars in the frames to generate a reliable PSF. Therefore, we used a variable aperture, which was calculated by evaluating a PSF for each frame using three stars (one target and two reference stars). For this, we defined an initial box around the stars (using the astrometric coordinates). The size of the box was estimated by checking the distance between the target and any nearby star to avoid any contamination in the box. We then fitted a 2D Gaussian profile to obtain the X and Y centroids, semimajor (a) and semiminor (b) axes,

¹<https://github.com/astropy/ccdproc>

²<https://numpy.org/doc/stable/reference/generated/numpy.rot90.html>

and the orientation of this profile. We then centred our aperture on the centroids, and the radius for the target aperture (r_T) was calculated as

$$r_T = 1.6 \times \sqrt{\text{FWHM}_a^2 + \text{FWHM}_b^2}, \quad (1)$$

where $\text{FWHM}_a = 2.35a$ and $\text{FWHM}_b = 2.35b$. The background was calculated using an annular aperture, with the inner radius (r_{Bin}) and the outer radius (r_{Bout}) given as

$$\begin{aligned} r_{\text{Bin}} &= r_T + 2; \\ r_{\text{Bout}} &= \sqrt{3r_T^2 + r_{\text{Bin}}^2}. \end{aligned} \quad (2)$$

The photometric errors were initially calculated from the routines in PHOTUTILS (Bradley et al. 2023), with the target flux and background flux as inputs. However, these errors were overestimated. Therefore, we calculated an overestimation scaling for individual targets using the Markov chain Monte Carlo (MCMC) method (see Section 5).

The pipeline produces the final LC with barycentric corrections based on Wright & Eastman (2014) and is implemented using BARYCORRPY.³ Barycentric corrections were incorporated by calculating the corrections for all four telescopes.

4 LIGHT CURVES

4.1 Detrending

The pipeline generates LCs spanning over 5 years of observations using relative photometry from four telescopes. This long coverage, therefore, results in various instrumental trends across the time-scale of observations. We used WOTAN (Hippke et al. 2019) in two steps to extract the final LC. First, we cleared out long-term trends with a window with a size of 60 times the EB period. Then we cleaned the short-term trends using a window sized between 1/6 and 1/2 of the EB period, depending on the scale of variations in each target. We used two methods in our detrending: `biweight` (Mosteller 1977) and `ramsay` (Ramsay 1977). Their use in our two steps varies for different iterations. We finally selected the output LC with the least variations and found that the best combination of a window and a particular method varied for different targets.

4.2 Eclipsing binary modelling

We used version 40 of JKTEBOP (Southworth 2013) for the modelling of the detrended LC. We selected the LC points with minimal errors for LC modelling. We started our modelling with initial estimates of the time of periastron passage (T_0) close to the first visible primary eclipse and a period (P) close to initial periodogram estimates. For some targets, we used some initial parameters from radial velocity (RV) modelling (see Appendix B). We also used initial parameters from the literature, if available. We kept the P , scale-factor (S), which controls the level of the out-of-eclipse fluxes in the LC, secondary-to-primary surface brightness ratio (J), inclination (i), radius ratio ($k = r_2/r_1$), and sum of fractional radii ($r_1 + r_2$) free for the first round of optimization. After this initial optimization, we kept the S fixed, and in addition to the previous set of free parameters, $e \cos \omega$ and $e \sin \omega$ (where e is the eccentricity and ω is the argument of periastron) were made free. Logarithmic limb-darkening (LD) was assumed, and approximate values for the coefficients were estimated from

Claret (2017) using prior information, if available. For the rest of the coefficients, we used estimates for a solar-like star. A few iterations with LD coefficients free were executed before fixing them to a robust value obtained from these iterations. Again multiple iterations were made with the above-mentioned parameters free, before proceeding to error estimation using the Monte Carlo (MC) method in JKTEBOP. For this setup, we also kept the third light parameter (l_3) free and then ran the MC module in JKTEBOP for 10 000 iterations. The best-fitting LC models for all the targets are shown in Fig. 1. The orbital and stellar parameter estimates are given in Tables 1 and 2.

5 ECLIPSE TIMING VARIATIONS

A tertiary around a binary system can produce three classes of perturbation (Brown 1936). They are (i) short-period perturbations of the order of the inner orbital period (P_1), (ii) long-period perturbations of the order of the outer orbital period (P_2), and (iii) apse-node perturbations of order (P_2^2/P_1). The current setup of Solaris cannot constrain the short-period perturbations, but long-term monitoring of the EB allows us to look for long-period perturbations.

5.1 Minima time extraction

To obtain the eclipse times we followed the formalism from Mikulášek (2015) to fit the morphology of individual eclipses with the following function:

$$f(T_i^j, \theta) = \alpha_0 + \alpha_1 \psi(T_i^j, T_0^j, d, \Gamma), \quad (3)$$

where Γ defines the kurtosis of the eclipse and d defines the depth. α_0 is the magnitude zero-point shift, and α_1 is a multiplicative constant of the eclipse profile function (ψ), which is written as

$$\psi(T_i^j, T_0^j, d, \Gamma) = 1 - \left\{ 1 - \exp \left[1 - \cosh \left(\frac{T_i^j - T_0^j}{d} \right) \right] \right\}^\Gamma, \quad (4)$$

where the time of the minimum of the j -component (T_0^j ; where $j=p$ for the primary and $j=s$ for the secondary) is the parameter that is important for this work. This formalism was incorporated in an eclipse fitting code used in Marcadon et al. (2020), which can effectively calculate the morphology of eclipses and extract the ET (Fig. 2). The errors in the measurements were calculated using MCMC fitting. This fitting also corrects for the overestimation of magnitude errors of the LC. This was done for one eclipse and then the calculated correction factor was applied to all of the photometric observations of a target.

We also checked for timing error estimates (TEEs) for our targets using the basic form of the TEE as given in Deeg & Tingley (2017),

$$\sigma_t = \frac{\sigma_{F_V} T_V}{2\Delta F}, \quad (5)$$

where σ_{F_V} is the photometric error on the time-scale of ingress and egress (varying from 0.005 to 0.4 in flux units), T_V is the summed duration of ingress and egress (assumed to be equal to the eclipse duration), and ΔF is the depth of the eclipse in flux units. We obtained TEE in the range of 0.1–1.8 times the MCMC errors, varying mostly owing to the σ_{F_V} (which is dependent on the out-of-eclipse noise). We adopted only the MCMC errors, as they are more cautious estimates for most of our ETs. The ETs were obtained in two filters (I and V) for both primary and secondary eclipses.

³<https://pypi.org/project/barycorppy/>

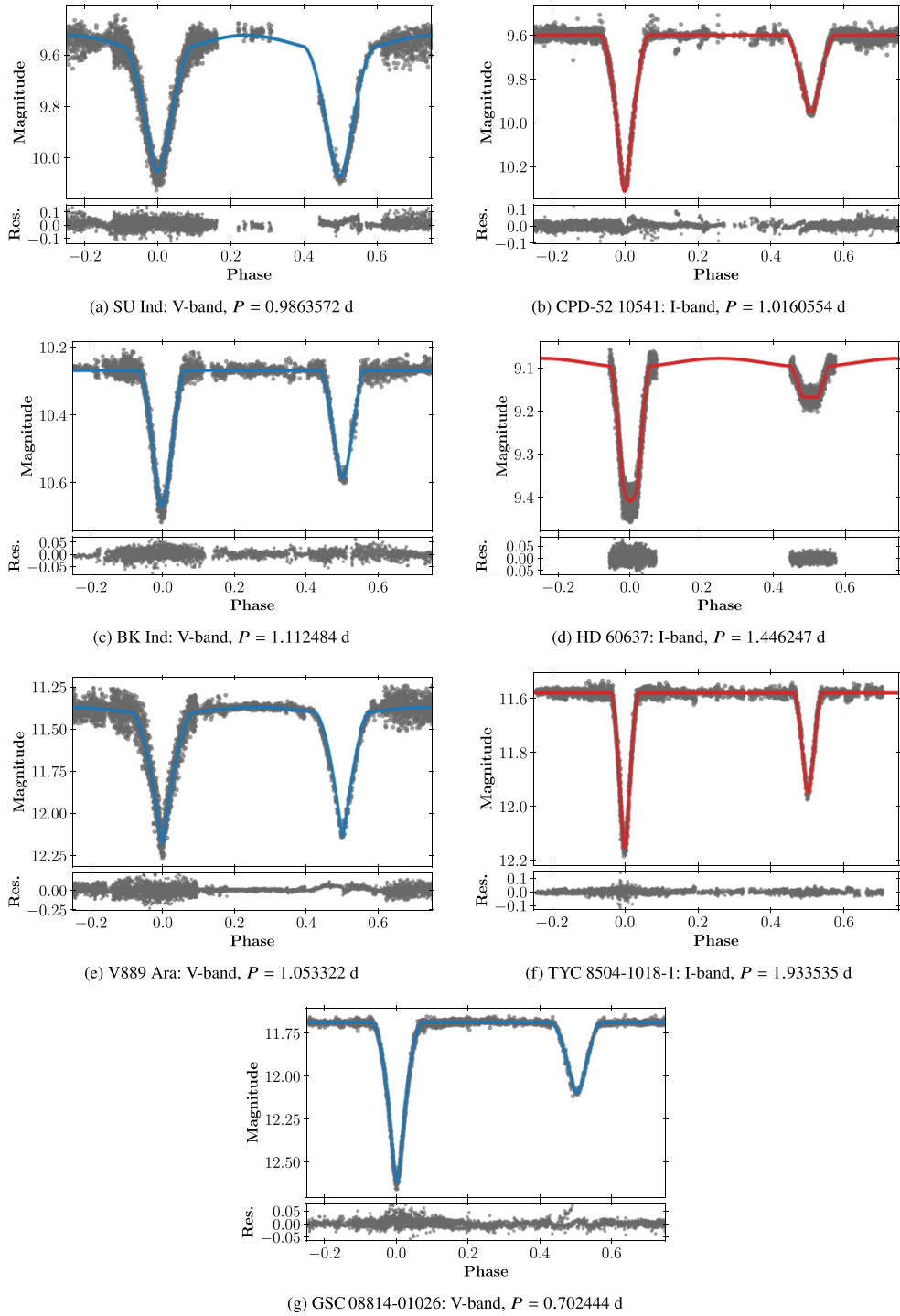
56 *A. Moharana et al.*

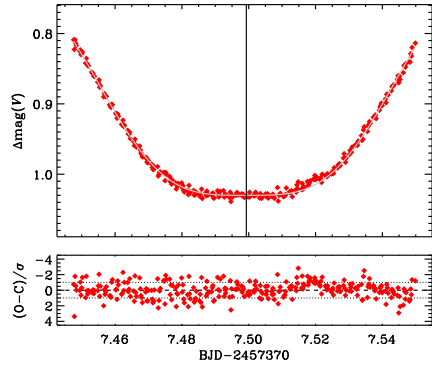
Figure 1. JKTEBOP LC models for the detrended Solaris LC. The fits are on the LC segments with errors < 2 per cent. Red and blue lines denote models for the *I* and *V* filter, respectively.

Table 1. Orbital parameters from light-curve fitting with JKTEBOP.

Target	P	T_0 (−2457000 BJD)	i	$e \cos \omega$	$e \sin \omega$
SU Ind	$0.9863572^{+0.0000003}_{-0.0000003}$	$211.1200375^{+0.00000970}_{-0.00000970}$	$81.226^{+0.461}_{-0.353}$	$-0.00513^{+0.00028}_{-0.00027}$	$0.01942^{+0.00455}_{-0.00390}$
CPD-52 10 541	$1.0160554^{+0.0000002}_{-0.0000002}$	$627.8944633^{+0.0000307}_{-0.0000297}$	$89.086^{+0.193}_{-0.160}$	$0.00063^{+0.00006}_{-0.00006}$	$0.00602^{+0.00077}_{-0.00079}$
BK Ind	$1.1124839^{+0.0000007}_{-0.0000007}$	$277.0137632^{+0.0002209}_{-0.0002243}$	$82.830^{+1.762}_{-0.983}$	$0.00065^{+0.00099}_{-0.00099}$	$-0.01774^{+0.01065}_{-0.01242}$
HD 60 637	$1.4462474^{+0.0000006}_{-0.0000006}$	$373.1600044^{+0.0000691}_{-0.0000679}$	$89.455^{+0.471}_{-0.834}$	$0.00050^{+0.00051}_{-0.00053}$	$0.00848^{+0.00311}_{-0.00498}$
V889 Ara	$1.0533224^{+0.0000009}_{-0.0000010}$	$255.0194406^{+0.0004229}_{-0.0004040}$	$89.921^{+0.049}_{-0.644}$	$-0.00020^{+0.00125}_{-0.00123}$	$-0.04304^{+0.00642}_{-0.00647}$
TYC 8504-1018-1	$1.9335349^{+0.0000005}_{-0.0000005}$	$289.4887875^{+0.0001061}_{-0.0001061}$	$89.084^{+0.263}_{-0.210}$	$-0.00016^{+0.00013}_{-0.00013}$	$0.01073^{+0.00322}_{-0.00345}$
GSC 08814-01026	$0.7024442^{+0.0000004}_{-0.0000004}$	$627.1265947^{+0.0000340}_{-0.0000348}$	$87.876^{+0.101}_{-0.098}$	0 (fixed)	0 (fixed)

Table 2. Stellar parameters from light-curve fitting with JKTEBOP.

Target	r_1	r_2	J	l_3
SU Ind	$0.2845^{+0.0083}_{-0.0095}$	$0.2885^{+0.0106}_{-0.0101}$	$1.0416^{+0.0032}_{-0.0037}$	$-0.017^{+0.019}_{-0.017}$
CPD-52 10 541	$0.2245^{+0.0002}_{-0.0002}$	$0.1898^{+0.0003}_{-0.0003}$	$0.7332^{+0.0011}_{-0.0010}$	$0.066^{0.003}_{-0.003}$
BK Ind	$0.2275^{+0.0098}_{-0.0314}$	$0.1722^{+0.0328}_{-0.0188}$	$0.7715^{+0.0200}_{-0.0175}$	$0.0183^{+0.0586}_{-0.0656}$
HD 60 637	$0.2352^{+0.008}_{-0.0008}$	$0.1093^{+0.0012}_{-0.0014}$	$0.2877^{+0.0038}_{-0.0039}$	$-0.047^{+0.16}_{-0.023}$
V889 Ara	$0.2450^{+0.0042}_{-0.0041}$	$0.2437^{+0.0031}_{-0.0046}$	$0.9834^{+0.0213}_{-0.0214}$	$-0.014^{+0.011}_{-0.011}$
TYC 8504-1018-1	$0.1326^{+0.0007}_{-0.0007}$	$0.1055^{+0.0005}_{-0.0006}$	$0.7323^{+0.0221}_{-0.0220}$	$0.106^{+0.009}_{-0.009}$
GSC 08814-01026	$0.2295^{+0.0013}_{-0.0012}$	$0.1959^{+0.0023}_{-0.0018}$	$0.595^{+0.024}_{-0.022}$	$-0.025^{+0.014}_{-0.013}$

**Figure 2.** Eclipse fitting of the Solaris observations of HD 60637 (primary eclipse) using our eclipse fitting code.**Table 3.** Linear ephemeris from fits to timing measurements.

Target	P_C	T_0^{Cp} (−2457000 BJD)	rms (s)
SU Ind	0.9863 ± 0.0114	213.1 ± 5.5	91
CPD-52 10 541	1.0161 ± 0.0104	241.8 ± 4.8	64
BK Ind	1.1125 ± 0.0130	248.1 ± 5.4	88
HD 60 637	1.4462 ± 0.0167	377.5 ± 2.7	43
V889 Ara	1.0533 ± 0.0111	223.4 ± 3.9	49
TYC 8504-1018-1	1.9335 ± 0.0312	289.5 ± 4.61	106
GSC 08814-01026	0.7024 ± 0.0008	231.7 ± 1.1	40

5.2 Calculating variations

For the ETV plots, we first calculated the reference parameters from a linear fit to cycle-number versus T_0^p . This gave us the reference primary epoch ($T_0^{\text{Cp}}(0)$) and an estimate of the reference period (P_C), as listed in Table 3. The corresponding secondary epoch ($T_0^{\text{Cs}}(0)$)

was calculated from the relationship (Kallrath & Milone 2009)

$$T_0^{\text{Cs}} - T_0^{\text{Cp}} - \frac{P_C}{2} = \frac{P_C}{\pi} e \cos \omega (1 + \text{cosec}^2 i), \quad (6)$$

where $e \cos \omega$ and i were taken from the LC solutions. The final ET value (OC_X^j), for different cycle-numbers X, was calculated as

$$\begin{aligned} OC_X^j &= T_0^j(X) - (T_0^{\text{Cj}}(0) + X P_C) \\ &\Rightarrow OC_X^j = T_0^j(X) - T_0^{\text{Cj}}(X). \end{aligned} \quad (7)$$

This gave us our final ETV plots for both primary and secondary eclipses (Fig. 3).

We then took all the observed ET points and looked for periodic variations using a Lomb–Scargle periodogram⁴ (Lomb 1976; Scargle 1982). We normalized the peaks using the standard normalization in the periodogram to be able to compare it with false alarm levels (FALs) for every target. We drew different FALs calculated from false alarm probabilities (FAPs) using the bootstrap method in the module. The periodograms from all the targets are shown in Fig. 4.

6 RESULTS

A signal detection was incurred if $FAP < 0.001$ per cent. For $FAP > 1$ per cent, we incurred no detection.

6.1 No detection

6.1.1 SU Ind

SU Ind was discovered as an EB by Hoffmeister (1956), and is also flagged as a spectroscopic binary in the RAVE DR6 catalogue. The only LC modelling comes from Budding et al. (2004), who did not use any RVs and assumed both the mass (q) and radii (k) ratios to be nearly equal to 1. The derived masses and radii of both components

⁴<https://docs.astropy.org/en/stable/timeseries/lombscargle.html>

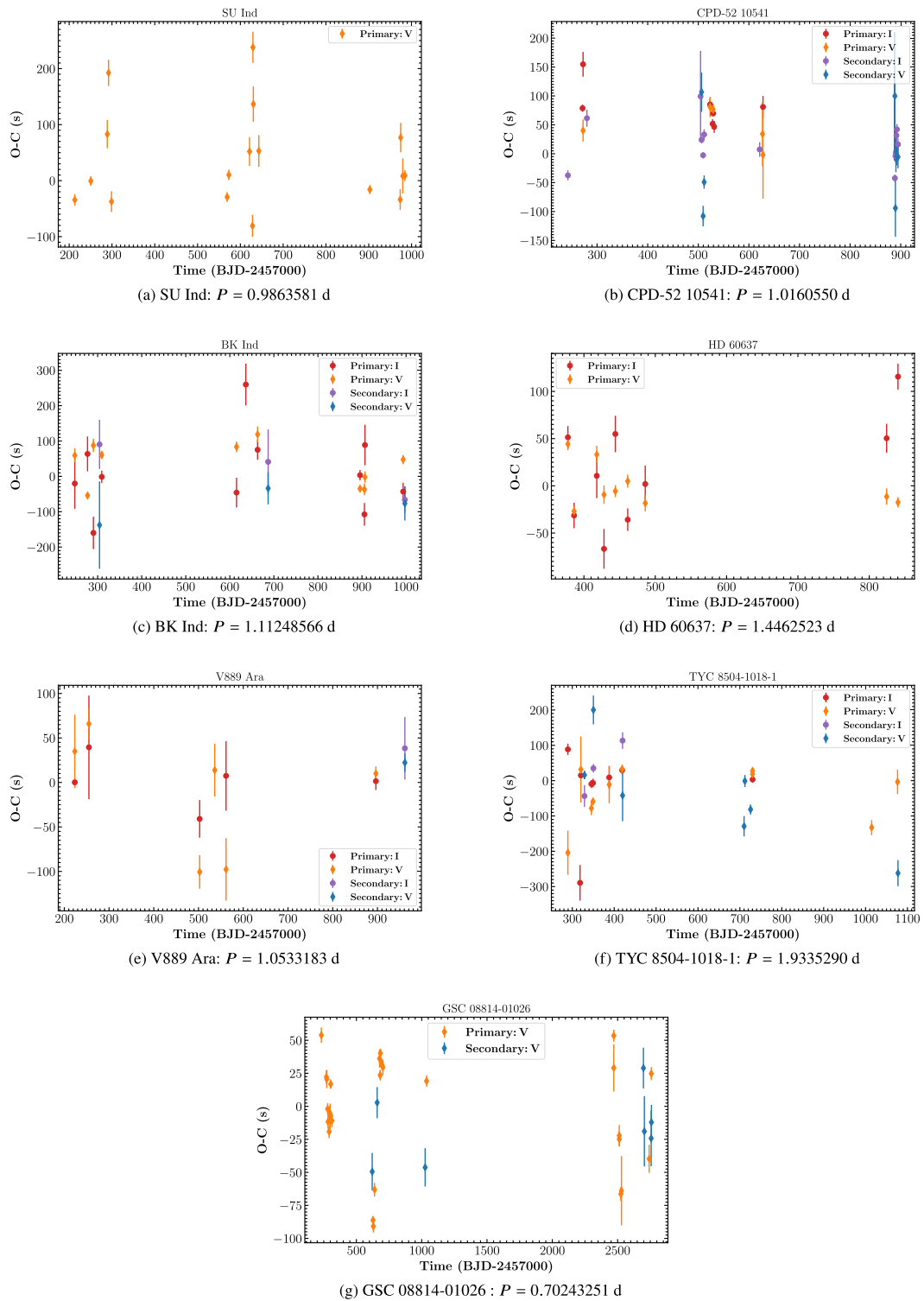
58 *A. Moharana et al.*

Figure 3. Solaris ETs for the primary (red and orange points, *I* and *V* band respectively) and secondary eclipses (blue and purple points, *I* and *V* band respectively) for all seven targets.

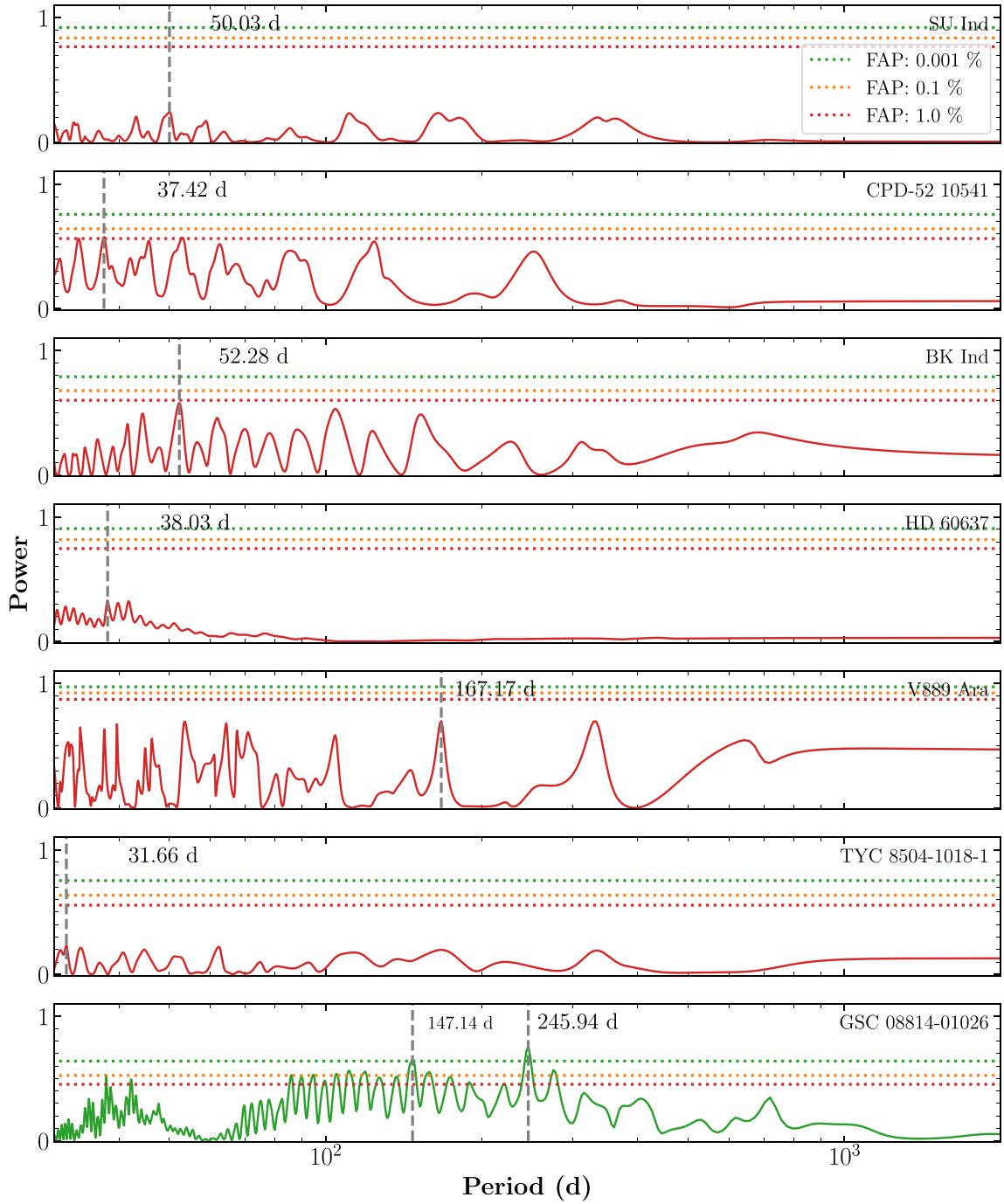


Figure 4. Lomb-Scargle periodograms for all the targets obtained using the Solaris ET. The green, orange, and red lines represent levels corresponding to a FAP less than 0.001 per cent, 0.1 per cent, and 1 per cent respectively. The dashed vertical lines mark the highest period visible in each of the periodograms. The green periodogram of GSC 08814-01026 marks the detection of two prominent peaks over the green level.

60 *A. Moharana et al.*

are thus $\sim 1.20 M_{\odot}$ and $\sim 1.50 R_{\odot}$ (with $r_1 = 0.2707 \pm 0.0054$ and $k = r_2/r_1 = 0.9927 \pm 0.0163$). These authors also determined the period to be 0.9863575 d. No RV solution has been published to date, but we have acquired nine spectra with the CHIRON spectrograph at the SMARTS 1.5-m telescope (Cerro Tololo, Chile) as part of the Comprehensive Research with Échelles on the Most interesting Eclipsing binaries (CRÉME; Hełminiak et al. 2022) survey (see Appendix B).

Our data show that the period is 0.9863573 d. Notably, the spectroscopic mass ratio is significantly lower than 1 ($q = 0.966 \pm 0.018$) and the (more massive) primary is fainter ($J = 1.0416$), even though both components are nearly equal in size (Table 2). Our solution provides masses and radii larger than those given by Budding et al. (2004).

The ET measurements were possible to obtain only for the primary eclipse in the *V* band. Despite the large scatter of ETs, no significant periodicity was found. However, the scatter is strictly dominated by measurements with larger individual errors. The rms of our ET data is 91.49 s (0.001058 d).

6.1.2 CPD-52 10541

CPD-52 10541 was discovered as an Algol-type eclipsing binary through the ASAS survey (ASAS J171606-5253.3; Pojmanski 2002). It has been registered in various catalogues, including Gaia DR3, but there has been no mention of its binarity. No RV or LC analysis is available in the literature. Along with the Solaris photometry, we have acquired eight high-resolution spectra of CPD-52 10541 through the CRÉME survey. The spectra were taken with the FEROS spectrograph (Kaufer et al. 1999) attached to the MPG 2.2-m telescope (La Silla, Chile) and are available in the ESO archive. We derived RV measurements and fitted the RV curves using the general methodology of the CRÉME survey (see Appendix B).

The period of CPD-52 10541 is 1.016055 d, and the inclination is close to 89° . The primary is larger and brighter, with $J = 0.7332$, with the relative radii for the primary and secondary being 0.2245 ± 0.0002 and 0.1898 ± 0.0003 , respectively. Combining the LC solution with the RV solution (Fig. 5) gives masses and radii of $M_1 = 1.075 \pm 0.028 M_{\odot}$, $R_1 = 1.200 \pm 0.010 R_{\odot}$ and $M_2 = 0.908 \pm 0.021 M_{\odot}$, $R_2 = 1.014 \pm 0.008 R_{\odot}$. CPD-52 10541 has an ET in both the bands (*I* and *V*) for primary and secondary eclipses. No periodicity was found in the ET. The rms of the ET is 63.79 s (0.0007 d).

6.1.3 BK Ind

Kazarovets et al. (1999) were the first to classify BK Ind as an Algol-type binary. Pojmanski (2002) initially determined the period to be 1.11249 d, which is close to our estimate ($P = 1.112 4839$ d). Recently, Sürgit et al. (2020) presented a full physical model, based on the RV and LC, as well as a series of timing measurements collected from the literature. The derived values of masses and radii are $M_1 = 1.16 \pm 0.05 M_{\odot}$, $R_1 = 1.33 \pm 0.03 R_{\odot}$ and $M_2 = 0.98 \pm 0.04 M_{\odot}$, $R_2 = 1.00 \pm 0.03 R_{\odot}$, leading to $r_1 = 0.229 \pm 0.003$ and $r_2 = 0.172 \pm 0.004$, with an inclination $i = 81.^{\circ}97 \pm 0.^{\circ}07$.

We find the inclination to be $i = 82.83^{+1.76}_{-0.98}$, and the fractional radii $r_1 = 0.227^{+0.010}_{-0.031}$, $r_2 = 0.172^{+0.033}_{-0.019}$, which are consistent with the estimates in Sürgit et al. (2020). We present new ET measurements for both primary and secondary eclipses in the *I* and *V* bands. Sürgit et al. (2020) concluded that there is no significant variation visible in their ET data. Similarly, we do not spot any significant period in our periodogram with Solaris observations. The rms of our data is 88.28.

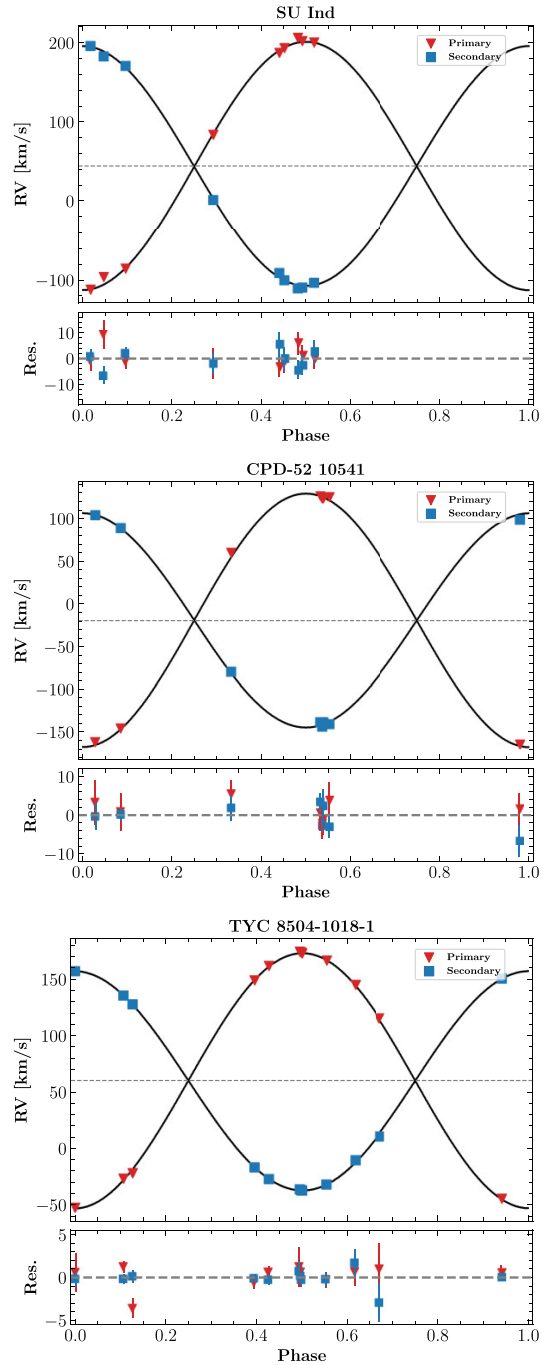


Figure 5. RV (red and blue symbols) and orbital fits (black lines) for SU Ind, CPD-52 10541, and TYC 8504-1018-1. The corresponding residuals with their error bars are presented in the lower panels of the respective figures.

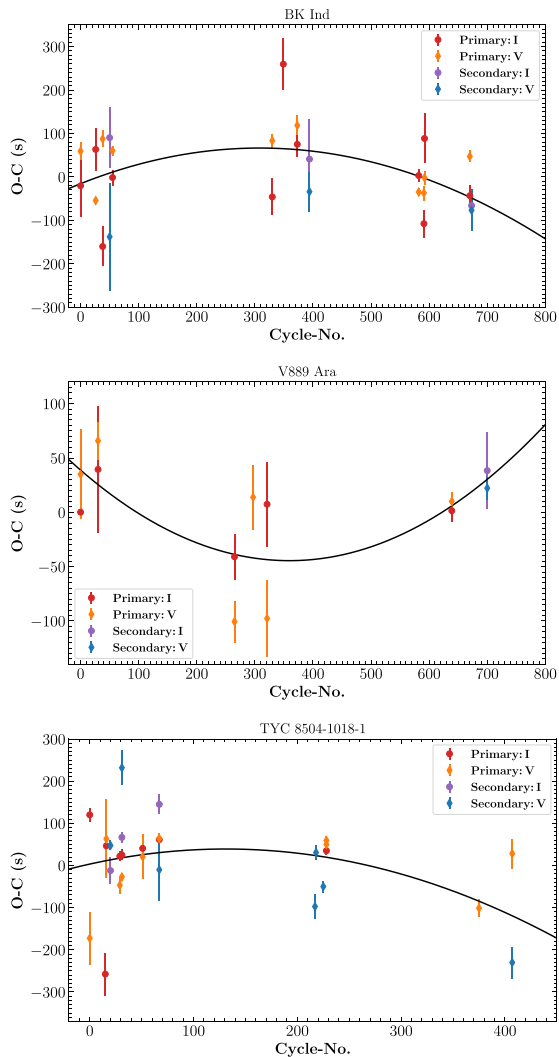


Figure 6. Parabolic fits for BK Ind, V889 Ara, and TYC 8504-1018-1. The respective \dot{P} for the targets are -0.00172 , 0.00129 and -0.0041 s/cycle.

We found a parabolic trend in the ETV, so we fitted for the rate of change of period (\dot{P}) as given in

$$T_0^j(X) = T_0^{\text{OCj}}(0) + X P_{\text{OC}} + \frac{1}{2} \dot{P} X^2. \quad (8)$$

Substituting values from equation (7) we have

$$OC_X^j = \frac{1}{2} \dot{P} X^2. \quad (9)$$

This gave us a parabolic fit to the ETV (Fig. 6) with $\dot{P} = -0.00172$ s/cycle. The periodogram did not change much after removing the parabolic trend, and periods were still below the detection FAL.

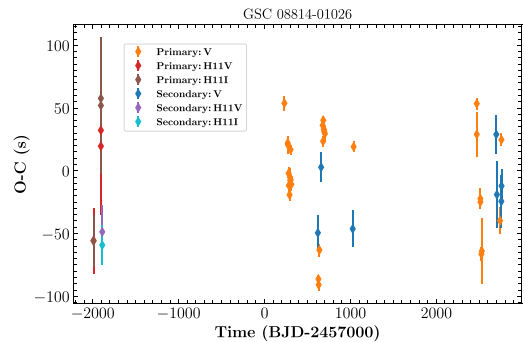


Figure 7. Additional ET for GSC 08814-01026 obtained from PROMPT and Elizabeth Telescope (marked together as H11). The ETVs were calculated using the same T_0^{OCp} and P_{OC} as used in the GSC 08814-01026 ETV in Fig. 3.

6.1.4 HD 60637

HD 60637 was discovered as an eclipsing binary through the ASAS survey (ASAS J073507-0905.7) and studied in detail by Helminiak et al. (2019). The absolute masses and radii were determined based on multiband photometry and high-resolution spectroscopy. They reported the values $M_1 = 1.452 \pm 0.034 M_{\odot}$ and $R_1 = 1.635 \pm 0.012 R_{\odot}$ for the primary, $M_2 = 0.808 \pm 0.013 M_{\odot}$ and $R_2 = 0.819 \pm 0.011 R_{\odot}$ for the secondary, and an inclination of 87.91 ± 0.01 . In our analysis, we obtained fractional radii of $r_1 = 0.2352 \pm 0.0008$ and $r_2 = 0.1093 \pm 0.0013$, which is $3.5-3.8\sigma$ distant from the results of Helminiak et al. (2019). Applying their spectroscopic solution, we obtain $R_1 = 1.660 \pm 0.012 R_{\odot}$ and $R_2 = 0.772 \pm 0.011 R_{\odot}$.

The period of HD 60637 is 1.4462474 d. Large differences in masses and radii between the components, and an inclination angle close to 90° ($89.455^{+0.471}_{-0.834}$), are reflected in the fact that the secondary eclipse is shallow and total, which makes it less useful for ET measurements. Thus our Solaris ETs are limited to the primary eclipse in both the V and I bands. No significant periodicity was identified. The rms of our ET is 42.88 s (0.0005 d).

6.1.5 V889 Ara

V889 Ara was registered as an eclipsing binary in the INTEGRAL-OMC catalogue of optically variable sources (Alfonso-Garzón et al. 2012). No LC or RV solutions have been published so far. V889 Ara is a system in which the two components have similar radii ($r_2/r_1 = 0.9947$) and surface brightness ($J = 0.9834$). We have mostly primary eclipses for the system, with only one secondary ET in the I band and V band each. No periodicity was found in the ET. With a linear fit, the rms of our ET is 48.66 s (0.0006 d). Similar to BK Ind, we also see a parabolic trend here (Fig. 6) for which the fit gave $\dot{P} = 0.00129$ s/cycle. But even with the removal of this trend, we see no significant peak in the periodogram.

6.1.6 TYC 8504-1018-1

TYC 8504-1018-1 was discovered as an Algol-type eclipsing binary through the ASAS survey (ASAS J040237-5502.5). It is flagged as a spectroscopic binary in the RAVE DR6 catalogue (Steinmetz et al. 2020), but no RV or LC solutions have been published to date. It has also been observed as part of the CRÉME survey, with eight spectra coming from the CHIRON spectrograph and four from the CORALIE

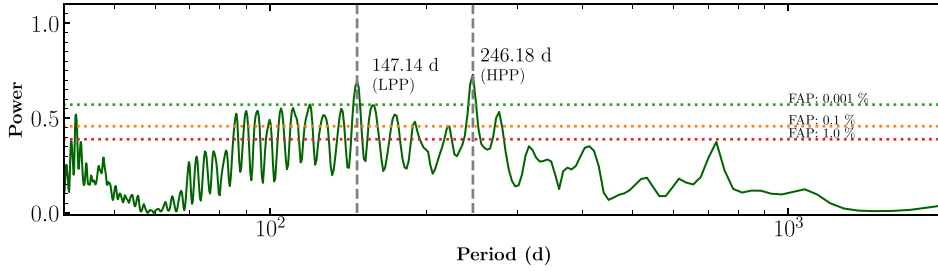
62 *A. Moharana et al.*

Figure 8. Lomb–Scargle periodogram for GSC 08814-01026 using all available ET points in Table 5.

Table 4. Parameters of orbital fits of all ET points of GSC 08814-01026.

Parameter	LPP		HPP	
	Value	1σ error	Value	1σ error
P_2 (d)	146.170	0.080	245.006	0.270
$asin i_2$ (au)	0.65760	0.28702	0.13802	0.00373
e_2	0.979	0.016	0.320	0.036
T_{02} (BJD-2450000)	7498.638	1.436	5968.190	3.085
ω_2 ($^\circ$)	356.148	1.626	19.196	3.976
A_3 (s)	70.038	39.566	65.644	1.808
$f(m_3)$ (M_\odot)	1.7756	2.3249	0.0058	0.0005
$M_{3, \min}$ (M_\odot)	3.6087	4.3363	0.2668	0.0113
$Red.\chi^2$	23.84		18.89	

instrument at the 1.2-m Euler telescope (La Silla, Chile). The estimated masses and radii are $1.005 \pm 0.008 M_\odot$ and $1.067 \pm 0.006 R_\odot$ for the primary, while for secondary the corresponding masses and radii are $0.864 \pm 0.004 M_\odot$ and $0.849 \pm 0.005 R_\odot$ (see Appendix B for details).

The rms of our ET data is 106.09 s (0.0012 d) with the linear ephemeris. A fit for the slight parabolic trend (Fig. 6) gave us $\dot{P} = -0.0041$, but its removal did not help in finding any significant peak in the periodogram.

6.2 Detection

6.2.1 GSC 08814-01026

This system was discovered as an Algol-type eclipsing binary through the ASAS survey (ASAS J212954–5620.1). It has been studied in detail by Helminiak et al. (2011), who derived $i = 87.^\circ 4 \pm 1.^\circ 3$, $P_{\text{orb}} = 0.7024303 \pm 0.0000007$ d, and the following masses and radii for its components: $M_1 = 0.833 \pm 0.017 M_\odot$, $R_1 = 0.845 \pm 0.012 R_\odot$ ($r_1 = 0.223 \pm 0.002$); $M_2 = 0.703 \pm 0.013 M_\odot$, $R_2 = 0.718 \pm 0.017 R_\odot$ ($r_2 = 0.186 \pm 0.002$). This system has the shortest orbital period and lowest stellar masses in our sample. It is also the most active one and is known to have spots that evolve quickly in time.

The rms of our ET data for linear ephemerides is 39.61 s (0.0005 d). With just the Solaris observations, we found few peaks with FAP < 0.001 per cent, with a period ~ 246 d dominating. This motivated us to extract minima times from three primary eclipses and one secondary eclipse from the Elizabeth Telescope (at the South African Astronomical Observatory) and the 0.4-m Panchromatic Robotic Optical Monitoring and Polarimetry Telescopes (PROMPT, at the Cerro Tololo Inter-American Observatory) in both the V and I bands (from Helminiak et al. 2011). We mark these observations as H11 in

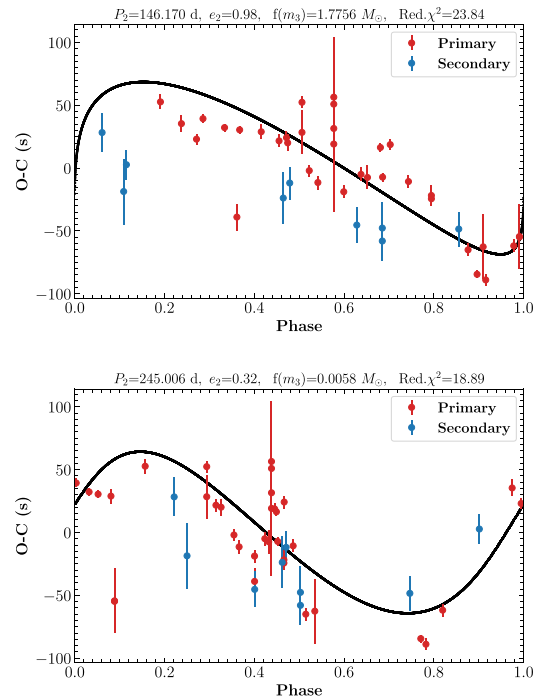


Figure 9. Phased ETV fit using OCFIT for LPP (top) and HPP (bottom). The red points denote all the primary ETs, while the blue represents the secondary ETs.

our ETV plots (Fig. 7). A periodogram search into this new set of ET observations makes the high-power peak (HPP) period change slightly to 246.18 d, while the low-power peak (LPP) stays the same (Fig. 8).

To check for the possibility of a realistic orbit for these two periods, we used the O–C fitting code OCFIT⁵ (Gajdoš & Parimucha 2019). For our fit, we used only the primary ET points and searched for an orbital fit based on the model of Irwin (1952). We constrained the range of the sine of the semimajor axis ($asin i_2$) to between 0.01 and 5 au, and the time of pericentre passage of the third body (T_{02}) to between 2 455 000 BJD and 2 460 000 BJD, while the other parameters such as eccentricity (e_2) and longitude of pericentre of the

⁵<https://github.com/pavolgaj/OCFit>

Table A1. Calculated and observed minima times of GSC 08814–01026 used for the companion search.

Cycle no.	Calculated T_0 (BJD-2457000)	Observed T_0 (BJD-2457000)	1σ error (d)	Telescope	Primary/Secondary
0	231.6578692	231.6584926	0.0000677	Solaris:V	P
55	270.2916538	270.2919106	0.0000606	Solaris:V	P
59	273.1013836	273.1016216	0.0000784	Solaris:V	P
69	280.1257081	280.1256847	0.0000525	Solaris:V	P
73	282.9354378	282.9353027	0.0000620	Solaris:V	P
85	291.3646272	291.3644052	0.0000572	Solaris:V	P
93	296.9840868	296.9840283	0.0000648	Solaris:V	P
96	299.0913841	299.0912967	0.0001111	Solaris:V	P
102	303.3059788	303.3061733	0.0000422	Solaris:V	P
103	304.0084113	304.0083270	0.0000410	Solaris:V	P
115	312.4376006	312.4374750	0.0000565	Solaris:V	P
563	627.1273370	627.1263387	0.0000365	Solaris:V	P
567	629.9370668	629.9360156	0.0000548	Solaris:V	P
580	639.0686886	639.0679579	0.0000596	Solaris:V	P
634	677.0000407	677.0004597	0.0000796	Solaris:V	P
641	681.9170679	681.9173408	0.0000477	Solaris:V	P
644	684.0243652	684.0248308	0.0000396	Solaris:V	P
654	691.0486897	691.0490713	0.0000372	Solaris:V	P
661	695.9657168	695.9660773	0.0000358	Solaris:V	P
671	702.9900413	702.9903836	0.0000691	Solaris:V	P
1147	1037.3478862	1037.3481078	0.0000505	Solaris:V	P
3187	2470.3100785	2470.3106980	0.0000529	Solaris:V	P
3247	2512.4560253	2512.4557376	0.0000653	Solaris:V	P
3264	2524.3973769	2524.3966084	0.0000610	Solaris:V	P
3271	2529.3144041	2529.3136641	0.0003034	Solaris:V	P
3187	2470.3100785	2470.310415	0.0002064	Solaris:V	P
3247	2512.4560253	2512.4557684	0.0000925	Solaris:V	P
3573	2741.4490031	2741.4485431	0.0001230	Solaris:V	P
3596	2757.6049494	2757.6052358	0.0000573	Solaris:V	P
554	621.1569573	621.1563849	0.0001637	Solaris:V	S
608	659.0883094	659.0883419	0.0001365	Solaris:V	S
1131	1026.4604793	1026.4599441	0.0001679	Solaris:V	S
3520	2704.5715957	2704.5713762	0.0003077	Solaris:V	S
3510	2697.5472713	2697.5476062	0.0001792	Solaris:V	S
3594	2756.5515968	2756.5513158	0.0002441	Solaris:V	S
3597	2758.6588942	2758.6587546	0.0001521	Solaris:V	S
–3163	–1990.1359614	–1990.1366046	0.0003016	PROMPT:V	P
–3041	–1904.4392028	–1904.4388293	0.0003852	ET:V	P
–3041	–1904.4392028	–1904.4389760	0.0006351	PROMPT:V	P
–3019	–1888.6341767	–1888.6347400	0.0002448	ET:V	S
–3163	–1990.1359614	–1990.1366088	0.0002379	PROMPT:I	P
–3041	–1904.4392028	–1904.4385349	0.0005458	PROMPT:I	P
–3041	–1904.4392028	–1904.4386004	0.0006285	ET:I	P
–3019	–1888.6341767	–1888.6348619	0.0001843	ET:I	S

orbit (ω_2) were kept free in their physically possible ranges. To centre our searches around LPP and HPP, we restricted the tertiary’s orbital period (P_2) to about 140–150 d and 240–250 d in two separate runs. The initial optimization was executed with genetic algorithms (Weise 2011). We further calculated the errors using the MCMC algorithm, implemented in the code using PYMC (Patil, Huard & Fønnesbeck 2010), which included 1000 burn-in iterations followed by 10 000 iterations. This gave us two possible orbital solutions where the LPP signal has a mass-function ($f(m_3)$) $1.7756 M_\odot$ and the HPP $f(m_3)$ is $0.0058 M_\odot$. We estimated the tertiary mass using the equation from Gajdoš & Parimucha (2019),

$$f(m_3) = \frac{(M_3 \sin i_2)^3}{M^2} = \frac{(a_2 \sin i_2)^3}{P_2^2}, \quad (10)$$

where M_3 is the tertiary mass, M is the total mass of the system, a_2 is the semimajor axis of the outer orbits, and i_2 is the inclination of the tertiary orbit. As we do not have an estimate of i_2 , we estimated the minimum mass of the tertiary ($M_{3,\min}$) using the total mass of the inner binary (M_B) from Hełminiak et al. (2011). From equation (10), we get

$$M_{3,\min}^3 - f(m_3)M_{3,\min}^2 - 2f(m_3)M_B M_{3,\min} - f(m_3)M_B^2 = 0. \quad (11)$$

Solving this cubic equation gives us a $M_{3,\min}$ of LPP as $3.6087 M_\odot$, while that of the HPP is consistent with an M dwarf star ($0.2668 M_\odot$). A $\sim 3.6 M_\odot$ star would have dominated the flux in the photometric (large I_3) and/or spectroscopic (visible in cross-correlation functions) solutions of Hełminiak et al. (2011), which is not the case. The semi-amplitude (A_3) of the LPP signal is higher than the A_3 of HPP, but its large errors bring it close to the rms. The reduced χ^2 of the fits

64 *A. Moharana et al.*

favours the HPP solution. We also found that the LPP signal was not visible in the periodogram when we removed the HPP signal from the ET. The details of both the fits are tabulated in Table 4.

Because GSC 08814-01026 is an active system, these signals could be artefacts of starspot migration. A study by Tran et al. (2013) showed that the effect of starspots on ETV curves can be identified by the anticorrelated nature of the primary and secondary ETV curves. Therefore, we over-plotted the secondary ET on the phased orbital solutions for the corresponding periods to check for any visible anticorrelation (Fig. 9). We did not find any significant anticorrelation, but because our secondary ETs are sparse in number, we do not entirely rule out the possibility of the periodic signals being due to starspots. With the current observations though, we expect the LPP to be a result of spot migration, which is corroborated by the high e_2 value (0.98) and larger-than-value errors on the estimated mass.

7 CONCLUSIONS

In this work, we report the first results from the ETV search for circumbinary companions using the Solaris network. The accuracy and cadence are well suited for ET extraction, with the possibility of obtaining ETs with a precision of a few seconds. We extracted ETs for seven targets varying over 2 years. We report on the detection of a companion around the eclipsing binary GSC 08814-01026, about which we conclude the following.

(i) There are two possible periods, 146 (± 1) d and 245 (± 1) d, for the companion, with the periodogram power and χ^2 of orbital fit favouring the 245-d period.

(ii) The 146-d period corresponds to an above-solar-mass star ($3.6087 M_{\odot}$), while the 245-d period corresponds to an M dwarf star ($0.2668 M_{\odot}$) orbiting around the inner binary in an orbit of eccentricity 0.32.

(iii) There is a possibility of the signal arising from activity, but with the current observations of the secondary ET, it seems unlikely for the 245-d period signal. However, based on the high eccentricity (0.98) of the orbital fit and the large errors in the mass estimate, the 146-d period is more likely to be a result of stellar activity. Furthermore, if a companion of mass $\sim 3.6 M_{\odot}$ existed, it would dominate the flux in the observations, which would be contradictory to Helminiak et al. (2011).

With the current set of observations, we conclude that GSC 08814-01026 has an M dwarf-like companion in an orbit of about 245 d, making it a candidate compact hierarchical triple (Borkovits 2022). A follow-up with radial velocities would surely help to confirm this detection. Nonetheless, Solaris is proved to be a useful telescope network to look for further circumbinary companions.

ACKNOWLEDGEMENTS

The authors thank the referee, Dr Hans Deeg, for his comments, which improved the quality of this work. This project is funded by the National Science Center (NCN), Poland, with the help of grant no. 2017/27/B/ST9/02727.

AM is supported by NCN grant no. 2021/41/N/ST9/02746. FM gratefully acknowledges support from the National Aeronautics and Space Administration (NASA) *TESS* Guest Investigator grant 80NSSC22K0180 (PI A. Prša).

The authors would like to thank Michał Drzał for his help in setting up the astrometric routine in the photometric pipeline. This research

has made use of the SIMBAD database (Wenger et al. 2000), operated at CDS, Strasbourg, France.

DATA AVAILABILITY

The minima times of all the targets are available along with the online version of this paper. The Solaris light curves and the radial velocities used in this work will be made available on request.

REFERENCES

- Abt H. A., Levy S. G., 1976, *ApJS*, 30, 273
- Alfonso-Garzón J., Domingo A., Mas-Hesse J. M., Giménez A., 2012, *A&A*, 548, A79
- Applegate J. H., 1992, *ApJ*, 385, 621
- Baglin A. et al., 2006, in 36th COSPAR Scientific Assembly, 36. COSPAR, Paris, p. 3749
- Bakos G., Noyes R. W., Kovács G., Stanek K. Z., Sasselov D. D., Domsa I., 2004, *PASP*, 116, 266
- Balaji B., Croll B., Levine A. M., Rappaport S., 2015, *MNRAS*, 448, 429
- Batten A. H., 1973, *Binary and Multiple Systems of Stars*. Pergamon Press, Oxford, UK
- Borkovits T., 2022, *Galaxies*, 10, 9
- Borkovits T., Hajdu T., Sztakovics J., Rappaport S., Levine A., Bíró I. B., Klagyivik P., 2016, *MNRAS*, 455, 4136
- Borucki W. J. et al., 2010, *Science*, 327, 977
- Bradley L. et al., 2023, *astropy/photutils*: 1.8.0. Available at: <https://doi.org/10.5281/zenodo.6825092>.
- Bradstreet D. H., Guinan E. F., 1994, in Shafter A. W. ed., *ASP Conf. Ser.* Vol. 56, *Interacting Binary Stars*. Astron. Soc. Pac., San Francisco, p. 228
- Brown E. W., 1936, *MNRAS*, 97, 62
- Budding E., Rhodes M., Priestley J., Zeilik M., 2004, *Astron. Nachrichten*, 325, 433
- Chandler S. C., 1888, *AJ*, 7, 169
- Claret A., 2017, *A&A*, 600, A30
- Deeg H. J., Tingley B., 2017, *A&A*, 599, A93
- Fekel F. C., Jr, 1981, *ApJ*, 246, 879
- Finsen W. S., Worley C. E., 1970, *Republic Obser. Johannesburg Circular*, 129, 203
- Gajdoš P., Parimucha Š., 2019, *Open European J. Variable Stars*, 197, 71
- Hajdu T., Borkovits T., Forgács-Dajka E., Sztakovics J., Marschalkó G., Benkő J. M., Klagyivik P., Sallai M. J., 2017, *MNRAS*, 471, 1230
- Hajdu T., Borkovits T., Forgács-Dajka E., Sztakovics J., Marschalkó G., Kutrovátz G., 2019, *MNRAS*, 485, 2562
- Hajdu T., Matécsa B., Sallai J. M., Bódi A., 2022, *MNRAS*, 516, 5165
- Helminiak K. G. et al., 2011, *A&A*, 527, A14
- Helminiak K. G. et al., 2017, *MNRAS*, 468, 1726
- Helminiak K. G. et al., 2019, *A&A*, 622, A114
- Helminiak K. G. et al., 2021, *MNRAS*, 508, 5687
- Helminiak K. G., Marcadon F., Moharana A., Pawar T., Konacki M., 2022, in Szuszkiewicz E., ed., *Polish Astron. Soc. Meeting Series*, 12. Polish Astronomical Society, Warsaw, p. 163
- Hipke M., David T. J., Mulders G. D., Heller R., 2019, *AJ*, 158, 143
- Hoffmeister C., 1956, *Veroeffentlichungen Sternwarte Sonneberg*, 3, 1
- Irwin J. B., 1952, *ApJ*, 116, 211
- Kahraman Aliçavuş F. et al., 2023, *MNRAS*, 520, 1601
- Kalimeris A., Rovithis-Livaniou H., Rovithis P., 2002, *A&A*, 387, 969
- Kallrath J., Milone E. F., 2009, *Eclipsing Binary Stars: Modeling and Analysis*. Springer-Verlag, New York
- Kauffer A., Stahl O., Tubbesing S., Nørregaard P., Avila G., Francois P., Pasquini L., Pizzella A., 1999, *The Messenger*, 95, 8
- Kazarovets E. V., Samus N. N., Durelevich O. V., Frolov M. S., Antipin S. V., Kireeva N. N., Pastukhova E. N., 1999, *Information Bull. Variable Stars*, 4659, 1
- Konacki M., Muterspaugh M. W., Kulkarni S. R., Helminiak K. G., 2010, *ApJ*, 719, 1293
- Kozłowski S. K., Konacki M., Sybilski P., 2011, *MNRAS*, 416, 2020

- Kozłowski S. K., Sybilski P. W., Konacki M., Pawłaszek R. K., Ratajczak M., Helminiak K. G., Litwicki M., 2017, *PASP*, 129, 105001
- Lang D., Hogg D. W., Mierle K., Blanton M., Roweis S., 2010, *AJ*, 137, 1782
- Lomb N. R., 1976, *Ap&SS*, 39, 447
- Marcadon F., Helminiak K. G., Marques J. P., Pawłaszek R., Sybilski P., Kozłowski S. K., Ratajczak M., Konacki M., 2020, *MNRAS*, 499, 3019
- Mikulášek Z., 2015, *A&A*, 584, A8
- Moharana A., Helminiak K. G., Marcadon F., Pawar T., Konacki M., Ukita N., Kambe E., Maehara H., 2023, *MNRAS*, 521, 1908
- Mosteller F., 1977, *Data Analysis and Regression: A Second Course in Statistics*. Addison-Wesley Pub. Co., Reading, MA
- Patil A., Huard D., Fomesbeck C. J., 2010, *J. Stat. Softw.*, 35, 1
- Pojmanski G., 1997, *Acta Astronomica*, 47, 467
- Pojmanski G., 2002, *Acta Astronomica*, 52, 397
- Ramsay J. O., 1977, *J. Am. Statist. Assoc.*, 72, 608
- Ratajczak M. et al., 2021, *MNRAS*, 500, 4972
- Ricker G. R. et al., 2015, *J. Astron. Tel. Instr. Syst.*, 1, 014003
- Scargle J. D., 1982, *ApJ*, 263, 835
- Southworth J., 2013, *A&A*, 557, A119
- Steinmetz M. et al., 2020, *AJ*, 160, 83
- Street R. A. et al. 2003, in Deming D., Seager S.eds, *Scientific Frontiers in Research on Extrasolar Planets*, ASP Conference Series, 294. p. 405
- Sürgit D., Erdem A., Engelbrecht C. A., Marang F., 2020, *MNRAS*, 493, 2659
- Sybilski P., Konacki M., Kozłowski S. K., 2010, *MNRAS*, 405, 657
- Tran K., Levine A., Rappaport S., Borkovits T., Csizmadia S., Kalomeni B., 2013, *ApJ*, 774, 81
- Udalski A., Szymanski M., Kaluzny J., Kubiak M., Mateo M., 1992, *AcA*, 42, 253
- Weise T., 2011, *Global Optimization Algorithms: Theory and Application*. Thomas Weise, Available at <https://freecomputerbooks.com/Global-Optimization-Algorithms.html>
- Wenger M., et al. 2000, *Astron. Astrophys. Suppl. Ser.*, 143, 9
- Woźniak P. R. et al., 2004, *AJ*, 127, 2436
- Wright J. T., Eastman J. D., 2014, *PASP*, 126, 838
- Zucker S., Mazeh T., 1994, *ApJ*, 420, 806

SUPPORTING INFORMATION

Supplementary data are available at *MNRAS* online.

ETV_tables.dat

Please note: Oxford University Press is not responsible for the content or functionality of any supporting materials supplied by the authors. Any queries (other than missing material) should be directed to the corresponding author for the article.

APPENDIX A: ET MEASUREMENTS

The ET of GSC08814-01026 is given in Table A1. The ETs for the other six targets are available in the online version of this paper.

APPENDIX B: NEW RV MEASUREMENTS AND SOLUTIONS

Here we describe the RVs of three systems from this study – SU Ind, CPD-52 10541, and TYC 8504-1018-1 – which did not have any RV solutions previously, and which were observed as part of the CRÉME survey, together with HD 60637 (Helminiak et al. 2019) and several other systems published to date.

Observations of those three systems were taken between 2012 and 2015 for CPD-52 10541 and TYC 8504-1018-1, and in 2021 for SU Ind. Spectra were reduced with dedicated pipelines. RV calculations were made using our implementation of the TODCOR routine (Zucker & Mazeh 1994), and orbital fits with the V2FIT code (Konacki et al. 2010). Detailed descriptions of the implemented methodology can be found in previous publications that are based on CRÉME data (see e.g. Helminiak et al. 2017; Marcadon et al. 2020; Helminiak et al. 2021; Ratajczak et al. 2021; Kahrman Aliçavuş et al. 2023; Moharana et al. 2023, and references therein).

The solutions are presented in Table B1 and Fig. 5. Individual measurements are available in the online version of this paper.

Table B1. Orbital solutions of SU Ind, CPD-52 10541, and TYC 8504-1018-1, based on CRÉME spectra and RV measurements, and physical parameters derived from a combination of RV and LC solutions.

Parameter	SU Ind	CPD-52 10541	TYC 8504-1018-1
<i>Orbital, from RVs only</i>			
K_1 [km s ⁻¹]	151.9(2.0)	125.1(1.6)	97.29(14)
K_2 [km s ⁻¹]	157.2(2.0)	148.0(1.4)	113.19(43)
γ [km s ⁻¹]	44.2(1.4)	-19.5(0.9)	60.20(19)
e	0.0(fix)	0.0(fix)	0.0(fix)
ω [°]	—	—	—
$a \sin(i)$ [R _⊙]	6.028(55)	5.486(40)	8.046(17)
$M_1 \sin^3(i)$ [M _⊙]	1.535(44)	1.162(26)	1.0044(80)
$M_2 \sin^3(i)$ [M _⊙]	1.483(43)	0.982(23)	0.8634(42)
rms_1 [km s ⁻¹]	3.68	3.36	1.05
rms_2 [km s ⁻¹]	4.12	3.01	1.33
N_{obs}	9	8	12
<i>Physical, from combining with LC solutions</i>			
M_1 [M _⊙]	1.590(46)	1.163(26)	1.005(8)
M_2 [M _⊙]	1.537(45)	0.983(23)	0.864(4)
a [R _⊙]	6.099(56)	5.487(40)	8.047(17)
R_1 [M _⊙]	1.735(57)	1.232(9)	1.067(6)
R_2 [M _⊙]	1.760(65)	1.041(8)	0.849(5)
$\log(g_1)$	4.161(28)	4.323(4)	4.384(5)
$\log(g_2)$	4.134(32)	4.395(5)	4.517(5)

This paper has been typeset from a $\text{\TeX}/\text{\LaTeX}$ file prepared by the author.

CHAPTER 3

Everything in the Arsenal: Extraction of absolute parameters

" Every day, it gets a little easier. But you gotta do it every day.
That's the hard part."

–Raphael Bob-Waksberg, Creator, Bojack Horseman

While the methods of extraction of absolute parameters of unresolved binaries have become common, extending it to triple systems is simple in theory but non-trivial in practice. In this chapter, I discuss the different methods used to get consistent stellar, orbital and atmospheric parameters of stars in a CHT.

3.1. Stellar and orbital parameters

A combination of LC and RV modelling of a SB2 EB can give quite precise and accurate masses and radii of two stars. While in a CHT, we can use the same method to extract parameters for the two stars in the inner binary. Some of these methods can also be extended to estimate the parameters of a triple system. We discuss our methodology for parameter extraction in the following sections.

3.1.1. Light curve modelling

The peculiar light curve of any EB, in a first approximation, is a geometrical tool to extract basic stellar parameters. Different configurations dictate the morphology of the light curve (LC). The geometry of any eclipse contains information about the relative

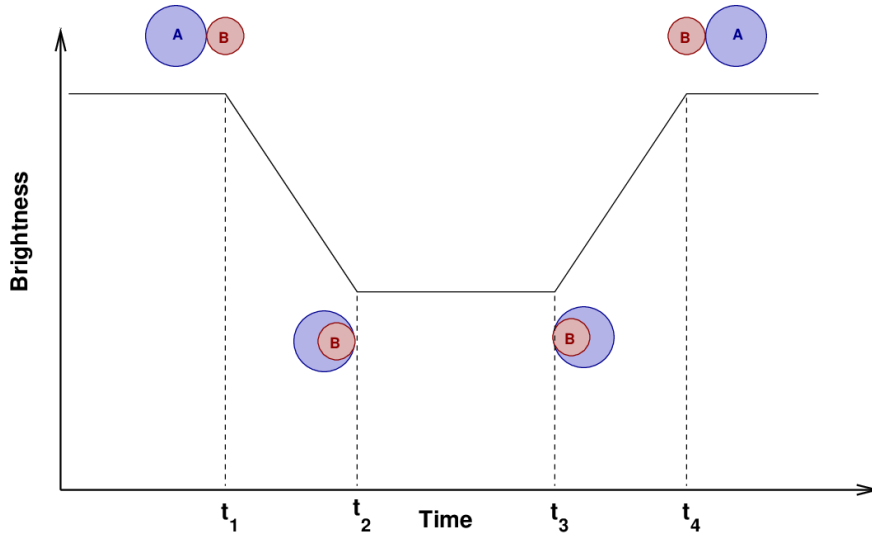


Figure 3.1 A simple, geometric model of an eclipse of two uniform disks. The important times for LC modelling are also marked. From: Michael Richmond (http://spiff.rit.edu/classes/phys370/lectures/eclipse_1/eclipse_1.html)

radii (r_1, r_2 , where $r = R/a$), temperature ratio (T_2/T_1), etc. Simple modelling would include identifying certain features in a LC and measuring their geometry.

Some of the important features are represented in [Figure 3.1](#). These are the time of ingress (t_1), start of complete eclipse (t_2), end of complete eclipse (t_3), and time of egress (t_4). Coupling these times with width of whole eclipse (δ_1), width of complete eclipse (δ_2), and depth of the eclipse (ϵ) can give us,

$$\begin{aligned}
 r_1 &= \frac{1}{2\sqrt[4]{\epsilon}} \sqrt{\sin \delta_1^2 - \sin \delta_2^2} \\
 r_2 &= \frac{\sqrt[4]{\epsilon}}{2} \sqrt{\sin \delta_1^2 - \sin \delta_2^2} \\
 T_2/T_1 &= \sqrt[4]{\frac{\epsilon_2}{\epsilon_1}}
 \end{aligned} \tag{3.1}$$

where, for period P , we have,

$$\begin{aligned}
 \delta_1 &= \pi(t_4 - t_1)/P \\
 \delta_2 &= \pi(t_3 - t_2)/P
 \end{aligned} \tag{3.2}$$

While this basic treatment is useful, we use more complex codes which include Roche distortions, stellar spot variations, limb-darkening, etc.

The Roche model is one of the most accurate models of binary star geometry. The Roche model (named after its formulator, E.A. Roche) assumes that both the stars are point objects surrounded by massless envelopes, the periods of free non-radial oscillations are negligible, and the stars rotate as a rigid body. Referring to [Figure 3.2](#) and star M_1 as

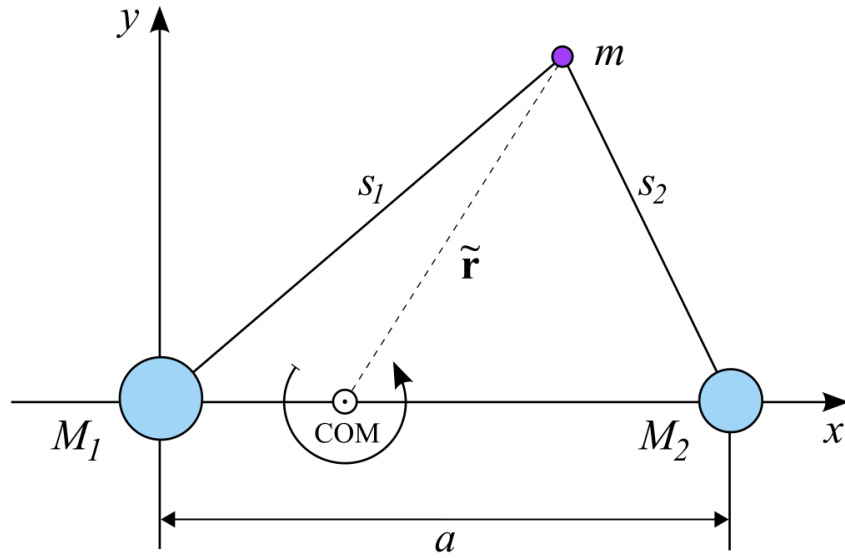


Figure 3.2 Geometry of a binary system in the Roche model. Figure credits: [Prša \(2018\)](#)

origin, we can represent the effective potential ψ , on a particle of mass m from two stars of masses M_1 and M_2 (at a distance a from each other) as ([Prša 2018](#)),

$$\psi = -\frac{GM_1}{s_1} - \frac{GM_2}{s_2} - \frac{1}{2}\omega^2\tilde{r}^2 \quad (3.3)$$

where ω is the angular velocity of the system and \tilde{r} is the distance of m from the centre of mass (COM) of the system. Using transformations to spherical coordinates ($x = \lambda r$; $y = \mu r$; $z = \nu r$), $q = M_2/M_1$, and Kepler's law ($\omega^2 a^3 = G(M_1 + M_2)$) we get,

$$\psi(r, \lambda, \nu) = -\frac{GM_1}{a} \left[\frac{a}{r} + q \left(\frac{a}{\sqrt{r^2 - 2ar\lambda + a^2}} - \frac{r\lambda}{a} \right) + \frac{r^2}{2a^2}(1+q)(1-\nu^2) + \frac{q^2}{2(1+q)} \right] \quad (3.4)$$

For computational purposes, we can re-write this equation in terms of dimensionless potential Ω and distance $\varrho = r/a$ as,

$$\Omega = \frac{1}{\varrho} + q \left(\frac{1}{\sqrt{\varrho^2 - 2\varrho\lambda + 1}} - \varrho\lambda \right) + \frac{(1+q)(1-\nu^2)\varrho^2}{2} \quad (3.5)$$

This is referred to as the modified Kopal potential ([Kopal 1959](#)). and it defines the shape of a binary star ([Figure 3.3](#)).

PHysics Of Eclipsing BinariEs 2 (PHOEBE2) is a PYTHON based EB modelling code which includes the Roche model and other advanced physics. It models a binary by discretising

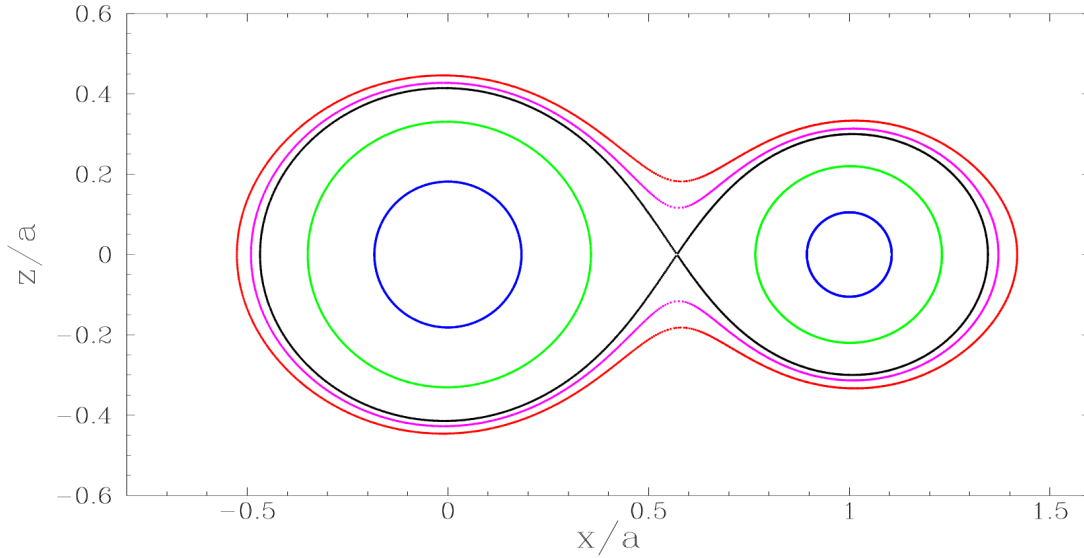


Figure 3.3 Different Roche potentials for different binary morphologies. The blue and green lines show the potential for detached systems, black for semi-detached and pink and red represent contact systems. Figure credits: [Prša \(2018\)](#).

the surface into triangles and calculating fluxes from the visible elements. This allows us to model contact, semi-detached and detached systems. Another benefit of surface modelling is that we can physically add and model stellar spots in addition to the variation from the eclipses. We use `PHOEBE2` for cases where the variability due to spots is large and substantially affects the eclipse depths. `PHOEBE2` offers optimisation of the parameters using Nelder-Mead optimisation ([Nelder & Mead 1965](#)) and sampling of the errors using the Markov Chain Monte Carlo (MCMC) algorithm. The parameter space that we explore in `PHOEBE2` includes (i) inclination of inner binary (i_A) (ii) eccentricity (e_A) (iii) argument of periastron (ω) (iv) temperatures of the stars (v) third-light (L_3) (vi) individual radii of the stars (given the semi-major axis a_A) (vii) latitude, longitude, temperature and size of the stellar spots, and (viii) luminosities of the stars.

We also use a faster code, the FORTRAN based `JKTEBOP` ([Southworth 2013](#)). `JKTEBOP` is a modelling code based on the old Eclipsing Binary Orbit Program (EBOP) code ([Etzel 1981](#)). `JKTEBOP` models a star as a sphere or as a biaxial spheroid and calculates the LC by numerical integration of concentric circles. This allows it to fit only detached eclipsing binaries. It calculates light curves by numerical integration of concentric circles over each star. The optimisation is done with the Levenberg-Marquardt algorithm ([Moré 1978](#)) to find the best-fit models. It also includes several limb-darkening and gravity-darkening laws. It is possible to model small variations due to spots and pulsations using sines and polynomials. It allows for times of minimum light, spectroscopic light ratios, third light values, and orbital eccentricity to be included directly as observed quantities to constrain the solution. The final sampling and estimation of errors are done using Monte Carlo (MC) and bootstrapping simulations. Some of the parameter space used in `JKTEBOP`

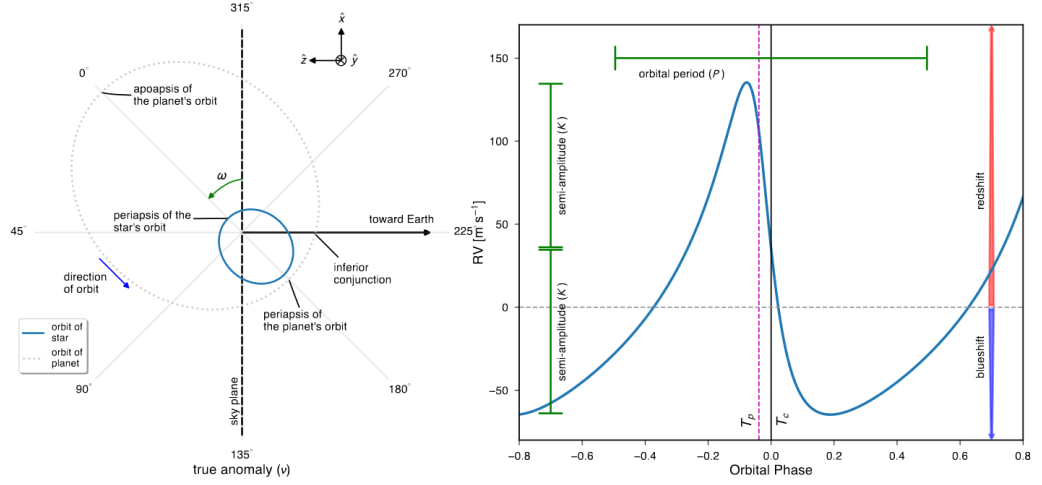


Figure 3.4 Translating RV from a 3D geometry. (Left) Top-down view of a 2-body orbit (a planet and a star here) with relevant parameters labelled. The orbit of interest, and the one which is translated, is in blue and in the same plane as the paper. (Right) The RV translation of the motion of the star. Figure credits: [Fulton et al. \(2018\)](#).

modelling involves (i) scale-factor (Sf; determines the scaling or the magnitude of out-of-eclipse portion), (ii) surface brightness ratio (J), (iii) L_3 , (iv) e_A and ω in the form of $e \sin \omega$ and $e \cos \omega$, (v) i_A , (vi) radius ratio (k), (vii) sum of fractional radii ($r_1 + r_2$), where the fractional radii are represented as radius divided by a_A .

3.1.2. Radial velocity modelling

Radial Velocity (RV) modelling has become comparatively complex as we now have ultra-precise RV measurements to detect exoplanets. While we can now model components of stellar activity ([Meunier 2021](#)), low-amplitude stellar pulsations ([Netto et al. 2021](#)), multi-planet systems ([Kosiarek et al. 2021](#)), we use the basic Keplerian signature of stellar bodies to model our systems with some additional components. The standard Keplerian velocity equation of a star can be written as,

$$\boldsymbol{\nu} = (\nu_x, \nu_y, \nu_z) = \frac{an}{r} \left(-a\vec{P} \sin E + a\vec{Q} \sqrt{1 - e^2} \cos E \right) \quad (3.6)$$

where, $n = 2\pi/P_1$, $r = a(1 - e \cos E)$, and the vectors are defined as,

$$\vec{P} = \vec{l} \cos \omega + \vec{m} \sin \omega \quad (3.7)$$

$$\vec{Q} = -\vec{l} \sin \omega + \vec{m} \cos \omega \quad (3.8)$$

$$\vec{l} = \cos \Omega \hat{x} + \sin \Omega \hat{y} \quad (3.9)$$

$$\vec{m} = -\cos i \sin \Omega \hat{x} + \cos i \cos \Omega \hat{y} + \sin i \hat{z} \quad (3.10)$$

where, E is the eccentric anomaly, P_1 is the orbital period, a , e , i , ω , Ω are standard orbital parameters. The z-component of $\boldsymbol{\nu}$ is the RV we observe and it is represented as,

$$\nu_z = K(\cos f + \omega + e \cos \omega) \quad (3.11)$$

with,

$$K = \frac{an \sin i}{\sqrt{1 - e^2}} \quad (3.12)$$

$$\tan \frac{f}{2} = \sqrt{\frac{1 + e}{1 - e}} \tan \frac{E}{2} \quad (3.13)$$

where f is the true anomaly. All the above expressions are derived with respect to the centre of mass of the binary. These equations transform the 3D orbital motion to a 2D variation plot (see [Figure 3.4](#)) which are modelled with the expression for ν_z .

The above equations are invoked in the RV modelling code `v2FIT` ([Konacki et al. 2010](#)) which we use for our work. `v2FIT` is a FORTRAN based code which calculates components of tidal distortion (ν_{tides}), relativistic effects (ν_{GR}), and RV of the centre of mass of the binary (ν_{COM}), and models them as,

$$\nu_{Total} = \nu_{com} + \nu_z + \nu_{tides} + \nu_{GR} \quad (3.14)$$

In all of our cases (DEB as inner binary), we use only the first two components as the ν_{GR} and ν_{tides} are negligible.

The presence of a third body around a DEB manifests itself in variations of the ν_{com} . We can treat these variations and the tertiary's RV measurements (if ST3) as a binary system itself, with **its own** COM velocity: γ . This gives us more constraints on the orbital parameters of the third body. If we have a ST2 we can constrain the period, eccentricity and periastron longitude, while we can get an estimate of the minimum mass of the tertiary only.

3.1.3. Numerical integration of dynamics

The accurate orbital parameters obtained enable us to probe the significant dynamical changes in these compact systems. The major orbital parameters that drive the dynamics are usually the masses, semi-major axes or periods, and all inclinations, including mutual inclination (i_m). While we get almost all orbital parameters from combined LC and RV analysis, we still lack the information about the longitude of ascending nodes (Ω_A and Ω_{AB} for inner and outer orbit respectively) and i_m . An estimate of the range of the i_m can be calculated from the constraints arising due to geometry, using i_A and i_{AB} . Simplifying the calculations from [Gronchi & Tommei \(2007\)](#), we get,

$$\cos i_m = \cos(\Omega_A - \Omega_{AB}) \times \sin i_A \sin i_{AB} + \cos i_A \cos i_{AB} \quad (3.15)$$

Since the value of $\cos(\Omega_A - \Omega_{AB})$ can vary between -1 and 1, we estimate the range of $\cos i_m$ to be,

$$\cos i_m \geq \cos i_A \cos i_{AB} - \sin i_A \sin i_{AB} \quad (3.16)$$

$$\cos i_m \leq \cos i_A \cos i_{AB} + \sin i_A \sin i_{AB} \quad (3.17)$$

Using trigonometric identities, we get the range of i_m to be,

$$i_A - i_{AB} \leq i_m \leq i_A + i_{AB} \quad (3.18)$$

This is the solution when the cosine of i_m is positive. There exists another set of solutions for a negative cosine configuration,

$$180 - (i_A + i_{AB}) \leq i_m \leq 180 - (i_A - i_{AB}) \quad (3.19)$$

To further constrain this range, we rule out the unrealistic i_m by looking at average i_A variations in the numerical integration of orbital parameters and comparing with the i_A from the observations.

We use `REBOUND`¹, an open-source collisional N-body code (Rein & Liu 2012) for the numerical integration of orbital parameters. `REBOUND` can also be used to simulate collision-less problems such as the three-body hierarchical orbit in our case. We use the symplectic integrator `WHFAST` which is designed for long-term integration of gravitational orbits (Rein & Tamayo 2015). `WHFAST` uses mixed variables (Jacobi and Cartesian) and also a symplectic corrector which ensures accurate and fast integration of the N-body dynamical equations. The general setup is defined by masses and orbital parameters obtained with our observations. The values of inclinations, ω and other orientation parameters are also taken from our observations.

Further, we use the `REBOUNDX` (Tamayo et al. 2020) library for adding in tidal forces and dissipation to this setup. The implementation uses a constant time-lag model from (Hut 1981) to raise tides on the larger (and more massive) stars. The constant time-lag parameter (τ) is given by,

$$\tau = \frac{2R^3}{GMt_f} \quad (3.20)$$

where R , M are the radius and mass of the body with tides. Convective friction time (t_f) and tidal Love number are taken from the `REBOUNDX` setup². The other inputs from observations include the rotation frequency of the secondary and its radius. Using this setup, we simulate the systems for a time equal to the time between the observation of the first and last LC of the corresponding systems. We track the inclination changes of the inner binary for different values of Ω_{AB} (and assuming $\Omega_A = 0^\circ$) and then compare it with the observations to obtain possible i_{mut} .

¹<https://github.com/hannorein/rebound>

²https://github.com/dtamayo/reboundx/blob/master/ipython_examples/TidesConstantTimeLag.ipynb

3.2. Atmospheric parameters

For a single isolated star, it is easy (relatively) to extract basic atmospheric parameters, as one can use single-epoch, medium-resolution spectra. The problem with the extraction of spectra for binary stars increases three-fold. On top of having an extra companion in the spectra, we have moving spectral lines due to the Doppler shifts caused by the orbital motion of the binary stars. With three stars, the problem gets severely complicated. Three moving spectral components, changing angles between stars, and merging line profiles are only a few of the obstacles that we faced while tackling this problem. In the following sections, we discuss the general methodology to identify, separate and analyse the components that we find in triple star spectra.

3.2.1. Spectral disentangling

Spectral disentangling (hereafter: disentangling) is a process to separate the individual spectra of the components from the composite spectra of the multiple systems. Disentangling is different from other methods of extracting component spectra (e.g., [Tkachenko 2015](#)) in the way that spectra are model-independent. This is favourable for cases where we do not know the spectral features of a component in a certain evolutionary phase/state ([Shenar et al. 2020](#)). The mathematical formulation has been developed for almost 30 years ([Bagnuolo & Gies 1991](#); [Simon & Sturm 1994](#); [Hadrava 1995](#)). But it is only in the new millennium that we got access to freely available codes for disentangling (see [Seeburger et al. 2024](#) for an overview). For our work we used two disentangling codes, with different mathematical setups, which are discussed below.

3.2.1.1. Fourier-space disentangling

The classical disentangling problem for components $n = 1, 2, \dots, N$ with $t = 1, 2, \dots, T$ epochs of spectra, can be represented as a convolution,

$$I(x, t) = \sum_{l=1}^N I_l(x) * \delta(x - v_l(t)) \quad (3.21)$$

where $I_l(x)$ is the component spectra and $x = c \ln \lambda$ represents the velocity space. A simple Fourier transform changes the convolution of functions to a product of Fourier modes,

$$\tilde{I}(y, t) = \sum_{l=1}^N \tilde{I}_l(y) \exp(iy v_l(t)) \quad (3.22)$$

this significantly decreases the dimensionality of the problem. If each spectrum was sampled in P pixels, then Fourier disentangling decreases set of $T \times P$ equations in $N \times P$ unknowns to $T \times ((P + 1)/2)$ and $N \times ((P + 1)/2)$, where P is odd. The resultant matrix equation is then solved using single value decomposition (SVD; [Simon & Sturm 1994](#)).

FD3 (Ilijic et al. 2004) uses this principle to extract the component spectra for a triple system using optimisation of orbital elements. The optimisation of the above equation is done in the code using single value decomposition (SVD). We use a modified version of FD3 where we update the value of certain constants and samples in the logarithm of base 10. This version of the code is available at https://github.com/ayushmoharana/fd3_initiator.

3.2.1.2. Velocity-space disentangling

When the orbital parameters of systems are not well-constrained (large number of variables), and the observed spectra are limited, we can resort to disentangling in the velocity space. For the velocity space disentangling, we use the shift-and-add algorithm (González & Levato 2006) implemented in the code `DISENTANGLING_SHIFT_AND_ADD`³ (DSAA; Shenar et al. 2020, 2022). In its truest mathematical sense, the algorithm used is a method of spectral decomposition (see Hadrava 2009 for a better mathematical description). In practice, it is similar to that of the disentangling method of Bagnuolo & Gies (1991). DSAA disentangles spectra by applying simple velocity shifts corresponding to one component and creating a single spectrum. For the j th iteration in the routine, the reconstructed spectra can be represented as,

$$\begin{aligned} A^j &= \langle S_i(x + v_{a,i}) - B^{j-1}(x - v_{b,i} + v_{a,i} + v_{c,i}) - C^{j-1}(x - v_{c,i} + v_{b,i} + v_{a,i}) \rangle_i \\ B^j &= \langle S_i(x + v_{b,i}) - A^{j-1}(x - v_{a,i} + v_{b,i} + v_{c,i}) - C^{j-1}(x - v_{c,i} + v_{b,i} + v_{a,i}) \rangle_i \\ C^j &= \langle S_i(x + v_{c,i}) - A^{j-1}(x - v_{c,i} + v_{a,i} + v_{b,i}) - B^{j-1}(x - v_{b,i} + v_{a,i} + v_{c,i}) \rangle_i \end{aligned} \quad (3.23)$$

where S_i is the i th observed spectra, $\langle \rangle_i$ denotes average over all i , and $v_{x,i}$ denotes the RV for x -component in the i th spectra. The original code takes in orbital parameters along with a list of times of epoch and the spectra to disentangle the spectra. We modified the code to use the precise RV for each component to calculate the shifts for every epoch. Some constraints which we use from our preliminary RV analyses are γ velocity of the CHT, and COM velocity of the binary.

3.2.1.3. Bias progression and cleaning trends

We do not normalise the disentangled spectra further, as it gives us normalised spectra. But there is a need to clean some spurious patterns affecting the products of disentangling. The disentangled spectra have trends in the continuum which were a result of bias in normalisation, light-fraction variation etc. (Hensberge et al. 2008). The amplitude of these trends varies depending on the number, the extent of convolution of line profiles and the wavelength range of the spectra used for disentangling (Figure 3.5; right). Further, it depends on the spectrograph, which can be attributed to either the stability of the spectrograph or the accuracy of the spectral reduction method. These trends are additive. Therefore a sinusoidal, polynomial or a combination of both can be used to model and

³https://github.com/TomerShenar/Disentangling_Shift_And_Add

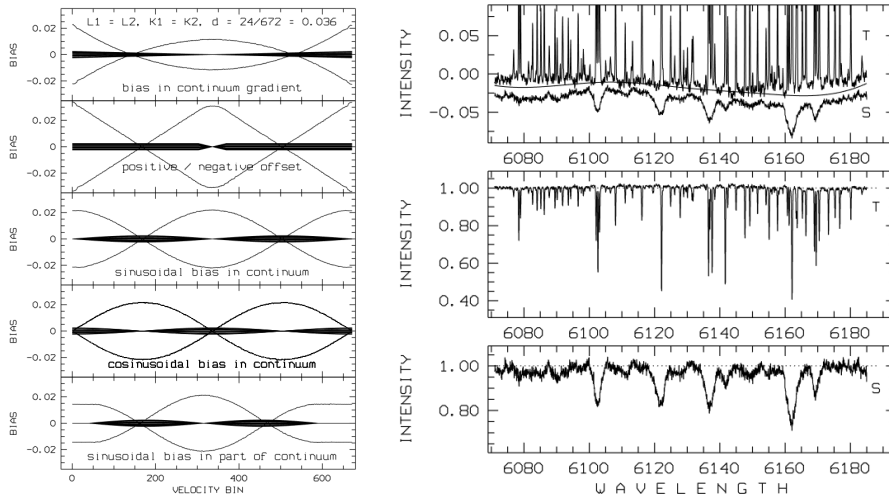


Figure 3.5 (Left) Examples of bias progression in disentangled spectra. (Right) A method to model the bias signals and remove it to get clean spectra. Figure credits: [Hensberge et al. \(2008\)](#).

subtract these signals. The bias signals are visible in all the components and are anti-correlated with one or two other components in an ST2 or an ST3 system. Inverting two signals in velocity-space can help constrain the signal better and remove it ([Figure 3.5](#); right). Details of the cleaning methods and precautions for data reduction are available in [Hensberge et al. \(2008\)](#)

3.2.2. Spectral analysis

The final disentangling product undergoes a lot of processes from its original state in a composite spectrum. Therefore, if a large chunk of spectra undergoes SPD, it is likely that the line depths deviate (even though on small scales) from their true depths for certain lines (usually broad lines). Therefore, a better approach for spectral analysis would be to analyse a lot of spectral lines simultaneously to obtain atmospheric parameters from disentangled spectra. While grid fitting seems to be the first approach for this, the density of the grid limits the errors on the obtained parameters. A better approach would be to do a grid fitting with χ^2 minimisation, but with finer grids being calculated at each instance of minimisation check. This is one of the reasons why we use *iSPEC* ([Blanco-Cuaresma et al. 2014](#); [Blanco-Cuaresma 2019](#)) for our spectroscopic analysis.

iSPEC is an open-source spectral analysis framework that can be used from PYTHON3 scripts or visual interface (which we use in our work). *iSPEC* includes several radiative transfer codes like *SPECTRUM*, *SME*, *MOOG*, *TURBOSPECTRUM*, and *SYNTHÉ*. Meanwhile, for stellar atmospheres it uses two different sets of grids: (i) MARCS-GES ([Gustafsson et al. 2008](#)) and (ii) Kurucz-ATLAS9 ([Kurucz 2005](#)).

For the measurement of effective temperature (T_{eff}), metallicity ($[M/H]$) and log of surface gravity ($\log g$), the synthetic spectral fitting (SSF) technique. SSF technique generates

synthetic spectra on the go and then does a χ^2 optimisation at selected spectral lines. This method is better with respect to a simple grid fitting [Blanco-Cuaresma \(2019\)](#). We implement different fitting procedures for the eclipsing stars and the tertiary, respectively. For the eclipsing stars, we fix the $\log g$ estimated from LC and RV modelling using,

$$\log(g) = \log\left(\frac{A_c^2 M}{R^2}\right), \quad (3.24)$$

where M is the mass (in M_\odot), R is the radius (in R_\odot) calculated from LC and RV modelling, and $A_c \equiv \sqrt{GM_\odot/R_\odot}$ ($= 168.589888477$) is a constant necessary for transformation to solar units. We also fix the projection of rotational velocity ($v \sin i$) from BF (see [section 2.1](#)). The setup for synthetic spectra generation includes model atmospheres from MARCS ([Gustafsson et al. 2008](#)), solar-abundances from [Asplund et al. \(2009\)](#) and the radiative transfer code SPECTRUM⁴. The fitting was done in selective regions that were generated on the line lists from the *Gaia*-ESO Survey (GES; [Gilmore et al. 2012](#); [Randich et al. 2013](#)) version 5.0, which covers the wavelength range of 420nm-920nm. We calculate the parameters using two different line lists (details in [Appendix A](#)). We first fit for T_{eff} , $[M/H]$, $[\alpha/Fe]$ and $v \sin i$ using line-list LL1, which is prescribed for abundance measurement. We adopt the $[M/H]$ and α from this run and then fit for T_{eff} , and $v \sin i$ using line-list LL2, which is prescribed for parameter estimate. For the eclipsing systems, we kept the $\log g$ fixed as the values that we obtain from LC and RV modelling as the spectroscopic $\log g$ matched well but had lower precision. We kept the $\log g$ free for the tertiary spectra.

In ST3 cases, we also calculated the radii R (in R_\odot) of the tertiary stars using $\log(g)$ (in dex) from spectra, by using [Equation 3.24](#) to solve for R :

$$R = A_c \times \sqrt{\frac{M}{10^{\log(g)}}}, \quad (3.25)$$

where M is the mass of the tertiary calculated from LC and RV fitting (in M_\odot).

The abundances were calculated using the SSF method and LL1 line-list. The optimisation was done with free abundance and $[M/H]$ for a particular element. We consider the abundances of the elements whose lines were sufficiently available in the range of the disentangled spectra. The abundances were obtained in the 12-scale as $A(X)$, where, $A(X) = \log\left(\frac{n_X}{n_H}\right) + 12$, in which n_X and n_H are the number of atoms of the element X and of hydrogen, respectively.

Increasing the number of stars increases the complexity of the method of parameter extraction. This is reason why we need to combine all the above listed methods to create

⁴<http://www.appstate.edu/~grayro/spectrum/spectrum.html>

Parameters	Methods
Stellar Physical (e.g, mass, radius)	LC, RV, ETV
Atmospheric (e.g, T_{eff} , $[M/H]$, $\log(g)$)	Spectral Analysis
Orbital (e.g, P , e , a , i)	RV, LC, ETV
Systemic Physical (e.g, age, distance, evolution)	Spectral Analysis, Isochrones

Table 3.1 Table of the planned properties to be studied and the methods to obtain them.

a complete picture of CHTs (or triples in general). An overview of the different methods and the parameters they give are listed in [Table 3.1](#).

CHAPTER 4

Written in the stars: Parameters to evolution and dynamics

"She knew this was a power that should belong only to the stars."

– Liu Cixin, Author, *The Three-Body Problem*

A part of this chapter has been accepted for publication in Monthly Notices of Royal Astronomical Society as 'Detached eclipsing binaries in compact hierarchical triples: triple-lined systems BD+442258 and KIC 06525196', Moharana, Ayush ; Helminiak, K. G. ; Marcadon, F. ; Pawar, T. ; Konacki, M. ; Ukita, N. ; Kambe, E. ; Maehara, H. , MNRAS, Volume 521, Issue 2, May 2023, Pages 1908-1923.

The absolute, consistent, and precise parameters obtained give us a lot of scope for the exploration of different properties of CHTs. Using the set of independent methods (described in [chapter 3](#)) it is possible to probe the evolution of stars in CHT. The first test which would come to mind is the test for co-evolution of the CHT components. In the co-evolution of multiple systems, one assumes that the stars are formed out of the same molecular cloud and therefore have the same metallicity. If there is no interaction between the components while evolving, the stars evolve as single stars and will fit the same isochrone (also assuming they form at a comparatively similar time). Isochrone fitting using MESA Isochrones and Stellar Tracks (MIST) is our preliminary analysis to check the age and the consistency of our metallicity estimates. The evolutionary state can be also verified from the atmospheric parameters and abundances of each star.

Once we constrain the evolutionary state, we can look to understand the dynamical evolution. This is complicated in a CHT as the compactness of the system makes the



radial and mass changes due to the evolution of a star significant. This calls for a joint stellar and dynamical evolution modelling. We use `REBOUNDX` along with MESA stellar tracks to simulate our systems to check their long-term stability. We also add in additional physical processes modelled using our measurements of the stellar and atmospheric parameters.

4.1. Detached eclipsing binaries in compact hierarchical triples

A proof-of-concept of the work described above is detailed in the following paper. This paper gives an interesting comparison between two systems with similar binaries but different tertiaries. Here, we report the discovery of a ST3 CHT BD+44 2258 and a new analysis of a previously identified CHT KIC 06525196. This is the first photometric and spectroscopic study of BD+44 2258 and gives the first spectroscopic estimates of the atmospheric parameters of KIC 06525196.



Detached eclipsing binaries in compact hierarchical triples: triple-lined systems BD+442258 and KIC 06525196

Ayush Moharana ^{1,★}, K. G. Hełminiak ¹, F. Marcadon,^{1,2} T. Pawar,¹ M. Konacki,³ N. Ukita,^{4,5} E. Kambe⁶ and H. Maehara⁴

¹*Nicolaus Copernicus Astronomical Center, Polish Academy of Sciences, ul. Rabiańska 8, PL-87-100 Toruń, Poland*

²*Department of Astrophysics and Planetary Sciences, Villanova University, 800 East Lancaster Avenue, Villanova, PA 19085, USA*

³*Nicolaus Copernicus Astronomical Center, Polish Academy of Sciences, ul. Bartycka 18, PL-00-716 Warszawa, Poland*

⁴*Okayama Astrophysical Observatory, National Astronomical Observatory of Japan, 3037-5 Honjo, Kamogata, Asakuchi, Okayama 719-0232, Japan*

⁵*The Graduate University for Advanced Studies, 2-21-1 Osawa, Mitaka, Tokyo 181-8588, Japan*

⁶*Subaru Telescope, National Astronomical Observatory of Japan, 650 North Aohoku Place, Hilo, HI 96720, USA*

Accepted 2023 February 23. Received 2023 February 22; in original form 2022 October 20

ABSTRACT

Compact hierarchical triples (CHTs) are systems with the tertiary star orbiting the inner binary in an orbit shorter than 1000 d. CHT with an eclipsing binary as its inner binary can help us extract a multitude of information about all three stars in the system. In this study, we use independent observational techniques to estimate the orbital, stellar, and atmospheric parameters of two triple-lined CHT: BD+44 2258 and KIC 06525196. We find that the masses of stars in BD+44 2258 are 1.011 ± 0.029 , 0.941 ± 0.033 , and $0.907 \pm 0.065 M_{\odot}$ while in KIC 06525196 the estimated masses are 1.0351 ± 0.0055 , 0.9712 ± 0.0039 , and $0.777 \pm 0.012 M_{\odot}$. Using spectral disentangling, we obtained individual spectra of all the stars and combined it with light-curve modelling to obtain radii, metallicities, and temperatures. Using stellar evolution models from MESA, we constrain the $\log(\text{age})$ of BD+44 2258 to be 9.89 and 9.49 for KIC 06525196. Two stars in BD+44 2258 are found to be sub-giants while all three stars in KIC 06525196 are main-sequence stars. We constrain the mutual inclinations to certain angles for BD+44 2258 and KIC 06525196 using numerical integration. Integrating with tidal interaction schemes and stellar evolution models, we find that KIC 06525196 is a stable system. But the inner binary of BD+44 2258 merges within 550 Myr. The time of this merger is affected by the orientation of the tertiary, even rushing the collapse by ~ 100 Myr when the mutual inclination is close to 90° .

Key words: binaries: eclipsing – binaries: spectroscopic – stars: evolution – stars: fundamental parameters – stars: individual: BD+44 2258, KIC 06525196 – stars: kinematics and dynamics.

1 INTRODUCTION

The multiplicity of stars is a well-established phenomenon (Duchêne & Kraus 2013). The incidence of multiplicity varies with the spectral type of the stars. Multiplicity is 44 per cent among the solar-like stars, out of which 8 per cent are triple stars (Raghavan et al. 2010). These numbers increase in O, B, and A types (Shatsky & Tokovinin 2002; Kobulnicky & Fryer 2007; Mason et al. 2009). There have been a lot of studies towards understanding binaries that has created an almost complete picture of their evolution and formation. The next step in decoding the multiple architecture is understanding triple systems.

Binary formation channels can be largely classified into disc instability, core-fragmentation, and N -body interactions. The complexity of formation increases in a triple system with a combination of these formation channels being responsible for their formation (Tokovinin 2021). Most of the studies to understand these scenarios using orbital architectures, metallicity variation among stars, and mass

distributions in triples, have been usually restricted to wide triples (Tokovinin 2017, 2022; Lee et al. 2019).

The evolution of triple stars also departs from the simplified evolution of a single star. A triple-star system has the additional complexity of multiple dynamical interactions. The outer companion can directly alter the formation of the components of the inner binary, leading to their apparent difference in properties (e.g. apparent age; Marcadon et al. 2020), and has been used in explaining various evolutionary phenomena of single and binary stars.

Hierarchical triple systems have been intensely studied in order to understand the formation of closest main-sequence binary systems (Eggleton & Kiseleva-Eggleton 2001; Naoz & Fabrycky 2014; Moe & Kratter 2018). One of the probable theories of the formation of blue straggler stars involves perturbations from a third body (Perets & Fabrycky 2009). One in a thousand high-mass X-ray binaries evolve through interaction with a third star to form low-mass X-ray binaries (Eggleton & Verbunt 1986). Asymmetry of Planetary Nebulae has been linked to evolution in a triple system (Akashi & Soker 2017; Jones, Pejcha & Corradi 2019) and has even been suspected to play a role in driving white dwarf mergers towards type Ia supernova explosions (Maoz, Mannucci & Nelemans 2014).

* E-mail: ayushm@ncac.torun.pl

Recent population synthesis studies have shown that 65–75 per cent of triples undergo mass transfer (Toonen et al. 2020). Hamers & Dosopoulou (2019) have shown that this can occur uniformly throughout the orbit or at certain points due to eccentricity and inclination changes known as von Zeipel–Lidov–Kozai (ZLK) oscillations (von Zeipel 1910; Kozai 1962; Lidov 1962). Furthermore, these systems perturb Roche lobe potentials and also undergo Roche lobe over flow, which can occur for the three individual stars and can be circumbinary too. Therefore, understanding the stellar evolution coupled with the dynamical evolution is important when studying triples. Most of the known triple systems have long tertiary periods and therefore their dynamical effects can have time-scales of decades or centuries. There is a subset of these triples, called compact hierarchical triples (CHTs), which offer more potential for observational astrophysics (Borkovits 2022). The time-scale of the changes due to these interactions is short in CHT and can be observed easily over a few years, e.g. vanishing eclipses of HS Hya (Zasche & Paschke 2012) or re-appearing eclipses of V907 Sco (Zasche et al. 2023). These are triples with the outer orbit period shorter than 1000 d. Due to this, dynamical processes in CHTs can be observed in time-scales of years. CHTs were thought to be rare (Tokovinin 2004) but with new space-based photometric missions we are discovering more of these systems (Rappaport et al. 2013; Borkovits et al. 2016).

Detached eclipsing binaries (DEBs) are known as the source of the most accurate stellar parameters (e.g. mass, radius, etc.). Accuracy of less than 1 per cent can be attained by coupling high-precision photometry and high-resolution spectroscopy (Torres, Andersen & Giménez 2010). The accuracy is robust and independent of different models and methods, even varying slightly due to different numerical implementations (Maxted et al. 2020; Korh et al. 2021).

If a CHT has a DEB as its inner binary, there is an added advantage of obtaining accurate stellar parameters of not only the binary but of the tertiary as well (Helminiak et al. 2017). Using light-curve modelling, eclipse timing variations, spectral analysis, and RVs, we can obtain an accurate picture of the orbits, geometry, stellar parameters, metallicity, age, and evolutionary status.

There has been a surge in interest in CHT recently. *Kepler* (Howell et al. 2014) and *Transiting Exoplanet Survey Satellite* (*TESS*) both have been crucial in detection and analysis of these systems (Borkovits et al. 2015, 2020). Tertiary stars in CHT have been found to host tidally induced pulsations (Fuller et al. 2013). Ongoing projects are using triply eclipsing triples (TETs) to characterize CHT (Rappaport et al. 2022). Studies even show that CHT can produce exotic Thorne–Żytkow objects (Eisner et al. 2022). Last but not the least, CHTs have proven to be useful to study ZLK oscillations and their effect on stellar evolution (Borkovits et al. 2022). Though most of these studies have provided us with mass and radii of all the stars in a CHT, the tertiary radii space is dominated by TET or planar systems.

In this paper, we report the detection of a DEB in a CHT, BD+44 2258 ($\alpha = 13:15:06.66$, $\delta = 44:02:33.48$; hereafter BD44). BD44 has been previously observed in ultraviolet (*GALEX*; Bianchi et al. 2011) and X-ray (*ROSAT*; Voges et al. 1999) but as a single source. We obtain stellar, orbital, and atmospheric parameters of all the stars in BD44 and a previously detected CHT, KIC 06 525 196 ($\alpha = 19:30:52.32$, $\delta = 41:55:20.81$; hereafter KIC65) with *TESS* photometry and *HIDES* spectroscopy. We explain the different observations and methods used for extracting parameters in Sections 2 and 3. We use these parameters to estimate the age and evolutionary stages of the components. Further, using the orbital parameters, we study the evolution and stability of the systems as explained in Section 4.

2 OBSERVATIONS

2.1 Photometry

We use photometry from *TESS* (Ricker et al. 2015) for our light curves (LCs).¹ BD44 (TIC 284595199) has 2-min cadence photometry obtained from Sectors 16, 22, and 49. KIC65 was a target from the main *Kepler* mission field, and these data have been analysed in Helminiak et al. (2017). In addition to this, the *TESS* 2-min cadence photometry (TIC 137757776) is available from Sectors 40 and 41. In this work, we only model a segment of *TESS* data from Sector 41 for KIC65 while for BD44 we use segments from Sectors 16, 22, and 49. These segments were selected on the basis of spot variability in the LCs. This was also the reason for selecting only Sector 41 for KIC65 because the overall structure of the LC was similar in both sectors but Sector 41 has fewer fluctuations than Sector 40. The structure of the LC for BD44 changes in the sectors and therefore we model all the sectors to check for consistency.

We filtered out the points that had the best quality flag for our purposes. There seems to be no other star in the Full Frame Image of BD44 but there seems to be some contamination for KIC65. For BD44, we compared normalized LCs obtained using different apertures on the FFIs only to find they all are identical when normalized. Therefore, we consider that any third light that would show up from LC modelling will be solely due to the third star. We considered the simple added photometry or SAP fluxes for modelling both our systems.

2.2 Spectroscopy

We use spectra collected with the *HIDES* (Izumiura 1999; Kambe et al. 2013), attached to the 1.88-m telescope at the Okayama Astrophysical Observatory. Observations were conducted in the fibre mode with an image slicer ($R \sim 50000$), without I_2 , and with ThAr lamp frames taken every 1–2 h. The spectra are composed of 62 rows covering 4080–7538 Å, of which we use 30 (4365–6440 Å) for radial velocity (RV) calculations. A detailed description of the observing procedure, data reduction, and calibrations is presented in Helminiak et al. (2016).

For KIC65, we used exactly the same set of 14 spectra and RV measurements as in Helminiak et al. (2017). For BD44, we took a total of 28 spectra.

3 ANALYSIS

In the following sections, we use A–B notation to denote the CHT, where B is the tertiary. A is the eclipsing binary with components Aa and Ab. Aa corresponds to the primary classified according to temperature, usually the deepest eclipse in the LC if not affected by spots. Since we would be talking about six stars in total (three in each of the two CHT), we use the short form for the star’s name along with the alphabetical notation to exclusively denote each star, e.g. the secondary (cooler star in the binary) of KIC65 is referred as KIC65Ab.

3.1 RV extraction and fitting

Since both targets were observed with the same spectrograph as part of the same programme, the approach to RV calculations and fitting

¹From GI programmes: G022003, G022062, G04047, G04171, and G04234.

1910 *A. Moharana et al.*

was essentially identical. It is described in detail in Helminiak et al. (2017), but we summarize it here briefly.

The RVs were calculated with a TODCOR method (Zucker & Mazeh 1994) with synthetic spectra computed with ATLAS9 code as templates. Measurement errors were calculated with a bootstrap approach and used for weighting the measurements during the orbital fit, as they are sensitive to the signal-to-noise ratio (SNR) of the spectra and rotational broadening of the lines. Though this code is optimized for double-lined spectroscopic binaries and provides velocities for two stars (u_1 , u_2), it can still be used in triple-lined systems as well. The RVs of the eclipsing pair were found from the global maximum of the TODCOR map since in both targets these components contribute more to the total flux than the third star. The tertiary's velocities were found from a local maximum, where u_1 was set for the tertiary, and u_2 for the brighter component of the eclipsing pair. This scheme was used previously for KIC65 in Helminiak et al. (2017), and the *rms* of the resulting tertiary's RVs was comparable to the stability of the instrument estimated from RV standard stars. In some cases, the velocity difference between two components was too small to securely extract their individual RVs, and measurements were taken only for the remaining one. For this reason, each component of a given triple may have a different number of RV data.

The orbital solutions were found using our own procedure called v2FIT (Konacki et al. 2010). It applies a Levenberg–Marquardt minimization scheme to find orbital parameters of a double-Keplerian orbit, which can optionally be perturbed by a number of effects, like a circumbinary body. The fitted parameters are orbital period P , zero phase T_p ,² systemic velocity γ , velocity semi-amplitudes $K_{1,2}$, eccentricity e , and periastron longitude ω , although in the final runs, the last two parameters were usually kept fixed to zero. We also included the difference between systemic velocities of two components, $\gamma_2 - \gamma_1$, and a circumbinary body on an outer orbit, parametrized analogously by orbital parameters P_3 , T_3 , K_3 , e_3 , and ω_3 . In such case, γ is defined in the code as the systemic velocity of the whole triple.

Systematic errors that come from fixing a certain parameter in the fit are assessed by a Monte Carlo procedure, and other possible systematics (like coming from poor sampling, small number of measurements, pulsations, etc.) by bootstrap analysis. All the uncertainties of orbital parameters given in this work already include the systematics.

In addition, for each observation where three sets of lines were sufficiently separated, we also calculated the systemic velocities $\gamma(t_i)$ of the inner pair, using the formula:

$$\gamma(t_i) = \frac{v_1(t_i) + qv_2(t_i)}{1 + q}, \quad (1)$$

where $v_{1,2}(t_i)$ are the measured RVs of the inner binary, and q is the mass ratio, found from the RV fit with a circumbinary perturbation. With these values as the centre-of-mass (COM) RVs of the binary and RVs of the tertiary component, we can treat the long-period outer orbit as an SB2 (Fig. 1), and independently look for its parameters. The final values of P_3 , K_3 , e_3 , etc., actually come from such fits.

²Defined as the moment of passing the pericentre for eccentric orbits or quadrature for circular.

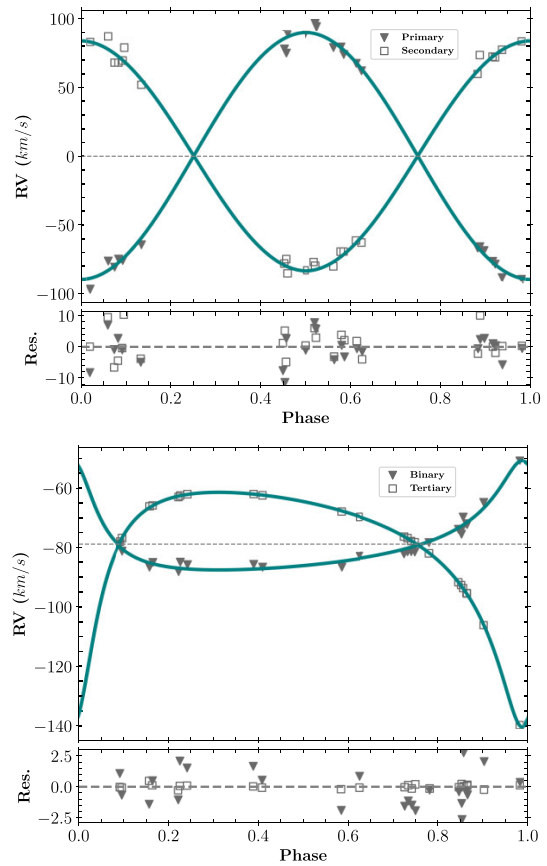


Figure 1. Phased RV profiles of BD44, for the inner binary (top) and the whole system (COM of the binary versus the tertiary). The green lines are the best v2FIT models. Though the tertiary has a good fit, the residuals from the binary fit contribute to the final uncertainties in the tertiary parameters.

3.2 Broadening functions

Broadening function (BF) is a representation of the spectral profiles in velocity space. BF contains the signature of the RV shifts of different lines and also intrinsic stellar effects like rotational broadening, spots, pulsations, etc. (Rucinski 1999a). The BF was calculated using the algorithm described in Rucinski (1999b). We modified a single-order BF code, BF-RVLOTTER,³ to calculate multi-order BF and also fit the function with multiple Gaussian or rotation functions. The BF was calculated in a wavelength range of 5050–5600 Å. We used a synthetic solar-type spectrum with zero projected rotational velocity [$v \sin(i)$] as our template. The final BF generated was smoothed with a Gaussian smoother of a 3 km s⁻¹ rolling window. Three clear peaks were visible in all epochs of spectra which implied that we did not observe the system spectra during eclipses of any of the three stars. The peaks were fitted with the rotational profile from Gray (2005),

$$G(v) = A \left[c_1 \sqrt{1 - \left(\frac{v}{v_{\max}} \right)^2} + c_2 \left(1 - \left(\frac{v}{v_{\max}} \right)^2 \right) \right] + lv + k, \quad (2)$$

³<https://github.com/mrawls/BF-rvplotter>

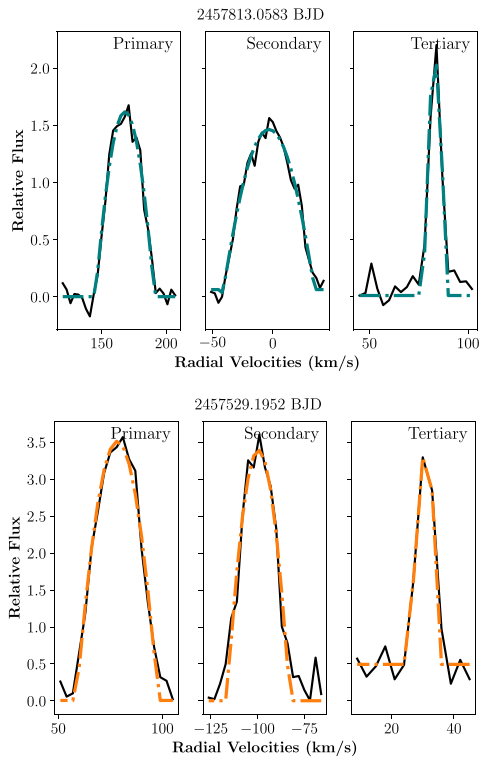


Figure 2. Broadening functions for all the three components of BD44 (top) and KIC65 (bottom). The green and orange dashed line represents best-fitting rotational profile for BD44 and KIC65, respectively. The sharp kinks or distortions on the BF peaks are most likely due to spots.

where A is the area under the profile and v_{\max} is the maximum velocity shift that occurs at the equator. c_1 and c_2 are constants that are a function of limb darkening themselves while l and k are correction factors to the BF ‘continuum’. The fits revealed distortions (sharp kinks) of the BF from the ideal rotational profiles (Fig. 2). These are most likely due to spots, and this gives us a qualitative idea about the relative number of spots on the stars. These fits for different epochs were used to (i) calculate light contributions (the parameter A) from different companions, and (ii) make an initial estimate of $v \sin(i)$ (the parameter v_{\max}) for spectral analysis. We also used BF to calculate RVs and found them consistent with the TODCOR RVs. Therefore, for the sake of consistency and familiarity, we used RVs from TODCOR.

3.3 Spectral disentangling

A detailed study of stellar evolution needs a model-independent estimate of stellar metallicity. To estimate atmospheric parameters and abundances, we need spectra for all three stars in the CHT. We use the technique of spectra disentangling (hereafter SPD; Simon & Sturm 1994; Hadrava 1995), for separating individual spectra of the component stars from the composite spectra. This method, though, takes in the assumption that the line profiles are not intrinsically variable. This would mean that we should consider only the out-of-eclipse spectra so as to avoid such variability during the eclipse (e.g. Rossiter–McLaughlin effect). One of the advantages of this

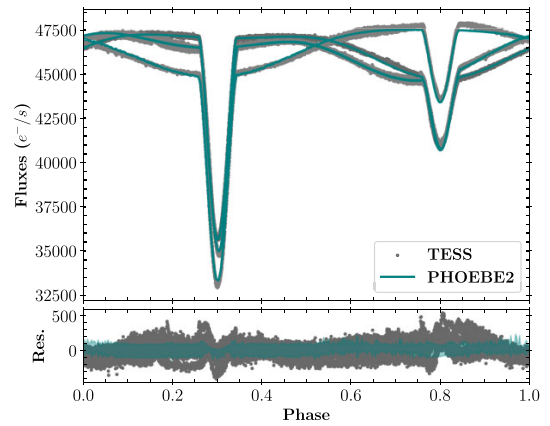


Figure 3. Phased TESS LC (for stable segments from all sectors) for BD44. The green lines represent best-fitting PHOEBE 2 model. The shaded areas are translated from the adopted errors of the MCMC solution from Sector-16.

method is that it can detect faint companions, i.e. < 3 per cent light contribution (Holmgren et al. 1999; Mayer, Harmanec & Pavlovski 2013). This, though, requires good phase coverage and high signal-to-noise ratio.

For our purpose, we used a PYTHON-based wrapper⁴ around the disentangling code FDBINARY (Ilijic et al. 2004), which can disentangle up to three components. The wrapper takes two inputs: (i) an estimate of orbital parameters and (ii) RV corrections and light ratios at each epoch of spectra used from disentangling. We used the solution from RV fitting as starting values in our optimization. The light ratios at every epoch were calculated from the BFs. To make the computation easy and avoid any wavelength dependence, we divided the total spectral range into four sections with overlapping regions. The final disentangled spectra were stitched after normalization, and removal of the edges of the segmented-disentangled spectra. The overlapping regions acted as check points for normalization as they helped us choose the normalization function that gave the same line depths for a particular, overlapping spectral line. The errors of the disentangled spectra were taken as the sum of errors calculated from SNR, and flux-scaled residuals from the disentangled routine.

3.4 Light-curve fitting

We use the version 4 of PHOEBE 2 code⁵ (Prša et al. 2016; Horvat et al. 2018; Conroy et al. 2020; Jones et al. 2020) for our LC modelling. PHOEBE 2 models eclipsing binaries (or single stars) by discretizing the surface of each star. It also distorts the stellar surfaces according to their Roche potentials. The key feature that made us choose this code is its ability to model spots and also solve the inverse problem with spot parameters free for optimization.

The first look on the LCs of BD44 and KIC65 suggests the presence of cold spots in the stars. Comparing the light curve of the different sectors reveals that the spots are time-evolving. We therefore approach our modelling by dividing the light-curve into segments with relatively stable spot signatures. While we model all available sectors for BD44 (Fig. 3), we only model only Sector-41 for KIC65 (Fig. 4). Further, the distortions on the BF suggest

⁴https://github.com/ayushmoharana/fd3_initiator

⁵<http://phoebe-project.org/>

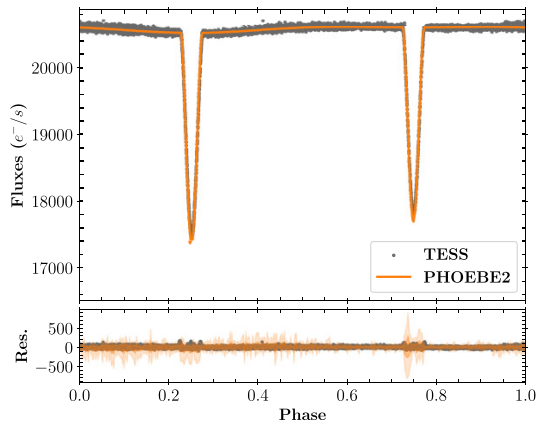
1912 *A. Moharana et al.*

Figure 4. Phased *TESS* LC for KIC65. The orange lines represent best-fitting PHOEBE 2 model. The shaded areas are translated from the adopted errors of the MCMC solution from Sector-41.

the secondary to be more active than the primary for both stars. Therefore, in our models, we assume more spot(s) on the secondary than the primary. The third light (l_3) is expected in a triple-lined CHT unless the signatures are removed with detrending methods. The l_3 is highly degenerate with the inclination (i) too. Estimating l_3 for our systems, from LC, adds another level of complexity with the cold spots affecting the depths of the eclipse. We assume that the values of light fractions obtained from BF of optical spectra are similar to the light fraction of the components in the *TESS* band. Therefore, we start with an initial l_3 equal to the flux fraction of the tertiary from BFs.

Considering the above assumptions and fixing parameters obtained from RV fitting, i.e. mass ratio (q), semimajor axis (a), and period of the binary (P_b), we used *lc_geometry* estimator in PHOEBE 2 for initial parameter estimates. We then added spots one by one and minimizing overall trends in the residuals manually. We added 1 spot on the secondary of KIC65 and stopped at three spots (2 on secondary, 1 on primary) for BD44. More spots would have compromised our computational resources. We then optimized for stellar parameters using Nelder–Mead (Nelder & Mead 1965) optimization module in PHOEBE 2. The optimized parameters include radii of primary and secondary (R_{Aa} and R_{Ab} , respectively), time of superconjunction (T_0), ratio of secondary temperature to the primary temperature (T_{ratio}), P_A , l_3 , i_A , and passband luminosity of the primary (L_{Aa}). Since the RV fitting did not show any substantial eccentricity for the binary (e_A), we kept it fixed at zero which also reduced the computational cost. After minimizing the residuals below 1 per cent of the total flux, we optimized for all spot parameters (colatitude⁶ c^{spot} , longitude l^{spot} , relative temperature T^{spot} , and radius r^{spot}) for all the three spots. We then randomly optimized, combinations of spot parameters and stellar parameters, to check the robustness of the optimization.

We calculated the errors through the Monte Carlo Markov chain (MCMC) sampling, implemented in EMCEE (Foreman-Mackey et al. 2013, 2019) and available as a sampler in PHOEBE 2. We decided on eight parameters to be sampled including the relative temperature of the biggest spot in both the systems (T_{Ab}^{spot}). Due to the lack of computational resources, our initial sampling consisted of 40 walkers and was sampled till we got stable chains for 1000 iterations. Then

⁶Co-latitude is measured along the spin axis with the North pole as 0° .

we started from this sample space and ran another sampling for 3500 stable chains with 80 walkers. To further check the convergence, we use autocorrelation plots (Box & Jenkins 1976) with Bartlett’s formula (Francq & Zakořan 2009) to find the minimum limit for autocorrelated chains. The uncertainties represent 68.27 per cent confidence interval. To validate our results, we translated the errors on the light curves and also the residuals (Figs 3 and 4). The corner plots from the final MCMC chains for BD44 and KIC65 are shown in Fig. 5 and Fig. 6, respectively.

3.5 Spectroscopic analysis

We used ISPEC (Blanco-Cuaresma et al. 2014; Blanco-Cuaresma 2019) for spectroscopic analysis. Before the analysis, we prepared the spectra by correcting the RV offsets that was present in the SPD products. We fitted and corrected the continuum for the SPD spectra using a spline function of degree 3, consisting of 30–150 splines, depending on the component. We used the synthetic spectral fitting (SSF) method where ISPEC generates synthetic spectra on the go for the fitting. We used line masks for specific regions, generated by the spectral synthesis code SPECTRUM⁷ to calculate the χ^2 . The regions were generated on the line lists from Gaia-ESO Survey (GES; Gilmore et al. 2012; Randich, Gilmore & Gaia-ESO Consortium 2013) version 5.0 that covers the wavelength range of 420–920 nm. There are two sets of GES line lists available in ISPEC, which we use (i) list for abundances estimates (LL_a) and (ii) list for parameter estimate (LL_p). The spectral synthesis was again done using SPECTRUM with model atmospheres from Gustafsson et al. (2008). The solar abundances were chosen from Grevesse, Asplund & Sauval (2007). In our initial test runs, with all parameters free, we found that the $\nu \sin i$ values were consistent with the values obtained from BFs. Therefore in our further runs, we fixed the respective $\nu \sin i$ for the components. Using LL_a, we did a search for metallicity, [M/H], on all three stars of the two CHTs. Since the [M/H] of the stars of the respective CHT were consistent within the uncertainty range, we averaged the [M/H] estimates for the system and fixed it for further runs. In the final runs, we fixed the $\log(g)$ (obtained from LC models) for primary and secondary. The limb darkening coefficient (values were taken from Claret & Bloemen 2011) and resolution were kept fixed while macro-turbulence velocity was calculated automatically from an empirical relation established by GES and built in the code. For the estimation of temperatures [and $\log(g)$ for the tertiary], we selected only the part of the spectra with SNR of more than 40 (more than 18 for the tertiary). We chose LL_p for this fitting. The best-fitting synthetic spectra for all the stars in the study are shown in Fig. 7. We also calculated the radii R (in R_\odot) of the tertiary stars using $\log(g)$ (in dex) from spectra, by applying the formula:

$$R = A_c \sqrt{\frac{M}{10^{\log(g)}}}, \quad (3)$$

where M is the mass of the tertiary calculated from LC and RV fitting (in M_\odot) and $A_c \equiv \sqrt{GM_\odot}/R_\odot (= 168.589888477)$ is a constant necessary for transformation to solar units.

We calculated the α -enhancement with LL_a and fixed the rest of the parameters as given in Table 1. Using this set-up, the abundances⁸ were calculated using the SSF method but with free abundance and

⁷<http://www.appstate.edu/~grayro/spectrum/spectrum.html>

⁸The abundances were obtained in the 12-scale as $A(X)$, where $A(X) = \log\left(\frac{n_X}{n_H}\right) + 12$, in which n_X and n_H are the number of atoms of the element X and of hydrogen, respectively.

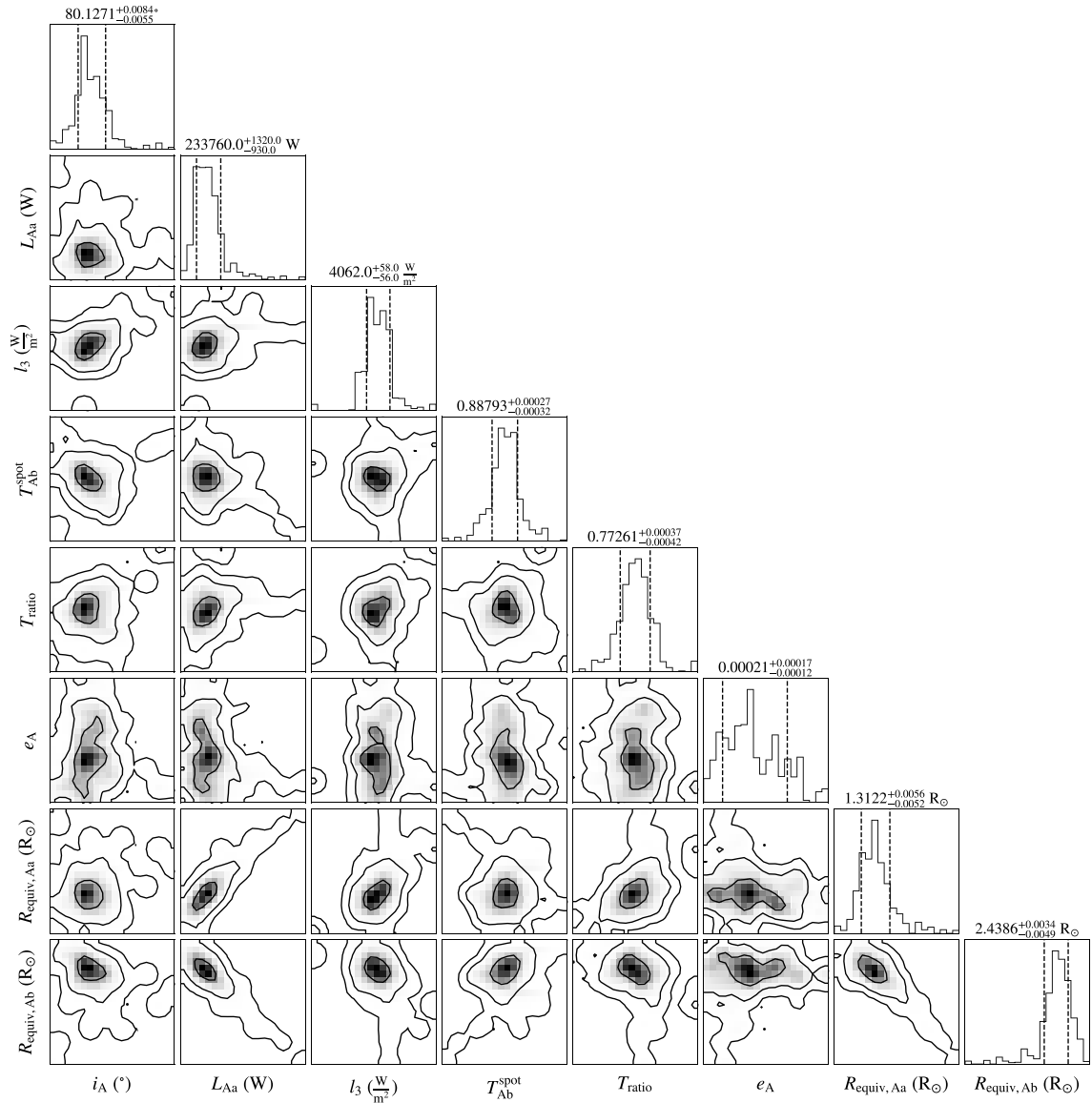


Figure 5. Corner plot for MCMC parameters from LC fitting of BD44. The contours on the maps correspond to 1σ , 2σ , and 3σ errors on the distribution. The effect of spots is visible in the distorted maps of the eccentricity parameter space.

[M/H] for a particular element. We did not consider the abundances of the elements where we got large errors and/or where [M/H] was out of the pre-calculated bounds.

3.6 Isochrone fitting

The age of each system was estimated with a grid of isochrones generated using a dedicated web interface,⁹ based on the Modules

for Experiments in Stellar Astrophysics (MESA; Paxton et al. 2011, 2013, 2015, 2018), and developed as part of the MESA Isochrones and Stellar Tracks project (MIST v1.2; Choi et al. 2016; Dotter 2016). The grid was prepared for iron abundance, [Fe/H]¹⁰, values from -4.0 to 0.50 dex with 0.05 dex steps, as well as for ages $10^{8.6}$ – $10^{10.2}$ Gyr, in logarithmic scale, every $\log(\text{age}) = 0.01$.

¹⁰It is reasonable to assume that without significant deviations from solar amounts of α -elements, the iron abundance [Fe/H] sufficiently approximates the amount of metals [M/H].

⁹<http://waps.cfa.harvard.edu/MIST/>

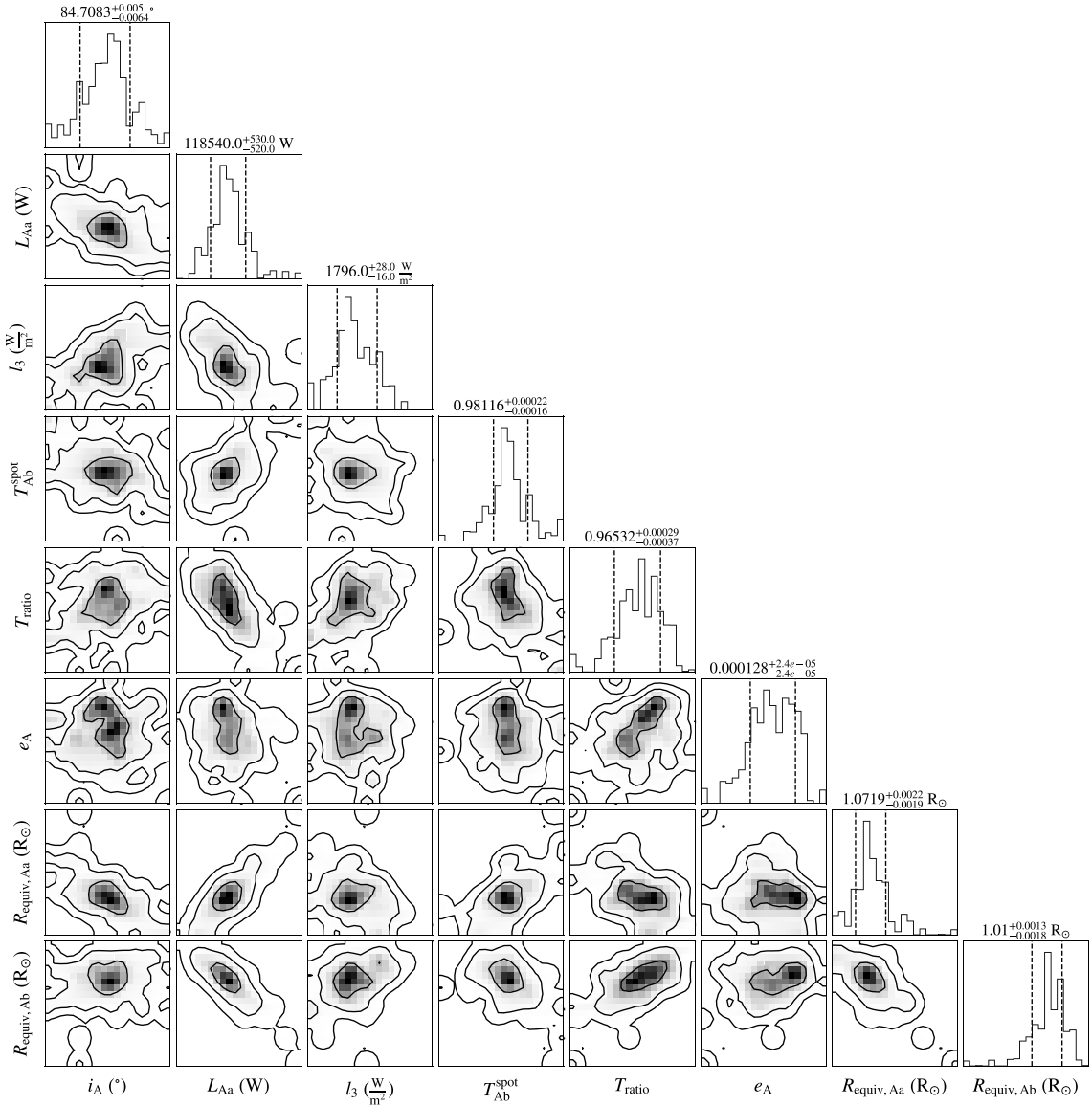
1914 *A. Moharana et al.*

Figure 6. Corner plot for MCMC parameters from LC fitting of KIC65. The contours on the maps correspond to 1σ , 2σ , and 3σ errors on the distribution. The effect of spots is visible in the distorted maps of the eccentricity parameter space. Also note that the distortion of the radii parameter space is smaller than that of BD44.

On each isochrone we were looking for a triplet of points that simultaneously best reproduce the observed values of any selected parameters from the following: masses $M_{1,2,3}$, radii $R_{1,2,3}$, and effective temperatures $T_{1,2,3}^{\text{eff}}$ of three components, flux ratio of the inner binary's components l_2/l_1 in the given band, as well as the $[\text{Fe}/\text{H}]$, and distance d . The method of simultaneously obtaining distances and reddening $E(B - V)$ reproduced by a given model (triplet of points on an isochrone) is described in Appendix A, as well as in Helminiak et al. (2021). In the recent 3rd *Gaia* Data Release (GDR3; Gaia Collaboration 2022),

solutions from the *Part 1. Main Source* have high value of the RUWE parameter (~ 2.6), and better solutions, with significantly different distances, are presented in *Part 3. Non-single stars*. We used the latter ones as the constraints in our isochrone fitting.

It is worth noting that the ISPEC value of $[\text{M}/\text{H}]$ was also used as a constraint, and the 'best fitting' $[\text{Fe}/\text{H}]$ was searched for in the fitting process. For this reason, the values of $[\text{Fe}/\text{H}]$ (assumed equivalent to $[\text{M}/\text{H}]$, since $[\alpha/\text{Fe}] = 0$) may not be the same as $[\text{M}/\text{H}]$ found from spectra. In the literature, isochrone or evolutionary track fitting

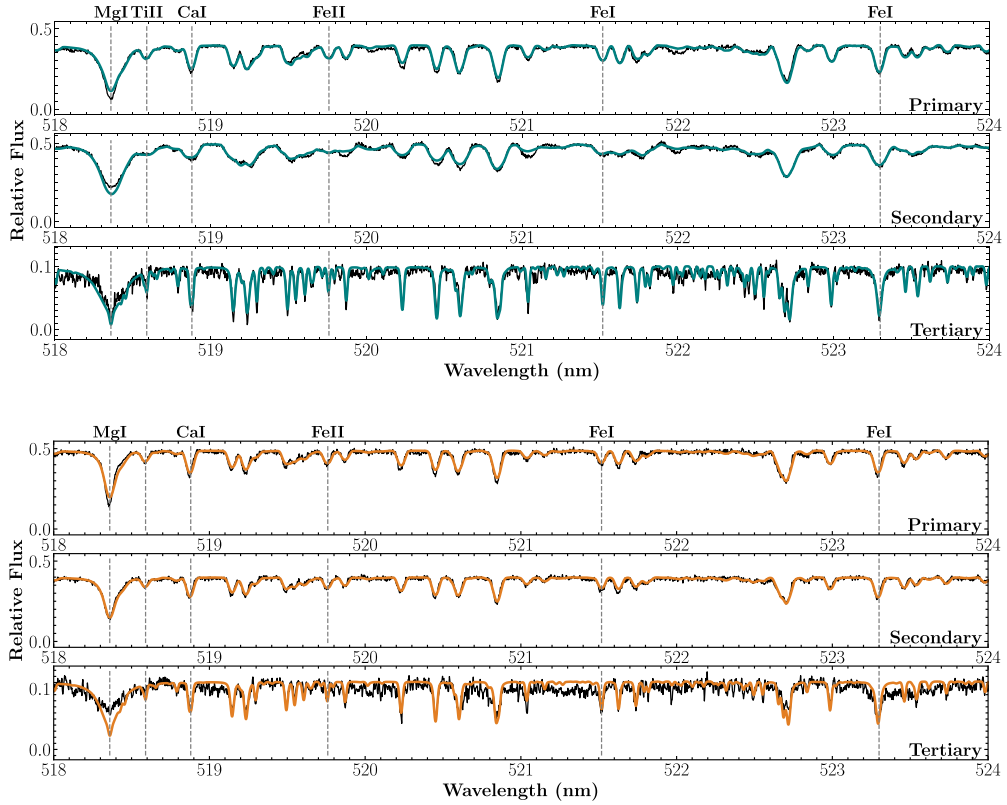


Figure 7. A section of the disentangled spectra and the best-fitting synthetic template of all the components of BD44 (top) and KIC65 (bottom). The fit was obtained through the SSF method available in ISPEC. While the SNR of the primary and secondary vary between 50–60, the tertiary component has an SNR ~ 18 . The section contains one of the wings of the Mg triplet and several Fe lines.

is often made under the assumption of fixed $[M/H]$. We find this approach incorrect.

3.7 Numerical integration of orbital dynamics

The accurate orbital parameters obtained enable us to probe the significant dynamical changes in these compact systems. The major orbital parameters that drive the dynamics are usually the masses, semimajor axes or periods, and all inclinations, including mutual inclination (i_m). While we get almost all orbital parameters from combined LC and RV analysis, we still lack the information about the longitude of ascending nodes (Ω_A and Ω_{AB} for inner and outer orbit, respectively) and i_m . An estimate of the range of the i_m can be calculated from the constraints arising due to geometry, using i_A and i_{AB} . Simplifying the calculations from Gronchi & Tommei (2007) we get,

$$\cos i_m = \cos(\Omega_A - \Omega_{AB}) \times \sin i_A \sin i_{AB} + \cos i_A \cos i_{AB}. \quad (4)$$

Since the value of $\cos(\Omega_A - \Omega_{AB})$ can vary between -1 and 1 , we estimate the range of $\cos i_m$ to be,

$$\cos i_m \geq \cos i_A \cos i_{AB} - \sin i_A \sin i_{AB}, \quad (5)$$

$$\cos i_m \leq \cos i_A \cos i_{AB} + \sin i_A \sin i_{AB}. \quad (6)$$

Using trigonometric identities, we get the range of i_m to be,

$$i_A - i_{AB} \leq i_m \leq i_A + i_{AB}. \quad (7)$$

This is the solution when the cosine of i_m is positive (say configuration A). There exists another set of solution for a negative cosine configuration (say configuration B),

$$180 - (i_A + i_{AB}) \leq i_m \leq 180 - (i_A - i_{AB}). \quad (8)$$

This gives us a range of 0° – 169.4° (for Config.A) or 10.6° – 180° (Config.B) for the i_m of KIC65. While for BD44, we get a range of 3.98° – 156.27° (Config.A) or 23.73° – 176.02° (Config.B). To further constrain this range, we rule out the unrealistic i_m by looking at average i_A variations in the numerical integration of orbital parameters, and comparing with the i_A from the observations. For our work, we use REBOUND¹¹, an open-source collisional N -body code (Rein & Liu 2012). REBOUND can also be used to simulate collisionless problems such as the three-body hierarchical orbit in our case. We use the symplectic integrator WHFAST which is designed for long-term integration of gravitational orbits (Rein & Tamayo 2015). WHFAST uses mixed variables (Jacobi and Cartesian) and also a symplectic corrector which ensures accurate and fast integration of the N -body dynamical equations. The general set-up is defined by

¹¹<https://github.com/hannorein/rebound>

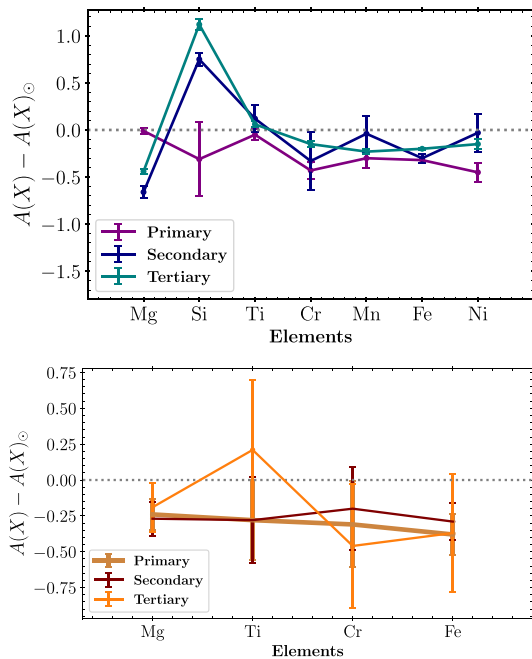
1916 *A. Moharana et al.*

Figure 8. Abundance variation for all three stars in BD44 (top) and KIC65 (bottom). The plotted abundances are relative to solar abundances, which is denoted by the dotted line.

masses and orbital parameters obtained with our observations. The values of inclinations, ω and other orientation parameters are also taken from our observations (Table 1). Further, we use the REBOUNDX (Tamayo et al. 2020) library for adding in tidal forces and dissipation to this set-up. The implementation uses a constant time-lag model from Hut (1981) to raise tides on the larger (and more massive) stars. The constant time-lag parameter (τ) is given by,

$$\tau = \frac{2R^3}{GMt_f}, \quad (9)$$

where R , M are the radius and mass of the body with tides (BD44Ab and KIC65Aa in our case), t_f is convective friction time that is assumed as 1 yr as described in REBOUNDX set-up,¹² and G is the gravitational constant. The other inputs from observations include the rotation frequency of the secondary and its radius. The tidal Love number of degree 2 (`tctlk2`) is assumed to be 0.01. Using this set-up, we simulate the systems for a time equal to the time between the observation of the first and last LC of the corresponding systems, i.e. 2.7 yr for BD44 and 6.9 yr for KIC65. We track the inclination changes of the inner binary for different values of Ω_{AB} (and assuming $\Omega_A = 0^\circ$) and then compare it with the observations.

A long-term look at such close systems ($P_A \sim 3d$) would require a coupled stellar evolution and dynamical evolution treatment. For this, we use the `parameter-interpolation` module in REBOUNDX. We update the radius and masses in the numerical simulation from MIST evolutionary tracks for the tidal stars (BD44Ab and KIC65Aa) in the inner binary. We start with an integration time-step

of 1/30 times the inner binary period but update the integration time-step, if the orbit shrinks, so that we can track close encounters or collisions. With this set-up, we simulate our systems for 600 Myr.

4 RESULTS AND DISCUSSION

4.1 Physical parameters of the binary

The binary components of the two systems are found to be of similar orbital configurations. This gives us an interesting case of comparing the effect of the tertiary on the binary system. The inner mass ratio of BD44 is 0.931 (or 1/1.074) while for KIC65 it is 0.9383. The corresponding inner orbit periods of BD44 and KIC65 are 3.472 6217 and 3.420 5977 d, respectively. The differences in the binaries of the two systems appear when we look at the LC solutions. The radius of the most massive star in BD44 is larger ($R_{Ab} = 2.4387^{+0.0035}_{-0.0048} R_\odot$) but it corresponds to the secondary (shallower) eclipse in the LC. This is also evident from the light fractions obtained from the BF and also the fast rotation as reflected in the high $v\sin(i)$. Going by the convention, we will address this star as the secondary (BD44Ab; thus, the secondary-to-primary mass ratio is >1). The primary of BD44 (BD44Aa) is inflated compared to the solar radius ($R_{Aa} = 1.3118^{+0.0056}_{-0.0053} R_\odot$). Both the stars in KIC65 are very much solar-like ($R_{Aa} = 1.0719^{+0.0019}_{-0.0020} R_\odot$ and $R_{Ab} = 1.0101^{+0.0017}_{-0.0014} R_\odot$). A quick look at the MCMC corner plots (Fig. 5) tells us that the uncertainty on radii measurements is mostly affected by degeneracy in L_{Aa} which is itself degenerate with l_3 . The e_A is adopted to be zero for both systems. But the MCMC maps show shifts of 2σ and 3σ from zero, for BD44 (Fig. 5) and KIC65 (Fig. 6), respectively. This small eccentricity can possibly be induced in the LC due to spots or be due to perturbations from the tertiary star. Unfortunately with current observations, it is difficult to decouple these effects.

The temperatures of the BD44 binary stars are lower ($T_{Aa}^{\text{eff}} = 5822 \pm 202$ K and $T_{Ab}^{\text{eff}} = 5449 \pm 100$ K) compared to those of KIC65 ($T_{Aa}^{\text{eff}} = 6490 \pm 129$ K and $T_{Ab}^{\text{eff}} = 6397 \pm 123$ K). While the similar temperatures of KIC65Aa and KIC65Ab can explain the similar eclipse depths, we expect a temperature ratio of 0.772 (compared to 0.936 from the spectral analysis) from the LC fitting of BD44. This discrepancy can arise due to the cold spots in BD44, which affect the spectroscopic temperature measurement.

The stars in BD44 have quite different $v\sin(i)$ with the BD44Aa having a value of 23.21 km s^{-1} compared to 39.60 km s^{-1} for BD44Ab. KIC65 has similar $v\sin(i)$ for the stars in the inner binary as expected from stars with similar radii. But when comparing with calculated synchronized velocities, we find that the observed velocities are larger than expected. The $v\sin(i)$ of the tertiary of KIC65 and BD44 are similar.

Both KIC65 and BD44 are metal-poor systems having $[M/H] -0.28 \pm 0.22$ and -0.24 ± 0.21 , respectively. While most of the stars are found to be α -enhanced systems, BD44Ab and BD44B were the only stars with negative α . We calculated the abundances of some elements whose lines showed up on the spectra. We compare the abundances (see Tables 2 and 3) for all three stars, in both the systems, in Fig. 8. While all the stars in KIC65 have similar abundances (within error bars), BD44Ab and BD44B have a rise in $A(\text{Si})$ and a dip in $A(\text{Mg})$ compared to BD44Aa (Fig. 8). The total set of all parameters is given in Table 1 for comparison.

4.2 Physical parameters of the tertiary

The tertiary stars orbit the inner binary with the periods of 254.84 ± 0.05 and 418.0 ± 0.4 d for BD44 and KIC65, respectively.

¹²We followed the process of adding tides as explained in <https://github.com/dtamayo/reboundx/blob/master/ipynb/examples/TidesConstantTimeLag.ipynb>.

Table 1. All adopted parameters for BD44 and KIC65 (except i_m). Unsymmetrical errors correspond to uncertainties estimated using MCMC sampling.

	BD +44 2258			KIC 06525196		
	Orbital parameters			Orbital parameters		
	Aa–Ab	A–B		Aa–Ab	A–B	
t_0 (BJD – 2450000)	8740.8268426			2421.6563579		
P (d)	3.4726217 ± 0.0000015			254.84 ± 0.05		
a (R_\odot)	12.06 ± 0.12			240.2 ± 3.3		
e	0.000 ^a			0.598 ± 0.002		
i (deg)	$80.1271^{+0.0084}_{-0.0057}$			$76.15^{+1.91}_{-1.61}$		
ω (deg)	–			203.0 ± 0.2		
q	1.074 ± 0.021			0.465 ± 0.019		
K_1 (km s^{-1})	89.66 ± 0.98			18.30 ± 0.75		
K_2 (km s^{-1})	83.47 ± 1.37			39.39 ± 0.22		
	Stellar and atmospheric parameters					
	Aa	Ab	B	Aa	Ab	B
Flux fraction (from spectroscopy)	0.3758 ± 0.0268	0.5139 ± 0.0285	0.1104 ± 0.0088	0.4851 ± 0.0225	0.4010 ± 0.0154	0.1139 ± 0.0181
Flux fraction (from photometry)	$0.4021^{+0.0039}_{-0.0030}$	$0.5101^{+0.0021}_{-0.0031}$	$0.0878^{+0.0016}_{-0.0015}$	$0.4990^{+0.0101}_{-0.0084}$	$0.4060^{+0.0051}_{-0.0068}$	$0.0950^{+0.0033}_{-0.0034}$
M (M_\odot)	0.941 ± 0.033	1.011 ± 0.029	0.907 ± 0.065	1.0351 ± 0.0055	0.9712 ± 0.0039	0.777 ± 0.012
R (R_\odot)	$1.3118^{+0.0056}_{-0.0053}$	$2.4387^{+0.0035}_{-0.0048}$	$1.67^{+0.70}_{-0.59}$	$1.0719^{+0.0020}_{-0.0019}$	$1.0101^{+0.0014}_{-0.0017}$	$0.74^{+0.80}_{-0.38}$
T_{eff} (K)	5822 ± 202	5449 ± 100	5261 ± 181	6490 ± 129	6397 ± 123	5393 ± 319
$\log(g)$ (dex)	4.19^b	3.69^b	3.95 ± 0.39	4.39^b	4.41^b	4.58 ± 0.63
v_{mic} (km s^{-1})	2.36 ± 0.75	1.78^c	1.19 ± 0.5	1.39 ± 0.54	1.18 ± 0.53	1.5^c
v_{mac} (km s^{-1}) ^c	4.69	3.76	3.43	9.28	8.43	5.94
$v \sin(i)$ (km s^{-1})	23.21 ± 2.19	39.60 ± 3.26	5.34 ± 1.41	20.69 ± 1.45	18.39 ± 1.15	5.23 ± 1.34
α (dex)	0.21 ± 0.12	-0.22 ± 0.08	-0.21 ± 0.11	0.07 ± 0.11	0.16 ± 0.11	0.29 ± 0.24
	System parameters					
$\log(\text{age})$ (dex)	$9.89^{+0.03}_{-0.05}$			9.49 ± 0.06		
$[M/H]_{\text{ispec}}$ (dex)	-0.24 ± 0.21			-0.28 ± 0.22		
$[Fe/H]_{\text{isoc}}$ (dex)	$-0.40^{+0.15}_{-0.10}$			$-0.45^{+0.15}_{-0.35}$		
$E(B - V)^d$ (mag)	$0.176^{+0.019}_{-0.049}$			$0.053^{+0.040}_{-0.030}$		
Distance ^d (pc)	$194.5^{+3.3}_{-10.3}$			$220.01^{+2.26}_{-1.68}$		

Note. ^a Fixed while optimization. ^b Fixed from LC fitting solutions. ^c Obtained from empirical tables. ^d Based on isochrone fitting.

Table 2. Abundances of individual elements of the components of BD44. Solar abundances are presented for comparison (Asplund et al. 2009).

Elements	Primary	Secondary	Tertiary	Solar
¹² Mg	7.59 ± 0.03	6.94 ± 0.06	7.16 ± 0.03	7.60 ± 0.04
¹⁴ Si	7.20 ± 0.39	8.26 ± 0.07	8.63 ± 0.06	7.51 ± 0.03
²² Ti	4.90 ± 0.06	5.25 ± 0.14	5.01 ± 0.03	4.95 ± 0.05
²⁴ Cr	5.21 ± 0.09	5.31 ± 0.31	5.49 ± 0.03	5.64 ± 0.04
²⁵ Mn	5.13 ± 0.10	5.39 ± 0.19	5.20 ± 0.03	5.43 ± 0.05
²⁶ Fe	7.18 ± 0.03	7.20 ± 0.05	7.30 ± 0.01	7.50 ± 0.04
²⁸ Ni	5.77 ± 0.10	6.19 ± 0.20	6.07 ± 0.05	6.22 ± 0.04

Table 3. Abundances of individual elements of the components of KIC65.

Elements	Primary	Secondary	Tertiary	Solar
¹² Mg	7.36 ± 0.11	7.33 ± 0.12	7.41 ± 0.17	7.60 ± 0.04
²² Ti	4.67 ± 0.28	4.67 ± 0.30	5.16 ± 0.49	4.95 ± 0.05
²⁴ Cr	5.33 ± 0.30	5.44 ± 0.29	5.17 ± 0.43	5.64 ± 0.04
²⁶ Fe	7.12 ± 0.14	7.21 ± 0.13	7.13 ± 0.41	7.50 ± 0.04

They are different in both mass and radius. The mass of the tertiary in BD44 is close to solar ($0.907 \pm 0.065 M_\odot$) while tertiary of KIC65 is less massive ($0.777 \pm 0.012 M_\odot$). The estimated radii have large errors, but a comprehensive look at all the signatures suggests that the tertiary in BD44 has an inflated atmosphere and therefore a radius larger than one expected for a main-sequence star of this mass. The tertiary of KIC65 is most likely to have a radius of $0.74 R_\odot$. The stars themselves are orbiting with different periods around

the inner binary system. The tertiary of BD44 is in an orbit with higher eccentricity ($e_{AB} = 0.598$) than KIC65 ($e_{AB} \sim 0.3$; Fig. 9). These different configurations will mostly affect the time-scale of secular perturbations which depend on e_{AB} (Ford, Kozinsky & Rasio 2000).

4.3 Possible mutual inclinations

Short-term numerical integration gave us an estimate of inclination changes of the inner binary (Δi_A) for different values of Ω_{AB} . We then obtained observed Δi_A by using inclination values obtained by Helminiak et al. (2017) for KIC65, subtracted from the values obtained in this work. While for BD44 we used the inclinations observed in Sector-16 and Sector-49 of *TESS* LCs (Table 4). This gave us possible values of Ω_{AB} for the observed Δi_A (Fig. 10). We then used equation (4) to translate the possible Ω_{AB} values to possible i_m values for all possible configurations (Table 5).

4.4 Age and evolution

Isochrone fitting puts the $\log(\text{age})$ for BD44 between 9.84 and 9.92 (95 per cent confidence level), for metallicity range of -0.25 to -0.50 dex. The formally best fit was found for $\log(\text{age}) = 9.89$ (7.8 Gyr) and $[Fe/H] = -0.40$ dex. While the primary of BD44, BD44Aa, is a main-sequence star, BD44Ab is a sub-giant. With the large uncertainties in the parameters of BD44B, it is hard to determine its evolutionary state. But the simultaneous mass–radius and mass–temperature isochrone fit depicts it as a sub-giant star (Fig. 11). The

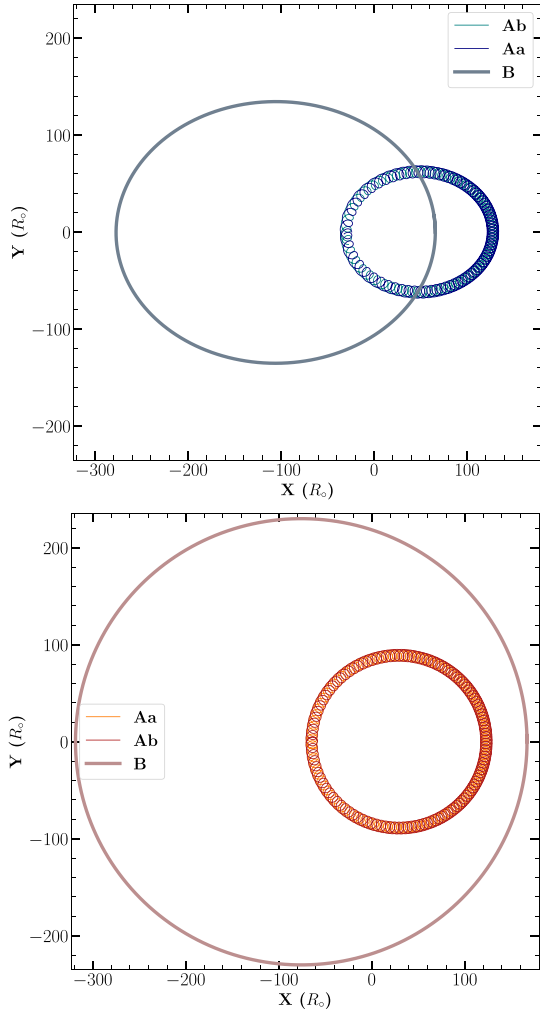
1918 *A. Moharana et al.*

Figure 9. Orbital path of all the stars of BD44 (top) and KIC65 (bottom). The orbits are viewed perpendicular to the orbital plane of the inner binary (for $i_m = 4^\circ$) and are integrated over one outer-orbit period.

Table 4. Variation of i_A over time.

System	Initial i_A (deg)	Final i_A (deg)	Time (yr)
BD44	80.1271 ± 0.008	80.1521 ± 0.017	2.7
KIC65	85.15 ± 0.34	84.7083 ± 0.005	6.9

other signatures of BD44B being a sub-giant are found in (i) large amplitude of BF (Fig. 2), and (ii) similar abundances (Fig. 8) as that of the BD44Ab (which is a sub-giant itself). However, with the available data, we cannot completely rule out the possibility that it is a main-sequence star, less massive and smaller than the primary.

The isochrone-based, reddening-free distance was found to be 194.5 pc, which is significantly larger than the GDR3 Part 3 value of 165.8 ± 0.6 pc. The distribution of acceptable models is very skewed, and none of the acceptable models reached a distance lower than 184 pc. The tension is probably caused by the tertiary, which was formally found to be less massive but seemingly more evolved than

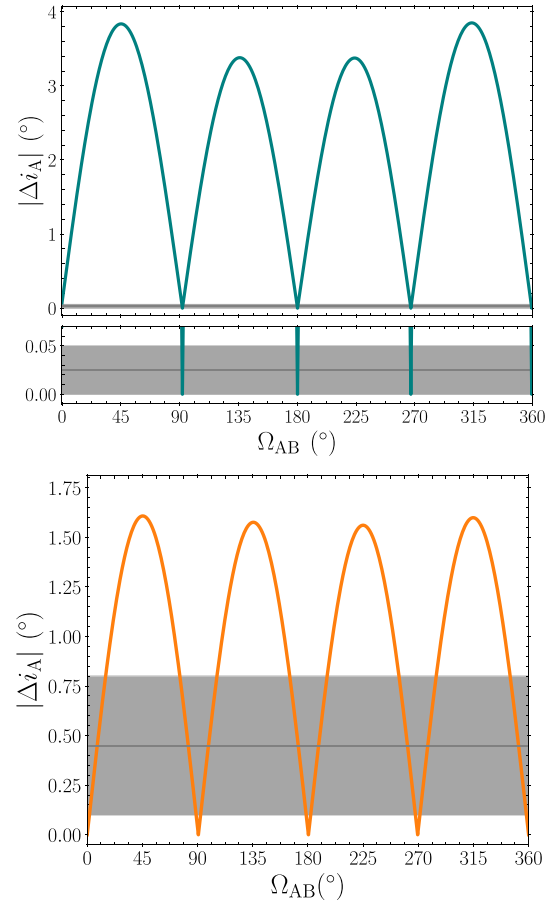


Figure 10. Variation of $|\Delta i_A|$ from numerical simulations for different values of Ω_{AB} , for BD44 (top) and KIC65 (bottom). The timescale of the simulation corresponds to the length of the available LCs. The grey lines show the observed $|\Delta i_A|$ with the shaded regions representing the errors in measurements. The overlapping regions represent the possible values of Ω_{AB} . The lower panel of the top figure represents a zoomed-in view of the observed variations.

Table 5. Estimates of mutual inclination for possible values of Ω_{AB} .

System	Ω_{AB}	i_m	
		Config.A	Config.B
BD44	359.46 ± 0.76	4.03 ± 0.10	175.97 ± 0.01
	266.97 ± 0.79	90.56 ± 0.76	89.45 ± 0.76
	180.23 ± 0.83	156.27 ± 0.01	23.73 ± 0.01
	92.16 ± 0.80	89.71 ± 0.77	90.29 ± 0.77
KIC65	353.80 ± 4.85	6.18 ± 4.83	173.82 ± 4.83
	269.41 ± 11.12	90.09 ± 11.02	89.91 ± 11.02
	180.42 ± 11.18	164.60 ± 0.30	15.40 ± 0.30
	90.67 ± 11.10	90.16 ± 11.00	89.83 ± 11.00
	6.19 ± 4.85	6.17 ± 4.83	173.83 ± 4.83

the primary. Its parameters could probably be better determined with additional observations around the outer orbit's pericentre, where the tertiary's RVs reach their minimum. It should also be noted that the GDR3 solution is of worse quality than for KIC65.

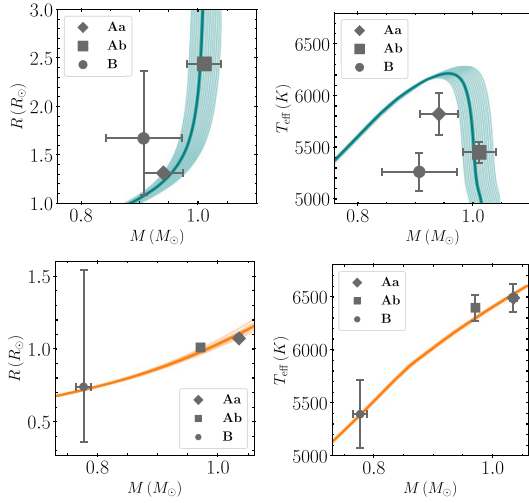


Figure 11. Mass–radius (left column) and mass–temperature (right column) isochrone fits for BD44 (top; in green) and KIC65 (bottom; in orange). The shaded area represents the parameter space corresponding to the errors of the fitting. The respective measurements from the stars are plotted in grey. The size of the points are relative to their radii.

Even though having the binary stars with masses similar to BD44, both the primary and secondary of KIC65 are main-sequence stars along with its tertiary. This immediately suggests that KIC65 is significantly younger than BD44. The fitting procedure for KIC65 resulted in $\log(\text{age}) = 9.49$ (3.1 Gyr) and $[\text{Fe}/\text{H}] = -0.45$ dex, with the 95 per cent confidence level ranges of 9.43 to 9.55, and -0.80 to -0.30 dex, respectively. The isochrone-based reddening-free distance ($\sim 220 \pm 2$ pc) is in excellent agreement with, and of comparable precision to, the GDR3 solution for an astrometric binary model (222.3 ± 1.7 pc), even when it was not used as a constraint.

4.5 Dynamical evolution

Long-term evolution of KIC65 shows that the system is stable for 600 Myr more. But BD44 becomes a binary system within 550 Myr due to the collision/merger of the inner binary. This collision will be driven by increasing tidal forces due to the increasing radius of the sub-giant BD44Ab (Fig. 12: upper panel). The radius of the star will exceed the Roche limit (Eggleton 1983) at around 450 Myr and will drive the merger process unless the formation of a contact binary stabilizes this system. This merger is mostly due to the tides in the inner binary as a lack of tertiary companion would have only delayed the merger by a few Myrs (Fig. 12: lower panel) for most of the estimated i_m . But a i_m near 90° will make the system merge faster (< 400 Myr) than the lower values of i_m (Fig. 13).

4.6 Spot evolution

The light curve of BD44 is highly varying over different sectors owing to the migrating and evolving cold spots. The activity of BD44 is corroborated by its ultraviolet and X-ray emissions. The distortions on the BF of the stars in BD44 indicate the secondary (BD44Ab) to have more spots. The occurrence of the fast evolving and migrating spots is common on sub-giant stars. The biggest spot on the secondary is still visible in the newest Sector-49 of *TESS* observations. This

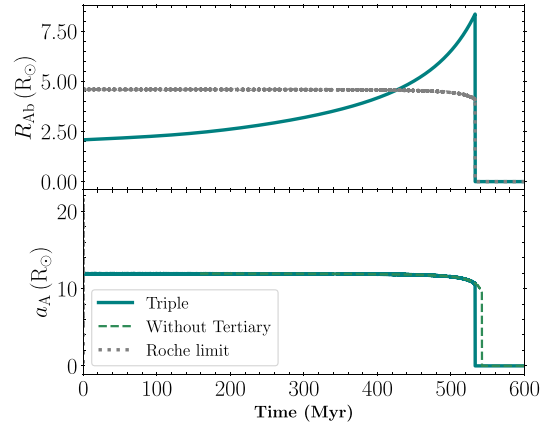


Figure 12. Variation of the radius of BD44Ab and the semimajor axis of the inner binary of BD44 as simulated in REBOUNDX for $i_m = 4^\circ$. The radius variation is interpolated from MIST grids. The grey dotted line in the top panel shows Roche limit for the system. The dashed line in the lower panel shows the change in the collision time if no tertiary star was present.

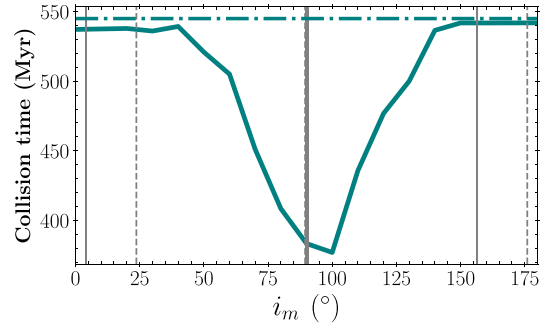


Figure 13. The simulated collision time of the inner binary of BD44 for different mutual inclinations. The green dot-dashed line shows the time for collision without a tertiary companion. The vertical grey lines represent the possible values of i_m . Solid lines represent possible i_m for Config.A while dashed lines are for Config.B.

Table 6. Spot parameters for the coldest spot on the secondary of BD44. The parameters have been obtained for each sector using PHOEBE 2 modelling.

Parameters	S16	S22	S49
T_{seg} (BJD-2457000)	1740.8270	1900.5753	2640.2640
$i_{\text{Ab}}^{\text{spot}}$ (deg)	42.846	37.311	39.611
$T_{\text{Ab}}^{\text{spot}}$	0.8988	0.9296	0.8500
$c_{\text{Ab}}^{\text{spot}}$ (deg)	22.000	35.745	21.913
$l_{\text{Ab}}^{\text{spot}}$ (deg)	0.000	29.975	180.233

enabled us to study its migration. We used spot parameters obtained from LC fitting using PHOEBE 2, from different sectors, to quantify the migration (see Table 6). Using the values of longitudes and the mid-times of the first primary eclipse (T_{seg}) for each segment, we calculated the rate of change of the longitude. We found that the spot moves $\sim 0.696^\circ$ per orbital cycle of the inner binary. The spot moves from a longitude of 0° – 180° in 2.5 yr. Extrapolating this, we get a spot migration period of 5 yr. The migration is most probably caused

1920 *A. Moharana et al.*

by differential rotation because the spot in question is near the poles, as seen in low c^{spot} values (Fig. 14). Petit et al. (2004) represents the differential rotation as,

$$\Omega(c^{\text{spot}}) = \Omega_{\text{eq}} - \Delta\Omega \cos^2(c^{\text{spot}}) \quad (10)$$

where Ω is the differential rotation as a function of co-latitude (or latitude), Ω_{eq} is the rotation at the equator, and $\Delta\Omega$ is the difference in rotation rate between the pole and the equator. Calculating an estimate of $\Delta\Omega$ in BD44Ab gives us $\Delta\Omega = 0.0044 \pm 0.0004 \text{ rad d}^{-1}$. This small differential rotation has been seen in the K1 sub-giant primary in the RS CVn system HR 1099 (Petit et al. 2004) and also K-type main sequence of V471 Tau (Hussain et al. 2006) with $\Delta\Omega = 0.0152 \pm 0.0008 \text{ rad d}^{-1}$ and $\Delta\Omega = 0.0016 \pm 0.0060 \text{ rad d}^{-1}$, respectively.

5 CONCLUSIONS

We obtained independent measurements of different parameters for two triple-lined CHT. Using LC modelling, RV modelling, and SPD followed by spectral analysis, we obtained stellar, orbital, and atmospheric parameters of all the six stars in the two CHTs. A multiparameter isochrone fitting constrained the ages of the two systems to be of the order of Gyrs. Isochrones, along with abundances obtained from the disentangled spectra, helped us classify the evolutionary state of the tertiary in the two systems. Furthermore, we gathered the following information about the two systems:

(i) **KIC65:** The period ratio of the CHT is ≈ 122 . All stars in the system are main-sequence stars. The system is a metal-poor one and is α -enhanced. The tertiary has five possible configurations of mutual inclination with a possibility of near co-planar orbit. Due to the comparatively smaller mass of the tertiary and a wider orbit, the system is stable in the long term for all values of mutual inclinations. The distance estimated in our study is consistent with the distance obtained in *Gaia*-DR3.

(ii) **BD44:** This system is a relatively tighter CHT with a period ratio ≈ 73 . But still, this system is well above the dynamical instability¹³ limit as defined in Mardling & Aarseth (2001). The system consists of one main-sequence star (almost at the turn-off) and two sub-giant stars. The abundance patterns of the two sub-giant stars are similar while the main sequence differs in Mg and Si abundances. The system has large and cold spots that affect the measurement of some of our parameters. By using the spots, we were able to calculate a differential rotation in the sub-giant of the inner binary. This sub-giant component of the inner pair also contributes significantly to tidal forces. Numerical simulations with tidal interactions show that the inner binary will collide/merge in a few hundred of Myrs due to the radius of the sub-giant exceeding the Roche limit. This leaves behind a wide binary unless the formation of a contact binary stabilizes the system. The tertiary does hasten this merger but the effects are drastic if the tertiary is orbiting in an orbit perpendicular to the inner binary orbit.

Both the targets can benefit from further photometric and spectroscopic observations that will improve the estimate of obtained parameters. The photometric observations themselves will be quite crucial to check for inclination variations of the inner binary and therefore will give better constraints on the mutual inclination. This will be helpful in constraining evolution scenarios of the

¹³This limit is derived for prograde co-planar motion.

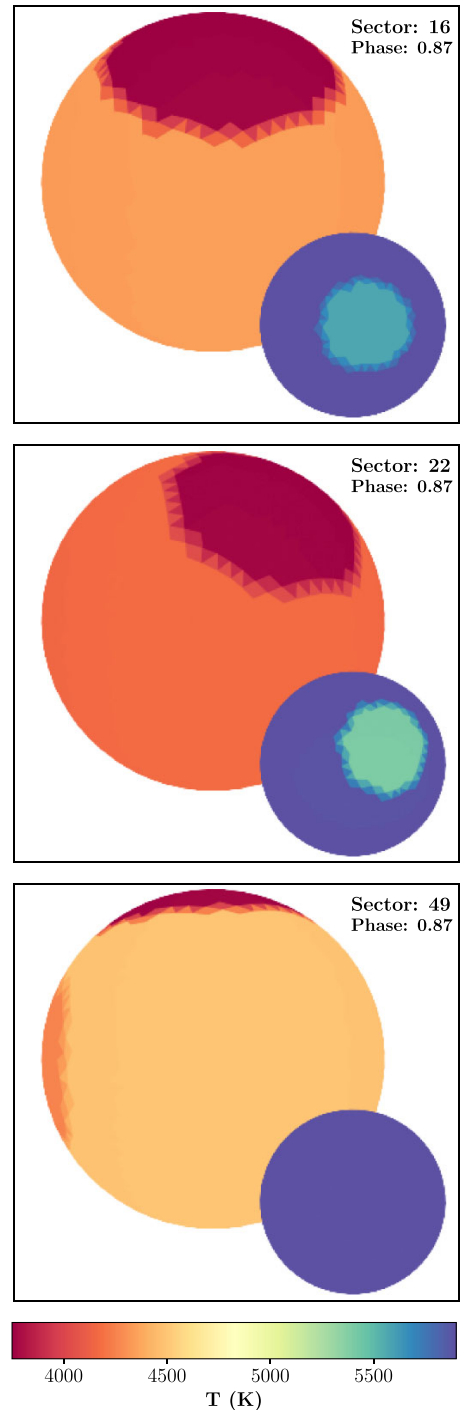


Figure 14. Spot positions on the inner binary stars of BD44 (at the same phase) for Sector-16 (top), Sector-22 (middle), and Sector-40 (bottom) as obtained with PHOEBE2 modelling. The stable-spot near the pole of the secondary is the spot that affects the eclipse depths the most and is the one that migrates with a time-scale of ~ 5 yr.

CHT as well as star formation scenarios of these close triples. Nevertheless, this study shows that the use of parameters obtained using independent observations is crucial for the realistic modelling of CHT.

ACKNOWLEDGEMENTS

The authors thank the referee for the invaluable comments and suggestions. The authors thank Dr Kyle Conroy and Dr Andrej Prša for their valuable suggestions and help with PHOEBE 2. The authors also acknowledge Dr Hanno Rein for his help in setting up REBOUND simulations. This work was funded by the Polish National Science Centre (NCN) through grant no. 2021/41/N/ST9/02746. AM, FM, TP, and MK were supported by NCN through grant no. 2017/27/B/ST9/02727. FM gratefully acknowledges support from the NASA TESS Guest Investigator grant 80NSSC22K0180 (PI: A. Prša). This paper includes data collected with the *TESS* mission, obtained from the Mikulski Archive for Space Telescopes (MAST) data archive at the Space Telescope Science Institute (STScI). Funding for the *TESS* mission is provided by the NASA Explorer Program. STScI is operated by the Association of Universities for Research in Astronomy, Inc., under NASA contract NAS 5-26555. This work also presents results from the European Space Agency (ESA) space mission *Gaia*. *Gaia* data are being processed by the Gaia Data Processing and Analysis Consortium (DPAC). Funding for the DPAC is provided by national institutions, in particular, the institutions participating in the Gaia MultiLateral Agreement (MLA).

DATA AVAILABILITY

The *TESS* data used in this article are public and hosted on MAST. The data can be accessed from <http://dx.doi.org/10.17909/fp8v-570>. The spectroscopic data will be made available upon request.

REFERENCES

- Akashi M., Soker N., 2017, *MNRAS*, 469, 3296
 Asplund M., Grevesse N., Sauval A. J., Scott P., 2009, *ARA&A*, 47, 481
 Bianchi L., Herald J., Efremova B., Girardi L., Zabot A., Marigo P., Conti A., Shiao B., 2011, *Ap&SS*, 335, 161
 Blanco-Cuaresma S., 2019, *MNRAS*, 486, 2075
 Blanco-Cuaresma S., Soubiran C., Heiter U., Jofré P., 2014, *A&A*, 569, A111
 Borkovits T., 2022, *Galaxies*, 10, 9
 Borkovits T., Rappaport S., Hajdu T., Sztakovics J., 2015, *MNRAS*, 448, 946
 Borkovits T., Hajdu T., Sztakovics J., Rappaport S., Levine A., Břrů I. B., Klagyivik P., 2016, *MNRAS*, 455, 4136
 Borkovits T., Rappaport S. A., Hajdu T., Maxted P. F. L., Pál A., Forgács-Dajka E., Klagyivik P., Mitnyan T., 2020, *MNRAS*, 493, 5005
 Borkovits T., Rappaport S. A., Toonen S., Moe M., Mitnyan T., Csányi I., 2022, *MNRAS*, 515, 3773
 Box G. E. P., Jenkins G. M., 1976, *Holden-Day Series in Time Series Analysis*, Holden-Day Inc., St. San Francisco, CA, United States
 Cardelli J. A., Clayton G. C., Mathis J. S., 1989, *ApJ*, 345, 245
 Choi J., Dotter A., Conroy C., Cantiello M., Paxton B., Johnson B. D., 2016, *ApJ*, 823, 102
 Claret A., Bloemen S., 2011, *A&A*, 529, A75
 Conroy K. E. et al., 2020, *ApJS*, 250, 34
 Dotter A., 2016, *ApJS*, 222, 8
 Duchêne G., Kraus A., 2013, *ARA&A*, 51, 269
 Eggleton P. P., 1983, *ApJ*, 268, 368
 Eggleton P. P., Kiseleva-Eggleton L., 2001, *ApJ*, 562, 1012
 Eggleton P. P., Verbunt F., 1986, *MNRAS*, 220, 13P
 Eisner N. L. et al., 2022, *MNRAS*, 511, 4710
 Ford E. B., Kozinsky B., Rasio F. A., 2000, *ApJ*, 535, 385
 Foreman-Mackey D., Hogg D. W., Lang D., Goodman J., 2013, *PASP*, 125, 306
 Foreman-Mackey D. et al., 2019, *J. Open Source Softw.*, 4, 1864
 Franc C., Zakořan J.-M., 2009, *J. Time Ser. Anal.*, 30, 449
 Fuller J., Derekas A., Borkovits T., Huber D., Bedding T. R., Kiss L. L., 2013, *MNRAS*, 429, 2425
 Gaia Collaboration: Vallenari A., et al., 2022, *Gaia Data Release 3*, arXiv e-prints, arXiv:2208.00211
 Gilmore G. et al., 2012, *The Messenger*, 147, 25
 Gray D. F., 2005, *The Observation and Analysis of Stellar Photospheres*. Cambridge Univ. Press, Cambridge
 Grevesse N., Asplund M., Sauval A. J., 2007, *Space Sci. Rev.*, 130, 105
 Gronchi G. F., Tommei G., 2007, *Discrete Continuous Dyn. Syst. B*, 7, 755
 Gustafsson B., Edvardsson B., Eriksson K., Jørgensen U. G., Nordlund Å., Plez B., 2008, *A&A*, 486, 951
 Hadrava P., 1995, *A&AS*, 114, 393
 Hamers A. S., Dosopoulou F., 2019, *ApJ*, 872, 119
 Helminiak K. G., Ukita N., Kambe E., Kozłowski S. K., Sybilski P., Ratajczak M., Maehara H., Konacki M., 2016, *MNRAS*, 461, 2896
 Helminiak K. G. et al., 2017, *MNRAS*, 468, 1726
 Helminiak K. G. et al., 2021, *MNRAS*, 508, 5687
 Holmgren D. E., Hadrava P., Harmanec P., Eenen P., Corral L. J., Yang S., Ak H., Bozić H., 1999, *A&A*, 345, 855
 Horvat M., Conroy K. E., Pablo H., Hambleton K. M., Kochoska A., Giammarco J., Prša A., 2018, *ApJS*, 237, 26
 Howell S. B. et al., 2014, *PASP*, 126, 398
 Hussain G. A. J., Allende Prieto C., Saar S. H., Still M., 2006, *MNRAS*, 367, 1699
 Hut P., 1981, *A&A*, 99, 126
 Ilijic S., Hensberge H., Pavlovski K., Freyhammer L. M., 2004, in *Hilditch R. W., Hensberge H., Pavlovski K.*, eds, *ASP Conf. Ser. Vol. 318, Spectroscopically and Spatially Resolving the Components of the Close Binary Stars*. Astron. Soc. Pac., San Francisco, p. 111
 Izumiura H., 1999, in *Chen P. Sed.*, Proc. 4th East Asian Meeting on Astronomy, Observational Astrophysics in Asia and its Future. Kunming Yunnan Observatory, p. 77
 Jones D., Pejcha O., Corradi R. L. M., 2019, *MNRAS*, 489, 2195
 Jones D. et al., 2020, *ApJS*, 247, 63
 Kambe E. et al., 2013, *PASJ*, 65, 15
 Kervella P., Thévenin F., Di Folco E., Ségransan D., 2004, *A&A*, 426, 297
 Kobulnicky H. A., Fryer C. L., 2007, *ApJ*, 670, 747
 Konacki M., Muterspaugh M. W., Kulkarni S. R., Helminiak K. G., 2010, *ApJ*, 719, 1293
 Korth J., Moharana A., Pešta M., Czavalinga D. R., Conroy K. E., 2021, *Cont. Astron. Observ. Skalnaté Pleso*, 51, 58
 Kozai Y., 1962, *AJ*, 67, 591
 Lee A. T., Offner S. S. R., Kratter K. M., Smullen R. A., Li P. S., 2019, *ApJ*, 887, 232
 Lidov M. L., 1962, *Planet. Space Sci.*, 9, 719
 Maoz D., Mannucci F., Nelemans G., 2014, *ARA&A*, 52, 107
 Marcadon F., Helminiak K. G., Marques J. P., Pawłaszczek R., Sybilski P., Kozłowski S. K., Ratajczak M., Konacki M., 2020, *MNRAS*, 499, 3019
 Mardling R. A., Aarseth S. J., 2001, *MNRAS*, 321, 398
 Mason B. D., Hartkopf W. I., Gies D. R., Henry T. J., Helsel J. W., 2009, *AJ*, 137, 3358
 Maxted P. F. L. et al., 2020, *MNRAS*, 498, 332
 Mayer P., Harmanec P., Pavlovski K., 2013, *A&A*, 550, A2
 Moe M., Kratter K. M., 2018, *ApJ*, 854, 44
 Naoz S., Fabrycky D. C., 2014, *ApJ*, 793, 137
 Nelder J. A., Mead R., 1965, *Comput. J.*, 7, 308
 Paxton B., Bildsten L., Dotter A., Herwig F., Lesaffre P., Timmes F., 2011, *ApJS*, 192, 3

1922 *A. Moharana et al.*

- Paxton B. et al., 2013, *ApJS*, 208, 4
 Paxton B. et al., 2015, *ApJS*, 220, 15
 Paxton B. et al., 2018, *ApJS*, 234, 34
 Perets H. B., Fabrycky D. C., 2009, *ApJ*, 697, 1048
 Petit P. et al., 2004, *MNRAS*, 348, 1175
 Prša A. et al., 2016, *ApJS*, 227, 29
 Raghavan D. et al., 2010, *ApJS*, 190, 1
 Randich S., Gilmore G., Gaia-ESO Consortium, 2013, *The Messenger*, 154, 47
 Rappaport S., Deck K., Levine A., Borkovits T., Carter J., El Mellah I., Sanchis-Ojeda R., Kalomeni B., 2013, *ApJ*, 768, 33
 Rappaport S. A. et al., 2022, *MNRAS*, 513, 4341
 Rein H., Liu S. F., 2012, *A&A*, 537, A128
 Rein H., Tamayo D., 2015, *MNRAS*, 452, 376
 Ricker G. R. et al., 2015, *J. Astron. Telesc. Ins. Syst.*, 1, 014003
 Rucinski S., 1999a, *Turkish J. Phys.*, 23, 271
 Rucinski S., 1999b, in Hearnshaw J. B., Scarfe C. D. eds, *ASP Conf. Ser. Vol. 185, IAU Colloq. 170: Precise Stellar Radial Velocities*. Astron. Soc. Pac., San Francisco, p. 82
 Shatsky N., Tokovinin A., 2002, *A&A*, 382, 92
 Simon K. P., Sturm E., 1994, *A&A*, 281, 286
 Tamayo D., Rein H., Shi P., Hernandez D. M., 2020, *MNRAS*, 491, 2885
 Tokovinin A., 2004, *Revista Mexicana de Astronomia y Astrofisica Conference Series, IAU Colloquium*, vol. 21, p. 7, IA, UNAM
 Tokovinin A., 2017, *ApJ*, 844, 103
 Tokovinin A., 2021, *Universe*, 7, 352
 Tokovinin A., 2022, *ApJ*, 926, 1
 Toonen S., Portegies Zwart S., Hamers A. S., Bandopadhyay D., 2020, *A&A*, 640, A16
 Torres G., Andersen J., Giménez A., 2010, *A&AR*, 18, 67
 Voges W. et al., 1999, *A&A*, 349, 389
 von Zeipel H., 1910, *Astron. Nachr.*, 183, 345
 Zasche P., Paschke A., 2012, *A&A*, 542, L23
 Zasche P., Vokrouhlický D., Barlow B. N., Mašek M., 2023, *AJ*, 165, 81
 Zucker S., Mazeh T., 1994, *ApJ*, 420, 806

SUPPORTING INFORMATION

Supplementary data are available at *MNRAS* online.

Please note: Oxford University Press is not responsible for the content or functionality of any supporting materials supplied by the authors. Any queries (other than missing material) should be directed to the corresponding author for the article.

APPENDIX A: DISTANCE AND REDDENING ESTIMATES FROM THE ISOCHRONES

The reddening-free distances d_0 are estimated simultaneously with the reddening $E(B - V)$, using the available observed total magnitudes in different filters, and the predicted total brightness of the system in the same filters, for a given triplet of points (=stellar masses) on the same isochrone. We use the T_{eff} -surface brightness relations from Kervella et al. (2004), to calculate the distances d_λ and distance moduli $(m - M)_\lambda = 5 \log(d_\lambda) + 5$ in each band. To obtain the extinction-free modulus $(m - M)_0$, we fit a straight line on the A_λ versus $(m - M)_\lambda$ plane, where the A_λ are extinction coefficients in each band. We followed the extinction law of Cardelli, Clayton & Mathis (1989) $A_U:A_B:A_V:A_R:A_I:A_J:A_H:A_K = 4.855:4.064:3.1:2.545:1.801:0.88:0.558:0.36$, which assumes $R_V = 3.1$. The slope of the fitted line in this approach is the reddening $E(B - V)$, while the intercept is the extinction-free modulus $(m - M)_0$, which can be translated into the distance d_0 . In the isochrone fitting process, where the distance is used as one of the constraints, the reproduced d_0 value is the one that is being compared with d .

APPENDIX B: RADIAL VELOCITIES

The RVs for BD44, extracted using TODCOR method, are given in Table B1.

Table B1. RV measurements of BD44.

BJD-2450000	v_1 (km s ⁻¹)	ϵ_1 (km s ⁻¹)	v_2 (km s ⁻¹)	ϵ_2 (km s ⁻¹)	γ (km s ⁻¹)	ϵ_γ (km s ⁻¹)	v_3 (km s ⁻¹)	ϵ_3 (km s ⁻¹)
7022.350624	-21.499	0.697	-146.291	0.505	-81.664	0.754	-78.406	0.079
7061.170892	13.564	0.428	-149.393	0.973	-65.001	0.956	-106.205	0.100
7062.263807	-	-	-3.669	0.863	-	-	-	-
7110.041913	-22.493	0.471	-139.493	0.394	-78.901	0.654	-78.143	0.075
7111.161334	-160.274	0.578	3.675	0.355	-81.230	0.878	-76.942	0.086
7142.999934	-148.156	0.714	-23.570	0.426	-88.090	0.746	-63.215	0.083
7144.008005	-13.377	0.565	-161.962	1.019	-85.013	0.929	-62.731	0.135
7148.097089	-16.490	1.381	-160.184	0.379	-85.768	1.023	-62.282	0.077
7490.046763	-164.541	1.803	-2.964	0.496	-86.641	1.250	-68.064	0.227
7526.015228	-10.156	2.387	-159.806	0.391	-82.306	1.452	-76.503	0.095
7528.026002	-164.479	1.040	7.485	0.497	-81.571	1.032	-77.027	0.140
7530.053976	-13.474	1.193	-154.691	0.526	-81.558	0.965	-78.010	0.087
7539.052136	-	-	-41.870	0.339	-	-	-	-
7540.110845	3.205	0.606	-166.138	0.514	-78.439	0.925	-82.127	0.123
7755.261393	-6.755	0.688	-164.869	0.429	-82.985	0.881	-69.878	0.103
7813.057543	-146.164	2.782	2.688	0.778	-74.399	1.660	-92.769	0.105
7813.175027	-137.988	1.525	-8.703	0.446	-75.657	1.037	-	-
7814.125822	-3.179	1.464	-141.592	0.745	-69.911	1.081	-93.820	0.093
7816.093416	-150.858	2.080	12.322	0.828	-72.185	1.402	-95.491	0.128
7816.322403	-152.826	2.013	13.918	0.420	-72.435	1.343	-95.617	0.126
7846.107080	16.267	1.456	-123.088	0.526	-50.919	1.051	-139.779	0.231
7891.177386	-14.944	1.876	-163.681	0.491	-86.653	1.240	-66.297	0.118
7892.950768	-152.526	0.821	-12.576	0.450	-85.053	0.839	-66.027	0.078
7894.027357	-	-	-154.775	0.303	-	-	-	-
7950.023399	-3.531	0.670	-173.935	0.750	-85.687	0.978	-62.241	0.097
7954.983416	-164.296	0.700	-3.259	0.266	-86.656	0.882	-62.650	0.101
8066.362164	-156.728	2.378	14.806	0.152	-74.028	1.496	-91.838	0.117

Table C1. Spot parameters for spots on primary (Aa) and secondary (Ab) of BD44.

Parameters	S16	S22	S49
T_{Aa}^{spot}	0.9535	0.9362	1.04848
T_{Ab}^{spot1}	0.9922	0.9806	0.9545
T_{Ab}^{spot2}	0.8988	0.9296	0.8499
r_{Aa}^{spot} (deg)	29.449	29.846	33.943
r_{Ab}^{spot1} (deg)	31.9971	30.446	11.390
r_{Ab}^{spot2} (deg)	42.846	37.311	39.611
c_{Aa}^{spot} (deg)	80.735	69.893	80.735
c_{Ab}^{spot1} (deg)	90.977	89.047	90.977
c_{Ab}^{spot2} (deg)	22.000	35.745	21.913
l_{Aa}^{spot} (deg)	180.000	194.891	84.0973
l_{Ab}^{spot1} (deg)	162.488	196.044	262.305
l_{Ab}^{spot2} (deg)	0.000	29.975	180.233

APPENDIX C: SPOT PARAMETERS

The PHOEBE 2 model for BD44 included one spot on the Aa star and two on the Ab star. While we considered the most stable spot

(spot-2 on Ab) for our calculations of differential rotation, the other parameters are important while modelling the LC and are given in Table C1. The spot parameters vary over the three *TESS* sectors: Sector-16 (S16), Sector-22 (S22), and Sector-49 (S49).

APPENDIX D: BF FITTING TABLES

The BF fitting was done on multiple spectra of different epochs. Though the profile of every fit was similar, the flux fraction of each component varied slightly, which was necessary to consider while spectral disentangling. This variation was noticed for $v_{\text{sin}(i)}$ too but their variations were not significant to consider during spectral analysis. The complete tables for these parameters are available in the online version.

This paper has been typeset from a $\text{\TeX}/\text{\LaTeX}$ file prepared by the author.

CHAPTER 5

Three in a crowd: Distributions of CHT parameters

ସୀମାହୀନ ଆଶା ମୋର,
ନିତି ଗଢ଼େ, ନିତି ଭାଙ୍ଗେ ||

“Boundless hope of mine,
Every day they are built, every day they break. ”

– Akshaya Mohanty, Odia musician and songwriter

*A part of this chapter is to be submitted for publication in *Astronomy and Astrophysics* as ‘Spectroscopy of Eclipsing Compact Hierarchical Triples: Double-lined and triple-lined systems’, Moharana, Ayush ; Helminiak, K. G. ; Marcadon, F. ; Pawar, G. ; Pawar, T.; Konacki, M.*

5.1. Orbital elements from CHT searches

The first systematic search for hierarchical triples, which found CHTs too, was the search with ETV in *Kepler* data (Borkovits et al. 2016). The next big search also used the same technique but was carried out using OGLE observations (Hajdu et al. 2019). The most recent was done using the *Gaia* RUWE (Renormalised Unit Weight Error) parameter (Czavalinga et al. 2023). All these studies added around 400 CHTs. These searches managed to estimate (although not always accurately) some orbital elements of these systems. This prompted statistical studies of these parameter distributions. While Borkovits et al. (2016) was the first to find a peculiar peak around 0.2 to 0.3 in the outer eccentricity distribution (Figure 5.1; left), Czavalinga et al. (2023) derived an analytical function to create an empirical model for all the observed CHTs (Figure 5.1; right).

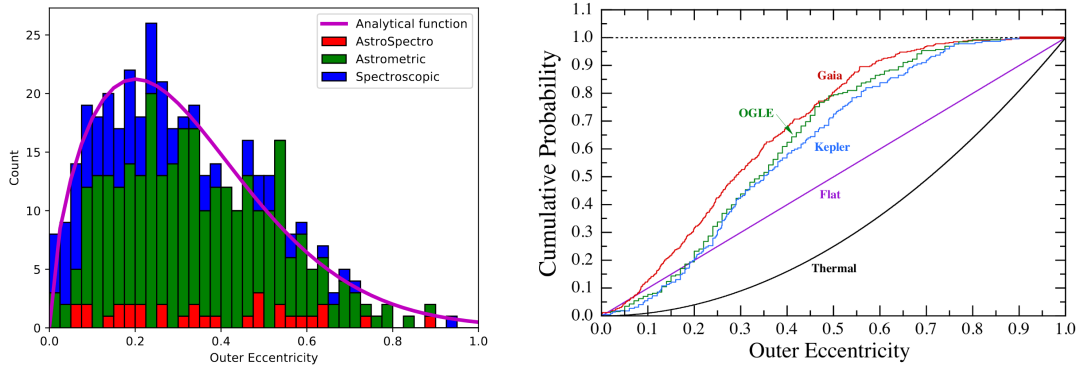


Figure 5.1 Distributions of outer orbital eccentricities. (Left) Differential probability distribution of the outer orbit eccentricities for GAIA hierarchical triple star candidates. Different colours represent different types of Gaia NSS orbital solutions. The magenta line shows the analytical function described in [Czavalinga et al. \(2023\)](#). (Right) Cumulative eccentricity distributions. Green – OGLE; blue – *Kepler*; red – GAIA; purple – $dN/de = \text{constant}$; black – a so-called thermal distribution with $dN/de \propto e$. Figures from [Czavalinga et al. \(2023\)](#).

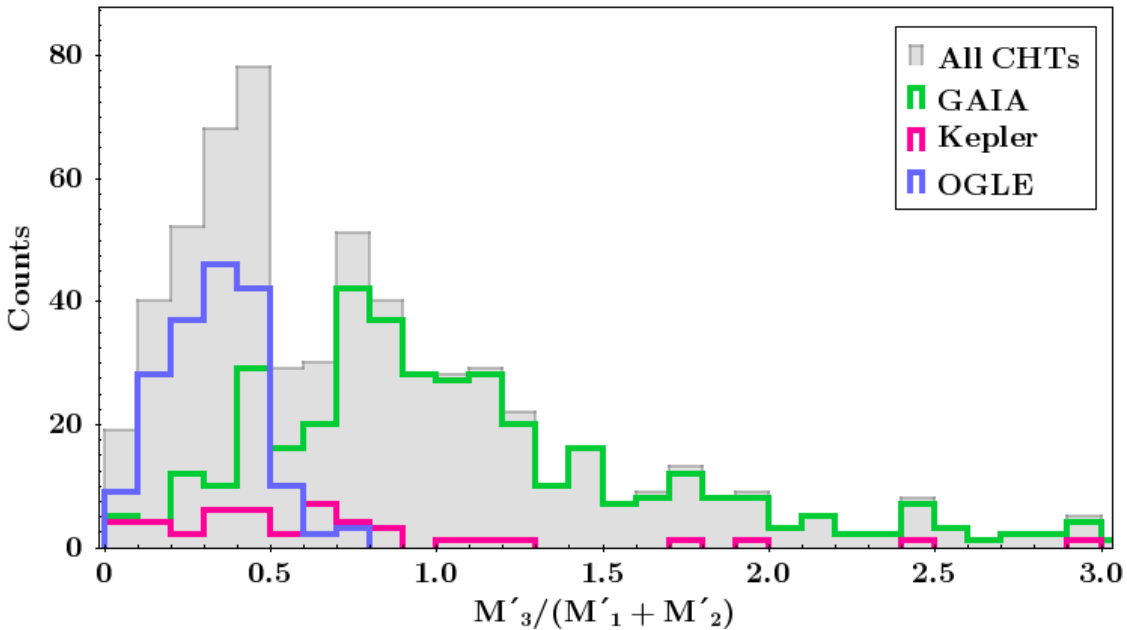


Figure 5.2 Approximate tertiary to binary mass ratio, $M'_3/(M'_1 + M'_2)$, from different CHT searches. GAIA- green, *Kepler* - red, and OGLE - blue. The two prominent peaks are approximately around 0.4 and 0.9.

While these searches did not provide dynamical masses for all the systems, we can generate *ad hoc* masses to probe the mass-ratio distribution of these systems. Using Kepler's laws (see [Appendix B](#)), and approximating the inner binary to be $2 M_{\odot}$, we calculate the approximate tertiary to inner binary mass ratio ($M'_3/(M'_1 + M'_2)$). The distribution of this mass ratio reveals two peaks approximately around 0.4-0.5 and 0.8-0.9 ([Figure 5.2](#)). For reference, $M'_3/(M'_1 + M'_2)$ of 0.5 represents a scenario where all three stars are of the same mass. While 1.0 represents a scenario where the tertiary is of the same mass as the whole binary, and therefore more massive than the individual stars. If we look closer at the distribution, the 0.4 peak belongs to the OGLE CHTs, while the GAIA CHTs favour the 0.9 peak. The *Kepler* CHTs are spread roughly homogeneous, although their number is relatively low. Interestingly, the binaries in OGLE were mostly contact binaries and the tertiaries in GAIA were comparatively brighter in flux.

This brings forward a lot of questions. Are all these trends due to a different formation scenario? Is there less of a BD desert analogue around contact binaries? Is the eccentricity distribution an artefact of star formation or due to orbital resonance?

Surely, there is a need for a more detailed study of these to probe some of these questions. A detailed study where we look at precise masses, orbital configuration, composition, and age of the system.

5.2. Spectroscopy of Eclipsing Compact Hierarchical Triples

With a motivation to increase the number of detailed CHT parameters, and use them to see the multi-parameter dependency of the above distributions, we try to solve more CHT with spectroscopic observations coupled to the already available *TESS* photometry. The next paper, which has been submitted to *Astronomy and Astrophysics*, explores these avenues. In the paper we discover three new CHTs and provide their spectroscopic and photometric analysis. We present the first spectroscopic analysis of a previously identified CHT. We also present new distributions of precise CHT metallicity and age estimates.

Spectroscopy of Eclipsing Compact Hierarchical Triples

I. Low-mass double-lined and triple-lined systems

Ayush Moharana¹, K. G. Hełminiak¹, F. Marcadon², T. Pawar¹, G. Pawar¹, M. Konacki^{1,3}, A. Jordán^{4,5,6},
R. Brahm^{4,5,6}, and N. Espinoza⁷

¹ Nicolaus Copernicus Astronomical Center, Polish Academy of Sciences, ul. Rabiańska 8, 87-100 Toruń, Poland

² Villanova University, Dept. of Astrophysics and Planetary Sciences, 800 East Lancaster Avenue, Villanova, PA 19085, USA

³ Nicolaus Copernicus Astronomical Center, Polish Academy of Sciences, ul. Bartycka 18, 00-716 Warszawa, Poland

⁴ Facultad de Ingeniería y Ciencias, Universidad Adolfo Ibáñez, Av. Diagonal las Torres 2640, Peñalolén, Santiago, Chile

⁵ Millennium Institute for Astrophysics, Monseñor Nuncio Sótero Sanz 100, Of. 104, Providencia, Santiago, Chile

⁶ Data Observatory Foundation, Eliodoro Yáñez 2990, Providencia, Santiago, Chile

⁷ Space Telescope Science Institute, 3700 San Martin Dr., Baltimore 21218, MD, USA

Received May 10, 2024

ABSTRACT

Context. Eclipsing Compact Hierarchical Triples (ECHT) are systems with the tertiary star orbiting an eclipsing binary (EB) in an orbit of fewer than 1000 days. In a CHT, all three stars exist in a space less than 5 AU in separation. A low-mass CHT is an interesting case to understand multiple star and planet formation at such small scales.

Aims. In this study of, we combine spectroscopy and photometry to estimate the orbital, stellar and atmospheric parameters of stars in a sample of CHTs. Using the complete set of parameters we aim to constrain the metallicity and age of the systems.

Methods. We use time-series spectroscopy to obtain radial velocities (RV) and disentangled spectra. Using RV modelling, EB light curve modelling, and spectral analysis, we estimated the metallicities and temperatures. Using isochrone fitting, we constrain the ages of the system. We then combine observations of masses, outer eccentricity (e_2), orbital periods and age estimates of the systems from the literature. We compare the distributions of e_2 , and tertiary mass ratio ($q_3 = M_3/(M_1 + M_2)$) for three different metallicity ranges and for old and young systems.

Results. We estimate masses, radii, temperatures, metallicity and age of a total of 12 stars in 4 CHTs. The CHT, CD-32 6459 shows signs of von Zeipel-Lidov-Kozai oscillations while CD-62 1257 can evolve to form a triple common envelope. The rest of the CHTs are old and have an M-dwarf tertiary.

We find that the q_3 distribution for CHTs with sub-solar metallicity has a uniform distribution but the systems with solar and above-solar metallicity peak between 0.5 and 1. When dividing them according to their ages, we found the q_3 of old systems around 0.5. e_2 favours a value around 0.3 irrespective of metallicity or age. The distributions are biased by the lack of observations and observing methods and therefore call for more observations of low-mass CHTs.

Key words. binaries: eclipsing – binaries: spectroscopic – stars: fundamental parameters – stars: evolution – stars: formation – stars: individual: CD-32 6459; CD-62 1257; CD-58 963; BD+11 359

1. Introduction

Stellar multiplicity is a well-established phenomenon (Duchêne & Kraus 2013). While thousands of binaries and multiples were observed (Herschel et al. 1874) in the 19th century, Harrington (1972) was one of the first to use the observations to understand multiple stars as a separate population. Later in time, with better samples and improved theories, we started having a better understanding of triple (and multiple) stars around the new millennium (Eggleton & Kiseleva 1995; Mardling & Aarseth 2001).

The previous and present decade saw a revolution in observing and understanding multiple stars. While it was the radial velocity surveys (Tokovinin 2004) that helped us identify different hierarchies of multiple-star systems, most of the new detections have been from photometric surveys like Optical Gravitational Lensing Experiment (OGLE; Udalski et al. 1992), and the All Sky Automated Survey (ASAS; Pojmanski 1997). Recently, space-based surveys like *Kepler* (Borucki et al. 2010) and the Transiting Exoplanet Survey Satellite (*TESS*; Ricker et al. 2015)

have been revolutionary in detecting and characterising binaries, triples and multiple stars.

Triples, especially, have a renewed interest recently. They are emerging as possible explanations for several problems in stellar astrophysics. This includes triple dynamics as an explanation for asymmetry of planetary nebula (Jones et al. 2019) formation of Thorne-Zytków objects (Eisner et al. 2022), blue-stragglers (Perets & Fabrycky 2009), recurrent novae (Knigge et al. 2022) and Type Ia supernovae (Naoz & Fabrycky 2014).

A special class of triple stars, i.e., compact hierarchical triples (CHTs) have seen increased incidence rates which is surprising as they were considered rare before (Tokovinin 2004). CHT are hierarchical systems where the tertiary orbits an inner binary with an orbital period of less than 1000 days (Borkovits 2022). This, in principle, can cause dynamic changes in these systems which can be characterised by a few years of observation. If we have an eclipsing binary as the inner binary, we can extract the parameters of each component in the system. This has led to eclipse timing programs helping us find hundreds of

new CHT from different eclipsing binaries catalogues (Borkovits et al. 2016; Hajdu et al. 2019; Mitnyan et al. 2024).

Estimate of precise stellar and orbital parameters of CHT opens up an avenue to study stellar evolution coupled with dynamical evolution. Further, using the distribution of orbital parameters and masses, we can understand star formation at scales where, usually, planet formation occurs (≤ 5 AU). While triply eclipsing systems (E3CHT) can provide ultra-precise mass and radius measurements (Borkovits et al. 2019), using time-series spectroscopy of doubly eclipsing systems (E2CHT) can also help us fill the same parameter space (Moharana et al. 2023).

In this paper, we present the total parameters of 4 E2CHTs using *TESS* photometry and high-resolution spectroscopy. Two of these systems, CD-58 963 (hereby CD58) and BD+11 359 (hereby BD11) are spectroscopic double-lined systems (ST2) while CD-62 1257 (hereafter CD62) and CD-32 6459 (hereby CD32) are triple-lined (ST3) systems. Three of these systems (CD32, CD62, and BD11) are newly identified CHTs.

CD32 was first classified as an eccentric EB by (Shivvers et al. 2014) using observations from the All Sky Automated Survey (ASAS; Pojmanski 2002). (Kim et al. 2018) was the first to observe the variation of eclipse times in the system, but they did not find any LTTE signatures. While these works provide accurate estimates of period and eccentricity, we provide the first measurements of stellar parameters of the eclipsing binary stars and the tertiary companion. Though CD32 is not a CHT by the strictest of definitions (outer period \sim 1300d), we try to see if they are any different.

CD62 was first flagged as an EB in the first *TESS* EB catalogue (Prša et al. 2022). The first LC analysis was done by Ulař & Ayan (2023), but with the assumption that the system is a binary. This affected the estimated parameters as the tertiary in the system contributes a significant amount of third-light (\sim 50%), which was assumed to be zero in their analysis.

CD58 was first identified as a multiple system with EB by Borkovits et al. (2020). It was one of the first CHTs discovered with *TESS*, as it is in the Continuous Viewing Zone (CVZ) and has been observed since the first year of *TESS*. With eclipse timing from Wide-Angle Search for Planets (WASP; Pollacco et al. 2006), Borkovits et al. (2020) showed that CD58 is a hierarchical quadruple on a wide 2661 d orbit around the CHT. We do not find any signs of the quadruple but the point to note is that we do not have good coverage over the quadruple period. CD58 is the tightest CHT in this sample, with an outer-orbit period of 76.32 d. Such systems are considered very rare, as it is difficult to survive the migration evolution from early formation (Tokovinin & Moe 2020).

BD11 was identified as an EB in the ASAS survey and its first spectroscopic and LC solution was given by Helminiak et al. (2009). Later, Kozłowski et al. (2014) used it as a test object for their BACHES spectrograph and also presented an initial orbital solution. None of those works notes BD11 as a triple.

2. Observations

2.1. Photometry

All of the targets were observed by *TESS*¹ for at least two sectors. For our work, we choose the best sectors considering (i) Minimal cadence (ii) Low stellar activity/ out-of-eclipse variations (iii) long-term coverage to detect eclipse depth

¹ Through Guest Investigator (GI) programs G011083, G04047, G05078 (PI: Helminiak), and G05003 (PI: Prša). CD58 was also included in the *TESS* Core Target Sample (CTL) during Cycle 1.

variations (if any). We extract light curves (LC) using the LIGHTKURVE² package. We extracted the photometry using the standard pipeline aperture.

While CD32 (TIC 24972851) and CD58 (TIC 220397947) are well isolated in the *TESS* frames, CD62 (TIC 387107961) and BD11 (TIC 408834852) have close-by stars. We checked for any contaminant signature (e.g., pulsations, eclipses, transits) but did not find any, and therefore used the pipeline photometry.

The detrending was done with WOTAN³ (Hippke et al. 2019). We used the bi-weight de-trending method in a window 0.5–3 times the orbital period (depending on the trends). The normalised output from WOTAN was then converted to the magnitude scale by using zero-points which adjusted the out of eclipse magnitude to the *TESS* magnitude registered in the *TESS* catalogue.

2.2. Spectroscopy

The spectroscopy was obtained from a set of high-resolution spectrographs which includes a Fibre-fed Extended Range Optical Spectrograph (FEROS; R \sim 48,000) at the MPG/ESO 2.2m telescope in La Silla (Kaufer et al. 1999), CHIRON (R \sim 28,000 in the fiber mode) at CTIO 1.5m telescope in Cerro Tololo (Tokovinin et al. 2013), CORALIE (R \sim 70,000) at the 1.2m Euler telescope in La Silla (Queloz et al. 2000), High-Resolution Spectrograph (HRS; R \sim 67,000) at 9.2m SALT in Sutherland (Crause et al. 2014), and the High Accuracy Radial velocity Planet Searcher (HARPS; R \sim 115,000) at the ESO 3.6m telescope in La Silla (Mayor et al. 2003). Additionally, for BD11 we also used RV measurements from Helminiak et al. (2009), which were based on data obtained with the University College London Echelle Spectrograph (UCLES) at the 3.9m AAT in Siding Spring Observatory. We did not use BACHES data from Kozłowski et al. (2014), as they are of significantly lower quality.

The CORALIE and FEROS spectrographs both work in a simultaneous object-calibration manner. Spectra were reduced with the dedicated python-based pipeline (Jordán et al. 2014; Brahm et al. 2017), optimised to derive high-precision radial velocities, which also performs barycentric corrections. The pipeline reduces CORALIE spectra to 70 rows spanning from 3840 to 6900 Å, out of which we use only 45 rows (4400–6500 Å), to avoid the broad H α line and the blue part with a very low signal. For FEROS the output is reduced to 21 rows covering 4115–6519 Å, of which we use 20 (4135–6500 Å).

The CHIRON spectra were reduced with the pipeline developed at Yale University (Tokovinin et al. 2013). Wavelength calibration is based on ThAr lamp exposures taken just before the science observation. Barycentric corrections are not applied by the pipeline, thus we were calculating them ourselves under IRAF⁴ with *bvcor* task.

The HRS spectra were obtained by the long-term programme 2021–2-MLT-006 which focused on spectroscopic monitoring of CHTs. They were made available after reduction with the MIDAS HRS pipeline (Kniazev et al. 2016, 2017). While the products included spectra in the blue arm (370–550 nm) and the red arm (550–890 nm), we used the blue arm to avoid contamination by the static telluric lines. The barycentric correction has also been done with the *bvcor*.

² <https://docs.lightkurve.org/>

³ <https://github.com/hippke/wotan>

⁴ IRAF is distributed by the National Optical Astronomy Observatory (NOAO), which is operated by the Association of Universities for Research in Astronomy (AURA) under cooperative agreement with the National Science Foundation. <http://iraf.noao.edu/>

Table 1. All the spectroscopic observations used for radial velocity extraction. A subsample of these observations is used for further analysis (see Sec.3.4).

Targets	CD32	CD62	CD58	BD11
FEROS	4	8	-	11
CHIRON	15	12	-	-
CORALIE	1	6	-	5
HRS	4	8	13	-
HARPS	-	-	-	2
UCLES	-	-	-	5 ^a
Total	24	34	13	23

^a From [Helminiak et al. \(2009\)](#)

The HARPS data were reduced on-site, including wavelength calibration and barycentric correction, with the ESO's Data Reduction System (DRS). They are available through the ESO Archive.

3. Analysis

3.1. RV extraction and fitting

The RVs were calculated with a TODCOR method ([Zucker & Mazeh 1994](#)) with synthetic spectra computed with ATLAS9 code as templates. Measurement errors were calculated with a bootstrap approach, and used for weighting the measurements during the orbital fit, as they are sensitive to the signal-to-noise ratio (SNR) of the spectra and rotational broadening of the lines. Though this code is optimised for double-lined spectroscopic binaries and provides velocities for two stars (u_1, u_2), it can still be used for triple-lined systems (ST3) as well. In an ST3, the tertiary's velocities were found from a local maximum, where u_1 was set for the tertiary, and u_2 for the brighter component of the eclipsing pair.

The orbital solutions were found using our procedure called v2FIT ([Konacki et al. 2010](#)). It applies a Levenberg-Marquardt minimisation scheme to find orbital parameters of a double-Keplerian orbit, which can optionally be perturbed by several effects, like a circumbinary body. We fit for binary period (P_A), time of periastron passage of the inner orbit (T_{pA}), inner eccentricity (e_A), argument of periastron (ω), semi-amplitudes of the eclipsing binary (K_{Aa}, K_{Ab}), projection of the semi-major axis ($a_A \sin i_1$), and gamma velocity (γ_A). The fitting follows the procedure defined in [Helminiak et al. \(2017\)](#), [Moharana et al. \(2023\)](#), and references therein.

In addition, for each observation where three sets of lines were sufficiently separated, we also calculated the systemic velocities $\gamma(t_i)$ of the inner pair, using the formula:

$$\gamma(t_i) = \frac{v_1(t_i) + qv_2(t_i)}{1 + q}, \quad (1)$$

where $v_{1,2}(t_i)$ are the measured RVs of the inner binary, and q is its mass ratio, found from the RV fit with a circumbinary perturbation. With these values as the centre-of-mass (COM) RVs of the binary, and RVs of the tertiary component, we can treat the long-period outer orbit as a spectroscopic double-lined system, and independently look for its parameters. The final values of P_{AB} , K_{out} , e_{AB} etc., come from such fits. For the triple spectroscopic double-lined systems (ST2), this is the only way of estimating the orbital parameters of the third body and its minimum mass (M_B^{min}).

The results of our orbital RV fits are presented in Table 2. The RV measurements and modelled curves are shown in section 3

and Figure 3 for the ST3 and ST2 cases, respectively. Individual measurements are given in Table A.

3.2. Light curve fitting

We use version 40 of the JKTEBOP code ([Southworth 2013](#)) for our LC modelling. JKTEBOP models a star as a sphere or as a biaxial spheroid and calculates the LC by numerical integration of concentric circles. This allows it to fit only detached eclipsing binaries. With binary periods of more than two days, JKTEBOP is well suited for solving our systems. We model every *TESS* sector separately except for CD58, where we model only half of the LC for a sector. For our modelling process, we first fix certain parameters from RV modelling, and/or from prior knowledge about the type of stars. The fixed parameters are (i) mass-ratio (q), and (ii) limb-darkening coefficients. We take initial values for P_A from the RV solution but vary them during our modelling. We also take a visual estimate of the time of super-conjunction (T_0^A) and optimise it later. We optimise the following light curve parameters: (i) P_A , (ii) T_0^A , (iii) scale-factor (Sf; determines the scaling or the magnitude of out of eclipse portion), (iv) surface brightness ratio (J), (v) third-light (L_3), (vi) e_A and ω in the form of $e \sin \omega$ and $e \cos \omega$, (vii) inclination of inner binary (i_A), (viii) radius ratio (k), and (ix) sum of fractional radii ($r_1 + r_2$) where the fractional radii are represented as radius divided by the semi-major axis (a_A). The optimisation is iterated until we get the best fit. To test the convergence, we randomly fix certain parameters and optimise the others to check the stability. We then estimate the errors on the parameters by using the Monte Carlo (MC) module available on JKTEBOP. We followed this exact prescription for all the targets except CD58. CD58 has shallow eclipses (the primary eclipse has a depth of ~ 0.04 mag) and shows stellar activity which varies with every sector. On top of that, the tertiary orbital period is 77 d. This causes eclipse timing variations that affect radii measurement in one *TESS* sector and that is why we use half a sector for our modelling. To get a consistent solution over sectors, we first fix the third light to zero. JKTEBOP allows to set light ratio from spectroscopy as a constraint. So we constrain the optimisation by fixing the light ratio of the components as the values obtained from broadening function (BF) fitting (see Sec.3.4.1). The rest of the optimisation process is the same as before. The MC for CD58 is initiated with the final optimised parameters but without the constraints from the light ratio. The final fits to the LC are shown in Figure 3. The final results for all the targets for all the modelled sectors are given in Appendix B. We adopt the final estimates of all the parameters as the average of all the sectors.

3.3. Estimate of orbital configuration

Combining both the LC and RV analyses, we can get a picture of the orbital architecture of the systems, except the estimate of the mutual inclination (i_{mut}). This is possible for both ST2 and ST3 systems if we observe dynamical effects in eclipse timing variations. For ST3 systems specifically, we can estimate the i_{mut} using inclinations of the binary (i_A) and tertiary (i_{AB}) orbits. Using equations described in [Moharana et al. \(2023\)](#), we get two different set of limits for the i_{mut} .

Using the estimated value of i_{mut} for ST3 systems, and an arbitrary value for ST2 systems, we can simulate the orbits using numerical integration using REBOUND⁵ ([Rein & Liu 2012](#)) to get

⁵ <https://github.com/hannorein/rebound>

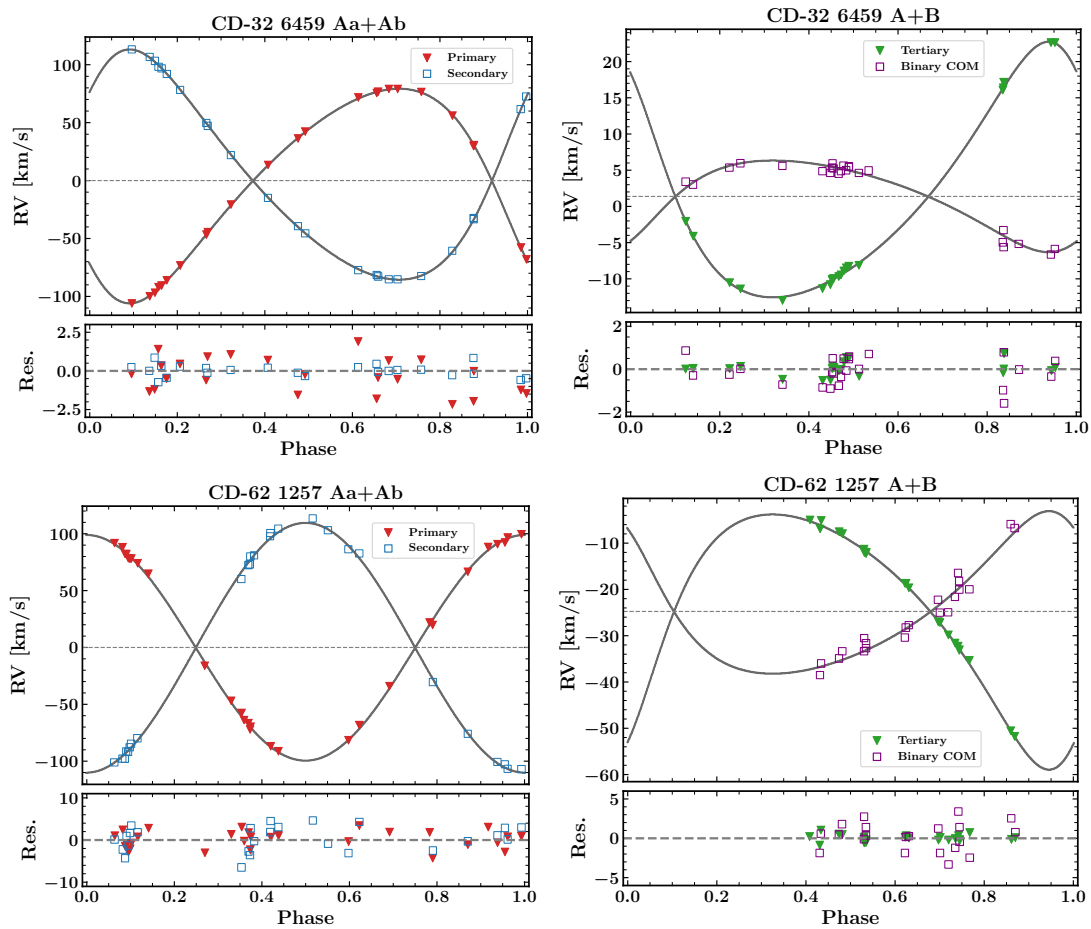


Fig. 1. Radial velocities and orbital solutions of the ST3 systems CD32 (top) and CD62 (bottom). The left panels present the inner binary Aa+Ab corrected for its COM. Primary components are marked with red triangles and the secondary with blue squares. The right panels present the outer orbit, with the inner binary’s COM (calculated with Eq. 3.1) with purple squares, and the tertiary’s RVs with green triangles. The dashed line marks the γ velocity of the whole system.

the architecture of the systems. The configuration of the orbits in the XZ plane (axis Z is towards the observer) is shown in Figure 4.

3.4. Spectroscopic analysis

For our spectroscopic analysis, we need a set of homogeneous spectroscopic data, i.e. from a single instrument. We selected a set of time-series spectroscopy for each target with clean line profiles and good SNR. This resulted in a set of 9 CHIRON spectra for CD32, 7 HRS spectra for CD62, 13 HRS spectra for CD58, and 8 FEROS spectra for BD11. All further analyses are done on these sets of spectra.

3.4.1. Broadening functions

We use broadening functions (BF; Rucinski 1999) to (i) estimate light-fractions (LF_{obs}^x), and (ii) estimate projection of rotational velocity ($v_x \sin i$) of component x . The BF is generated with a variation of the BF code, BF-RVLOTTER⁶. Clean (where we can

⁶ <https://github.com/mrawls/BF-rvplotter>

clearly see all spectral components) BF were modelled with the rotational profile from Gray (2005),

$$G(v) = A \left[c_1 \sqrt{1 - \left(\frac{v}{v_{\text{max}}} \right)^2} + c_2 \left(1 - \left(\frac{v}{v_{\text{max}}} \right)^2 \right) \right] + lv + k \quad (2)$$

where A is the area under the profile and v_{max} is the maximum velocity shift that occurs at the equator. c_1 and c_2 are constants that are a function of limb darkening themselves while l and k are correction factors to the BF “continuum”. The final LF_{obs}^x and $v_x \sin i$ is taken as the average of all the epochs of spectra, with respective standard deviations as errors. These values are presented in the lower panel of Table 3.

3.4.2. Spectral disentangling

We separate the individual spectra from the composite spectra using the method of spectral disentangling with the shift-and-add algorithm (González & Levato 2006) implemented in the

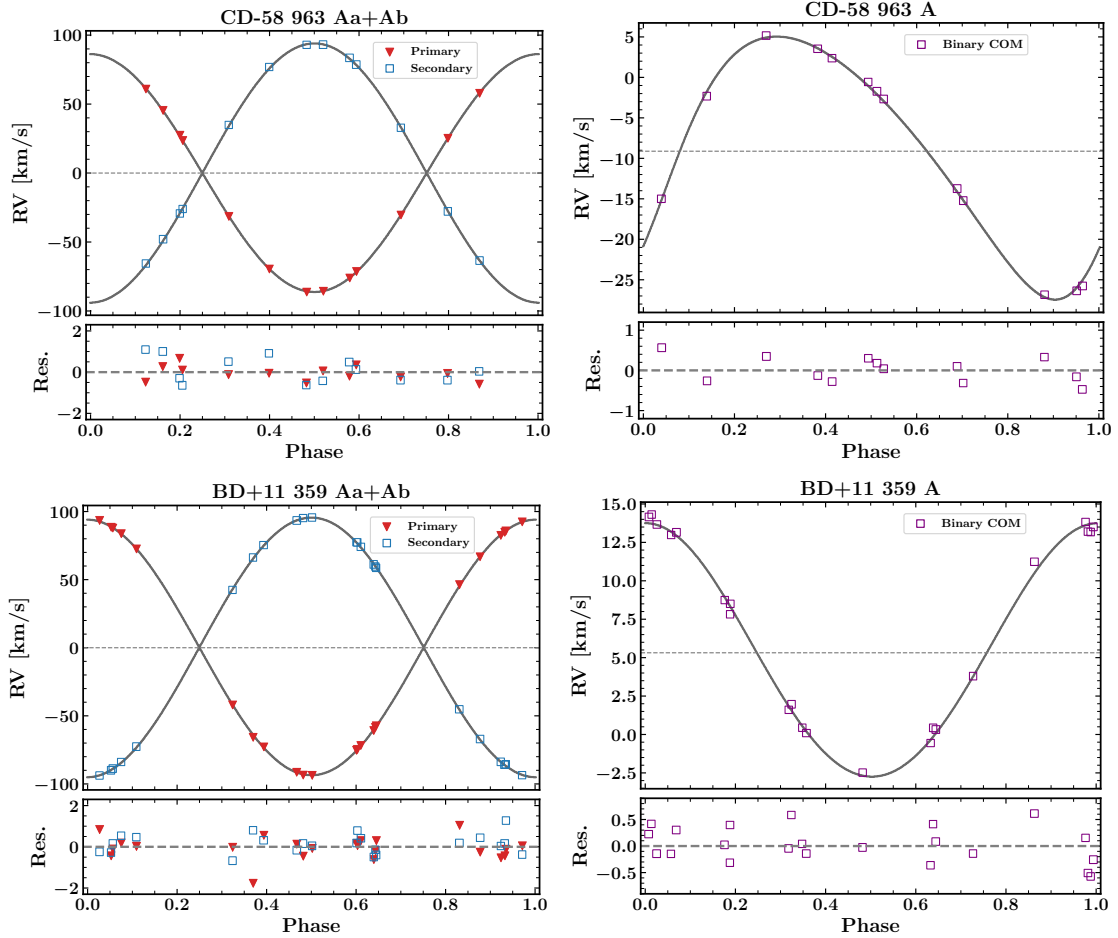


Fig. 2. Same as Fig. 3 but for ST2 systems CD58 (top) and BD11 (bottom). Since there are no RVs of the tertiary, the right panels show only the binary’s COM.

code `DISENTANGLING_SHIFT_AND_ADD`⁷ (DSAA; Shenar et al. 2020, 2022). DSAA disentangles spectra in velocity-space by applying simple velocity shifts corresponding to one component and creating an averaged spectra. This is iterated for every component until the final individual spectra have no contribution from the rest of the components. The code takes in orbital parameters along with a list of times of epoch to disentangle the spectra. We disentangled spectra in the wavelength range of 4870 Å to 5300 Å. This region was selected to avoid wide lines and due to the availability of sufficient narrow lines for spectral analysis. We initially assumed equal light fractions for the component. The final disentangled spectra were accepted after using DSAA for 30,000 iterations. In addition to the convergence checks built into the code, we also calculate cross-correlation plots on the final output to check for any contaminant lines in the spectra due to the disentangling process. The disentangled spectra had trends in the continuum which were a result of bias in normalisation, light-fraction variation etc. (Hensberge et al. 2008). The amplitude of these trends varies depending on the number, the extent of convolution of line profiles and the wavelength range

⁷ https://github.com/TomerShenar/Disentangling_Shift_And_Add

of the spectra used for disentangling. Further, it depended on the spectrograph, which we attribute to either the stability of the spectrograph or the accuracy of the spectral reduction method. To address the first source of bias, we selected the best spectra by preliminary trials with wavelength range and set of spectra. Further, we cleaned this additive form of bias by modelling this trend and subtracting it from the component spectra following the process in Hensberge et al. (2008). We then scale the spectra for a component x to the observed values (from BF) of light-fraction, using the formula,

$$f_{\text{new}}^x = (f_{\text{ini}}^x - 1) \times (LF_{\text{ini}}^x / LF_{\text{obs}}^x) + 1 \quad (3)$$

3.4.3. Synthetic spectral fitting

For the measurement of effective temperature (T_{eff}), metallicity ($[M/H]$) and log of surface gravity ($\log g$), we used `ISPEC` (Blanco-Cuaresma et al. 2014; Blanco-Cuaresma 2019) on the disentangled spectra. All the disentangled spectra were checked for any RV offset caused by the disentangling method. We do not normalise the spectra further, as the `SPD` and the bias-cleaning already give us normalised spectra. We obtain the atmospheric parameters using the synthetic spectral fitting (SSF) technique. SSF

Table 2. Orbital parameters of the binary and tertiary orbit obtained by RV modelling using v2FIT. For ST2 systems we only present parameters from orbital fitting of the centre-of-mass RV of the inner-binary.

Parameters	CD32	CD62	CD58	BD11
Binary orbit				
P_A [d]	4.0217043(20)	2.7147422 ^a	3.5519749(47)	3.6049188(63)
T_{pA} [BJD - 2450000]	5917.6859(40)	6952.0938(13)	8385.0959(3920)	2448.3527(64)
e_A	0.2276(12)	0 ^a	0.00028(22)	0 ^a
ω_A [deg]	128.45(30)	0 ^a	161.46(39.41)	0 ^a
K_{Aa} [km/s]	92.27(26)	98.75(36)	86.11(31)	94.90(14)
K_{Ab} [km/s]	98.97(13)	109.29(41)	93.86(38)	93.43(12)
$a_A \sin i_1$ [R_\odot]	14.807(23)	11.166(30)	12.639(34)	13.423(13)
γ_A [km/s]	1.58(20)	-23.35(36)	-9.12(13)	5.31(10)
Tertiary orbit				
P_{AB} [d]	1372.1218 ^a	441.615(110)	76.319(169)	168.581(305)
T_{pAB} [BJD - 2450000]	5237.44(6.4)	5866.33(2.79)	5414.62(10.05)	5340.47(15.05)
e_{AB}	0.2688(50)	0.2997(144)	0.2148(96)	0.0250(209)
ω_{AB} [deg]	38.89(1.67)	217.57(1.91)	232.97(3.06)	359.22(36.28)
K_A [km/s]	6.28(18)	17.48(96)	16.20(18)	8.20(15)
K_B [km/s]	17.65(08)	27.47(64)	-	-
$a_{AB} \sin i_2$ [R_\odot]	625.44(6.610)	374.49(10.13)	-	-
γ_{AB} [km/s]	1.45(7)	-24.76(23)	-	-
Mass estimates				
$M_{Aa} \sin^3 i_1$ [M_\odot]	1.3928(6)	1.3305(11)	1.1190(100)	1.2377(36)
$M_{Ab} \sin^3 i_1$ [M_\odot]	1.2986(8)	1.2023(9)	1.0266(84)	1.2573 (40)
$M_A \sin^3 i_2$ [M_\odot]	1.2846(247)	2.2058(1511)	-	-
$M_B \sin^3 i_2$ [M_\odot]	0.4576(201)	1.4045(1437)	-	-

^a Fixed during optimisation.

technique generates synthetic spectra on the go and then does a χ^2 optimisation at selected spectral lines. This method is better compared to a simple grid fitting (Blanco-Cuaresma 2019). We implement different fitting procedures for the eclipsing stars and the tertiary respectively. For the eclipsing stars, we fix the $\log g$ estimated from LC and RV modelling using,

$$\log(g) = \log\left(\frac{A_c^2 M}{R^2}\right), \quad (4)$$

where M is the mass (in M_\odot), R is the radius (in R_\odot) calculated from LC and RV modelling, and $A_c \equiv \sqrt{GM_\odot/R_\odot}$ ($= 168.589888477$) is a constant necessary for transformation to solar units. The resolution of FEROS and HRS was high enough to give us precise projected rotational velocity ($v \sin i$) from SSF, but for CHIRON we fixed it to the value obtained with BF. The setup for synthetic spectra generation includes model atmospheres from MARCS⁸ (Gustafsson et al. 2008), solar abundances from Asplund et al. (2009) and the radiative transfer code SPECTRUM⁹. We calculate the parameters using two different line lists. We first fit for T_{eff} , $[M/H]$, α and $v \sin i$ using line-list LL1, which is prescribed for abundance measurement. We adopt the $[M/H]$ and α from this run and then fit for T_{eff} , and $v \sin i$ using line-list LL2, which is prescribed for parameter estimate. For the eclipsing systems, we kept the $\log g$ fixed as the values (Table 5 and Table 4) that we obtain from LC and RV modelling as the spectroscopic $\log g$ matched well but had lower precision. We kept the $\log g$ free for the tertiary spectra. The final spectroscopic estimates for all the systems are given in Table 3.

⁸ <https://marcs.astro.uu.se/>⁹ <https://www.appstate.edu/~grayro/spectrum/spectrum.html>**Table 3.** Atmospheric parameters obtained from our spectroscopic analysis using iSpec on the disentangled spectra. The lower section of the table shows estimates of $v \sin i$ and LF obtained from BF fitting.

Parameters	CD32	CD62	CD58	BD11
Synthetic spectral fitting				
$T_{\text{eff,Aa}}$	6674(248)	6729(263)	6478(171)	6342(181)
$T_{\text{eff,Ab}}$	6295(244)	6525(262)	63712 (177)	6553(178)
$T_{\text{eff,B}}$	6344(412)	6623(143)	-	-
$\log g_{Aa}$	4.21 ^a	4.17 ^a	4.25 ^a	4.14 ^a
$\log g_{Ab}$	4.25 ^a	4.23 ^a	4.35 ^a	4.17 ^a
$\log g_B$	3.8(5)	4.1(1)	-	-
$[M/H]_{Aa}$	-0.24(5)	0.31(7)	-0.34(6)	-0.07(2)
$[M/H]_{Ab}$	-0.26(1)	0.37(9)	-0.28(4)	-0.16(1)
$[M/H]_B$	0.66(3)	0.13(7)	-	-
α_{Aa}	0.12(6)	-0.00(8)	0.05(6)	-0.13(3)
α_{Ab}	-0.28(1)	-0.05(9)	0.08(4)	0.08(2)
α_B	0 ^a	-0.00(5)	-	-
$v_{\text{mic,Aa}}$	1.5(3)	1.5(3)	1.7(3)	2.1(1)
$v_{\text{mic,Ab}}$	0.1(1)	0.0	1.4(2)	2.6(1)
$v_{\text{mic,B}}$	1.49 ^b	2.4(2)	-	-
$v_{\text{mac,Aa}}$	11.06 ^b	11.05 ^b	9.25 ^b	7.8 ^b
$v_{\text{mac,Ab}}$	7.59 ^b	8.88 ^b	9.32 ^b	9.76 ^b
$v_{\text{mac,B}}$	8.25 ^b	15.38 ^b	-	-
$v_{Aa} \sin i_A$	0 ^a	30(2)	20(1)	23.90(39)
$v_{Ab} \sin i_A$	0 ^a	31(2)	18(1)	21.54(43)
$v_B \sin i_{AB}$	0 ^a	18(1)	-	-
Broadening functions				
$v_{Aa} \sin i_A$	15(2)	33(3)	23(3)	27.06(51)
$v_{Ab} \sin i_A$	11(3)	27(2)	19(3)	25.99(40)
$v_B \sin i_{AB}$	4(4)	25.5(5)	-	-
LF_{obs}^{Aa}	0.526(3)	0.28(1)	0.60(2)	0.526(2)
LF_{obs}^{Ab}	0.375(5)	0.16(2)	0.40(2)	0.474(2)
LF_{obs}^B	0.099(4)	0.56(2)	-	-

^a Fixed during optimisation. ^b Obtained from empirical tables.

Ayush Moharana et al.: Spectroscopy of Eclipsing Compact Hierarchical Triples

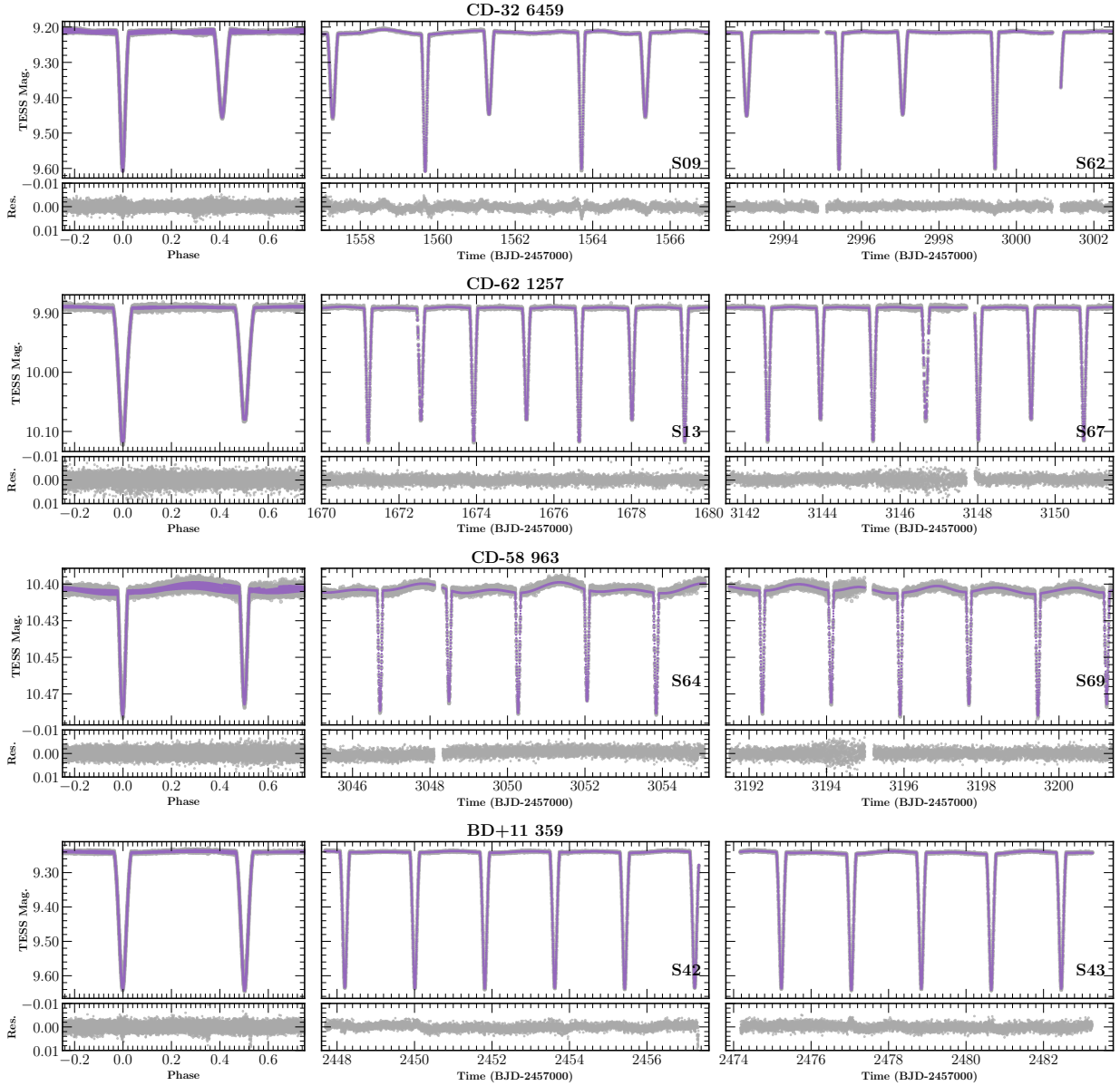


Fig. 3. JKTEBOP models (purple lines) for 2 sectors (first and the last used in our modelling) of *TESS* observations (centre and last panel). The variable stellar activity can be seen in the sector-wise observations and models. The eccentric and near-circular systems can be distinguished from the phased LC observations and models (first panel.)

3.5. Isochrone fitting

Most CHTs with detailed analysis have been found to have co-evolving stars. This implies that we can use a single isochrone to explain the masses, radii and temperatures of all stars. While there have been cases where non-coeval stars seem to exist in a CHT (Marcadon et al. 2020; David et al. 2019), we use this assumption as a check and estimate of the ages of the system as a whole. We use our own fitting code `ISOFTTER` which searches through the grid of MIST (MESA Isochrones and Stellar Tracks; Choi et al. 2016; Dotter 2016) and finds the best-fit model which explains the masses, radii, metallicity and temperatures of all three stars. There is also a possibility to add *Gaia* distances and

flux ratios as constraints in the minimisation routine. Details of the routine can be found in Moharana et al. (2023). We made two runs for the ST3 systems. In one run, we use the observed constraints from all three stars and in the other, we use only the inner binary (also adding the binary flux ratio as a constraint). The best-fit models tertiary models (in black) and binary models (in purple) are shown in Figure 6 and Figure 7 for CD32 and CD62 respectively. The same routine was used for the ST2s, with parameters of two stars, their flux ratio and *Gaia* distance used as constraints. Assuming co-evolution, we can also estimate the third star radius for a range of tertiary masses. We used this to estimate the radius and temperature of the ST2 tertiaries, assum-

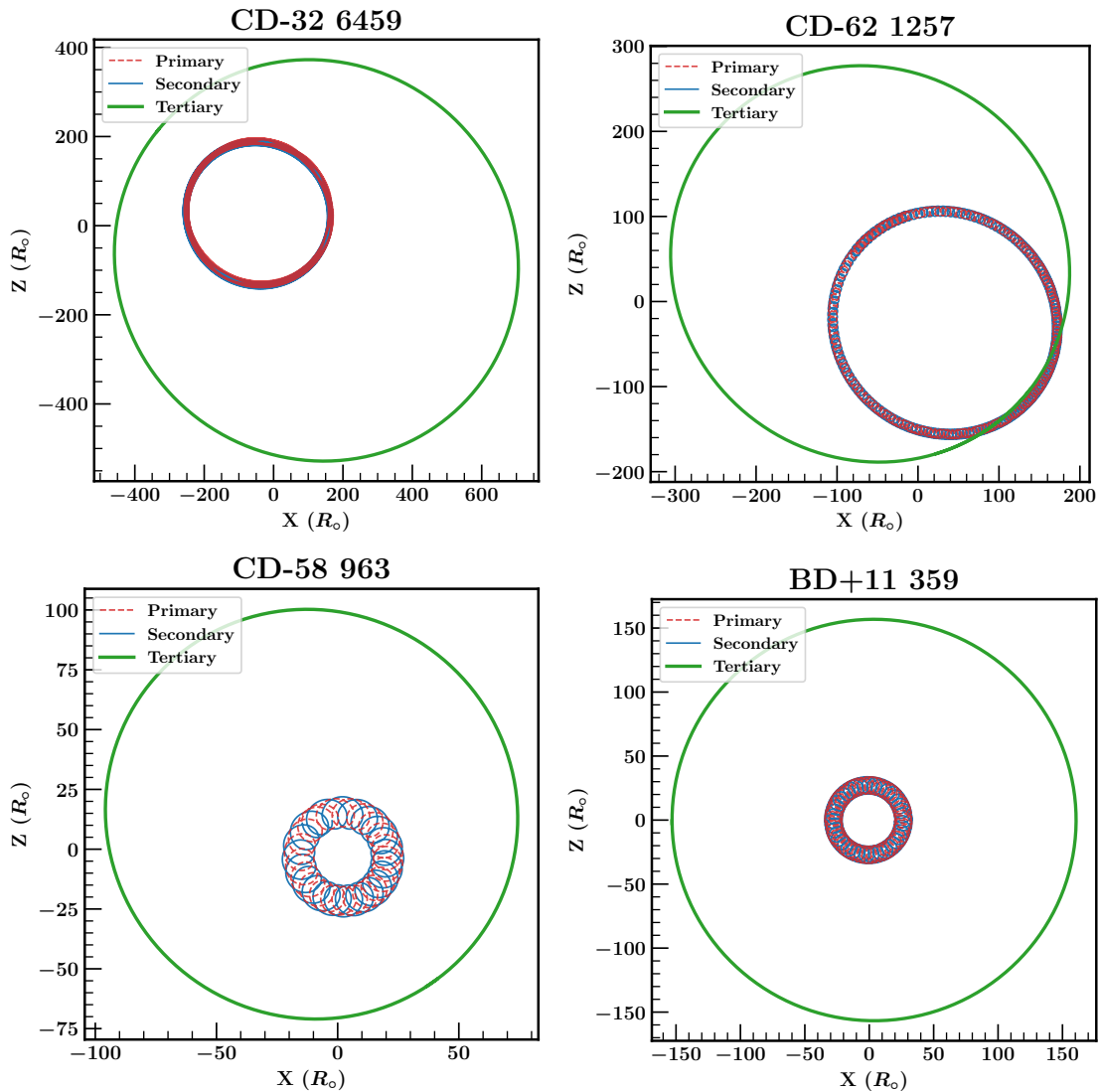


Fig. 4. Orbital configuration of the targets viewed perpendicular to the observers' plane (XY plane). The center-of-mass (COM) of the system is at (0,0).

ing M_3 between the lower limit from RV fits and M_2 . For ST2s we also reject models that predict distance more than 3σ away from the *Gaia* value.

4. Results and discussion

In the following text, we use A-B notation to denote the CHT, where B is the tertiary. A is the eclipsing binary with components Aa and Ab. Aa corresponds to the primary which is the most massive star in the inner binary. We use the short form for a star's name along with the alphabetical notation to exclusively denote each star, e.g., the secondary of CD62 is referred to as CD62Ab.

4.1. CD-32 6459: TIC024972851

CD32 is the widest of all our systems (largest a_{AB}). The inner binary is also the largest of all the four systems (largest a_A). The binary masses are above-solar with the primary and secondary mass of $1.406 M_{\odot}$ and $1.211 M_{\odot}$ respectively. With radii of $1.54 R_{\odot}$ and $1.44 R_{\odot}$ for the CD32Aa and CD32Ab respectively, the stars are in the main-sequence regime. It is the only system with a non-negligible eccentricity of $e_A = 0.221$, but with an inner binary period of around 4 d, the orbit should be circularised after about 500 Myr (according to the formalism of Zahn & Bouchet 1989). The mutual inclination regimes lay in two possible sets of solutions: (i) 34.3° to 136.7° or (ii) 43.3° to 145.7° . These limits are close to the limits for Von Zeipel-Lidov-Kozai (ZLK; von Zeipel 1910; Lidov 1962; Kozai 1962) oscillations, which could possibly be the reason behind the large e_A .

Ayush Moharana et al.: Spectroscopy of Eclipsing Compact Hierarchical Triples

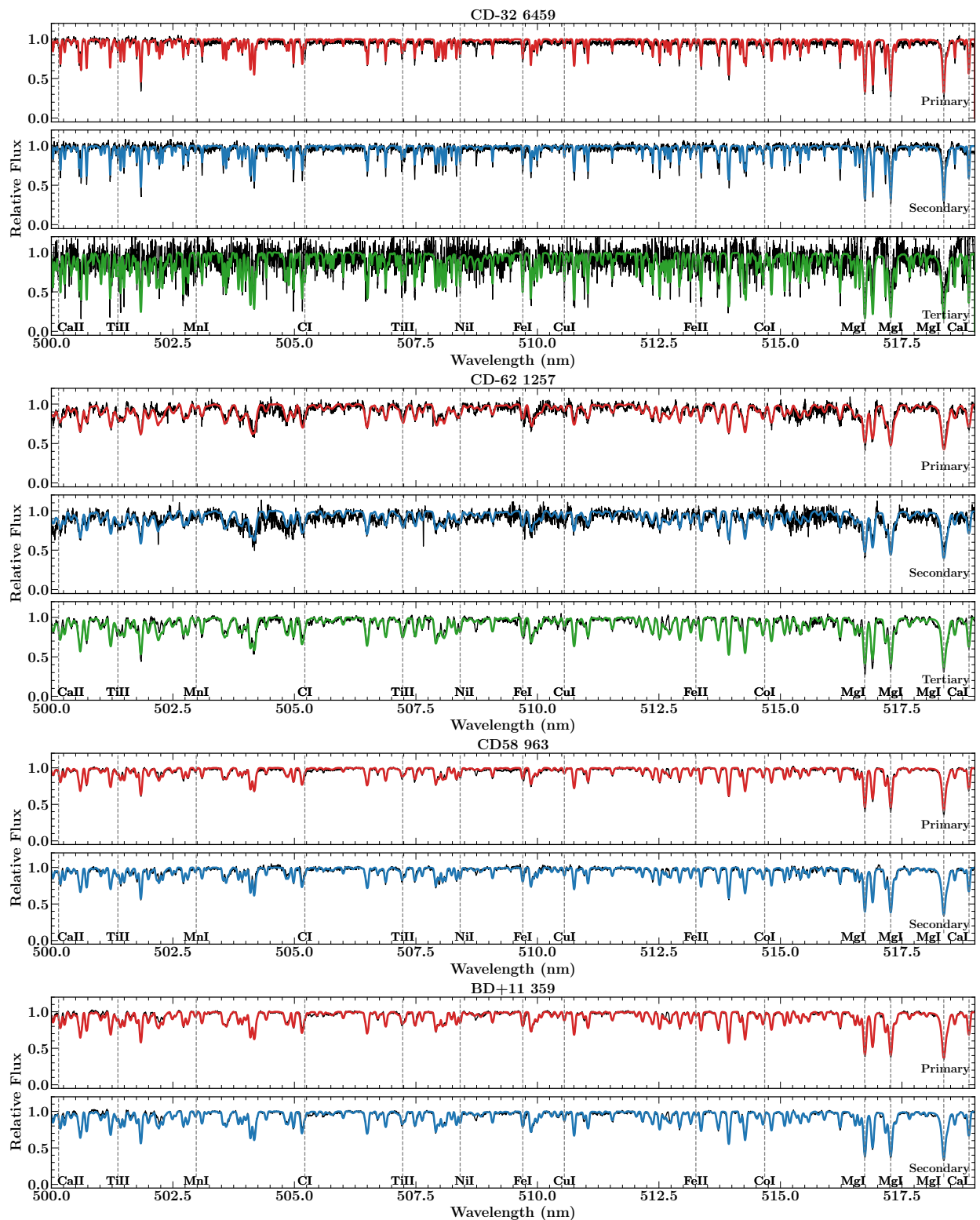


Fig. 5. Synthetic spectroscopic models of primary (red), secondary (blue), and tertiary (green) compared to the disentangled spectra (black) for the different systems. Panels for ST2 systems (CD58 and BD11) show only the primary and secondary spectral models.

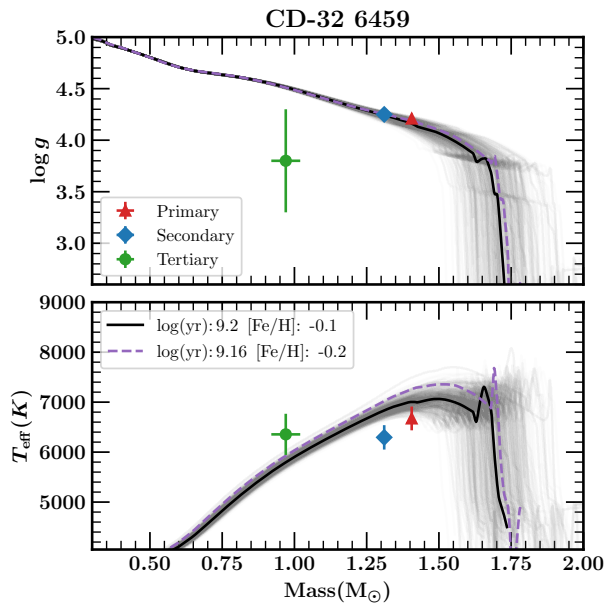


Fig. 6. Results of the isochrone fitting for CD32. Black line is the best-fitting isochrone for the run with all constraints (grey lines are exemplary of other isochrones within the constraints), purple line is for the run when only the inner binary was used. Apart from the low $\log(g)$ of the tertiary (mostly due to noisy disentangled spectrum), the parameters observed are consistent with isochrone estimates within 5σ errors.

The disentangled spectrum for CD32B is quite poor because of the faintness of the component, the comparatively low resolution ($\sim 28,000$) and a low number of spectra. Therefore we fix most of the atmospheric parameters using approximations for metallicity and α from the inner binary. The final $\log(g)$ and radius estimates had large error bars. The temperatures are above solar values and the system is metal-poor (-0.25 dex). Isochrone fitting with these values suggested a $\log(\text{age})$ of 9.2 or 1.58 Gyrs – more than the inner orbit circularisation time scale. While the estimated $\log(g)$ of CD32B is way off from the isochrone value, the temperature matched the isochrone temperature within 5σ errors. Because of the poor spectroscopic estimate, we adopt the isochrone radius estimate for the tertiary ($0.9 R_{\odot}$). Isochrones from binary fitting were consistent with the tertiary one. Therefore we consider this system as a co-evolving system.

4.2. CD-62 1257: TIC387107961

CD62 is the only system in the sample which has a tertiary more massive than the inner binary stars ($M_3 = 1.6 M_{\odot}$). This is quite clearly visible in the high third light in the LC and also prominent in the spectra and CCFs. The binary is relatively close with a period of 2.71456 d and a semi-major axis of $11.17 R_{\odot}$. The outer orbit is eccentric ($e_{AB} \sim 0.3$). The mutual inclination ranges are (i) 16.4° to 162.4° or (ii) 17.6° to 163.6° . Spectroscopic analysis shows that the system is metal-rich with the inner binary stars showing a $[M/H]$ value of 0.3 dex and the tertiary being at 0.13 dex. Isochrone fitting gives us an age of 2.45 Gyr for the tertiary-constrained case and 2.19 Gyr for the binary-constrained case but with a negative metallicity. The more massive tertiary seems to be still on the main sequence even though the isochrone $\log(g)$ expects it to be in the sub-giant phase. While the spectroscopic estimations are precise (compared to CD32B), our fitting is af-

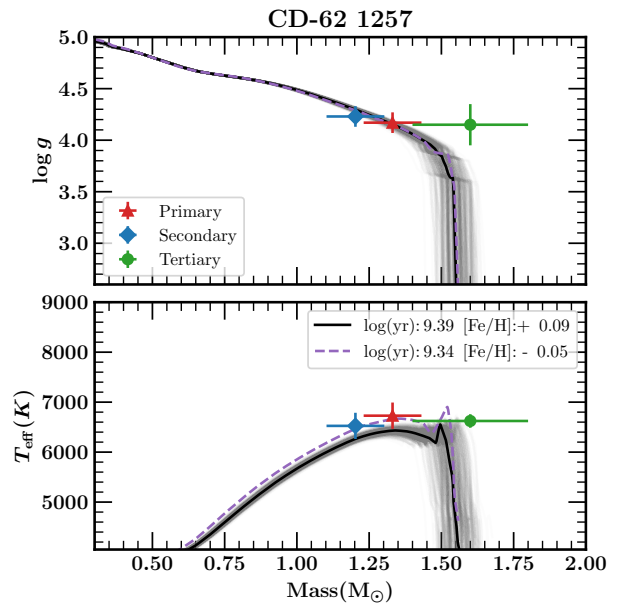


Fig. 7. Same as Figure 6 but for CD62.

ected by large errors in the CD62B's mass. While it is consistent with co-evolving temperatures, we do not completely rule out the case that the tertiary is evolving differently with its different metallicity and $\log(g)$. With the current configuration, CD62B seems to be evolving towards the red giant branch (RGB). Since the tertiary mass ratio is the highest in the sample, we check for the possibility of Roche lobe mass transfer and subsequently a triple common envelope (TCE) formation. We use a MESA evolutionary grid for a $1.6 M_{\odot}$ star to see the radius evolution. The calculation of the Roche limit was done using the expression in Eggleton (1983) and the assumption that the CHT is a wide binary with the eclipsing pair as a single star of mass of $\sim 2.5 M_{\odot}$. We found that the tertiary will evolve beyond the Roche limit in 20 Myr and can form a TCE (Figure 8).

4.3. CD-58 963: TIC220397947

CD58 has the shortest outer orbital period in our sample, and (most likely) the smallest a_{AB} . Borkovits et al. (2020) found a solution where the two stars, despite having slightly different masses (1.15 and $1.10 M_{\odot}$ at $i = 82.3^{\circ}$), had very similar radii ($\sim 1.21 R_{\odot}$). This led to the conclusion that the system is young (18.2 Myr). In our solution, the radii are significantly different from each other, and the inclination is somewhat lower. We obtained a good isochrone fit to our results for the age of 3.01 Gyr, with all the parameters (including *Gaia* distance) properly reproduced. It places all three stars on the main sequence. Despite masses close to solar, the Aa and Ab components are significantly hotter, due to their lower metallicity.

From the isochrone fit, we can also estimate the properties of the tertiary: $M_B = 0.45 M_{\odot}$, $R_B = 0.42 R_{\odot}$, $T_{\text{eff},B} = 3730$ K. The value of M_B is close to the lower limit from the RV solution, suggesting a nearly edge-on outer orbit, and likely a co-planar geometry.

There are several discrepancies between our results and Borkovits et al. (2020), mainly in the radii of Aa and Ab, and properties of the tertiary. One of the reasons behind those dis-

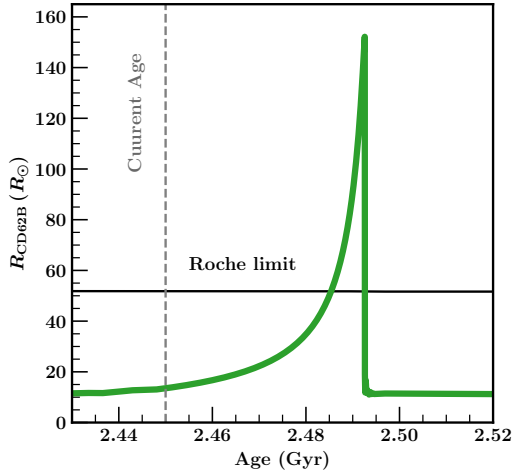


Fig. 8. The radius evolution of CD62B. The star evolves in the outer orbit of the CHT and reaches the Roche limit after 40 million years. This can prompt a mass transfer which leads to a triple common envelope system.

crepancies might be the extent of *TESS* data. New observations were obtained during the cycle 5 (Borkovits et al. 2020, only had access to cycle 1). By that time the shape of the LC has changed (Fig. 3), leading to different estimates of the radii and inclination. Furthermore, Borkovits et al. (2020) did not have any RV measurements, only ETVs of the inner binary, thus no direct, dynamical reference scale for masses and orbit sizes. We also argue that the presence of the fourth ($0.21 M_{\odot}$) body at the 2661 d orbit, did not affect our analysis, since its contribution to the total flux seems to be negligible, and our RV data were taken within a much shorter time frame.

4.4. BD+11 359: TIC408834852

BD11 was the first CHT identified in the CRÉME survey, already appearing (but not identified by name) in Figure 2 of Helminiak et al. (2015). In the solutions by Helminiak et al. (2009) and Kozłowski et al. (2014) one can note systematic effects in RV residuals. In those works, only a few RV measurements were used, and the system was treated as a “lone” binary, thus our current results are more reliable. The inner binary is composed of two main sequence stars of sub-solar metallicity and similar, yet unequal, masses, radii, and temperatures. We obtained a very good isochrone fit for the age of 2.95 Gyr. The fit predicts the tertiary to be a $0.58 M_{\odot}$, $0.54 R_{\odot}$, 4085 K dwarf. The mass is also close to the lower limit from RVs, which suggests an edge-on outer orbit, and possibly a co-planar geometry.

5. Distributions of parameters from detailed CHT solutions

While spectroscopy is important in extracting precise and accurate parameters of stars in E2CHT, many such detailed solutions have been obtained using E3CHT and photodynamical modelling of long-term LC. Such studies in the literature have estimated the metallicity of the systems (and sometimes of the

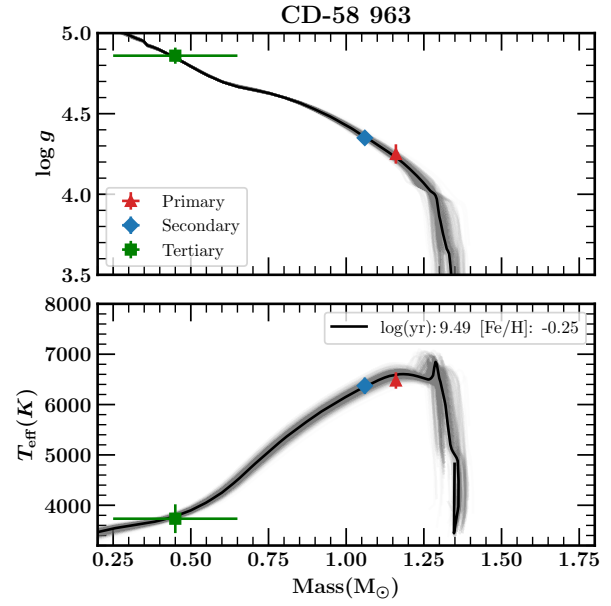


Fig. 9. Results of the isochrone fitting for CD58. The parameters observed for Aa+Ab are consistent with isochrone estimates within 3σ errors. Tertiary parameters are evaluated from the isochrone fit.

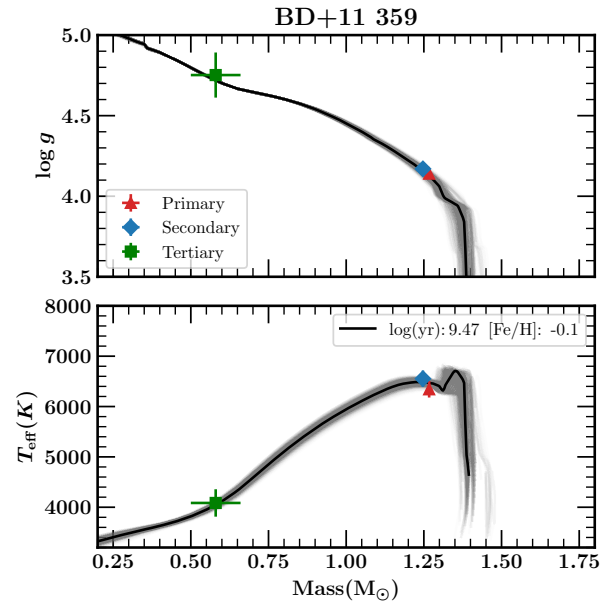


Fig. 10. Same as Fig. 9 but for BD11.

individual stars) but with the help of spectral energy distributions and isochrone fitting. While some part of the methodology assumes co-evolution and is model-dependent, it contributes substantially to the understanding of these rare systems. Going through the literature, we found 43 systems with such analysis (Table 6). To check for hints of formation and evolution channels, we look at statistics of all the well-studied systems. We add our measurements from Moharana et al. (2023, 2024) and this work. The distributions for outer eccentricity e_2 , the tertiary pe-

Table 4. Adopted values of all major parameters for the studied ST3 systems.

	CD-32 6459			CD-62 1257		
	Orbital Parameters					
	Aa–Ab		A–B	Aa–Ab		A–B
t_0 [BJD - 2450000]	8547.61072(1)			8654.922092(1)		
P [days]	4.02170747(4)		1372.1218 ^a	2.714577(2)		441.615(110)
a [R_\odot]	14.85(2)		802(10)	11.17(3)		392(14)
e	0.221(2)		0.2688(50)	0.007(3)		0.2997(144)
i [deg]	85.50(5)		51.2(5)	89.4(1)		73(4)
ω [deg]	130.0(4)		39(2)	129.5(7)		218(2)
q	0.9324(7)		0.36(2)	0.904(1)		0.64(8)
	Stellar and atmospheric parameters					
	Aa	Ab	B	Aa	Ab	B
M [M_\odot]	1.4058(7)	1.3107(9)	0.97(5)	1.331(1)	1.2025(9)	1.6(2)
R [R_\odot]	1.57(1)	1.44(1)	0.9(2) ^c	1.59(2)	1.43(3)	1.9(2)
T_{eff} [K]	6674(248)	6295(244)	6344(412)	6729(263)	6525(262)	6623(143)
$\log(g)$ [dex]	4.209(8)	4.254(9)	3.8(5)	4.17(1)	4.23(2)	4.1(1)
$v\sin(i)$ [km s ⁻¹]	15(2)	11(3)	4(4)	30(2)	27(2)	18(1)
α [dex]	0.12(6)	-0.28(1)	0.0 ^a	0.00(8)	-0.05(9)	0.00(5)
	System parameters					
$\log(\text{age})^c$ [dex]	9.2(2)			9.39(3)		
$[M/H]_{\text{ispec}}$ [dex]	-0.25(3)			0.27(4)		
$[Fe/H]_{\text{isoc}}^c$ [dex]	-0.1(2)			0.09(6)		
$E(B - V)^c$ [mag]	0.11(9)			0.03(2)		
Distance ^c [pc]	389(37)			432(11)		

^a Fixed during optimisation. ^b Obtained from empirical tables. ^c Based on isochrone fitting.

Table 5. Same as Table 4 but for ST2 systems.

	BD+11 359			CD-58 963		
	Orbital Parameters					
	Aa–Ab		A–B	Aa–Ab		A–B
T_0 [BJD - 2450000]	9448.20344(1)			9989.8842245(7)		
P [d]	3.604795(2)		168.581(305)	3.5520444(2)		76.319(169)
a [R_\odot]	13.46(1)		184.16 ^d	12.78(3)		105.43 ^d
e	0.0017(2)		0.0250(209)	0.02(2)		0.2148(96)
i [deg]	85.95(2)		-	81.58(6)		-
ω [deg]	90.6(5)		359(36)	179(7)		233(3)
q	0.984(4)		0.173(3)	0.92(8)		0.22(1)
	Stellar and atmospheric parameters					
	Aa	Ab	B	Aa	Ab	B
M [M_\odot]	1.267(4)	1.247(4)	0.58(8) ^c	1.16(1)	1.06(1)	0.45(2) ^c
R [R_\odot]	1.609(8)	1.554(8)	0.54(8) ^c	1.37(6)	1.16(6)	0.42(1) ^c
T_{eff} [K]	6342(181)	6553(178)	4085(272) ^c	6478(171)	6372(177)	3732(286) ^c
$\log(g)$ [dex]	4.143(5)	4.167(5)	4.7(1) ^c	4.25(4)	4.35(6)	4.86(5) ^c
$v\sin(i)$ [km s ⁻¹]	23.90(39)	21.54(43)	-	20(1)	18(1)	-
α [dex]	-0.13(3)	0.08(2)	-	0.05(6)	0.08(4)	-
	System parameters					
$\log(\text{age})^c$ [dex]	9.47(1)			9.49(1)		
$[M/H]_{\text{ispec}}$ [dex]	-0.12(1)			-0.31(4)		
$[Fe/H]_{\text{isoc}}^c$ [dex]	-0.10(4)			-0.15(6)		
$E(B - V)^c$ [mag]	0.09(1)			0.056(1)		
Distance ^c [pc]	253(2)			339(7)		

^a Fixed during optimisation. ^b Obtained from empirical tables. ^c Based on isochrone fitting. ^d From REBOUND

riod P_2 , and the tertiary to binary mass ratio ($\frac{M_3}{M_1+M_2}$) as a function of metallicity ($[Fe/H]$) are shown in Figure 11. We divide the $[Fe/H]$ into three regions (to account for any errors in measurements): sub-solar (< -0.15 dex), solar (-0.15 to $+0.15$ dex) and above-solar ($> +0.15$ dex). The mass ratio distributions (of $\frac{M_3}{M_1+M_2}$) for solar and above-solar metallicities both peak between 0.5 and 1, which are possible values for scenarios when

all the three masses are equal, and the tertiary and binary masses are equal, respectively. However, the sub-solar systems seem to be spread uniformly. The two solar and above-solar systems at the low $\frac{M_3}{M_1+M_2}$ end are eclipse depth variation (EDV) systems and one of them has $[Fe/H]$ very close to our limits for being metal-poor ($[Fe/H] = -0.12$). Interestingly, in a study of close binaries, Bate (2019) found that metal-poor environments have

low opacities and high cooling rates of dense gas which enhances small scale fragmentation in the star-forming cloud. Objects of all [Fe/H] show a favoured eccentricity of 0.3, and some E3CHT systems contribute to a peak at 0. This peak was observed in the *Kepler* sample of CHTs in Borkovits et al. (2016), Hajdu et al. (2019), and Czavalinga et al. (2023). We computed the cumulative distribution of e_2 for all [Fe/H] and found it to be similar to the above studies, which show a non-flat and non-thermal e_2 distribution (Figure 12; left). This eccentricity distribution was also observed in field binaries as noted by Duchêne & Kraus (2013). The lower [Fe/H] distribution shows signs of a flat distribution around 0.2 but this can be the result of an incomplete, low-number statistic. The P_2 distribution peaks below 200 days, which is likely a bias due to the majority of the systems being E3CHT. The lack of low $\frac{M_3}{M_1+M_2}$ for periods less than 200 days is suggestive of the brown-dwarf desert analogue, which we find to be [Fe/H] independent.

To see any signatures of dynamical changes of these distributions over time, we differentiated them based on the system age. Due to the lack of very young systems ($\log(\text{age}) \sim 6$), we made a separation of young and old systems at a $\log(\text{age})$ of 9. We see similar e_2 distributions with no drastic differences between the young and the old systems (Figure 12; right). Meanwhile, the young systems favoured a mass ratio closer to 1 than the old systems, which peaked at around 0.5 (Figure 13).

While the dependencies of these distributions are prone to error because of the small sample, it is an interesting property to study which could help us better understand star formation at these scales.

6. Conclusions

In this work, we present an analysis of three newly discovered and one already identified CHTs. We used LC modelling, RV modelling, spectral disentangling and spectral analysis to get orbital, stellar and atmospheric parameters of all three stars in ST3 systems and two stars in the inner binary of our ST2 systems. For ST3, we used the parameters of all three stars to constrain their ages and distances. For ST2 systems, we use parameters of the inner binary to estimate the ages and then estimate the tertiary mass and radius with constraints from the estimated minimum mass and *Gaia* distances. All inner binaries have their masses estimated with high or very high precision. Except for CD58 Aa+Ab, also the radii are precise to the level of 1% or better. The four systems are summarised below:

- CD-32 6459: The system is the widest in our sample. The tertiary is a $0.97 M_\odot$ main sequence star. This is a metal-poor system with an age of 1.58 Gyr. The inner binary is eccentric and has similar eccentricity to the tertiary orbit (~ 0.2). The mutual inclination limits are close to the limiting angle for ZLK oscillations, which could explain the large inner eccentricity.
- CD-62 1257: This is a system with the tertiary more massive and larger than the stars in the eclipsing pair. The tertiary will evolve below the Roche limit of the A-B orbit, and the system will undergo a TCE phase.
- CD-58 963: This is a system with the shortest P_2 and lowest mass in our sample. The inner binary, composed of 1.16 and $1.06 M_\odot$ stars, is accompanied by a $0.45 M_\odot$ red dwarf. Despite being previously suggested to be a young (~ 20 Myr) system (Borkovits et al. 2020), we found a good isochrone fit for an older age (~ 3 Gyr).

- BD+11 359: This system is the first CHT identified by the CRÉME survey. The inner binary, composed of 1.27 and $1.25 M_\odot$ stars, is accompanied by a $0.58 M_\odot$ red dwarf.

We compiled CHT systems from literature with age and metallicity estimates and used them with our results to look at the dependencies of tertiary mass ratio and eccentricity. We found that metal-poor stars have no preferred mass ratio but metal-rich and solar-metallicity stars prefer mass ratios around 0.5. We also found that older systems (>1 Gyr) also prefer the same mass ratio. The tertiaries eccentricities of all CHTs follow the same distribution which was observed previously for CHTs, and also field binaries. These distributions are biased due to the abundance of triply eclipsing systems. They also suffer from a lack of systems, and this is why there is a need for more homogeneous and detailed studies of CHT parameters.

Acknowledgements

The authors thank Dr. Tomer Shenar for his help with using his disentangling code, `DSAA`. This work is funded by the Polish National Science Centre (NCN) through grant 2021/41/N/ST9/02746. A.M., F.M., T.P., and M.K. are supported by NCN through grant no. 2017/27/B/ST9/02727. F.M. gratefully acknowledges support from the NASA TESS Guest Investigator grant 80NSSC22K0180 (PI A. Prša).

Observations for CD-62 1257, CD-32 6459, and CD-58 963 were obtained with the Southern African Large Telescope (SALT). Polish participation in SALT is funded by grant No. MEiN nr 2021/WK/01. This work is based on observations collected at the European Southern Observatory, Chile under programmes 088.D-0080, 089.D-0097, 089.C-0415, 090.D-0061, 091.D-0145, and through CNTAC proposals 2012B-036, 2013A-093, 2013B-022, 2014B-067, and 2015A-074.

This paper includes data collected with the TESS mission, obtained from the Mikulski Archive for Space Telescopes (MAST) data archive at the Space Telescope Science Institute (STScI). Funding for the TESS mission is provided by the NASA Explorer Program. STScI is operated by the Association of Universities for Research in Astronomy, Inc., under NASA contract NAS 5-26555. This work also presents results from the European Space Agency (ESA) space mission *Gaia*. *Gaia* data are being processed by the *Gaia* Data Processing and Analysis Consortium (DPAC). Funding for the DPAC is provided by national institutions, in particular, the institutions participating in the *Gaia* MultiLateral Agreement (MLA).

References

- Alonso, R., Deeg, H. J., Hoyer, S., et al. 2015, *A&A*, 584, L8
 Asplund, M., Grevesse, N., Sauval, A. J., & Scott, P. 2009, *ARA&A*, 47, 481
 Bate, M. R. 2019, *MNRAS*, 484, 2341
 Blanco-Cuaresma, S. 2019, *MNRAS*, 486, 2075
 Blanco-Cuaresma, S., Soubiran, C., Heiter, U., & Jofré, P. 2014, *A&A*, 569, A111
 Borkovits, T. 2022, *Galaxies*, 10, 9
 Borkovits, T., Derekas, A., Kiss, L. L., et al. 2013, *MNRAS*, 428, 1656
 Borkovits, T., Hajdu, T., Sztakovics, J., et al. 2016, *MNRAS*, 455, 4136
 Borkovits, T. & Mitnyan, T. 2023, *Universe*, 9, 485
 Borkovits, T., Mitnyan, T., Rappaport, S. A., et al. 2022, *MNRAS*, 510, 1352
 Borkovits, T., Rappaport, S., Kaye, T., et al. 2019, *MNRAS*, 483, 1934
 Borkovits, T., Rappaport, S. A., Hajdu, T., et al. 2020, *MNRAS*, 493, 5005
 Borkovits, T., Rappaport, S. A., Tan, T. G., et al. 2020, *Monthly Notices of the Royal Astronomical Society*, 496, 4624
 Borkovits, T., Rappaport, S. A., Toonen, S., et al. 2022, *Monthly Notices of the Royal Astronomical Society*, stac1983
 Borucki, W. J., Koch, D., Basri, G., et al. 2010, *Science*, 327, 977

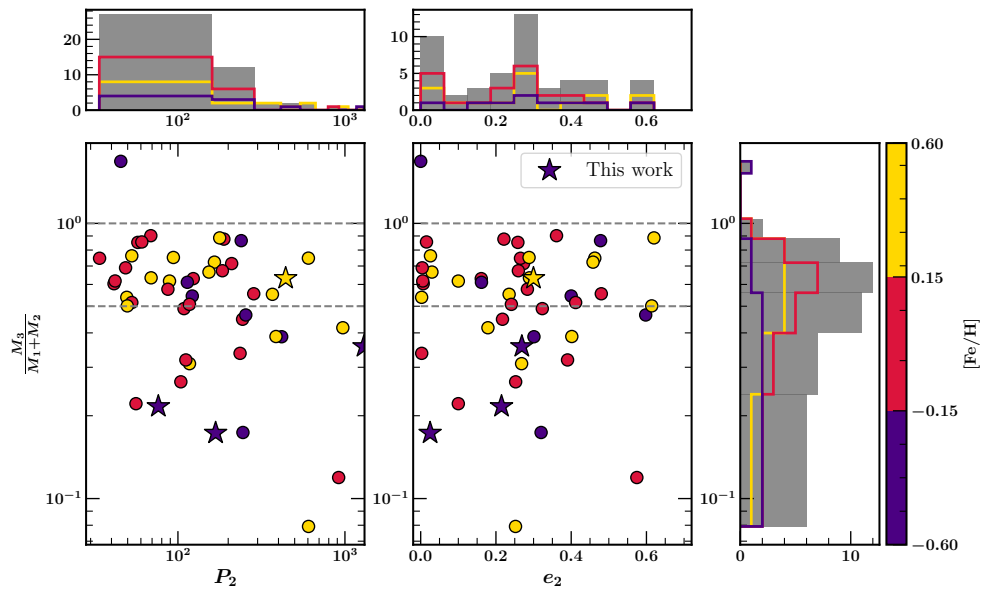


Fig. 11. The left panel shows the distribution of tertiary mass-ratio ($\frac{M_3}{M_1+M_2}$) and the tertiary period (P_2) for CHT with metallicity estimates. The panel to its right shows the distribution of $\frac{M_3}{M_1+M_2}$ with the eccentricity (e_2) of the outer orbit. The points have colours according to their systemic metallicity where metal-poor (<-0.15 dex) systems are purple, near solar-metallicity ($-0.15 \text{ dex} < [\text{Fe}/\text{H}] < 0.15$ dex) are in red, and metal-rich (>0.15 dex) CHT are in yellow. The narrow panels on each axes represent the histograms of the respective parameters with the coloured histograms representing the distributions for each metallicity group.

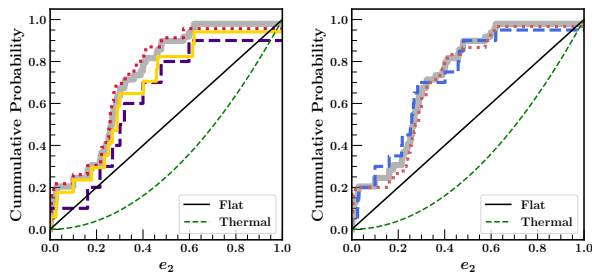


Fig. 12. Cumulative eccentricity (e_2) distribution of the tertiary orbit of CHTs list in Table 6. (Left) Cumulative e_2 distribution of CHTs of different metallicity. Yellow represents metal-rich, red represents solar and purple represents metal-poor samples. (Right) Cumulative e_2 distribution for young (blue) and old (red) systems. The black line represents the expected trend for a flat distribution and the green dashed line is the expected trend for a thermal distribution of e_2 .

Brahm, R., Jordán, A., & Espinoza, N. 2017, *PASP*, 129, 034002
 Choi, J., Dotter, A., Conroy, C., et al. 2016, *ApJ*, 823, 102
 Crause, L. A., Sharples, R. M., Bramall, D. G., et al. 2014, in *Society of Photo-Optical Instrumentation Engineers (SPIE) Conference Series*, Vol. 9147, Ground-based and Airborne Instrumentation for Astronomy V, ed. S. K. Ramesh, I. S. McLean, & H. Takami, 91476T
 Czavalinga, D. R., Borkovits, T., Mitnyan, T., Rappaport, S. A., & Pál, A. 2023, *MNRAS*, 526, 2830
 David, T. J., Hillenbrand, L. A., Gillen, E., et al. 2019, *ApJ*, 872, 161
 Derekas, A., Kiss, L. L., Borkovits, T., et al. 2011, *Science*, 332, 216
 Dotter, A. 2016, *ApJS*, 222, 8
 Duchêne, G. & Kraus, A. 2013, *ARA&A*, 51, 269
 Eggleton, P. & Kiseleva, L. 1995, *ApJ*, 455, 640
 Eggleton, P. P. 1983, *ApJ*, 268, 368
 Eisner, N. L., Johnston, C., Toonen, S., et al. 2022, *MNRAS*, 511, 4710
 Gaulme, P., Borkovits, T., Appourchaux, T., et al. 2022, *A&A*, 668, A173
 González, J. F. & Levato, H. 2006, *A&A*, 448, 283

Gray, D. F. 2005, *The Observation and Analysis of Stellar Photospheres* (Cambridge University Press)
 Gustafsson, B., Edvardsson, B., Eriksson, K., et al. 2008, *A&A*, 486, 951
 Hajdu, T., Borkovits, T., Forgács-Dajka, E., et al. 2019, *MNRAS*, 485, 2562
 Harrington, R. S. 1972, *Celestial Mechanics*, 6, 322
 Helminiak, K. G., Konacki, M., Ratajczak, M., et al. 2015, in *Astronomical Society of the Pacific Conference Series*, Vol. 496, Living Together: Planets, Host Stars and Binaries, ed. S. M. Rucinski, G. Torres, & M. Zejda, 76
 Helminiak, K. G., Konacki, M., Ratajczak, M., & Muterspaugh, M. W. 2009, *MNRAS*, 400, 969
 Helminiak, K. G., Konacki, M., Złoczewski, K., et al. 2011, *A&A*, 527, A14
 Helminiak, K. G., Ukita, N., Kambe, E., et al. 2017, *MNRAS*, 468, 1726
 Hensberge, H., Iljić, S., & Torres, K. B. V. 2008, *A&A*, 482, 1031
 Herschel, J. F. W., Main, R., & Pritchard, C. 1874, *MNRAS*, 40, 1
 Hippke, M., David, T. J., Mulders, G. D., & Heller, R. 2019, *AJ*, 158, 143
 Jones, D., Pejcha, O., & Corradi, R. L. M. 2019, *MNRAS*, 489, 2195
 Jordán, A., Brahm, R., Bakos, G. Á., et al. 2014, *AJ*, 148, 29
 Kauer, A., Stahl, O., Tubbesing, S., et al. 1999, *The Messenger*, 95, 8
 Kim, C. H., Kreiner, J. M., Zakrzewski, B., et al. 2018, *ApJS*, 235, 41
 Kniazev, A. Y., Gvaramadze, V. V., & Berdnikov, L. N. 2016, *MNRAS*, 459, 3068
 Kniazev, A. Y., Gvaramadze, V. V., & Berdnikov, L. N. 2017, in *Astronomical Society of the Pacific Conference Series*, Vol. 510, Stars: From Collapse to Collapse, ed. Y. Y. Balega, D. O. Kudryavtsev, I. I. Romanyuk, & I. A. Yakunin, 480
 Knigge, C., Toonen, S., & Boekholt, T. C. N. 2022, *MNRAS*, 514, 1895
 Konacki, M., Muterspaugh, M. W., Kulkarni, S. R., & Helminiak, K. G. 2010, *ApJ*, 719, 1293
 Kozai, Y. 1962, *AJ*, 67, 591
 Kozłowski, S. K., Konacki, M., Ratajczak, M., et al. 2014, *MNRAS*, 443, 158
 Lidov, M. L. 1962, *Planet. Space Sci.*, 9, 719
 Marcadon, F., Helminiak, K. G., Marques, J. P., et al. 2020, *MNRAS*, 499, 3019
 Mardling, R. A. & Aarseth, S. J. 2001, *MNRAS*, 321, 398
 Mayor, M., Pepe, F., Queloz, D., et al. 2003, *The Messenger*, 114, 20
 Mitnyan, T., Borkovits, T., Czavalinga, D. R., et al. 2024, *arXiv e-prints*, arXiv:2402.01486
 Mitnyan, T., Borkovits, T., Rappaport, S. A., Pál, A., & Maxted, P. F. L. 2020, *MNRAS*, 498, 6034
 Moharana, A., Helminiak, K. G., Marcadon, F., et al. 2023, *MNRAS*, 521, 1908
 Moharana, A., Helminiak, K. G., Marcadon, F., et al. 2024, *MNRAS*, 527, 53
 Naoz, S. & Fabrycky, D. C. 2014, *ApJ*, 793, 137
 Perets, H. B. & Fabrycky, D. C. 2009, *ApJ*, 697, 1048

Ayush Moharana et al.: Spectroscopy of Eclipsing Compact Hierarchical Triples

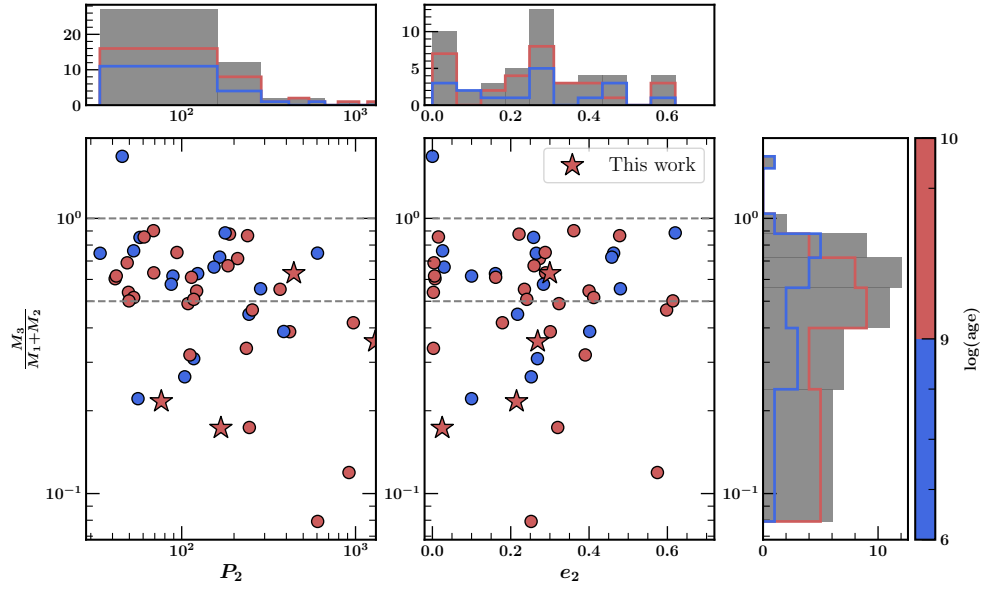


Fig. 13. Same as Figure 11 but systems are marked with colours according to their age estimate (in log scale). The systems in red are old systems with $\log(\text{age}) > 9$ (in Gyrs) while the systems in blue are classified as old with $\log(\text{age}) < 9$.

- Pojmanski, G. 1997, *Acta Astron.*, 47, 467
Pojmanski, G. 2002, *Acta Astron.*, 52, 397
Pollacco, D. L., Skillen, I., Collier Cameron, A., et al. 2006, *PASP*, 118, 1407
Prša, A., Kochoska, A., Conroy, K. E., et al. 2022, *ApJS*, 258, 16
Queloz, D., Mayor, M., Weber, L., et al. 2000, *A&A*, 354, 99
Rappaport, S. A., Borkovits, T., Gagliano, R., et al. 2022, *MNRAS*, 513, 4341
Rappaport, S. A., Borkovits, T., Gagliano, R., et al. 2023, *MNRAS*, 521, 558
Rappaport, S. A., Borkovits, T., Mitnyan, T., et al. 2024, *arXiv e-prints*, arXiv:2403.12041
Rein, H. & Liu, S. F. 2012, *A&A*, 537, A128
Ricker, G. R., Winn, J. N., Vanderspek, R., et al. 2015, *Journal of Astronomical Telescopes, Instruments, and Systems*, 1, 014003
Rucinski, S. 1999, in *Astronomical Society of the Pacific Conference Series*, Vol. 185, IAU Colloq. 170: Precise Stellar Radial Velocities, ed. J. B. Hearnshaw & C. D. Scarfe, 82
Shenar, T., Bodensteiner, J., Abdul-Masih, M., et al. 2020, *A&A*, 639, L6
Shenar, T., Sana, H., Mahy, L., et al. 2022, *A&A*, 665, A148
Shivvers, I., Bloom, J. S., & Richards, J. W. 2014, *MNRAS*, 441, 343
Southworth, J. 2013, *A&A*, 557, A119
Tokovinin, A. 2004, in *Revista Mexicana de Astronomia y Astrofisica Conference Series*, Vol. 21, *Revista Mexicana de Astronomia y Astrofisica Conference Series*, ed. C. Allen & C. Scarfe, 7–14
Tokovinin, A., Fischer, D. A., Bonati, M., et al. 2013, *PASP*, 125, 1336
Tokovinin, A. & Moe, M. 2020, *MNRAS*, 491, 5158
Udalski, A., Szymanski, M., Kaluzny, J., Kubiak, M., & Mateo, M. 1992, *Acta Astron.*, 42, 253
Ulaş, B. & Ayan, V. 2023, *Research in Astronomy and Astrophysics*, 23, 035016
von Zeipel, H. 1910, *Astronomische Nachrichten*, 183, 345
Zahn, J. P. & Bouchet, L. 1989, *A&A*, 223, 112
Zucker, S. & Mazeh, T. 1994, *ApJ*, 420, 806

Table 6. Table of CHTs with detailed parameters, and their sources. The systems are characterised according to their method of estimation of orbital parameters, metallicity, and ages.

System	P_1	P_2	Source
Triply Eclipsing			
HD 181068	0.9057	45.471	Derekas et al. (2011); Borkovits et al. (2013)
HD144548 ^a	1.6278	33.945	Alonso et al. (2015); David et al. (2019)
EPIC 249432662	8.1941	188.379	Borkovits et al. (2019)
TIC 209409435	5.7175	121.872	Borkovits et al. (2020)
TIC 278825952	4.7810	235.550	Mitnyan et al. (2020)
KIC 7955301	15.3183	209.760	Gaulme et al. (2022)
TIC 388459317	2.1849	89.0312	Borkovits et al. (2022)
TIC 193993801	1.4308	49.4020	Borkovits et al. (2022)
TIC 52041148	1.7872	177.8620	Borkovits et al. (2022)
TIC 242132789	5.1287	42.0317	Rappaport et al. (2022)
TIC 42565581 ^a	1.8235	123.5467	Rappaport et al. (2022)
TIC 54060695	1.0608	60.7759	Rappaport et al. (2022)
TIC 37743815	0.9069	68.7998	Rappaport et al. (2022)
TIC 456194776	1.7193	93.9150	Rappaport et al. (2022)
TIC 178010808	0.8264	69.0830	Rappaport et al. (2022)
TIC 294803663	2.2456	153.4260	Rappaport et al. (2023)
TIC 99013269	6.5344	604.2425	Rappaport et al. (2023)
TIC 332521671	1.2479	48.5848	Rappaport et al. (2023)
TIC 47151245	1.2025	284.3740	Rappaport et al. (2023)
TIC 276162169	2.5498	117.2700	Rappaport et al. (2023)
TIC 280883908	5.2418	184.5980	Rappaport et al. (2023)
TIC 229785001	0.9298	165.3700	Rappaport et al. (2023)
TIC 356324779	3.4717	87.0920	Rappaport et al. (2023)
TIC 81525800	1.6131	49.7500	Rappaport et al. (2023)
TIC 298714297	1.0729	117.2400	Czavalinga et al. (2023)
TIC 66893949	16.2900	386.4000	Czavalinga et al. (2023)
TIC 88206187	1.1846	52.9220	Czavalinga et al. (2023)
TIC 650024463	7.1978	108.7251	Rappaport et al. (2024)
TIC 133771812	12.3339	243.8900	Rappaport et al. (2024)
TIC 185615681	2.3180	56.0666	Rappaport et al. (2024)
TIC 176713425	1.8951	52.9430	Rappaport et al. (2024)
TIC 287756035	2.0822	367.9230	Rappaport et al. (2024)
TIC 321978218 ^a	0.5703	57.5354	Rappaport et al. (2024)
TIC 323486857	0.8850	41.4268	Rappaport et al. (2024)
Eclipse Depth Variation			
KIC 5731312	7.9465	917.0000	Borkovits et al. (2022)
KIC 5653126	38.4482	971.3900	Borkovits et al. (2022)
KIC 8023317	16.5754	605.4000	Borkovits et al. (2022)
KIC 6964043	10.6979	239.2519	Borkovits et al. (2022)
KIC 5771589	10.6791	113.8720	Borkovits & Mitnyan (2023)
Eclipse timing			
TIC 219885468	7.5128	111.5498	Borkovits & Mitnyan (2023)
KIC 9714358	6.4708	104.0830	Borkovits & Mitnyan (2023)
Spectroscopy			
BD+44 2258	3.4726	254.8400	Moharana et al. (2023)
KIC 6525196	3.4206	418.0000	Helminiak et al. (2017); Moharana et al. (2023)
GSC 08814-0102 ^b	0.7024	245.0000	Helminiak et al. (2011); Moharana et al. (2024)

^a Tertiary and binary have different age estimates. ^b $\log(\text{age})$ and $[\text{Fe}/\text{H}]$ from the inner binary

Appendix A: RV measurements

We present all RV measurements used in this work in Tables A.1 and A.2. We included the data from Helminiak et al. (2009) for BD11. When a measurement cannot be done at a certain epoch, due to for example line blending, it is marked with “—”. There is obviously no data for the tertiaries in ST2 systems.

Appendix B: JKTEBOP Tables

We made LC models with JKTEBOP for each TESS sector separately. The parameters obtained from the fitting for each fun are given in Table B.1 (CD32), Table B.2 (BD11), Table B.3 (CD62), and Table B.4.

Appendix C: ISOFITTER results

The isochrone fitting code ISOFITTER calculates grids of χ^2 using models from MIST and the measured parameters. In Appendix C we show the χ^2 map for isochrone metallicity ($[Fe/H]$), log of star age ($\log(\text{age})$), reddening free distance (D_0), extinction (as $E(B - V)$) and estimated radius of the tertiary (R_3). The top panel for each star shows grids where the χ^2 was weighted with *Gaia* distance and the lower panels were free of this weight. For ST3, we calculate separate grids using three-star constraints (TC; Appendix C-left) and binary constraints (BC; Appendix C-right). For the case of ST2 systems, we use only BC and we also show the expected mass of the tertiary (M_3) as well.

Ayush Moharana et al.: Spectroscopy of Eclipsing Compact Hierarchical Triples

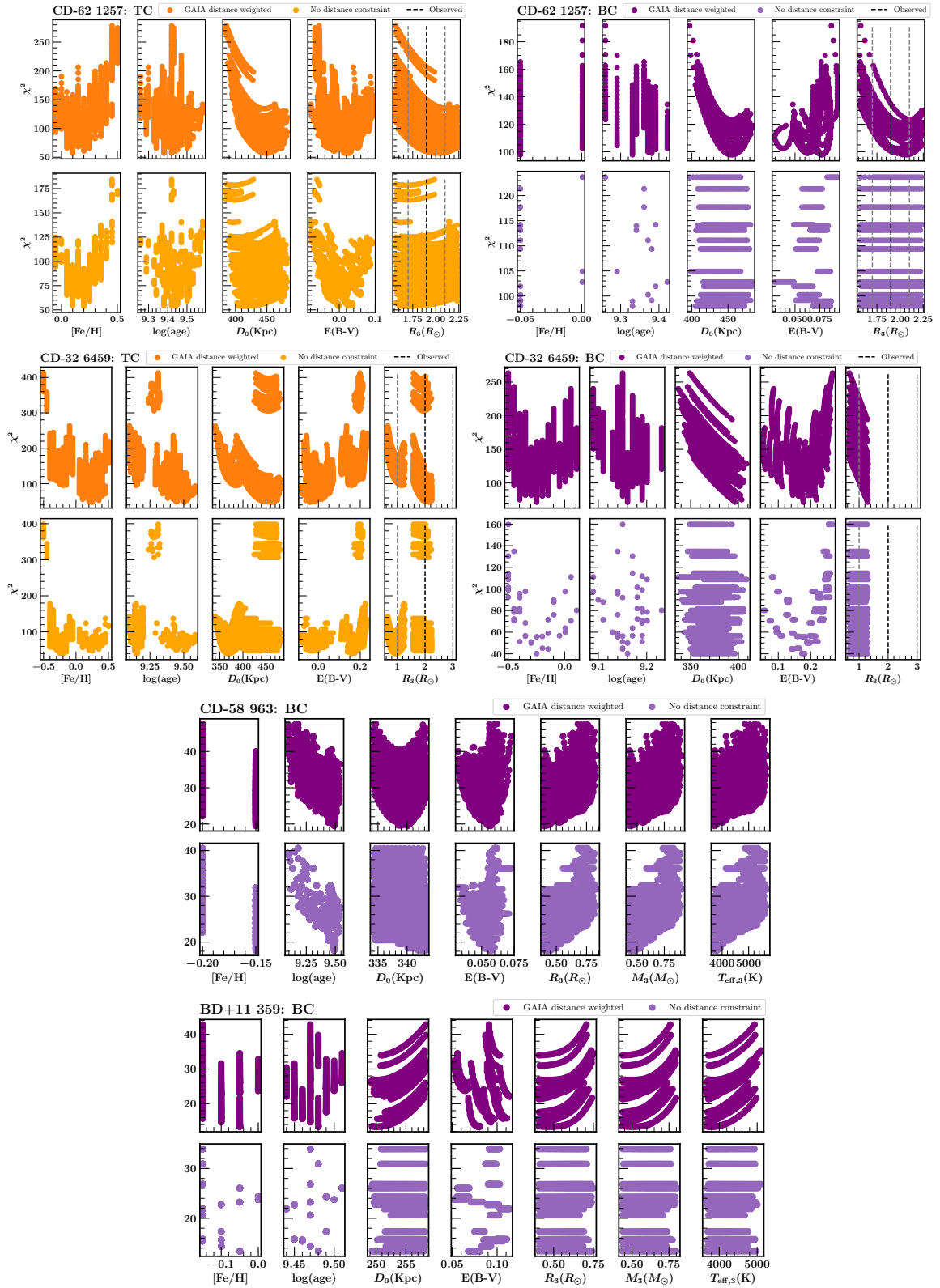


Fig. C.1. ISOFFITER χ^2 grids for specific parameters for different constraints. Orange denotes grids calculated with constraints from all stars while purple denotes grids calculated using only the eclipsing pair.

Table A.2. The RV measurements of ST2s used in this work. All values are given in km s^{-1} .

JD-2400000	v_{Aa}	\pm	v_{Ab}	\pm	v_{COM}	\pm	Inst.
CD-58 963							
59803.615462	29.174	0.922	-35.492	0.707	-1.766	0.293	HRS
59851.524928	-27.411	0.483	24.944	0.382	-2.361	0.156	HRS
59861.456438	76.812	0.458	-73.061	0.572	5.103	0.184	HRS
59872.465435	32.610	0.452	-30.733	0.503	2.303	0.171	HRS
59893.370953	61.685	0.461	-95.980	0.631	-13.752	0.194	HRS
59894.400083	-73.674	0.461	48.467	0.648	-15.234	0.197	HRS
59913.360440	-49.362	0.553	-1.266	0.614	-26.350	0.209	HRS
59914.342234	59.785	0.567	-118.984	0.726	-25.750	0.230	HRS
59920.309846	-60.173	0.564	34.240	0.665	-15.000	0.219	HRS
59946.440661	89.040	0.536	-89.817	0.648	3.463	0.211	HRS
59984.377028	-53.007	0.444	1.721	0.642	-26.822	0.193	HRS
60031.260702	68.260	0.475	-75.713	0.732	-0.626	0.214	HRS
60186.569821	-64.561	0.681	64.689	0.995	-2.720	0.298	HRS
BD+11 359							
55876.635630	-84.750	0.243	103.689	0.389	8.729	0.245	FEROS
55878.625064	95.977	0.368	-81.745	0.372	7.814	0.287	FEROS
55878.706579	91.328	0.602	-75.655	0.317	8.492	0.357	FEROS
56193.796462	-80.139	0.472	107.504	0.521	12.945	0.384	FEROS
56195.766059	105.649	0.405	-80.877	0.421	13.118	0.320	FEROS
56290.562677	-42.229	0.432	41.854	0.565	-0.517	0.386	FEROS
56291.565524	-74.618	0.281	76.734	0.497	0.463	0.301	FEROS
56292.551540	66.484	0.349	-66.822	0.657	0.354	0.389	FEROS
56517.837030	-51.987	0.825	79.353	0.833	13.166	0.643	FEROS
56518.805909	-47.078	1.219	74.302	0.843	13.135	0.800	FEROS
56519.828021	95.671	0.352	-70.041	0.558	13.466	0.352	FEROS
56137.878521	95.782	0.308	-89.616	0.363	3.811	0.260	HARPS
56179.805929	-61.640	0.362	90.403	0.332	13.784	0.269	HARPS
56237.643240	-55.525	0.888	59.706	0.403	1.637	0.502	CORALIE
56238.685091	86.698	0.746	-84.060	0.728	1.990	0.572	CORALIE
56242.736340	87.777	0.952	-88.218	0.794	0.471	0.677	CORALIE
56497.865091	56.496	0.715	-34.776	0.651	11.218	0.530	CORALIE
56619.641008	-73.217	0.807	71.866	1.177	-1.246	0.768	CORALIE
54727.175538	-58.281	0.781	59.466	0.624	0.129	0.545	UCLES
54748.173087	-93.788	0.438	90.371	0.464	-2.432	0.349	UCLES
54837.008123	85.826	0.659	-58.741	1.404	14.110	0.797	UCLES
54838.029710	-58.900	1.149	88.605	0.679	14.272	0.710	UCLES
54839.966130	97.981	0.699	-72.071	0.875	13.623	0.610	UCLES

Table B.1. JKTEBOP Solutions for CD32

Parameters	S09	S62
P [d]	4.021750(7)	4.021758(4)
T_0 [JD-2457000]	1547.610718(27)	2991.403699(14)
i [deg]	85.47(3)	85.52(2)
e	0.2254(11)	0.2174(8)
ω [deg]	129.1(2)	130.9(2)
J	0.857(13)	0.791(9)
$r_1 + r_2$	0.2033(2)	0.2034(2)
k	0.932(4)	0.900(6)
L_3	0.0936(33)	0.1080(25)

Table B.2. JKTEBOP Solutions for BD11

Parameters	S42	S43
P [d]	3.604797(3)	3.604807(3)
T_0 [JD-2457000]	2448.203442(14)	2477.041918(15)
i [deg]	85.96(1)	85.94(1)
e	0.0013(1)	0.0021(2)
ω [deg]	89.2(3)	91.9(2)
J	1.0034(2)	1.0047(1)
$r_1 + r_2$	0.234940(3)	0.23510(4)
k	0.965(5)	1.034(5) / 0.967(5)
L_3	0.0603(14)	0.0554(14)

Ayush Moharana et al.: Spectroscopy of Eclipsing Compact Hierarchical Triples

Table B.3. JKTEBOP Solutions for CD62

Parameters	S13	S66	S67
P [d]	2.714600(4)	2.714652(3)	2.714696(5)
T_0 [JD-2457000]	1654.922099(2)	3099.154856(20)	3129.016155(25)
i [deg]	89.53(6)	89.31(4)	89.34(5)
e	0.0133(7)	0.0031(7)	0.0044(8)
ω [deg]	88.3(1)	83.2(16)	85.6(9)
J	0.999(7)	0.924(6)	0.943(8)
$r_1 + r_2$	0.2512(1)	0.2528(1)	0.2527(1)
k	0.825(1)	0.814(1)	0.817(2)
L_3	0.5711(7)	0.5730(7)	.5728(9)

Table B.4. JKTEBOP Solutions for CD58

Parameters	S62	S63	S64	S67	S68	S69
P [d]	3.55385(4)	3.55137(4)	3.55174(4)	3.55173(8)	3.55174(4)	3.55155(4)
T_0 [JD-2457000]	2989.88257(8)	3021.85611(8)	3046.71543(8)	3128.41124(9)	3160.38653(8)	3192.34897(8)
i [deg]	81.93(1)	81.63(2)	81.59(1)	81.58(2)	81.56(1)	81.60(2)
e	0.228(3)	0.016(4)	0.018(5)	0.024(6)	0.015(4)	0.011(5)
ω [deg]	90.25(1)	94(1)	266(1)	92.3(6)	95(2)	265(3)
J	5.4(1)	1.04(4)	0.78(3)	1.12(6)	1.03(4)	0.83(3)
$r_1 + r_2$	0.2010(2)	0.1969(3)	0.1976(3)	0.1977(3)	0.1982(3)	0.1974(3)
k	0.511(7)	0.77(2)	0.92(2)	0.79(2)	0.80(1)	0.89(2)
L_3	0(fixed)	0(fixed)	0(fixed)	0(fixed)	0(fixed)	0(fixed)

CHAPTER 6

Conclusions

“Każdy przecież początek, to tylko ciąg dalszy, a księga zdarzeń, zawsze otwarta w połowie.”

After all, every beginning is only a continuation, and the book of events is always open halfway.

– Wisława Szymborska, Nobel laureate in Literature

The abundance of *Kepler* and *TESS* light curves have helped us find a new class of multiple stars called the CHTs. One of the reasons for such a special classification is because CHTs (specifically ECHTs) are gold mines of orbital architectures, dynamical processes and astrophysical data. While these stars were considered rare prior to 2004, the last decade has seen an exponential rise in the detection of these systems. Even then, the number of CHT candidates is around 400, out of which around 50 have been studied in detail. We started with the goal of detecting new CHTs and increasing the number of systems that have been studied in detail. But in this process, we also open up new avenues for discussion.

6.1. Detection of CHTs

The current sample of CHTs contains detections using 3 major methods. The most optimal and popular technique of ETVs, the most precise method using E3CHT, and the easiest method (excluding the method to model photocenter variations) of using *Gaia* binary models and binary catalogues. While the latest can be biased towards detecting brighter companions, E3CHTs are biased in orientation and ETVs are limited by the companion mass. While the first necessity for the statistical study of the rare CHT is the detection of

more systems, the use of different detection techniques is also necessary to create a more homogeneous sample of CHTs.

In this thesis, we attempt to address both of the above necessities. While space telescopes have been exemplary in detecting CHTs with the ETV method, we tried to do the same with ground-based telescopes. In [chapter 2](#), we showed that with efficient photometric pipeline, and an analytical eclipse modelling code, we can detect CHTs with low-mass tertiary companions. The complexity of this detection method also relies on the accurate identification of stellar activity and separating them out from the tertiary ETV signals. The first part of the *Solaris* campaign was successful in our first CHT detection in GSC 08814-01026, a pair of active K-type dwarfs. With future monitoring, we expect to detect more CHTs, but it is important to also use ground-based photometric surveys to monitor interesting and dynamically active CHTs. This will also help us understand how to direct other modes of observation to our rare targets.

To add diversity to the method of detection, we also use RVs of double-lined spectroscopic EBs to detect CHTs. The method of RV detection has no constraints except that the two stars in the inner binary of a CHT are visible clearly in the spectra. With modern upcoming methods of spectral analysis (*e.g.*, spectral disentangling, broadening functions), we would be without even fewer constraints. Our search for CHTs using RV started because of the precise spectroscopy available in the CRÉME survey. Following the RV variation of the centre of mass of the eclipsing pair and the tertiary RV (if available), CRÉME has detected 10 CHTs out of which 8 were discovered during the period of the thesis's work. While 2 of them are still in preparation for being published, we report the rest of the 4 discoveries namely, BD+44 2258, CD-32 6459, CD-62 1257, and BD+11 359. The advantage of having high-resolution spectroscopy is that one can use it to extract additional parameters which the photometric light curve cannot provide. This leads to the next avenue for discussion.

6.2. Extraction of absolute parameters

A spectroscopic double-lined EB is the source of precise and accurate stellar and orbital parameters. This is the reason they are used as calibrators or benchmark systems. A direct translation to triple systems would be a triple-lined triply eclipsing system. But unlike EBs, these systems are very specific in orientation as two orbital planes have to be aligned at similar angles. Therefore, to preserve the homogeneity of this orientation, it would be worthwhile to improve other avenues of parameter extraction, say a triple-lined triple system but with EB as the inner binary.

In [chapter 3](#), we presented the set of techniques which can extract the total set of stellar, orbital, and atmospheric parameters. While the methods are themselves not new, we present new ways of combining independent methods to get consistent, accurate and

precise parameters of all stars in a CHT. We use the methods of CCF (using the `TOPCOR` algorithm) and BF to extract precise RVs of stars in low-mass CHTs. We modelled the RVs using the code `v2FIT` which can model variations due to a third body.

We use modern EB modelling tools to obtain high-precision estimates of radii, eccentricity and inclination of the eclipsing pair in a CHT. In most of our systems, we present precise parameters, even in the presence of stellar activity.

A crucial step in our parameter extraction was spectral disentangling. In our work, used two codes, `FD3` and `DISENTANGLING_SHIFT_AND_ADD` to disentangle spectra with resolution between 28000 to 67000. We also showed that it is possible to extract spectra with small sample spectra. Some of the important considerations that we learnt from our work are listed below:

- Stability of spectrograph and reduction method is important. With low-mass CHTs, we sometimes work with a tertiary light fraction of ~ 0.1 or lower. In such cases, small biases in measurements are propagated and also amplified through the disentangling method (Hensberge et al. 2008). Such biases can be prominent in echelle spectra where order-wise disentangling can be used to avoid biases due to complex reduction methods like blaze correction.
- Post-processing is helpful in cases of low spectra. While with a clean set of spectra, we can get clean disentangled spectra, most of the time we have to reject few available observations due to superimposed spectral lines, low SNR, emission lines etc. In this case, post-processing of disentangled spectra is needed. While the cleaning of the bias can be done by simply subtracting the bias signal, it is the modelling of the signal which can be tricky.
- Disentangle in super-imposed segments. A good practice is to break the spectra into segments where the end of two segments superimpose with 2-3 common lines. This is a good way to compare line depths for bias cleaning and the convergence of the disentangling routine.

For spectral analysis on the disentangled spectra, we used `iSPEC`. For most of our targets, we got consistent solutions for effective temperatures, surface gravity, and metallicity. This was possible due to constrained parameters from several other techniques (*e.g.*, $v \sin i$ from BF). Therefore, CHTs can address the necessity for a test of multiple disentangling and spectroscopy with CHT benchmarks in the future.

6.3. Formation and evolution of CHTs

We used all the available parameters to get a detailed picture of 6 CHTs in [chapter 4](#) and [chapter 5](#). This picture includes the age of the system, the metallicity of the stars, stellar

activity, differential rotation, dynamical evolution and stability of the system. We list our major results for each of these six systems:

- **BD+44 2258:** This old system (~ 7.6 Gyr) consists of two sub-giants, one in the inner binary and the other one being the tertiary. In this system, we can see changes in the abundances of Mg and Si between the two sub-giant stars and the main sequence star. Whether this is an evolutionary change or a signature of dynamical interaction, is still an open question. The system will most probably merge due to tidal dissipation which is enhanced by the sub-giant tertiary.
- **KIC 06525196:** This is the first published CHT identified by the CRÉME survey, and this thesis expands our knowledge about it. All stars in this system are main-sequence stars. It is metal-poor, old, and nearly co-planar. Due to the comparatively smaller mass of the tertiary and a wider orbit, the system is stable in the long term for all values of mutual inclinations.
- **CD-32 6459:** The system is the widest in our sample. This is a metal-poor system with an age of 1.58 Gyr. The inner binary is eccentric and has similar eccentricity to the tertiary orbit (~ 0.2), despite the fact that the orbit should be circularised at the age of ~ 0.5 Gyr. This can be explained by the mutual inclination limits, which are close to the limiting angle for ZLK oscillations, which could excite the eccentricity of the inner pair.
- **CD-62 1257:** This is a system with the tertiary more massive and larger than the stars in the eclipsing pair. All stars are still on the main sequence, although the tertiary is close to the end of this phase, and will soon start to grow rapidly. The system will then undergo a TCE phase.
- **CD-58 963:** This is a system with the shortest P_2 and lowest mass in our sample. Despite being previously suggested to be a young (~ 20 Myr) system (Borkovits et al. 2020), we found it to be an older one (~ 3 Gyr).
- **BD+11 359:** This system is the first CHT identified by the CRÉME survey, although not properly studied to date. The inner binary, composed of 1.27 and 1.25 M_{\odot} stars, is accompanied by a 0.58 M_{\odot} red dwarf. This is also an old system.

In all our systems we found the stars to be co-evolving. Triple population synthesis (Toonen et al. 2020) predicts that around 70% of triple stars will merge. While we do see the possibility of mergers, and common envelope phases, it is surprising that these old systems have not interacted before. This questions the processes that we consider in the dynamical interaction of stars. This specifically reduces down to the question: is there a process which stabilises low-mass CHTs? The answer to this can lie in chemically

peculiar wide binaries and whether they are formed from CHTs. But still, then we need to better understand the current distribution of CHT parameters.

Our study on the distribution of CHT parameters ([chapter 5](#)) could not shed much light on evolution but it did inform us about the formation trends of CHTs. Approximating tertiary mass ratio (q_3) for large CHT surveys, we found that low-mass CHTs favour a q_3 around two regions: (i) 0.4-0.5, with the possibility of equal mass components, and (ii) 0.8-1.0, with the possibility that the binary and tertiary have the same mass. We found that metal-poor CHTs do not have any preferred q_3 and outer eccentricity distribution peaks at 0.3. The lack of preference in the mass ratio in metal-poor systems has also been seen in simulations of close binaries ([Bate 2019](#)). Meanwhile, the eccentricity peak is similar to the one found in field binaries ([Duchêne & Kraus 2013](#)). This shows that IMM still holds for CHTs in some regimes. We also found that a brown dwarf desert analogue exists for CHTs. But all these are results from small-scale statistics, and are therefore biased. This is why future observations are crucial for this emerging class of triple stars.

6.4. Future scope

The work with CHTs has just begun. With the upcoming PLATO mission, it will be possible to detect peculiar light curves of thousands of multiples and hopefully some more CHTs. Keeping that in mind, it would be worthwhile to identify dynamical systems which can be monitored in the future for ETVs, eclipse depth variation in EBs or even EBs turning to triply eclipsing systems. Our work also highlights the necessity of spectroscopic follow-up.

There have been few pulsators identified in CHTs. This is a field that can help us avoid the dependency on spectra for atmospheric parameters. [Miller et al. \(2020\)](#) developed a novel method to calculate precise temperatures for stars. While it is not extendable to multiples in the current form, it can be done in the near future to find CHT benchmarks.

The only parameter that we could not constrain with sufficient precision was mutual inclination. While this can be in principle done with ETV, we need long-term light curve coverage. Further, ETVs have detection limits dependent on tertiary masses. While the estimation of the mutual inclination of triples is usually done by astrometry, CHTs would require interferometry to resolve the separations of the outer orbit scale. While interferometry of the whole orbit is expensive, it is in principle possible to use one epoch of interferometry along with *Gaia* astrometry to solve the orbit and get a 3D picture.

We find ourselves in the golden period of multiple-star research. With all the scope and promise that we found in CHTs, it will be interesting to see if triples are the answers to the questions that binaries cannot answer.

APPENDIX A

Line lists for spectral fitting

In synthetic spectral fitting (SSF) using `iSPEC`, the choice of spectral modelling code and its corresponding line-list (LL) are important. SSF calculates the minimisation statistics. While the LLs are different for stars of different spectral types ([Blanco-Cuaresma et al. 2014](#)), a generalisation can be made for FGK-type stars. [Blanco-Cuaresma \(2019\)](#) made a detailed study on the estimation of atmospheric parameters using several spectral modelling codes and a combination of lines. This resulted in different sets of lines or LL, appropriate for different codes. For our work, we use two different LLs selected for the code `SPECTRUM`. The first LL (LL1) consists of lines appropriate for metallicity and abundance estimation. Therefore, we only take the [Fe/H] estimation from SSF using LL1. The second LL (LL2) is used to extract the rest of the atmospheric parameters. The LLs used (in the range of our spectra) are in [Table A.1](#) and [Table A.2](#).

Table A.1 LL1: Line list for metallicity and abundance estimation.

Element	Exc.	λ (nm)	Element	Exc.	λ (nm)	Element	Exc.	λ (nm)	Element	Exc.	λ (nm)
Fe	1	480.0649	Fe	1	498.4605	Co	1	514.9794	Sc	2	531.8349
Cr	1	480.1025	Fe	1	498.4629	Cu	1	515.3231	Cr	1	531.8771
Zr	1	480.587	Fe	1	498.5983	Ti	2	515.4068	Fe	1	531.9035
Ti	2	480.6321	Fe	1	499.1268	Mg	1	516.7322	Nd	2	531.981
Zr	1	480.947	Ti	2	499.6367	Ru	1	517.102	Fe	1	532.0036
Zn	1	481.0528	Ca	2	500.1479	Mg	1	517.2684	Pr	2	532.2771
Ni	1	481.1983	Fe	1	500.2792	Co	1	517.6076	Fe	1	532.4179
Cr	2	481.2337	Ni	1	500.3741	Mg	1	518.3604	Co	1	532.5274
Co	1	481.3476	Fe	1	500.4044	Ti	2	518.5902	Fe	2	532.5552
Zr	1	481.504	Mn	1	500.4894	Ca	1	518.8844	Fe	1	532.7252
Zr	1	481.563	Ti	2	500.5167	Y	2	520.5722	Cr	1	532.9138
Mn	1	482.352	Fe	1	500.5712	Cr	2	521.0865	Cr	1	532.9784
Cr	2	482.4127	Ti	1	500.9645	Ti	2	521.153	Fe	1	532.9989
Zr	1	482.804	Ti	2	501.3686	Co	1	521.2688	O	1	533.0741
V	1	483.1646	Ti	1	501.6161	Cu	1	521.8197	Co	1	533.1453
V	1	483.2426	Ti	1	502.0026	Ti	1	521.9701	Cr	2	533.4869
Sm	2	483.462	Fe	1	502.3186	Cu	1	522.0066	Ti	2	533.6786
Cr	2	483.6229	Fe	1	502.8126	Ni	1	522.029	Fe	1	533.9929
Cr	2	484.8235	Fe	1	502.9618	Fe	1	522.2395	Cr	1	534.0447
Ti	2	484.9168	Mn	1	502.9802	Ti	1	522.362	Co	1	534.2701
V	1	485.1482	Fe	1	503.0778	Ti	1	522.454	Ca	1	534.9465
Cr	2	485.6186	Sc	2	503.1021	Fe	1	522.5526	Co	1	535.204
Cr	2	486.4326	Fe	1	503.1914	Ti	2	522.6538	Co	1	535.9199
V	1	486.4731	Fe	1	503.6922	Co	1	523.0208	K	1	535.9573
Ti	2	486.561	Ti	1	503.9957	Fe	1	523.0691	Co	1	536.9589
Co	1	486.7869	Ni	1	504.2186	Fe	2	523.4623	Mn	1	537.7607
Ti	2	487.4009	Ti	1	504.3584	Cr	2	523.7328	C	1	538.0325
V	1	487.5493	Fe	1	504.4211	Sc	2	523.9813	Ti	2	538.1022
V	1	488.1556	V	2	504.73	Fe	1	524.2491	Fe	1	538.6333
V	2	488.3407	Fe	1	504.8436	Fe	1	524.3776	Cr	1	538.6968
Y	2	488.3682	C	1	505.2144	Cr	2	524.6768	Fe	1	538.9479
Cr	2	488.4607	Sm	2	505.275	Cr	1	524.7565	Ni	1	539.2331
Fe	1	489.6439	Fe	1	505.4642	Co	1	524.792	Fe	1	539.3167
Co	1	489.9513	Ti	1	506.5985	Cr	2	524.9437	Ti	2	539.6247
Y	2	490.0119	Ni	2	506.6328	Fe	1	525.3021	Ti	2	539.6561
Ti	2	491.1194	Cr	1	506.7713	Fe	1	525.3462	Fe	1	539.7618
Fe	1	491.8012	Ti	2	506.909	Mn	1	525.533	Fe	1	539.8279
Fe	1	491.8994	Ti	2	507.2286	Fe	2	525.6932	Mn	1	539.9475
Ti	1	491.9861	Fe	1	507.6264	Fe	1	525.7655	Fe	1	540.0501
Fe	1	492.0502	Zr	1	507.825	Pr	2	525.9728	Fe	1	541.2784
Fe	1	492.4301	Fe	1	507.9223	Ca	1	526.0387	Mn	1	541.3668
Fe	1	492.477	Fe	1	507.974	Mn	1	526.0759	Fe	2	541.407
Ni	1	492.5559	Sc	1	508.1574	Ca	1	526.1704	Ti	2	541.8768
Cr	1	493.6335	Fe	1	508.3338	Fe	1	526.3306	Cr	2	542.0922
Ni	1	493.7348	Mn	1	508.6765	Fe	2	526.4802	Fe	1	542.4068
Fe	1	493.8814	Fe	1	509.0773	Cr	1	526.5148	Ni	1	542.4645
Ni	1	494.5444	Gd	2	509.2249	Fe	1	526.7269	Fe	2	542.5249
Fe	1	494.5636	Ni	1	509.993	Ti	2	526.8608	Ti	1	542.9137
Fe	1	494.6387	Fe	1	510.403	Cr	1	527.2	Mn	1	543.2539
Sm	2	494.863	Fe	1	511.0413	Ce	2	527.4229	Fe	1	543.2948
Er	2	495.1743	Zr	2	511.227	Cr	2	527.9876	Fe	1	543.4524
Fe	1	495.7596	La	2	511.456	Co	1	528.0626	V	2	543.9303
Sr	1	496.2259	Ni	1	511.5392	Fe	1	528.3621	Co	1	544.4584
Fe	1	496.2572	Sm	2	511.669	Fe	2	528.4103	Fe	1	544.5042
Cr	1	496.4927	Mn	1	511.793	Fe	1	528.4425	Fe	1	544.6916
Ni	1	496.5167	Ti	1	512.0415	Nd	2	529.316	Fe	1	546.6396
Mn	1	496.5855	Y	2	512.3211	Cr	1	529.849	Fe	1	546.6987
Fe	1	496.6088	Fe	1	512.4619	Fe	1	529.8776	Mn	1	547.0631
Fe	1	496.9917	Fe	1	512.5117	Co	1	530.1041	Fe	1	547.2709
Sm	2	497.217	Fe	1	512.7359	Fe	1	530.23	Fe	1	547.3163
Ni	1	497.6325	Ti	2	512.9156	Cr	1	530.418	Fe	1	547.39
Fe	1	497.7648	Nd	2	513.059	Cr	2	530.5853	Fe	1	548.1243
Ti	2	498.1355	Fe	2	513.2661	Cr	2	530.8408	Co	1	548.3099
Ti	1	498.173	Pr	2	513.514	Cr	2	531.0686	Fe	1	548.3354
Fe	1	498.2499	Fe	2	513.6795	Cr	1	531.2856	Fe	1	548.7145
Na	1	498.2814	Co	1	514.6752	Cr	2	531.3563	Ti	1	549.0148
Fe	1	498.3853	Na	1	514.8838	Fe	1	531.7525	Ti	2	549.0693

Table A.2 LL2: Line list for parameters estimation.

Element	Exc.	λ (nm)	Element	Exc.	λ (nm)	Element	Exc.	λ (nm)
Fe	1	480.0649	Ti	1	504.3584	Fe	2	528.4103
Cr	1	480.1025	Fe	1	504.4211	Fe	1	528.4425
Ni	1	481.1983	Fe	1	504.8436	Cr	1	529.849
Fe	1	489.6439	Fe	1	505.4642	Fe	1	529.8776
Fe	1	491.8012	Ti	1	506.5985	Fe	1	530.23
Fe	1	491.8994	Cr	1	506.7713	Cr	1	530.418
Ti	1	491.9861	Ti	2	506.909	Cr	2	531.0686
Fe	1	492.0502	Fe	1	507.6264	Cr	1	531.2856
Fe	1	492.4301	Fe	1	507.9223	Fe	1	531.7525
Fe	1	492.477	Fe	1	507.974	Cr	1	531.8771
Ni	1	492.5559	Fe	1	508.3338	Fe	1	531.9035
Cr	1	493.6335	Fe	1	509.0773	Fe	1	532.0036
Ni	1	493.7348	Ni	1	509.993	Fe	1	532.4179
Fe	1	493.8814	Fe	1	510.403	Fe	2	532.5552
Ni	1	494.5444	Fe	1	511.0413	Fe	1	532.7252
Fe	1	494.5636	Ni	1	511.5392	Cr	1	532.9138
Fe	1	494.6387	Ti	1	512.0415	Cr	1	532.9784
Fe	1	495.7596	Fe	1	512.4619	Fe	1	532.9989
Fe	1	496.2572	Fe	1	512.5117	Ti	2	533.6786
Cr	1	496.4927	Fe	1	512.7359	Fe	1	533.9929
Ni	1	496.5167	Fe	2	513.2661	Cr	1	534.0447
Fe	1	496.6088	Fe	2	513.6795	Ti	2	538.1022
Fe	1	496.9917	Ti	1	521.9701	Fe	1	538.6333
Ni	1	497.6325	Ni	1	522.029	Cr	1	538.6968
Fe	1	497.7648	Fe	1	522.2395	Fe	1	538.9479
Ti	2	498.1355	Ti	1	522.362	Ni	1	539.2331
Ti	1	498.173	Ti	1	522.454	Fe	1	539.3167
Fe	1	498.2499	Fe	1	522.5526	Fe	1	539.7618
Fe	1	498.3853	Ti	2	522.6538	Fe	1	539.8279
Fe	1	498.4605	Fe	1	523.0691	Fe	1	540.0501
Fe	1	498.4629	Fe	2	523.4623	Fe	1	541.2784
Fe	1	498.5983	Cr	2	523.7328	Fe	2	541.407
Fe	1	499.1268	Fe	1	524.2491	Fe	1	542.4068
Ca	2	500.1479	Fe	1	524.3776	Ni	1	542.4645
Fe	1	500.2792	Cr	2	524.6768	Fe	2	542.5249
Ni	1	500.3741	Cr	1	524.7565	Ti	1	542.9137
Fe	1	500.4044	Cr	2	524.9437	Fe	1	543.2948
Fe	1	500.5712	Fe	1	525.3021	Fe	1	543.4524
Ti	1	500.9645	Fe	1	525.3462	Fe	1	544.5042
Ti	1	501.6161	Fe	2	525.6932	Fe	1	544.6916
Ti	1	502.0026	Fe	1	525.7655	Fe	1	546.6396
Fe	1	502.3186	Ca	1	526.0387	Fe	1	546.6987
Fe	1	502.8126	Fe	1	526.3306	Fe	1	547.2709
Fe	1	502.9618	Fe	2	526.4802	Fe	1	547.3163
Fe	1	503.0778	Cr	1	526.5148	Fe	1	547.39
Fe	1	503.1914	Fe	1	526.7269	Fe	1	548.1243
Fe	1	503.6922	Ti	2	526.8608	Fe	1	548.3099
Ti	1	503.9957	Cr	1	527.2	Fe	1	548.7145
Ni	1	504.2186	Fe	1	528.3621	Ti	1	549.0148

APPENDIX B

Mass distributions from surveys

There have been three major studies to look for hierarchical triples. While [Borkovits et al. \(2016\)](#) and [Hajdu et al. \(2019\)](#) used ETVs to extract the orbital parameters, [Czavalinga et al. \(2023\)](#) used the *Gaia* DR3 binary catalogue to identify systems whose outer orbits have been flagged as a binary. To get an estimate of mass ratio, we need to connect the orbital parameters with masses using tertiary mass function derived from Kepler's law,

$$f(m_C) = \frac{m_C^3 \sin^3 i}{(m_{\text{bin}} + m_C)^2} = \frac{P_2 K^3}{2\pi G} (1 - e^2)^{3/2} \quad (\text{B.1})$$

where m_C is the tertiary mass, m_{bin} is the total binary mass, P_2 is the period of the tertiary orbit, e is the tertiary orbit eccentricity and K is the semi-amplitude of RV signal or ETV signal. [Equation B.1](#) can be transformed into a cubic equation of $q = m_C/m_{\text{bin}}$ as the variable with the coefficients being functions of f and m_{bin} . For the ETV surveys, we have estimates of f . Therefore in such a case it is easy to numerically solve the following cubic equation, assuming a m_{bin} ,

$$m_{\text{bin}} q^3 - f q^2 - 2f q - f = 0 \quad (\text{B.2})$$

Solving this equation for parameters estimated from [Czavalinga et al. \(2023\)](#) is not straightforward as f is not available. The only unknown in the expression for f is K . For our approximation, we set

$$K = 2\pi a_2 / P_2 \quad (\text{B.3})$$

where a_2 is the outer orbit semi-major axis available from *Gaia* DR3 binary solutions. Using this we also estimate q distribution from all the surveys, assuming $m_{\text{bin}} = 2M_{\odot}$.

List of acronyms

A

AGB Asymptotic Giant Branch.

APOGEE Apache Point Observatory Galactic Evolution Experiment.

ASAS Automated All-Sky Survey.

B

BD Brown Dwarf.

BF Broadening Function.

C

CCF Cross Correlation Function.

CEE Common Envelope Evolution.

CF Core Fragmentation.

CHT Compact Hierarchical Triple.

CMD Colour-Magnitude Diagram.

COM Center Of Mass.

CoRoT Convection, Rotation and planetary Transits.

CTIO Cerro Tololo Inter-American Observatory.

CVZ Continuous Viewing Zone.

D

DEB Detached Eclipsing Binary.

DI Disk Instability.

E

E2CHT Doubly Eclipsing Compact Hierarchical Triples.

E3CHT Triply Eclipsing Compact Hierarchical Triples.

EB Eclipsing Binary.

EDV Eclipse depth variation.

EPRV Extreme Precision Radial Velocity.

ESO European Southern Observatory.

ET Eclipse Timing.

ETV Eclipse Timing Variations.

EZLK Eccentric von Zeipel-Lidov-Kozai.

G

GAIA Global Astrometric Interferometer for Astrophysics.

GC Globular Cluster.

GES GAIA ESO Survey.

GW Gravitational Wave.

H

HRS High-Resolution Telescope.

I

IMF Initial Mass Function.

IMM Independent Multiplicity Model.

L

LC Light Curve.

LL Line List (1,2).

LTTE Light Travel Time Effect.

M

MC Monte Carlo.

MCMC Markov Chain Monte Carlo.

MIEK Mass-loss Induced Eccentric ZLK.

MS Main Sequence.

MSC Multi Star Catalog.

MSS Multiple Star System.

O

OGLE Optical Gravitational Lensing Experiment.

P

PLATO PLANetary Transits and Oscillations of stars.

PN(e) Planetary Nebula(e).

R

RAVE Rad.

RGB Red Giant Branch.

RLOF Roche Lobe Over Flow.

RUWE Renormalised Unit Weight Error.

RV Radial Velocity.

S

SALT South African Large Telescope.

SB2 Spectroscopic Binary double-lined.

SSF Synthetic Spectral Fitting.

ST2 Spectroscopic triple, double-lined.

ST3 Spectroscopic triple, triple-lined.

T

TESS Transiting Exoplanet Survey Satellite.

TRGB Tip of Red Giant Branch.

W

WD White Dwarf.

Z

ZLK von Zeipel-Lidov-Kozai.

Bibliography

- Abt, H. A., & Levy, S. G. 1976, *ApJS*, 30, 273 ([ADS entry](#))
- Alibert, Y., Mordasini, C., Benz, W., & Winisdoerffer, C. 2005, *A&A*, 434, 343 ([ADS entry](#))
- Alonso, R., Deeg, H. J., Hoyer, S., Lodieu, N., Palle, E., & Sanchis-Ojeda, R. 2015, *A&A*, 584, L8 ([ADS entry](#))
- Antognini, J. M. O. 2015, *MNRAS*, 452, 3610 ([ADS entry](#))
- Applegate, J. H. 1992, *ApJ*, 385, 621 ([ADS entry](#))
- Asplund, M., Grevesse, N., Sauval, A. J., & Scott, P. 2009, *ARA&A*, 47, 481 ([ADS entry](#))
- Baglin, A., et al. 2006, in 36th COSPAR Scientific Assembly, Vol. 36, 3749 ([ADS entry](#))
- Bagnuolo, William G., J., & Gies, D. R. 1991, *ApJ*, 376, 266 ([ADS entry](#))
- Balaji, B., Croll, B., Levine, A. M., & Rappaport, S. 2015a, *MNRAS*, 448, 429 ([ADS entry](#))
- . 2015b, *MNRAS*, 448, 429 ([ADS entry](#))
- Bataille, M., Libert, A. S., & Correia, A. C. M. 2018, *MNRAS*, 479, 4749 ([ADS entry](#))
- Bate, M. R. 2019, *MNRAS*, 484, 2341 ([ADS entry](#))
- Batten, A. H. 1973, *Binary and multiple systems of stars* (Pergamon) ([ADS entry](#))
- Blaes, O., Lee, M. H., & Socrates, A. 2002, *ApJ*, 578, 775 ([ADS entry](#))
- Blanco-Cuaresma, S. 2019, *MNRAS*, 486, 2075 ([ADS entry](#))
- Blanco-Cuaresma, S., Soubiran, C., Heiter, U., & Jofré, P. 2014, *A&A*, 569, A111 ([ADS entry](#))
- Borkovits, T. 2022, *Galaxies*, 10, 9 ([ADS entry](#))

- Borkovits, T., Érdi, B., Forgács-Dajka, E., & Kovács, T. 2003, *A&A*, 398, 1091 ([ADS entry](#))
- Borkovits, T., Hajdu, T., Sztakovics, J., Rappaport, S., Levine, A., Bíró, I. B., & Klagyivik, P. 2016, *MNRAS*, 455, 4136 ([ADS entry](#))
- Borkovits, T., Rappaport, S. A., Hajdu, T., Maxted, P. F. L., Pál, A., Forgács-Dajka, E., Klagyivik, P., & Mitnyan, T. 2020, *MNRAS*, 493, 5005 ([ADS entry](#))
- Borkovits, T., Rappaport, S. A., Toonen, S., Moe, M., Mitnyan, T., & Csányi, I. 2022, *Monthly Notices of the Royal Astronomical Society*, stac1983 ([Link](#))
- Borkovits, T., et al. 2013, *MNRAS*, 428, 1656 ([ADS entry](#))
- Borucki, W. J., et al. 2010, *Science*, 327, 977 ([ADS entry](#))
- Bradstreet, D. H., & Guinan, E. F. 1994, in *Astronomical Society of the Pacific Conference Series*, Vol. 56, *Interacting Binary Stars*, ed. A. W. Shafter, 228 ([ADS entry](#))
- Cantiello, M., Mankovich, C., Bildsten, L., Christensen-Dalsgaard, J., & Paxton, B. 2014, *ApJ*, 788, 93 ([ADS entry](#))
- Chambliss, C. R. 1992, *PASP*, 104, 663 ([ADS entry](#))
- Chandler, S. C. 1888, *AJ*, 7, 169 ([ADS entry](#))
- Church, R. P., Dischler, J., Davies, M. B., Tout, C. A., Adams, T., & Beer, M. E. 2009, *MNRAS*, 395, 1127 ([ADS entry](#))
- Ciardi, D. R., Beichman, C. A., Horch, E. P., & Howell, S. B. 2015, *ApJ*, 805, 16 ([ADS entry](#))
- Claret, A., & Bloemen, S. 2011, *A&A*, 529, A75 ([ADS entry](#))
- Claret, A., & Torres, G. 2016, *A&A*, 592, A15 ([ADS entry](#))
- Conroy, K. E., Prša, A., Stassun, K. G., Orosz, J. A., Fabrycky, D. C., & Welsh, W. F. 2014, *AJ*, 147, 45 ([ADS entry](#))
- Czavalinga, D. R., Mitnyan, T., Rappaport, S. A., Borkovits, T., Gagliano, R., Omohundro, M., Kristiansen, M. H. K., & Pál, A. 2023, *A&A*, 670, A75 ([ADS entry](#))
- Czekala, I., et al. 2017, *ApJ*, 851, 132 ([ADS entry](#))
- David, T. J., Hillenbrand, L. A., Gillen, E., Cody, A. M., Howell, S. B., Isaacson, H. T., & Livingston, J. H. 2019, *ApJ*, 872, 161 ([ADS entry](#))
- Davis, P. J., Siess, L., & Deschamps, R. 2013, *A&A*, 556, A4 ([ADS entry](#))
- de Mink, S. E., Cantiello, M., Langer, N., Pols, O. R., Brott, I., & Yoon, S. C. 2009, *A&A*, 497, 243 ([ADS entry](#))
- De Silva, G. M., et al. 2015, *MNRAS*, 449, 2604 ([ADS entry](#))
- Debusscher, J., et al. 2013, *A&A*, 556, A56 ([ADS entry](#))

- Duchêne, G., & Kraus, A. 2013, *ARA&A*, 51, 269 ([ADS entry](#))
- Duquennoy, A., & Mayor, M. 1991, *A&A*, 248, 485 ([ADS entry](#))
- Duquennoy, A., Mayor, M., & Halbwachs, J. L. 1991, *A&AS*, 88, 281 ([ADS entry](#))
- Eggleton, P. P. 2002, in *Astronomical Society of the Pacific Conference Series*, Vol. 279, *Exotic Stars as Challenges to Evolution*, ed. C. A. Tout & W. van Hamme, 37 ([ADS entry](#))
- Eggleton, P. P., & Kiseleva-Eggleton, L. 2001, *ApJ*, 562, 1012 ([ADS entry](#))
- Eisner, N. L., et al. 2022, *MNRAS*, 511, 4710 ([ADS entry](#))
- El-Badry, K., Rix, H.-W., & Heintz, T. M. 2021, *MNRAS*, 506, 2269 ([ADS entry](#))
- Etzel, P. B. 1981, in *NATO Advanced Study Institute (ASI) Series C*, Vol. 69, *Photometric and Spectroscopic Binary Systems*, ed. E. B. Carling & Z. Kopal, 111 ([ADS entry](#))
- Fabrycky, D., & Tremaine, S. 2007, *ApJ*, 669, 1298 ([ADS entry](#))
- Fekel, F. C., J. 1981, *ApJ*, 246, 879 ([ADS entry](#))
- Fischer, D. A., & Valenti, J. 2005, *ApJ*, 622, 1102 ([ADS entry](#))
- Fischer, D. A., et al. 2016, *PASP*, 128, 066001 ([ADS entry](#))
- Freedman, W. L., et al. 2020, *ApJ*, 891, 57 ([ADS entry](#))
- Fulton, B. J., Petigura, E. A., Blunt, S., & Sinukoff, E. 2018, *PASP*, 130, 044504 ([ADS entry](#))
- Gaia Collaboration et al. 2016, *A&A*, 595, A1 ([ADS entry](#))
- Gies, D. R., Williams, S. J., Matson, R. A., Guo, Z., Thomas, S. M., Orosz, J. A., & Peters, G. J. 2012, *AJ*, 143, 137 ([ADS entry](#))
- Gilliland, R. L., et al. 2010, *PASP*, 122, 131 ([ADS entry](#))
- Gilmore, G., et al. 2012, *The Messenger*, 147, 25 ([ADS entry](#))
- González, J. F., & Levato, H. 2006, *A&A*, 448, 283 ([ADS entry](#))
- Grether, D., & Lineweaver, C. H. 2006, *ApJ*, 640, 1051 ([ADS entry](#))
- Gronchi, G. F., & Tommei, G. 2007, *Discrete and Continuous Dynamical Systems - B*, 7, 755
- Gustafsson, B., Edvardsson, B., Eriksson, K., Jørgensen, U. G., Nordlund, Å., & Plez, B. 2008, *A&A*, 486, 951 ([ADS entry](#))
- Hadrava, P. 1995, *A&AS*, 114, 393 ([ADS entry](#))
- . 2009, arXiv e-prints, arXiv:0909.0172 ([ADS entry](#))
- Hajdu, T., Borkovits, T., Forgács-Dajka, E., Sztakovics, J., & Bódi, A. 2022, *MNRAS*, 509, 246 ([ADS entry](#))

- Hajdu, T., Borkovits, T., Forgács-Dajka, E., Sztakovics, J., Marschalkó, G., & Kutrovátz, G. 2019, *MNRAS*, 485, 2562 ([ADS entry](#))
- Hamers, A. S., Rantala, A., Neunteufel, P., Preece, H., & Vynatheya, P. 2021, *MNRAS*, 502, 4479 ([ADS entry](#))
- Handler, G., et al. 2020, *Nature Astronomy*, 4, 684 ([ADS entry](#))
- Heath, R. M., & Nixon, C. J. 2020, *A&A*, 641, A64 ([ADS entry](#))
- Hełminiak, K. G., Konacki, M., Ratajczak, M., Jordán, A., Espinoza, N., Brahm, R., Kambe, E., & Ukita, N. 2015, in *Astronomical Society of the Pacific Conference Series*, Vol. 496, *Living Together: Planets, Host Stars and Binaries*, ed. S. M. Rucinski, G. Torres, & M. Zejda, 76 ([ADS entry](#))
- Hełminiak, K. G., Marcadon, F., Moharana, A., Pawar, T., & Konacki, M. 2022, in *Polish Astronomical Society Meeting Series*, Vol. 12, *XL Polish Astronomical Society Meeting*, ed. E. Szuszkiewicz, A. Majczyna, K. Małek, M. Ratajczak, E. Niemczura, U. Bąk-Stęślicka, R. Poleski, M. Bilicki, & Ł. Wyrzykowski, 163–166 ([ADS entry](#))
- Hełminiak, K. G., Ukita, N., Kambe, E., Kozłowski, S. K., Pawłaszek, R., Maehara, H., Baranec, C., & Konacki, M. 2017a, *A&A*, 602, A30 ([ADS entry](#))
- Hełminiak, K. G., et al. 2017b, *MNRAS*, 468, 1726 ([ADS entry](#))
- Hensberge, H., Ilijic, S., & Torres, K. B. V. 2008, *A&A*, 482, 1031 ([ADS entry](#))
- Herschel, W. 1786, *Philosophical Transactions of the Royal Society of London Series I*, 76, 457 ([ADS entry](#))
- . 1803, *Philosophical Transactions of the Royal Society of London Series I*, 93, 339 ([ADS entry](#))
- Howell, S. B., et al. 2014, *PASP*, 126, 398 ([ADS entry](#))
- Huber, D., et al. 2013, *ApJ*, 767, 127 ([ADS entry](#))
- Hut, P. 1981, *A&A*, 99, 126 ([ADS entry](#))
- Ilijic, S., Hensberge, H., Pavlovski, K., & Freyhammer, L. M. 2004, in *Astronomical Society of the Pacific Conference Series*, Vol. 318, *Spectroscopically and Spatially Resolving the Components of the Close Binary Stars*, ed. R. W. Hilditch, H. Hensberge, & K. Pavlovski, 111–113 ([ADS entry](#))
- Innanen, K. A., Zheng, J. Q., Mikkola, S., & Valtonen, M. J. 1997, *AJ*, 113, 1915 ([ADS entry](#))
- Jones, D., Pejcha, O., & Corradi, R. L. M. 2019, *MNRAS*, 489, 2195 ([Link](#))
- Kalimeris, A., Rovithis-Livaniou, H., & Rovithis, P. 2002, *A&A*, 387, 969 ([ADS entry](#))
- Kamiński, T., et al. 2021, *A&A*, 655, A32 ([ADS entry](#))

- Kang, Y.-W. 2010, *Journal of Astronomy and Space Sciences*, 27, 75 ([ADS entry](#))
- Kinoshita, H., & Nakai, H. 1999, *Celestial Mechanics and Dynamical Astronomy*, 75, 125 ([ADS entry](#))
- Konacki, M., Muterspaugh, M. W., Kulkarni, S. R., & Hełminiak, K. G. 2010, *ApJ*, 719, 1293 ([ADS entry](#))
- Kopal, Z. 1959, *Close binary systems* ([ADS entry](#))
- Korth, J., Moharana, A., Pešta, M., Czavalinga, D. R., & Conroy, K. E. 2021, *Contributions of the Astronomical Observatory Skalnaté Pleso*, 51, 58 ([ADS entry](#))
- Kosiarek, M. R., et al. 2021, *AJ*, 161, 47 ([ADS entry](#))
- Kozai, Y. 1962, *AJ*, 67, 591 ([ADS entry](#))
- Kratter, K. M., Matzner, C. D., Krumholz, M. R., & Klein, R. I. 2010, *ApJ*, 708, 1585 ([ADS entry](#))
- Kuffmeier, M., Calcutt, H., & Kristensen, L. E. 2019, *A&A*, 628, A112 ([ADS entry](#))
- Kurucz, R. L. 2005, *Memorie della Societa Astronomica Italiana Supplementi*, 8, 14 ([ADS entry](#))
- Lee, J.-E., et al. 2023, *ApJ*, 953, 82 ([ADS entry](#))
- Li, T., Bedding, T. R., Huber, D., Ball, W. H., Stello, D., Murphy, S. J., & Bland-Hawthorn, J. 2018, *MNRAS*, 475, 981 ([ADS entry](#))
- Lidov, M. L. 1962, *Planet. Space Sci.*, 9, 719 ([ADS entry](#))
- Looney, L. W., Mundy, L. G., & Welch, W. J. 2000, *ApJ*, 529, 477 ([ADS entry](#))
- Lu, W., Rucinski, S. M., & Ogłóza, W. 2001, *AJ*, 122, 402 ([ADS entry](#))
- Ma, B., & Ge, J. 2014, *MNRAS*, 439, 2781 ([ADS entry](#))
- Majewski, S. R., et al. 2017, *AJ*, 154, 94 ([ADS entry](#))
- Maoz, D., Mannucci, F., & Nelemans, G. 2014, *ARA&A*, 52, 107 ([ADS entry](#))
- Marcadon, F., Hełminiak, K. G., Marques, J. P., Pawłaszek, R., Sybilski, P., Kozłowski, S. K., Ratajczak, M., & Konacki, M. 2020, *MNRAS*, 499, 3019 ([ADS entry](#))
- Marcy, G. W., & Butler, R. P. 2000, *PASP*, 112, 137 ([ADS entry](#))
- Mardling, R. A., & Aarseth, S. J. 2001, *MNRAS*, 321, 398 ([ADS entry](#))
- Maxted, P. F. L., et al. 2020, *MNRAS*, 498, 332 ([ADS entry](#))
- Mazzola, C. N., et al. 2020, *MNRAS*, 499, 1607 ([ADS entry](#))
- McQuillan, A., Mazeh, T., & Aigrain, S. 2014, *ApJS*, 211, 24 ([ADS entry](#))

- Meltzer, A. S. 1957, *ApJ*, 125, 359 ([ADS entry](#))
- Meunier, N. 2021, arXiv e-prints, arXiv:2104.06072 ([ADS entry](#))
- Michaely, E., & Perets, H. B. 2014, *ApJ*, 794, 122 ([ADS entry](#))
- Miller, N. J., Maxted, P. F. L., & Smalley, B. 2020, *MNRAS*, 497, 2899 ([ADS entry](#))
- Mitnyan, T., Borkovits, T., Czavalinga, D. R., Rappaport, S. A., Pál, A., Powell, B. P., & Hajdu, T. 2024, arXiv e-prints, arXiv:2402.01486 ([ADS entry](#))
- Mitnyan, T., Borkovits, T., Rappaport, S. A., Pál, A., & Maxted, P. F. L. 2020, *MNRAS*, 498, 6034 ([ADS entry](#))
- Moe, M., & Di Stefano, R. 2017, *ApJS*, 230, 15 ([ADS entry](#))
- Moe, M., Kratter, K. M., & Badenes, C. 2019, *ApJ*, 875, 61 ([ADS entry](#))
- Moré, J. J. 1978, in *Lecture Notes in Mathematics*, Berlin Springer Verlag, Vol. 630 (Springer), 105–116 ([ADS entry](#))
- Mosser, B., et al. 2012, *A&A*, 548, A10 ([ADS entry](#))
- Naoz, S. 2016, *ARA&A*, 54, 441 ([ADS entry](#))
- Naoz, S., & Fabrycky, D. C. 2014, *ApJ*, 793, 137 ([ADS entry](#))
- Naoz, S., Farr, W. M., Lithwick, Y., Rasio, F. A., & Teyssandier, J. 2013, *MNRAS*, 431, 2155 ([ADS entry](#))
- Naoz, S., Farr, W. M., & Rasio, F. A. 2012, *ApJ*, 754, L36 ([ADS entry](#))
- Nelder, J. A., & Mead, R. 1965, *The Computer Journal*, 7, 308 ([Link](#))
- Netto, Y., Lorenzo-Oliveira, D., Meléndez, J., Yana Galarza, J., Haywood, R. D., Spina, L., & dos Santos, L. A. 2021, *AJ*, 162, 160 ([ADS entry](#))
- Offner, S. S. R., Kratter, K. M., Matzner, C. D., Krumholz, M. R., & Klein, R. I. 2010, *ApJ*, 725, 1485 ([ADS entry](#))
- Offner, S. S. R., Moe, M., Kratter, K. M., Sadavoy, S. I., Jensen, E. L. N., & Tobin, J. J. 2023, in *Astronomical Society of the Pacific Conference Series*, Vol. 534, *Protostars and Planets VII*, ed. S. Inutsuka, Y. Aikawa, T. Muto, K. Tomida, & M. Tamura, 275 ([ADS entry](#))
- Paczyński, B. 1971, *ARA&A*, 9, 183 ([ADS entry](#))
- Perets, H. B., & Fabrycky, D. C. 2009, *ApJ*, 697, 1048 ([ADS entry](#))
- Perpinyà-Vallès, M., Rebassa-Mansergas, A., Gänsicke, B. T., Toonen, S., Hermes, J. J., Gentile Fusillo, N. P., & Tremblay, P. E. 2019, *MNRAS*, 483, 901 ([ADS entry](#))
- Perryman, M. A. C., et al. 1997, *A&A*, 323, L49 ([ADS entry](#))
- Pietrzyński, G., et al. 2013, *Nature*, 495, 76 ([ADS entry](#))

- Pojmanski, G. 1997, *Acta Astronomica*, 47, 467 ([ADS entry](#))
- Pols, O. R., Tout, C. A., Schroder, K.-P., Eggleton, P. P., & Manners, J. 1997, *MNRAS*, 289, 869 ([ADS entry](#))
- Portegies Zwart, S. F., & van den Heuvel, E. P. J. 2016, *MNRAS*, 456, 3401 ([ADS entry](#))
- Preece, H. P., Hamers, A. S., Battich, T., & Rajamuthukumar, A. S. 2022, *MNRAS*, 517, 2111 ([ADS entry](#))
- Prša, A. 2018, *Modeling and Analysis of Eclipsing Binary Stars; The theory and design principles of PHOEBE* (Institute of Physics) ([ADS entry](#))
- Prša, A., et al. 2011, *AJ*, 141, 83 ([ADS entry](#))
- Raghavan, D., et al. 2010, *ApJS*, 190, 1 ([ADS entry](#))
- Randich, S., Gilmore, G., & Gaia-ESO Consortium. 2013, *The Messenger*, 154, 47 ([ADS entry](#))
- Rappaport, S., Deck, K., Levine, A., Borkovits, T., Carter, J., El Mellah, I., Sanchis-Ojeda, R., & Kalomeni, B. 2013, *ApJ*, 768, 33 ([ADS entry](#))
- Rappaport, S. A., et al. 2022, *MNRAS*, 513, 4341 ([ADS entry](#))
- . 2023, *MNRAS*, 521, 558 ([ADS entry](#))
- Rauer, H., et al. 2014, *Experimental Astronomy*, 38, 249 ([ADS entry](#))
- Rein, H., & Liu, S. F. 2012, *A&A*, 537, A128 ([ADS entry](#))
- Rein, H., & Tamayo, D. 2015, *MNRAS*, 452, 376 ([ADS entry](#))
- Reinhold, T., Reiners, A., & Basri, G. 2013, *A&A*, 560, A4 ([ADS entry](#))
- Ricker, G. R., et al. 2015, *Journal of Astronomical Telescopes, Instruments, and Systems*, 1, 014003 ([ADS entry](#))
- Riess, A. G., et al. 2016, *ApJ*, 826, 56
- Rohde, P. F., Walch, S., Clarke, S. D., Seifried, D., Whitworth, A. P., & Klepitko, A. 2021, *MNRAS*, 500, 3594 ([ADS entry](#))
- Rucinski, S. 1999, in *Astronomical Society of the Pacific Conference Series*, Vol. 185, IAU Colloq. 170: Precise Stellar Radial Velocities, ed. J. B. Hearnshaw & C. D. Scarfe, 82 ([ADS entry](#))
- Sana, H., et al. 2012, *Science*, 337, 444 ([ADS entry](#))
- Santos, N. C., Israelian, G., & Mayor, M. 2001, *A&A*, 373, 1019 ([ADS entry](#))
- Seeburger, R., Rix, H.-W., El-Badry, K., Xiang, M., & Fouesneau, M. 2024, *MNRAS*, 530, 1935 ([ADS entry](#))

- Shappee, B. J., & Thompson, T. A. 2013, *ApJ*, 766, 64 ([ADS entry](#))
- Shenar, T., et al. 2020, *A&A*, 639, L6 ([ADS entry](#))
- . 2022, *A&A*, 665, A148 ([ADS entry](#))
- Simon, K. P., & Sturm, E. 1994, *A&A*, 281, 286 ([ADS entry](#))
- Singh Rathour, R., Hajdu, G., Smolec, R., Karczmarek, P., Hócdé, V., Ziółkowska, O., Soszyński, I., & Udalski, A. 2024, arXiv e-prints, arXiv:2403.14039 ([ADS entry](#))
- Smeyers, P., & Willems, B. 2001, *A&A*, 373, 173 ([ADS entry](#))
- Smith, N., et al. 2018, *MNRAS*, 480, 1466 ([ADS entry](#))
- Southworth, J. 2013, *A&A*, 557, A119 ([ADS entry](#))
- Southworth, J., Bruntt, H., & Buzasi, D. L. 2007, *A&A*, 467, 1215 ([ADS entry](#))
- Stassun, K. G., Hebb, L., Lopez-Morales, M., & Prsa, A. 2009, arXiv e-prints, arXiv:0902.2548 ([ADS entry](#))
- Stebbins, J. 1911, *ApJ*, 34, 112 ([ADS entry](#))
- Steinmetz, M., et al. 2006, *AJ*, 132, 1645 ([ADS entry](#))
- Sterzik, M. F., & Tokovinin, A. A. 2002, *A&A*, 384, 1030 ([ADS entry](#))
- Tamayo, D., Rein, H., Shi, P., & Hernandez, D. M. 2020, *MNRAS*, 491, 2885 ([ADS entry](#))
- Tkachenko, A. 2015, *A&A*, 581, A129 ([ADS entry](#))
- Tkachenko, A., et al. 2014, *MNRAS*, 438, 3093 ([ADS entry](#))
- Tobin, J. J., et al. 2016, *Nature*, 538, 483 ([ADS entry](#))
- Tokovinin, A. 2004, in *Revista Mexicana de Astronomia y Astrofisica Conference Series*, Vol. 21, *Revista Mexicana de Astronomia y Astrofisica Conference Series*, ed. C. Allen & C. Scarfe, 7–14 ([ADS entry](#))
- Tokovinin, A. 2017a, *ApJ*, 844, 103 ([ADS entry](#))
- . 2017b, *ApJ*, 844, 103 ([ADS entry](#))
- . 2018, *ApJS*, 235, 6 ([ADS entry](#))
- . 2021, *Universe*, 7, 352 ([ADS entry](#))
- Tokovinin, A., & Moe, M. 2020, *MNRAS*, 491, 5158 ([ADS entry](#))
- Tokovinin, A. A. 1997, *A&AS*, 124, 75 ([ADS entry](#))
- Toonen, S., Boekholt, T. C. N., & Portegies Zwart, S. 2022, *A&A*, 661, A61 ([ADS entry](#))

- Toonen, S., Hamers, A., & Portegies Zwart, S. 2017, in American Astronomical Society Meeting Abstracts, Vol. 229, American Astronomical Society Meeting Abstracts #229, 326.05 ([ADS entry](#))
- Toonen, S., Portegies Zwart, S., Hamers, A. S., & Bandopadhyay, D. 2020, *A&A*, 640, A16 ([ADS entry](#))
- Torres, G., Andersen, J., & Giménez, A. 2010, *A&A Rev.*, 18, 67 ([ADS entry](#))
- Udalski, A., Szymanski, M., Kaluzny, J., Kubiak, M., & Mateo, M. 1992, *Acta Astronomica*, 42, 253 ([ADS entry](#))
- Vázquez-Semadeni, E., Palau, A., Ballesteros-Paredes, J., Gómez, G. C., & Zamora-Avilés, M. 2019, *MNRAS*, 490, 3061 ([ADS entry](#))
- Vogel, H. C. 1890, *PASP*, 2, 27 ([ADS entry](#))
- von Zeipel, H. 1910, *Astronomische Nachrichten*, 183, 345 ([ADS entry](#))
- Worley, C. E. 1967, in *On the Evolution of Double Stars*, ed. J. Dommanget, Vol. 17, 221 ([ADS entry](#))
- Wu, Y., & Murray, N. 2003, *ApJ*, 589, 605 ([ADS entry](#))
- Xia, F., Fu, Y., & Wang, X. 2019, *ApJ*, 882, 147 ([ADS entry](#))